THE ORIGIN AND EVOLUTION OF COLD GASEOUS STRUCTURES IN GALAXIES AND GALACTIC OUTFLOWS

by

David John Williamson

A thesis submitted to the faculty of
Saint Mary's University,
Halifax, Nova Scotia, Canada
in partial fulfillment of the requirements for the degree of

Doctor of Philosophy in Astronomy

Approved: Dr. Robert J. Thacker, Advisor

Approved: Dr. Robert Deupree, Reader

Approved: Dr. Marcin Sawicki, Reader

Approved: Dr. Hugo Martel, External Examiner

Department of Astronomy and Physics
Saint Mary's University
December 12th, 2013

ABSTRACT

THE ORIGIN AND EVOLUTION OF COLD GASEOUS
STRUCTURES IN GALAXIES AND GALACTIC OUTFLOWS

by David John Williamson

December 12th, 2013

This thesis examines the formation and evolution of cold gaseous structures in galaxies and galactic outflows in two distinct scenarios.

Previous analytic estimates of the viscous time-scale due to cloud-cloud collisions in Milky Way-like discs have produced values on the order of $t_\nu \sim 1000$ Gyr, and hence it has been concluded that cloud-cloud collisions are not important to the dynamical evolution of these galaxies. However, these estimates had not been tested with full three dimensional hydrodynamic simulations, which we perform using the smoothed particle hydrodynamics code HYDRA-OMP, making improvements to its parallelism to do so. These simulations produce a viscous time-scale of $t_\nu \sim 10$ Gyr, suggesting that while the effective viscosity is weak, it is not entirely insignificant. The discrepancy between the analytic and the numerical results is traced to an error in the analytic calculation.

Observations have revealed cold gas with large velocity dispersions (FWHM ~ 300 km/s) within the hot outflows of Ultra-luminous Infrared Galaxies (ULIRGs). This gas may trace its origin to the Rayleigh-Taylor (RT) fragmentation of a super-bubble wall. We model this scenario at two scales to attempt to recreate this effect in three-dimensional hydrodynamic simulations using FLASH. Although the models are not well-converged with respect to resolution, we are able to produce cold gas in outflows with large velocity dispersions (FWHM $\sim 200 - 300$ km/s). Our small-scale models indeed produce this cold gas through RT fragmentation of the super-bubble wall, but our large-scale models produce this cold gas by hot bubbles fragmenting the disc's gas into cold clumps which are then accelerated by thermal pressure, or by cooling within the outflow. We also make use of a sub-grid turbulence model. After several significant errors in a code supplied by a collaborator were corrected, this model produces simulations that are better converged, at the cost of smoothing away the cold gas.

SAINT MARY'S UNIVERSITY

GRADUATE COMMITTEE APPROVAL

THE ORIGIN AND EVOLUTION OF COLD GASEOUS STRUCTURES IN GALAXIES AND GALACTIC OUTFLOWS

by

David John Williamson

A thesis submitted to
Saint Mary's University
Halifax, Nova Scotia, Canada
in partial fulfilment of the requirements for the degree of

Doctor of Philosophy in Astronomy.

This thesis has been read by each member of the following graduate committee and by majority vote has been found to be satisfactory.

Date	Robert J. Thacker, Advisor
Date	Robert Deupree, Reader
Date	Marcin Sawicki, Reader
Date	Hugo Martel, External Examiner

ACKNOWLEDGMENTS

Thanks and appreciation are due to:

Rob Thacker, for guidance and support,

Evan Scannapieco, and Larry Widrow, for providing codes used in this work,

Brad Gibson, Chris Geroux, Jon Ramsey, Mark Richardson and Will Gray for helpful discussions,

My family, in New Zealand, Canada, and around the world, for love, patience, and understanding,

And of course, Sarah Williamson, for surviving, and providing ramen.

There is nothing stable in the world;

uproar's your only music.

JOHN KEATS

The LORD said to Moses,

"I am going to come to you in a dense cloud..."

EXODUS 19:9

Contents

List of Tables

List of Figures

Chapter 1

Introduction

This thesis details investigations into the origin and evolution of cold gaseous structures in galaxies and galactic outflows. We have investigated two distinct scenarios: firstly, the formation of giant molecular clouds in Milky-Way type disc galaxies and how collisions between these clouds can generate an *effective viscosity* (Bell 2002; Williamson & Thacker 2012); and secondly, the formation of cold gas in turbulent outflows from Ultra-luminous Infrared Galaxies (ULIRGs) (for reviews, see Lonsdale et al. 2006; Veilleux 2006), and how this cold gas can explain the broad line-widths of NaI[1] absorption in ULIRGs (as in Fujita et al. 2009). These investigations are performed using *hydrodynamic* simulations.

Galactic hydrodynamics is an important and theoretically complex field (for reviews see Baugh 2006; Benson 2010). Although by mass a galaxy mostly consists of dark matter, and most of the baryonic matter in evolved discs consists of stars and other compact objects, the diffuse gaseous components — the interstellar medium (ISM) within a galaxy, as well as the intergalactic medium (IGM) that fills the space between galaxies — are critical in determining most of the characteristics of a galaxy, from morphology to star formation rates. Furthermore, although the circumgalactic gas of a galaxy is diffuse, it can extend much further from the centre of a galaxy than the stellar component and thus can still have a very large total mass.

Hydrodynamics models the evolution of the gas of a galaxy using sets of differential equations (see section 1.1), such as the Navier-Stokes equations (Mihalas & Weibel Mihalas 1984; Shu 1992). These equations predict the change in macroscopic quantities such as density, temperature and pressure over time, given some set of initial conditions. Unfortunately, it is almost never possible to find an analytic

[1] In this work, NaI only refers to unionised atomic sodium, and not to sodium iodide.

solution to these equations — indeed, one of the Clay Mathematics Institute's "Millenium Problems" is to prove only the existence and smoothness of solutions to the Navier-Stokes equations (Carlson et al. 2006). Instead, we must perform numerical simulations to find approximate solutions to particular problems.

Two of the major formulations for solving the Navier Stokes (and other) equations over some region are the Lagrangian and the Eulerian approaches. The choice of approach determines how the differential equations are formulated and implemented numerically. In the Eulerian approach, fluid is interpreted as flowing through a fixed coordinate system. The equations are formulated to follow the evolution of the relevant hydrodynamic quantities (density, pressure, velocity etc.) at each point in this fixed grid. In the discretised (i.e. numerical) form, the simulated volume is divided into cells. The hydrodynamic quantities are assigned values at the centre or face of each cell to give a grid of values, and the changes in these quantities are calculated by discretised differential equations. Here, the discretised grid is stationary, and fluid moves through it. One Eulerian method for solving the Navier Stokes equations is the piecewise-parabolic method (PPM) (Colella & Woodward 1984; O'Shea et al. 2004). PPM is used by popular adaptive-mesh-refinement codes such as FLASH (Fryxell et al. 2000) and ENZO. By contrast, in the Lagrangian approach, the evolution equations follow infinitesimal parcels of mass, and not a fixed grid. The numerical form in this case expands these infinitesimal parcels into finite-sized cells which move with the fluid. These cells are often represented as *particles*, each containing a constant mass of fluid. In astronomy, this is often implemented with the Smooth Particle Hydrodynamics (SPH) algorithm, as in codes such as GADGET (Springel 2005), HYDRA (Thacker & Couchman 2006), or Gasoline (Wadsley et al. 2004). Other Lagrangian algorithms have also been implemented in astrophysics, including the AREPO code (Springel 2010). In addition, there are codes whose algorithms can not be completely categorized as entirely Lagrangian or entirely Eulerian. These include semi-Lagrangian schemes (Staniforth & Côté 1991) and arbitrary Eulerian-Lagrangian schemes (Hirt et al. 1974).

Each approach has strengths and weaknesses, with different methods being more useful in certain numerical applications. Eulerian methods allow a simple geometry — often a cartesian, spherical, or cylindrical mesh — which permits straightforward, stable, low-error calculations of quantities such as derivatives, and fluxes. In the Lagrangian formulation, local quantities may be less accurate as the location of fluid particles is non-uniform and the code may, depending upon the algorithm chosen, be harder to code. However, Lagrangian methods allow a more direct calculation of trajectories, which is particularly beneficial for a collisionless (i.e. pressureless) fluid, or in a simulation which combines a collisionless component and a collisional component, or in a simulation which requires a higher level of positional accuracy. Lagrangian methods can also benefit from a sort of automatic "refining" of resolution — regions with a high concentration of mass will naturally contain a higher concentration of fluid cells, and hence be better resolved, provided the specific implementation takes advantage of this (for example, an SPH code with an adaptive smoothing length). This concentration of resolution is beneficial if the high-density regions are the regions of interest — such as in a simulation of cosmological galaxy formation — but this also implies that low-density gas is poorly resolved. Hence an Eulerian approach is often a better choice if low-density regions are important, as in the case of shockwaves travelling into the intergalactic medium, for example. Low density regions can be better resolved in Lagrangian codes by methods such as particle splitting (Kitsionas & Whitworth 2002) algorithms (at the cost of introducing perturbations during the splitting procedure), or by using particles of lower mass in lower density regions (but only if low and high density regions do not mix well). By contrast, in Eulerian approaches it is trivial to maintain a fixed resolution across the entire domain, regardless of density. Eulerian methods can be (and often are) greatly improved by introducing *adaptive refinements* to increase the resolution in critical areas, but this comes at the cost of additional complexity. This method is known as Adaptive Mesh Refinement (AMR) (Berger & Oliger 1984).

In a numerical scheme, it is always necessary to discretise the fluid, thereby placing a limit on the smallest resolved length and mass scales. This discretisation can remove many important physical processes below the length scale, which must either be ruled-out as negligible, or must be included with some sort of sub-resolution model (e.g. Leonard 1974). Critically in galactic simulations, the formation of stars and their interactions with the interstellar medium (i.e. stellar feedback) are currently unresolved in all full-scale galactic simulations, and despite increasing computational power, are likely to remain unresolved for some time: to resolve both a 10 kpc radius dwarf galaxy and a solar-radius star requires resolution that extends to 11 orders of magnitude. As a result, the ongoing development of sub-grid models for star formation and feedback is one of the major contemporary sub-fields of galaxy modelling (e.g. Katz 1992; Ceverino & Klypin 2009; Christensen et al. 2010; Murante et al. 2010; Durier & Dalla Vecchia 2012; Hopkins et al. 2012a; Agertz et al. 2012). Other important sub-grid processes that must be modelled include turbulence, and chemical or radiative processes such as cooling.

To properly understand the ramifications of discretisation, we must "smooth" the Navier-Stokes equations, splitting the density and velocity fields into large-scale and small-scale components. The mathematical details of this procedure are explained in more detail in Section 4.3.1. The non-linearity of the equations produces an additional term in the smoothed Navier-Stokes equations (Lesieur et al. 2005; Schmidt et al. 2006), which can be represented by an additional tensor that depends on small-scale fluctuations of the fluid. Being analogous to the stress tensor, this can be considered as a source of effective pressure and viscosity due to small-scale effects. In this thesis, we focus on two interpretations of this effective stress tensor:

Firstly, it can be used to model sub-grid effects in numerical simulations, where smoothing the Navier-Stokes equations is necessary due to resolution limits. As noted, physics below the resolution limit is not explicitly captured in this situation, and this can be alleviated by the modifying the effective stress tensor to at least approximately provide the sub-grid terms, as a "sub-grid-scale stress tensor". One major application

of this is to include the effects of turbulence — which can be significant at small length-scales — and hydrodynamic models that include sub-grid-turbulence are called Large Eddy Simulations (LES) (Smagorinsky 1963; Lesieur et al. 2005; Garnier et al. 2009). This is the approach we use in Chapter 4, where we make use of a sub-grid turbulence model to investigate the development of small dense structures in ULIRG winds.

Secondly, we can use this tensor to interpret small-scale but resolved behaviour in terms of bulk properties. By representing a complex but computationally resolved small-scale phenomenon by a stress tensor, we can understand its large-scale effects though simple quantities such as an effective pressure or effective viscosity term, thus elucidating the significance of the small-scale process. This is the approach we use in Chapter 3, where we resolve collisions between clouds in simulations a galactic disc, and quantity the effects of these collisions by interpreting them as an effective viscosity.

These two interpretations represent two separate but related research themes, which — together with code development — compose the work performed for this thesis. In this chapter, we introduce the background of these two projects, in addition to general physics required for both. In section 1.1 we summarize the basic equations of hydrodynamics. In section 1.2 we summarize the technique of Smooth Particle Hydrodynamics, used by the simulation code HYDRA which was used to conduct our simulations in chapter 3. In section 1.3 we summarize the Adaptive Mesh Refinement technique used by the simulation code FLASH for our simulations in chapter 4. In section 1.4, we give some background on ULIRGs and their outflows, and in section 1.5 we give background on the formation of molecular clouds in galaxies — the two physical situations explored in our research projects. Finally in section 1.6 we give an outline of the format of the remaining chapters.

1.1 Basic Equations of Hydrodynamics

The fluid approximation allows us to express the state of a substance through large-scale quantities such as density, velocity, pressure, temperature, and internal

energy. These quantities are not independent, and are related by an equation of state. The equation of state reduces the degrees of freedom of the model, and so it is only necessary to know the values for some of these quantities in order to derive all of them. In hydrodynamics, a model is established by defining the fluid quantities across the chosen domain, setting the initial conditions and boundary conditions of these quantities, and applying the equations of hydrodynamics to determine the evolution of these quantities. Perhaps the most fundamental of these equations is the conservation equation.

The conservation equation for any fluid quantity $\mathcal{A}$ (which can be a scalar, vector, or tensor) is obtained from the Reynold's Transport Theorem (Mihalas & Weibel Mihalas 1984), which states that the rate of change of $\mathcal{A}$ integrated over some region is equal to the sum of the fluxes of $\mathcal{A}$ into the volume, and the sources and sinks within the volume. After some manipulation, this gives

$$\frac{\partial \mathcal{A}}{\partial t} + \nabla \cdot (\boldsymbol{v}\mathcal{A}) - \mathcal{S} = 0, \tag{1.1}$$

where $\mathcal{S}$ is the sum of all sources and sinks of $\mathcal{A}$, and has the same rank (i.e. whether the variable is a scalar, vector, or tensor) as $\mathcal{A}$. The Navier-Stokes equations are the conservation equations for momentum, found by setting $\mathcal{A} = \rho\boldsymbol{v}$ to produce

$$\frac{\partial \rho\boldsymbol{v}}{\partial t} + \nabla \cdot (\rho\boldsymbol{v} \otimes \boldsymbol{v}) - \boldsymbol{S} = 0, \tag{1.2}$$

where $\otimes$ represents an outer product, i.e. $[\rho\boldsymbol{v} \otimes \boldsymbol{v}]_{ij} = \rho v_i v_j$. The source term $\boldsymbol{S}$ is now a vector, equal to the sum of the effects of inertial forces (the divergence of the stress tensor $\boldsymbol{\sigma}$, defined below) and any external forces $\boldsymbol{f}$, which in astrophysical hydrodynamics is frequently gravity. Many fluids can be described as *Newtonian* fluids, defined by having a stress tensor $\boldsymbol{\sigma}$ equal to

$$\boldsymbol{\sigma}_{\mathrm{ij}} = -P\delta_{\mathrm{ij}} + \mu\left(\frac{\partial v_i}{\partial v_j} + \frac{\partial v_j}{\partial v_i}\right), \tag{1.3}$$

where μ is the physical viscosity, and P is the pressure. This decomposition is further discussed in section 4.3.1. For an inviscid fluid, $\mu = 0$, and pressure is the only internal force. The assumption of inviscidity can be a realistic approximation in many astrophysical applications, as the physical viscosity of the ISM can be very low, and the associated Reynold's number, given by the ratio of the internal forces to viscous forces is thus very high, perhaps exceeding 10^6 (e.g. Elmegreen & Scalo 2004). However, in many situations the viscosity can not be ignored, and the off-diagonal components of $\boldsymbol{\sigma}$ can become significant. The net effect of viscosity is to diffuse momentum while dissipating kinetic energy into heat.

Even for a non-Newtonian fluid (i.e. one where equation 1.3 is not applicable), $\boldsymbol{\sigma}$ can be split into a traceless component denoted $\boldsymbol{\tau}$, and a pressure component $-P\mathcal{I}$, where $\mathcal{I}$ is the identity matrix. Hence,

$$\boldsymbol{S} = \boldsymbol{f} + \nabla \cdot \boldsymbol{\sigma} = \boldsymbol{f} + \nabla \cdot \boldsymbol{\tau} - \nabla P \tag{1.4}$$

and so the Navier-Stokes equations can be written as

$$\frac{\partial \rho \boldsymbol{v}}{\partial t} + \nabla \cdot (\rho \boldsymbol{v} \otimes \boldsymbol{v}) = \boldsymbol{f} + \nabla \cdot \boldsymbol{\tau} - \nabla P. \tag{1.5}$$

By using the conservation of mass equation, i.e. the continuity equation

$$\frac{\partial \rho}{\partial t} + \nabla \cdot (\rho \boldsymbol{v}) = 0, \tag{1.6}$$

this can be rearranged to

$$\rho \left(\frac{\partial \boldsymbol{v}}{\partial t} + \boldsymbol{v} \cdot \nabla \boldsymbol{v} \right) = -\nabla P + \nabla \cdot \boldsymbol{\tau} + \boldsymbol{f}. \tag{1.7}$$

This is often expressed in terms of the convective derivative (also called the material derivative, the advective derivative, the Lagrangian derivative in addition to several

other names), written as D/Dt, and defined by

$$\frac{D(x)}{Dt} = \frac{\partial(x)}{\partial t} + \boldsymbol{v} \cdot \nabla(x). \tag{1.8}$$

Hence the Navier-Stokes equations can be compactly written as

$$\frac{\rho D\boldsymbol{v}}{Dt} = -\nabla P + \nabla \cdot \boldsymbol{\tau} + \boldsymbol{f}. \tag{1.9}$$

Similarly, the specific internal energy (e_i) equation can be derived from taking the basic energy conservation equation from equation 1.1 and subtracting the mechanical energy equation — that is, the dot product of $\boldsymbol{v}$ and equation. 1.5. This rearrangement gives

$$\rho\frac{De_i}{Dt} = (\boldsymbol{\sigma} \cdot \nabla) \cdot \boldsymbol{v} - \nabla \cdot \boldsymbol{q} + S, \tag{1.10}$$

where $\boldsymbol{q}$ represents the effects of conductive or radiative flux, and S represents source terms. In astrophysics, S can represent a number of processes such as energy feedback from supernovae, radiative energy loss, or heat generated by chemical and nuclear processes. The low densities of gas in the ISM and IGM do not generally permit efficient conduction of heat (although this may be significant in the intracluster medium (Bertschinger & Meiksin 1986; Narayan & Medvedev 2001; Zakamska & Narayan 2003; Voigt & Fabian 2004)), while the low optical depths of the ISM and IGM do not permit efficient absorption of radiation (as well as forcing a numerical calculation of radiative transfer to be a complex non-local calculation), so it is typically assumed that $\boldsymbol{q} = 0$.

One more equation is required to close this set of equations and allow solutions to be found. This (as mentioned above) is the equation of state, which is often given as a relationship between density, pressure and temperature. In astrophysical fluid dynamics it is common to assume the ideal gas law. The ideal gas law assumes that the components of a gas are point particles, and that interactions between particles are purely elastic collisions. This assumption is a good approximation at the

low densities and high temperatures common in astrophysics (the ISM and IGM in particular), where the distance between gas particles (atoms, ions, and molecules) is large compared than the size of the particles themselves. This equation of state is simply

$$P = nkT, \tag{1.11}$$

where n is the number density of all free particles, T is the temperature of the gas, and $k = 1.38 \times 10^{-16}$ erg/K is the Boltzmann constant. We also require an equation of state for the internal energy, which requires an additional approximation — that the gas behaves as if monoatomic — and this is

$$e_i = (3/2)nkT. \tag{1.12}$$

More complex equations of state are also used in astrophysics, particularly in stellar interiors where the high densities break the ideal gas assumptions. We assume an ideal gas equation of state throughout this thesis, and hence have a compact and complete set of hydrodynamic equations to solve in our simulations.

1.1.1 Cooling

Radiative cooling is an important process in many astrophysical processes. When two particles collide inelastically, either or both particles will be excited into a higher state. If an excited particle has sufficient time between collisions, it can decay to its ground state, emitting one or more photons. Conduction and convection of heat are not efficient in the interstellar medium, but this radiative process provides an avenue for energy to escape a region of gas, and hence cool it. By volume, the interstellar medium is almost entirely optically thin, and so we can often assume that any photon that is emitted from a region of fluid is completely lost to the system. This assumption is not accurate in dense optically thick regions such as molecular clouds, but with current technologies a full treatment of radiative transfer is computationally prohibitive. Approximate methods including absorption fractions and Hα regions

have recently come under investigation (Hopkins et al. 2012b, for example), but these models can be complex, and introduce additional model parameters, reducing the universality of the model.

As this cooling is a collisional process, its rate should be proportional to the square of n, the number density of collisional particles. Hence the rate at which internal energy (e_i) is lost due to radiative cooling is generally written as

$$\frac{De_i}{Dt} = -\Lambda(T, z)n^2, \tag{1.13}$$

where the cooling function $\Lambda(T, z)$ depends on the temperature, T, and the metallicity, z, of the gas. This is a complicated function incorporating the ionization and transition energies of Hydrogen and Helium, as well as incorporating the effects of metals. This function is often precalculated, and then interpolated from a table at run-time. HYDRA makes use of the tables of Sutherland & Dopita (1993), which we extend via an approximate method to lower temperatures using the values of Wada & Norman (2001). Our FLASH simulations make use of the tables of Raymond et al. (1976) and Sarazin (1986). Plots of $\Lambda(T, z)$ are given in chapters where necessary.

1.2 Smoothed Particle Hydrodynamics

Smoothed Particle Hydrodynamics (Gingold & Monaghan 1977; Lucy 1977; Monaghan 1992) is a Lagrangian method for solving the Navier-Stokes equations. In this approach, the density of a particle is calculated by "smoothing" over the masses of nearby particles. For a continuous medium, fluctuations of some field quantity $A(\boldsymbol{r})$ below some length scale (the smoothing length h) can be smoothed away by convolving the density with a mass-weighted kernel function,

$$A_{smooth}(\boldsymbol{r}) = \int A(\boldsymbol{r}')W(|\boldsymbol{r} - \boldsymbol{r}'|, h)\mathrm{d}\boldsymbol{r}', \tag{1.14}$$

or equivalently

$$A_{smooth}(\boldsymbol{r}) = \int \frac{A(\boldsymbol{r}')}{\rho}W(|\boldsymbol{r} - \boldsymbol{r}'|, h)\rho\mathrm{d}\boldsymbol{r}', \tag{1.15}$$

where the kernel function $W(|\boldsymbol{r}-\boldsymbol{r'}|,h)$ must satisfy

$$\lim_{h\to 0} W(|\boldsymbol{r}-\boldsymbol{r'}|,h) = \delta(\boldsymbol{r}-\boldsymbol{r'}) \tag{1.16}$$

and a normalisation requirement

$$\int W(|\boldsymbol{r}-\boldsymbol{r'}|,h)d\boldsymbol{r'} = 1. \tag{1.17}$$

Applying this smoothing procedure to a discretised system of particles converts the discretised distribution of fluid variables into a continuous function, allowing the equations of hydrodynamics to be applied. This integral is then represented by its discretised form, as a sum over the mass (m_i) and density (ρ_i) of all particles i,

$$A_{smooth}(\boldsymbol{r}) = \sum_i \frac{m_i A_i}{\rho_i} W(|\boldsymbol{r}-\boldsymbol{r}_i|,h). \tag{1.18}$$

The discrete to continuous transition can be seen by comparing this to equation 1.15. In practice, this operation is performed over a certain number of "neighbour" particles, and while W can be a simple Gaussian function, it is often more convenient to use a polynomial spline that vanishes to exactly zero after some distance (e.g. $|\boldsymbol{r}-\boldsymbol{r'}| = 2h$). Using a kernel of finite extent reduces the computational load in calculating this numerically, as contributions to the kernel need only be calculated for particles within this region — the *neighbouring particles*. HYDRA uses the B_2 spline (Monaghan & Lattanzio 1985),

$$W(|\boldsymbol{r}-\boldsymbol{r}_i|,h) = \frac{W_s(r/h)}{h^3}, \tag{1.19}$$

where if $x = r/h$,

$$W_s(x) = \frac{1}{4\pi}\begin{cases} 4-6x^2+3x^3, & 0\le x\le 1; \\ (2-x)^3, & 1<x\le 2; \\ 0, & x>2. \end{cases} \tag{1.20}$$

The gradient of the kernel used in HYDRA is not entirely consistent with equation 1.20, but is adjusted to give a small repulsive force for close particles (Thomas & Couchman 1992) to avoid artifical clustering (Schuessler & Schmitt 1981),

$$\frac{dW_s(x)}{dx} = -\frac{1}{4\pi}\begin{cases} 4, & 0 \leq x \leq 2/3; \\ 3x(4-3x), & 2/3 < x \leq 1; \\ 3(2-x)^2, & 1 < x \leq 2; \\ 0, & x > 2. \end{cases} \tag{1.21}$$

The choice of the smoothing length, h, has important consequences in both the results and performance of an SPH code. If h is too small, then too few particles will be smoothed over when calculating the smoothed quantities, causing (for example) shot noise in the density field. If h is too large, then the impact of important small-scale structure can be smoothed over, and the number of particles in the kernel sum can also grow to be large, increasing the computational load. Some approaches try to find a middle ground by varying h throughout time and space so the number of neighbouring particles — HYDRA (Thacker & Couchman 2006), the SPH code used in this thesis, attempts to maintain 52.

The kernel smoothing operation commutes with differentiation — e.g. we can calculate the gradient of a quantity by

$$\nabla A_{smooth}(\boldsymbol{r}) = \sum_i \frac{m_i A_i}{\rho_i} \nabla W(|\boldsymbol{r} - \boldsymbol{r}_i|, h), \tag{1.22}$$

and so it is not necessary to explicitly calculate a numerical derivative across the simulated domain. Making use of this feature, we can derive equations of motion for gas particles. First, we construct a momentum conservation equation — i.e. a form of $d\boldsymbol{v}/dt = \nabla P$. Symmetrizing the pressure gradient terms ensures the conservation of momentum and energy, and so the simplest symmetrized momentum conservation equation is

$$\frac{d\boldsymbol{v}_i}{dt} = -\sum_j m_j \left(\frac{P_i}{\rho_i^2} + \frac{P_j}{\rho_j^2} \right) \nabla_i W_{ij}, \tag{1.23}$$

where $W_{ij} = W(|\boldsymbol{r}_i - \boldsymbol{r}_j|, h)$. Mass conservation is ensured identically by

$$\rho_i = \sum_j m_j W_{ij}, \tag{1.24}$$

and thermal energy evolution by

$$\frac{de_i}{dt} = \sum_i m_i \frac{P_j}{\rho_j^2} \boldsymbol{v}_{ij} \cdot \nabla_i W_{ij}. \tag{1.25}$$

This, combined with an equation of state, provides us with a complete set of equations for the evolution of a fluid. Unfortunately, while this is "complete", in practice this technique is extremely inefficient at capturing and resolving shocks (see Monaghan 2005, for a discussion). Shocks can be better capturing by the inclusion of an artificial viscosity to prevent gas particles incorrectly interpenetrating during a converging flow (for instance). This is applied with the equations

$$\frac{du_i}{dt} = -\sum_i m_j \frac{\Pi_{ij}}{2} \boldsymbol{v}_{ij} \cdot \nabla W_{ij}, \tag{1.26}$$

and

$$\frac{d\boldsymbol{v}_i}{dt} = -\sum_i m_j \Pi_{ij} \nabla W_{ij}, \tag{1.27}$$

where the viscosity tensor is given by

$$\Pi_{ij} = \begin{cases} \frac{-\alpha c_{ij} \mu_{ij} + \beta \mu_{ij}^2}{\rho_{ij}} & \text{if } \boldsymbol{v}_{ij} \cdot \boldsymbol{r}_{ij} > 0, \\ 0 & \text{otherwise,} \end{cases} \tag{1.28}$$

where c_{ij} is the average sound speed of the two particles, μ_{ij} is the artificial viscosity, and α and β are model parameters. A typical choice for these is $\alpha = 1$ and $\beta = 2$

(Monaghan 2005). μ_{ij} is given by

$$\mu_{ij} = \frac{h_{ij}\boldsymbol{v}_{ij} \cdot \boldsymbol{r}_{ij}}{r_{ij}^2 + \eta h_{ij}}, \tag{1.29}$$

where h_{ij} is the average smoothing length, and $\eta = 0.01$ prevents μ_{ij} from becoming extremely large when r_{ij} is small. This formulation is also problematic, as the artificial viscosity acts to dissipate shear flows in addition to capturing shocks. Hence μ_{ij} is usually replaced by $\mu_{ij,\mathrm{Balsara}} = f_{\mathrm{Balsara}}\mu_{ij}$ (Balsara 1995), where f_{Balsara} is defined as

$$f_{\mathrm{Balsara}} = \frac{|\nabla \cdot \boldsymbol{v}|_i}{|\nabla \cdot \boldsymbol{v}|_i + |\nabla \times \boldsymbol{v}|_i + \eta_{\mathrm{Balsara}} h_{ij}}, \tag{1.30}$$

and $\eta_{\mathrm{Balsara}} = 0.0001 c_i/h_i$ prevents divide-by-zero errors. This equation is designed such that $\mu_{ij,\mathrm{Balsara}} = \mu_{ij}$ for a purely compressive flow (i.e. $|\nabla \cdot \boldsymbol{v}| \gg |\nabla \times \boldsymbol{v}|$), and $\mu_{ij,\mathrm{Balsara}} = 0$ for a pure sheer flow (i.e. $|\nabla \cdot \boldsymbol{v}| \ll |\nabla \times \boldsymbol{v}|$).

1.2.1 Gravitational Softening

Particle simulations with pure Newtonian self-gravity can be subject to extremely poor conservation of energy. This is caused by the sharp gradient in acceleration caused by the $F \propto 1/r^2$ Newtonian law for the gravitational force between particles. As particles are generally permitted to approach arbitrarily close to each other, this force can become arbitrarily large, requiring an extremely small time-step to ensure that particles conserve energy in a close encounter. For example, if a pair of particles are very close to each other during the acceleration calculation of one time-step, then both particles are provided with large accelerations and therefore large velocities. If the time-step is too large, these large velocities will move the particles to a large distance from each other on the next time-step. At these new positions, the gravitational force is much weaker, and the particles only decelerate a little: the particles have both had a net gain of kinetic energy, and the interaction has not conserved energy.

To help ensure conservation of energy, the gravitational force is "softened" (Hockney & Eastwood 1988). The softening typically takes the form of Plummer softening, where the gravitational potential between two particles of mass M and m separated by a distance r is defined as

$$\phi(r) = -\frac{GMm}{(r^2 + \epsilon^2)^{1/2}}, \tag{1.31}$$

where ϵ is the "softening length". This is equivalent to representing each particle as a distribution of mass with scale-length ϵ, and indeed this equation was first applied to model the finite size of galaxies (Aarseth 1963), but it is now commonly used in situations where the particles could be considered point objects (e.g. interactions between individual stars) in order to preserve numerical accuracy. In simulations of galaxies, this is a particularly apt approximation as the star, gas, and dark matter particles do not represent individual objects, but large quantities of stars, gas, or dark matter, and hence a finite distribution of mass is appropriate.

In SPH, it is desirable for the softening length to be similar to the smoothing length (Bate & Burkert 1997). If ϵ is too large, then at small scales pressure unrealistically dominates over gravity, suppressing collapse, while if ϵ is too small, then at small scales gravity unrealistically dominates over pressure, inducing unphysical collapse. Hence the choice of ϵ is crucial. In our SPH simulations, we vary the softening length to investigate its effects on our results.

1.3 Adaptive Mesh Refinment

The Adaptive Mesh Refinement (AMR) technique is a popular method for reducing the additional computational load caused by increasing the resolution of an Eulerian simulation. It is most commonly used in hydrodynamic simulations to solve the Navier-Stokes equations. In an Eulerian code a numerical solution can be found by converting the important equations (Navier-Stokes) into a discretised form — for example, exchanging every $\partial f/\partial x$ term with a $\Delta f/\Delta x$ term — and solving the

equations at discrete times until the simulation is complete. The computational load of this method increases on the number of cells in the domain, while the resolution increases as the cells decrease in size. Hence the goal is to have as few cells as possible, while having cells as small as possible — two contrary demands. However, it is possible to improve performance by noting that in many applications, high resolution is not necessary everywhere, but only in key areas of interest — for example, at the discontinuity between two constant density regions. Taking advantage of this, an irregular mesh can be produced where resolution varies in space, with the smallest high-resolution cells only in the regions where they are needed.

However, a static mesh can cause problems as it is difficult to predict which regions require high resolution, and these regions can change over time. This unpredictability is particularly a problem in simulations of turbulence. AMR attempts to resolve this problem by providing a mesh that *adapts*. Regions can be *refined* when they are insufficiently resolved by placing a high-resolution sub-grid in the region. To regain computational performance, regions that do not require high resolution — e.g. regions with low velocity variance — can be *derefined*, with the high-resolution sub-grid replaced by a lower resolution mesh.

The first implementations of AMR (Berger & Oliger 1984; Berger & Colella 1989) allowed a complex hierarchy of nested grids, where sub-grids can be rotated and combined to optimize their positions, at the cost of code complexity — indeed, this method has proven difficult to adapt into a modern parallel multiprocessor form. Khokhlov (1998) introduced a more straight-forward tree-based structure, where individual "parent" cells can be refined into a sub-grid of "child" cells who share the orientation of their parent. The simplest process here is (in three-dimensions) to refine a cell in a $2 \times 2 \times 2$ "octet" of cells, by bisecting the parent cell in each dimension. This refinement algorithm produces an oct-tree structure in the code, which is easier to maintain and parallelise. The performance of this method can be improved by refining blocks of cells instead of individual cells. The block-tree refinement method is popular, being implemented in the particle hydrodynamics code RAMSES (Teyssier

2002), as well as the library PARAMESH (MacNeice et al. 2000), which is used by FLASH (Fryxell et al. 2000).

1.3.1 PARAMESH AMR in FLASH

The PARAMESH package is an open-source package of Fortran subroutines for implementing parallel AMR. The "block oct-tree" structure allows this package to be easily applied to refine and parallelise an existing fixed-mesh serial code. Here, the domain of the simulation is decomposed into blocks of l^{dim} cells, where by default $l = 8$. Refinement is performed by placing an octet of these blocks within a parent block. By making use of this package, an application designer need only tackle the problem of solving the relevant equations across a single block on one processor.

FLASH makes use of the PARAMESH package, solving the hydrodynamic equations using the Piecewise Parabolic Method (Colella & Woodward 1984; Woodward & Colella 1984). PARAMESH also requires the refinement criteria to be set by the application designer. The default criterion in FLASH is based on Lohner (1987). An error term E_i is calculated and used as a basis for the refinement criterion. If E_i is above some value (0.8 by default), the block is refined, while E_i is below some value (0.2 by default), the block is derefined. This error term is essentially the 2nd derivative of some quantity A, normalised by the gradient of that quantity. When discretised, an extra term is included in the denominator to ensure that E_i does not become extremely large when small ripples pass through a region with low $\partial A/\partial x$. In one-dimension, the discretised form looks like

$$E_i = \frac{|A_{i+1} - 2A_i + 2A_{i-1}|}{|A_{i+1} - A_i| + |A_i - A_{i-1}| + \epsilon(|A_{i+1}| + 2|A_i| + |A_{i-1}|)} \tag{1.32}$$

where the constant $\epsilon = 0.01$. As this is a dimensionless quantity, A can be any variable that is defined for each cell. FLASH allows up to four refinement variables to be specified, refining if this criterion is met for any of these variables. We have selected density, pressure, and temperature as our refinement variables.

1.4 Ultraluminous Infrared Galaxies (ULIRGs)

Since we model ULIRG outflows, we briefly review salient issues in their discovery and properties.

1.4.1 Discovery and properies

ULIRGs (for further reviews, see Lonsdale et al. 2006; Veilleux 2006) are generally believed to be merger-induced dust-obscured starbursts supported by an active galactic nucleus (AGN) component. The first galaxies to fit the modern criteria of a ULIRG — that is, galaxies with $L_{8-1000\mu\mathrm{m}} > 10^{12} L_{\odot}$ were discovered in a 1985 survey of Infrared Astronomical Satellite (IRAS) sources (Houck et al. 1985). However, galaxies with strikingly large relative infrared to optical luminosities had been observed for some 10-15 years before the IRAS mission. Rieke & Low (1972) discussed the infrared-dominated emission from nuclear regions in some galaxies, and by 1979 (Lebofsky & Rieke 1979) it had been determined that the infrared emission was due to re-radiation of starlight by dust, and that these objects are associated with galaxy interactions.

While rare in the local universe, with a space density many orders of magnitude lower than "normal" galaxies (but possibly a few times the space density of QSOs), ULIRGs moved further into the spotlight when they were discovered to be at least two orders of magnitude more numerous at higher redshift. This makes ULIRGs significant, and perhaps the dominant population in infrared wavelengths at these early epochs. The study of these objects is thus important for probing galaxy formation and evolution in the early universe.

Many observations have focused on determining what powers the immense luminosities of these objects. These investigations have shown that most if not all ULIRGs are either in the process of merging, or have recently merged (Armus et al. 1987; Melnick & Mirabel 1990; Hutchings & Neff 1991; Clements et al. 1996; Surace et al. 1998). N-body simulations (Barnes & Hernquist 1992; Hopkins et al. 2006) have shown that during a merger, a large quantity of gas and dust is channelled into the

nucleus of the new galaxy. This concentration of gas can trigger a starburst — a region with an extremely high star formation rate, e.g. $100-1000 M_{\odot}/yr$ — or power an AGN — a violent accretion region around a super-massive black hole (SMBH). Regardless of the source of luminosity, it is almost certainly triggered by galactic interactions. Dust obscures both luminosity sources and reprocesses the emission into the infrared, giving the observed large infrared luminosities, but making it difficult to distinguish between a starburst and an AGN.

As a result, much emphasis has been placed on determining which of the powering mechanisms – AGNs or starbursts – is dominant, and how they relate to each other. Observations across many wavelengths (de Grijp et al. 1985; Genzel et al. 1998; Laurent et al. 2000; Farrah et al. 2005; Pérez-Torres et al. 2008) show evidence of both sources, with AGNs being more dominant in "warmer" ULIRGs. However the general consensus is that most ULIRGs are powered primarily by starbursts, and that AGNs only fulfil a secondary role.

It has also been proposed that ULIRGs are related to the super-luminous AGNs known as quasars. The most popular picture is an evolutionary sequence (Sanders et al. 1988; Hopkins et al. 2006): As two galaxies begin to merge, a massive cool starburst is initiated: a cool ULIRG. Next, the AGN is switched on, and starts heating the dust around it: a warm ULIRG. Eventually, the dust is blown away, and the galaxy becomes a "naked" quasar. Another scenario is that the dust around the nucleus of a quasar is toroidal (or asymmetric in some way) and so the AGN can only been seen from certain angles — a quasar is a ULIRG seen face-on, and a ULIRG is a QSO seen side-on (Lonsdale et al. 2006).

As already noted, the dominance of infrared galaxies appears to increase with redshift — the comoving density of infrared light due to 15μm sources is at least forty times higher at $z \sim 1$ than in the local universe (Lonsdale et al. 2006). Surveys have found a huge population of high-redshift sub-millimetre-bright optically-faint sources (Sub-millimetre Galaxies or SMGs), which taken together with reasonable extrapolation can account for the entire cosmic infrared background (Barger et al. 1999;

Blain et al. 1999). Simple photometric redshift estimates (Bertoldi et al. 2000; Fox et al. 2002; Webb et al. 2003; Borys et al. 2005) place most of these sources at $z > 2$ and almost all of them beyond $z \sim 1$, so these SMGs are probably ULIRGs of immense luminosity, with star formation rates of over $1000 M_\odot$/yr. These galaxies have disturbed morphologies (Smail et al. 1998; Conselice et al. 2003), indicative of ongoing interactions, consistent with their identification as ULIRGs. CO surveys (Genzel et al. 2003; Neri et al. 2003; Greve et al. 2005) show evidence for enormous masses of molecular gas within these galaxies, often in excess of $10^{11} M_\odot$, much greater than local ULIRGs and more comparable to high redshift radio galaxies — and so while SMGs appear to be closely related to local ULIRGs, they are indeed two physically distinct populations.

1.4.2 Cold gas in ULIRG outflows

There is also significant evidence that nuclear and galactic scale outflows are common in ULIRGs, and that these outflows are dominated by star formation. These have been detected in X-Ray (Heckman et al. 1996; McDowell et al. 2003; Ptak et al. 2003; Teng et al. 2009) and Hα (Colina et al. 2004) emission as hot lobes extending $10 - 15$ kpc beyond the infrared portion of the galaxy. Evidence of outflows has been detected in $\sim 75\%$ of ULIRGs, which is consistent with 100% when projection effects are taken into account. These "super-winds" are driven by the energy of supernovae from the starburst, with outflow rates comparable to the host's star formation rate ($\sim 10 - 1000 M_\odot$/yr), and correspondingly high luminosities ($10^{41} - 10^{44}$ erg/s) and projected velocities ($300 - 400$ km/s, with one example of 1100 km/s). They may in fact be the principal polluters of metal and dust in the IGM.

Several observations (e.g. Phillips 1993; Heckman et al. 2000; Martin 2005, 2006) have demonstrated the existence of cold gas with large velocity dispersions in these outflows. The presence of this gas provides a challenge to theoretical models which must explain how such a cold component (NaI and KI lines, with ionization potentials of 5.1 and 4.3 eV (Martin 2005)) can exist within a flow of very hot winds.

$T \sim 10^6$ K would be typical for a $v \sim 300$ km/s — we can estimate this with the equation $T = (13.6\ \mathrm{K\ s/km})v^2$, which comes from simple arguments for the post-shock temperature after an adiabatic Sedov-Taylor expansion (Shu 1992; Scannapieco & Oh 2004). These models must also explain the large velocity dispersion of this gas — i.e. the large non-thermal broadening of the NaI lines. A number of works have investigated explanations for the presence of the cold component, often supported by numerical calculations (Tomisaka & Ikeuchi 1986; Murray et al. 2005; Scannapieco & Brüggen 2010; Everett & Churchwell 2010). In these models, cold gas is either produced in the disc and then advected by ram-pressure, or produced by gas rapidly cooling within the wind through radiative processes.

In the simulations of Fujita et al. (2009), cold gas is produced by turbulence in the wind, which produces dense condensations that rapidly cool. Specifically, these condensations trace their origin to a super-bubble wall. A super-bubble is inflated by the outflow, driving a "snowplow" which builds up a dense bubble wall. The density of this bubble wall allows it to cool efficiently, due to the ρ^2 dependency in radiative cooling. This cold bubble wall is supported against gravity by the pressure of the hot low-density gas within the bubble cavity.

This situation is extremely susceptible to Rayleigh-Taylor (RT) (Taylor 1950; Sharp 1984) and Richtmyer-Meshkov (RM) (Richtmyer 1960; Meshkov 1969) instabilities. The RT instability occurs when a dense fluid is suspended above a lighter fluid in a gravitational field (or equivalently, when a light gas is accelerated into a dense gas). This instability causes the two fluids to penetrate each other with fingers or "mushroom-caps" of gas, mixing the fluids and breaking up the interface. The RM instability similarly produces the breakup of an interface between dense and less dense fluids, but in this case the fluids are accelerated by a sudden impulse such as a passing shock, instead of a constant acceleration from gravity.

Indeed, Fujita et al. (2009) found that the bubble wall fragments into dense clumps, which may well correspond to the cold gas observed in ULIRG outflows.

Originating as wind gas, these clumps have high outflow velocities and velocity dispersions (330 ± 110km/s and 170 ± 60km/s Martin (2005)), and can travel large distances into the outflow – if they are not destroyed by radiation or ram-pressure. While two dimensional simulations have probed this scenario, in chapter 4 we discuss the first three dimensional simulations to investigate this model.

1.5 Molecular Clouds in Galaxy Simulations

Since collisions between molecular clouds form one of the key themes in this thesis, we briefly review their properties.

1.5.1 Molecular Clouds

Giant molecular clouds (GMCs) are arguably the most important component of the interstellar medium and contain most of of the mass of the gaseous component of the disc, while having a small volume filling factor (McKee & Ostriker 1977). The molecules that make up these clouds are primarily H_2, which is difficult to directly observe. This difficulty is because molecular H_2 gas tends to only exist at temperatures too cold for strong black-body emission, and its neutrality reduces the cross-section for interactions that could excite the molecules and produce emission. Instead, tracers such as NaI or CO are used, as, for instance, the density of $n(H_2) \sim 100$ cm^{-3} required to excite the $J = 1 \rightarrow 0$ rotational line of CO matches the densities of giant molecular clouds (Solomon et al. 1987). Molecular clouds are stellar nurseries, where turbulence combined with the Jeans instability causes the cold dense gas to collapse into stars. The association of HII regions with molecular clouds (Scoville et al. 1987) is strong evidence of molecular clouds' key role in star formation.

While it is tempting to think of molecular clouds as well-constrained distinct objects as they appear to have sharp edges, these edges represent the transition between molecular and atomic gas (Larson 1994), and not a sharp cut-off in density; indeed, a molecular cloud can be contained in an extended atomic envelope of similar mass (Blitz 1988, 1991). Molecular clouds are also transient objects, with life-times

of $\sim 10^7$ yr (Blitz & Shu 1980; Larson 1981). Their irregular structures (as shown in IRAS (Scalo 1990) and Spitzer maps Flagey et al. (2009)) show that GMCs have not reached equilibrium configurations. Molecular clouds are also chemically unevolved, with lower dust depletion ratios than would be expected from long-lived objects (Larson 1994). The scarcity of molecular clouds without signs of star formation (Blitz 1991) shows that star formation starts very soon after a molecular cloud forms. Star formation gives a mechanism for the short life-times of molecular clouds as winds, radiation pressure, outflows, and supernovae from these newly formed stars will rapidly dissipate the cloud.

In fact, rather than discrete long-lasting structures, the consensus is that molecular clouds are highly turbulent (Schneider et al. 2011). Larson (1981) discovered that the power-law relationship between the velocity dispersion of a cloud and its luminosity matches that predicted by Kolmogorov's laws, that $\sigma \propto L^{\epsilon}$ where $\epsilon = 1/3$ for a self-similar "fractal" spatial structure. Later analysis (Solomon et al. 1987) of CO data from the Massachusetts-Stony Brook Galactic Survey (Clemens et al. 1997) found $\epsilon \sim 0.5$, which was originally interpreted as resulting from the virial theorem, but has more recently been shown to be equivalent to supersonic isothermal turbulence (e.g. Schmidt et al. 2009). This turbulence is driven on large-scales by spiral density waves, supernova explosions, and expanding HII regions, and on small scales by stellar winds and outflows.

Although it is generally agreed that molecular clouds are governed primarily by turbulence and not by self-gravity, the effects of self-gravity are still important. Clearly, at small scales gravitational collapse must be dominant in order for star formation to proceed. It has also been proposed that the line-width/size relation of molecular clouds can be explained if they consist of a hierachy of gravitational collapse (Goldreich & Kwan 1974), although this unfettered collapse results in unrealistically high star-formation rates (Zuckerman & Palmer 1974). Feedback from winds and outflows in the densest regions of a cloud could reduce the star formation rate and

alleviate this problem (Ballesteros-Paredes et al. 2011; Murray 2011). While turbulence is likely still the dominant factor in determining molecular cloud properties, feedback and self-gravity induce deviations from this "pure" turbulence.

The molecular cloud line-width/size relation is one of what is known as Larson's Laws, along with a density/size relation, that the surface density of molecular clouds is constant between clouds. However, this result is likely not an intrinsic characteristic, but instead is an effect caused by an intensity cutoff giving a comparatively small dynamic range.

Molecular clouds appear to be associated with spiral arms, with a longitude/velocity plot of molecular cloud phase-space density in the Milky Way showing several peaks (Scoville et al. 1987), including a peak in population at the $4-7$ kpc ring. Spiral density perturbations may encourage molecular cloud formation (Dobbs et al. 2006). These clouds are confined to a fairly thin disc, with a vertical position dispersion (i.e. perpendicular to the disc) of $\sim 30-50$ pc for $M_{\rm virial} \sim 5-20\times10^5 M_\odot$ GMCs. Lower mass GMCs have a larger vertical position dispersion, consistent with a cloud-cloud velocity dispersion that decreases as $M_{\rm virial}^{-1/2}$, as would be expected by equipartition of kinetic energy — this suggests that interactions between clouds are common, or that clouds live long enough to survive several interactions. To support these observations, we can perform simulations of a disc galaxy to observe the formation of molecular clouds, their interactions, and their effect on the galaxy as a whole.

1.5.2 Galaxy Simulations

Early multi-dimensional simulations of galactic discs and galaxy formation were two-dimensional collisionless models of secular discs (Hohl & Hockney 1969, for example) , i.e. discs of stars without a gas component, or a cosmological environment. While the environment was believed to be important for processes such as stripping gas (Fall & Efstathiou 1980), a secular disc model permits a smaller computational domain, and can help to disentangle secular disc evolution from environmental effects.

It was soon discovered that a cold, balanced disc would quickly break apart (Hockney & Hohl 1969) due to the Toomre instability (Toomre 1964), and that velocity dispersion between the star particles is required to stabilize the disc. These simulations shed light on the formation of large scale structures such as bars (Hohl 1976), although the formation of a stable barred galaxy also requires significant velocity dispersion.

The inclusion of hydrodynamics incorporated a new array of physics into these two-dimensional simulations, even at resolutions as low as 60x60 (Sanders & Huntley 1976). Early particle-based fluid simulations helped explain the origin of spiral density waves (Sanders 1977). At the same time, the formation of galaxies was also explored in a cosmological context, although at very low resolutions (e.g. particle numbers of $N = 100$ (Peebles 1971), $N = 300$ (Peebles 1970), N=1000 (Efstathiou & Jones 1979)), compared to modern simulations, such as the famous Millennium Run (Springel et al. 2005)) which contained more than 10^{10} particles, and more recent simulations that contain over 10^{11} particles (Angulo et al. 2012; Kim et al. 2011).

More recently, three dimensional high resolution (i.e. $N > 10^6$ particles) hydrodynamic simulations of galaxies have become routine. Many of these use realistic initial conditions from cosmological simulations (Guedes et al. 2011; Naab et al. 2007, for example), while others draw from analytic density distributions (Dobbs & Bonnell 2008; Wada & Norman 2001, for example) to better disentangle the various interacting processes in galactic evolution. These high resolution simulations are reaching a resolution where it is possible to resolve the formation of molecular clouds (Dobbs et al. 2006; Robertson & Kravtsov 2008; Dobbs & Bonnell 2008; Tasker & Tan 2009; Agertz et al. 2009, for example). This resolution allows us to investigate in detail the role of large-scale evolution on molecular clouds, and vice versa. In chapter 3 we perform hydrodynamic simulations of molecular clouds in an isolated disc to investigate molecular clouds as a source of effective viscosity.

1.6 Thesis Outline

This thesis is divided into six chapters. In this first introductory chapter, we have presented background information on ULIRGs and their outflows, on molecular clouds in a galactic context, and on our approach to performing simulations of these situations. In Chapter 2, we discuss the simulation codes we utilized, and the modifications that were made to conduct the research in this thesis. Chapter 3 details our investigation into the effective viscosity due to collisions between molecular clouds within a Milky Way-like galaxy, while Chapter 4 explains our simulations of ULIRG outflows and our sub-grid turbulence algorithm. These are followed by a brief conclusion in Chapter 5.

Chapter 2

Code Modifications

2.1 Introduction

The simulation work in this thesis utilizes a number of pre-existing analysis and parallel simulation codes. Some of the existing codes are publicly available, others were provided upon request. These codes were modified to adjust their physical assumptions and implementations to be more appropriate for the physical models we consider. In some cases it was also necessary to correct significant programming errors. In addition, a number of post-simulation analysis programs were written by the author. In this chapter we describe the modifications made to pre-existing codes, and briefly summarize the properties of FLASH and HYDRA-OMP, the two pre-existing codes used to perform our main simulations.

FLASH (Fryxell et al. 2000) is a commonly used Adaptive Mesh Refinement (AMR) code, maintained by the Flash Center for Computational Science based at the University of Chicago, originally funded by the US Department of Energy's Accelerated Strategic Computing Initiative. While FLASH is not an open-source code — users must request access, and are not permitted to distribute the code — it is nevertheless one of the most popular AMR codes in astrophysics[1]. The popularity of the code ensures that it is well tested, and provides a community of users to help new users. FLASH is designed in a modular fashion, allowing "modules" in sub-directories to override built-in subroutines in a manner similar to overriding in object-orientated languages (these "modules" should not be confused with the Fortran-90 language

[1] a list of papers making using of FLASH can be found at http://flash.uchicago.edu/site/publications/flash_pubs.shtml

"module" construct, even though FLASH is written in Fortran). Many of the included "modular" subroutines are place-holders for various source terms, such as heating from turbulence or feedback, or radiative cooling. FLASH is also designed such that it is trivial to add a new scalar field, and to use FLASH's standard routines to advect and diffuse this field over the simulation. FLASH is parallelized with MPI.

HYDRA-OMP is a parallel SPH code developed by Thacker & Couchman (2006). HYDRA-OMP differs from most SPH codes in that it uses an adaptive particle-mesh for long-range gravity, instead of a "tree code" as in the more popular SPH code GADGET-2 (Springel 2005), and other popular codes such as Gasoline (Wadsley et al. 2004). When modelling self-gravity, it is usually too computationally intensive to perform a direct sum of all Newtonian gravitational forces, and approximate methods are used instead. However, at short distances, these approximate methods are inadequate, and the $1/r^2$ calculation must be performed directly. As a result, most models that include self-gravity use a fast approximate method for gravitational forces between particles greater than some distance apart, and perform a direct sum of Newtonian forces for particles that are closer than this distance. The particle-mesh method maps particles to a low resolution mesh and makes use of the convolution theorem to calculate the graviational forces in this mesh. HYDRA's adaptive particle-mesh improves this by placing additional meshes in regions that require higher resolution. The more popular tree-code method used by GADGET-2 and Gasoline models gravity with a hierarchy of multipole expansions that follow the density distribution of the simulated region.

HYDRA is parallelized with Open-MP, a shared memory parallelization scheme, while GADGET uses MPI, a distributed memory parallelization scheme. As a shared-memory implementation, Open-MP is more efficient than a distributed memory method such as MPI for the same number of processors, as shared data does not need to be duplicated, and message passing is much more efficient. Open-MP is also conceptually simpler, and hence easier to implement and maintain. However, large shared memory machines are more expensive per processor than large distributed memory

machines, and there can be a "bandwidth bottleneck" when a large number of processors attempt to access memory simultaneously (Wulf & McKee 1995), and so most large applications are preferably developed in MPI.

The SMU Computational Astrophysics Laboratory *Cerberus* consists of shared-memory nodes of 16 or 32 processors each, totalling 304 processors, so an Open-MP implementation can use at most 32 processors, while an MPI implementation can use all 304. We have tested our SPH galaxy model with both GADGET-2 and HYDRA, and have found that our problem does not scale well with very large numbers of processors in GADGET-2, and that a shared-memory approach using only 16 or 32 processors allows us to retain the simplicity of Open-MP without a large reduction in performance. Our AMR ULIRG models in FLASH parallelize more efficiently, particularly as an external potential is used for gravity, so cells only need to know information about their immediate neighbours for hydrodynamics. In these models, MPI is efficient, and we use up to 192 processors per simulation.

2.2 HYDRA

2.2.1 Parallelization

HYDRA parallelizes in two ways. The larger refinements (including the full simulation box) are distributed across the entire machine, while the smaller refinements are farmed out to individual processors. The particle mesh (PM) calculation for each refinement is efficient, but the particle-particle (PP) calculation can be expensive, as it is an $O(n^2)$ algorithm. This cost amplifies the the load-balance problem caused by an uneven distribution of particles between cells within a refinement, and without a good parallelization scheme the entire machine can be left waiting for one processor to finish.

These cells are placed by the refinement algorithm. An initial grid of L^3 cells is placed over the entire simulated region, where a typical value of L is $L = 128$. Here the value of L is selected to achieve the most efficient balance of the PM and PP parts of the code. Areas of high density are refined, and an additional L^3 grid is placed in

each refinement. Direct N^2 particle-particle calculations are only performed between adjacent cells.

HYDRA was originally used as a code for cosmological simulations conducted using cubic periodic boxes. In a cosmological simulation, an initially near-uniform distribution of gas and dark matter collapses into a large number of density peaks which merge, producing galaxies in a hierarchical structure. In a large-scale simulation, there are many density peaks of similar magnitude. HYDRA has been optimized for this situation by parallelizing over cells, assigning groups of cells to each processor. This method works well if there are many more density peaks than processors, assuming both that the algorithm begins calculating the most time-consuming cells first, and that these peaks have broadly similar magnitude. A small number of very strong density peaks would cause a large number of particles to be in a small number of boxes, and this can cause severe load balance problems.

Unfortunately, this is indeed the case for an isolated simulation of a galaxy — in this case a large fraction of the particles of interest end up in a small number of cells. Here, even if a refinement is distributed across the entire machine, some processors may receive cells that are far more computationally expensive than others. We resolved this problem by modifying the distribution of cells across processors. If a cell contains a large number of particles, we found it is more efficient to split that *individual cell* across all processors — this is analogous to how the larger refinements were already treated in the code. We split a cell over all processors if it contains more than a threshold number of particles. The cells with few particles are distributed one cell at a time to a processor, and then once all of these "sparse" cells are complete, the PP calculation for each of the dense cells are parallelized over the whole machine. As shown in Fig. 2.1, in some cases this reduced the wall-clock time per time-step by a factor of 7. We found that setting the threshold to 2048 particles per cell produced optimal results — only for quite small numbers of particles was it efficient to assign a single processor to a cell.

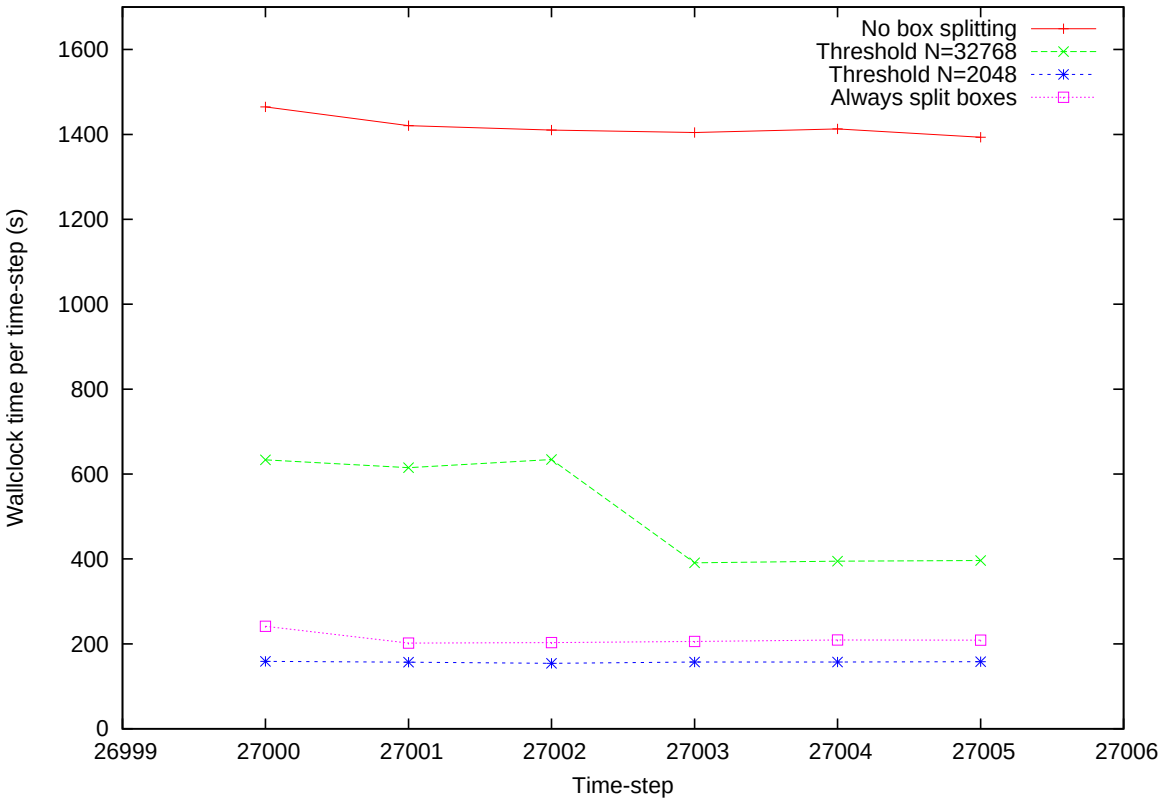

Figure 2.1: The elapsed wall-clock time per time-step in the advanced stages of a 16-thread OpenMP simulation – the initial conditions are the final output of LowSoftMW, described in chapter 3. Speed is greatly increased by splitting boxes, but the best results are when only moderately dense boxes are split.

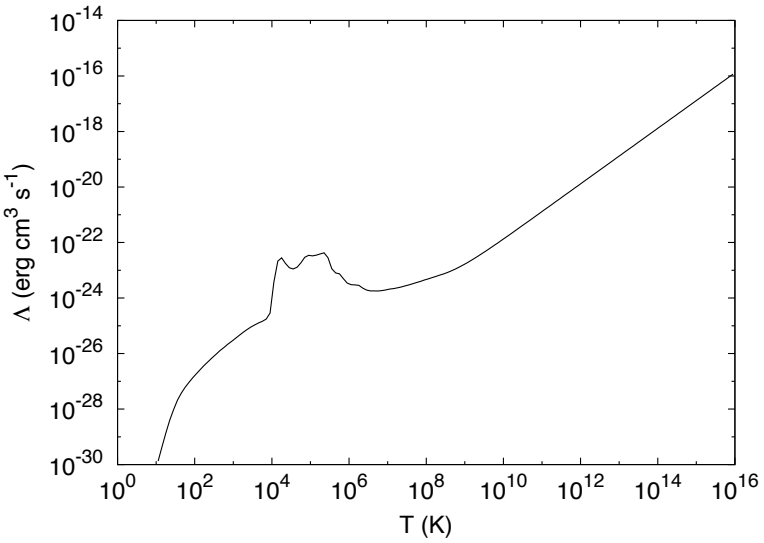

Figure 2.2: The cooling curve used in our models. Values below 10^4 K are from Wada & Norman (2001), while those above 10^4 K are from Sutherland & Dopita (1993).

2.2.2 Cooling

In HYDRA, the cooling function Λ (see equation 1.13) is interpolated from a table. As received, HYDRA makes use of the cooling function of Sutherland & Dopita (1993), which we have extended down to 10 K using the cooling function from Wada & Norman (2001), under the assumption of a constant metallicity of $Z = 0.1Z_{\odot}$. However, we generally set our temperature floor to 300 K to make our results more comparable with Tasker & Tan (2009), except in cases where we explicitly investigate the effect of a lower floor. The combined cooling curve is plotted in Fig. 2.2. At high remperatures ($T \gg 10^4$ K), free-free interactions dominate and $\Lambda \propto T^{1/2}$. At intermediate temperatures ($T \gg 10^4$ K), collisional line exication of Hydrogen and Helium produce two additional peaks. At lower temperatures ($T < 10^4$ K), molecular-line cooling decomes dominant, and the effects of metallicity become more critical.

2.2.3 Dynamic Temperature Floor

We use a method similar to Robertson & Kravtsov (2008) to ensure that the Jean's mass is resolved in our simulations. This is to satisfy the Truelove et al. (1997) criterion and avoid artificial fragmentation – crucial in simulations of cloud formation. The method is in the form of a dynamic pressure floor. The Jeans mass is defined as

$$m_{\rm Jeans} = \frac{\pi^{5/2} c_s^3}{6 G^{3/2} \rho^{1/2}} \tag{2.1}$$

(Jeans 1902). Bate & Burkert (1997) noted that for SPH simulations each particle should satisfy $2 N_{neigh} m_{gas} < m_{\rm Jeans}$ (where N_{neigh} is the number of SPH neighbours for the particle and m_{gas} is the gas particle mass) to avoid artificial fragmentation. This requirement is equivalent to the statement that

$$h_{\rm Jeans} = \frac{\pi^{5/2} c_s^3}{6 G^{3/2} N_{neigh} m_{gas} \rho^{1/2}} < N_{\rm Jeans} \tag{2.2}$$

with $N_{\rm Jeans}$ set to 2. In an ideal gas $c_s \propto \sqrt{e}$, so we can fulfil this criterion by applying

$$e \rightarrow e \times \left(\frac{N_{\rm Jeans}}{h_{\rm Jeans}} \right)^{2/3} \tag{2.3}$$

whenever $h_{\rm Jeans} < N_{\rm Jeans}$.

We found spurious string-like structures forming within clouds even for moderately high values of $N_{\rm Jeans}$, and found that $N_{\rm Jeans} = 50$ removed these structures and resulted in a more homogeneous interior for clouds.

2.3 FLASH

The major additions to the standard FLASH code were the inclusion of the source term subroutines such as sub-grid turbulence, and galaxy initial condition generation subroutines by Scannapieco & Brüggen (2008). We made some modifications to the initial conditions and feedback routines to produce our models in Chapter 4, but we did not significantly modify the general algorithm for sub-grid turbulence.

However, the version of the code received by the author contained a number of unintended features, which took significant time and effort to unearth and correct.

2.3.1 Correcting Code Errors

We solved the following errors:

1. The order of subroutine within the *SourceTerms* routine was incorrect, causing guard cells (defined below) to be inconsistently updated
2. The turbulent diffusion subroutine did not loop over all the required cells in a block
3. The numerical error in the turbulent diffusion subroutine was directionally dependent
4. The calculation of temperature was sensitive to numerical error because it was not correctly accounted for when determining the time-step
5. The positions of feedback bubbles in the simulation were incorrect due to a typographical error
6. Some other minor typographical errors that we do not document here

2.3.1.1 Guard Cells & Diffusion: Order of Physics Steps

As mentioned in section 1.3.1, the PARAMESH library used by FLASH decomposes the domain of the simulation into small blocks of fixed size (e.g. $8 \times 8 \times 8$), which are distributed between processors. To model certain physical processes such as diffusion, cells within a block must have information on their neighbours, and so each PARAMESH block contains a 4-cell thick "wall" of guard cells — cells copied from neighbouring blocks (see Fig.2.3). If these guard cells are not appropriately updated before a diffusion step, then cells near the border of a block will calculate incorrect fluxes. In the *SourceTerms* subroutine of FLASH, both the heating and cooling subroutines were called before the new turbulence subroutine, neither of which updates

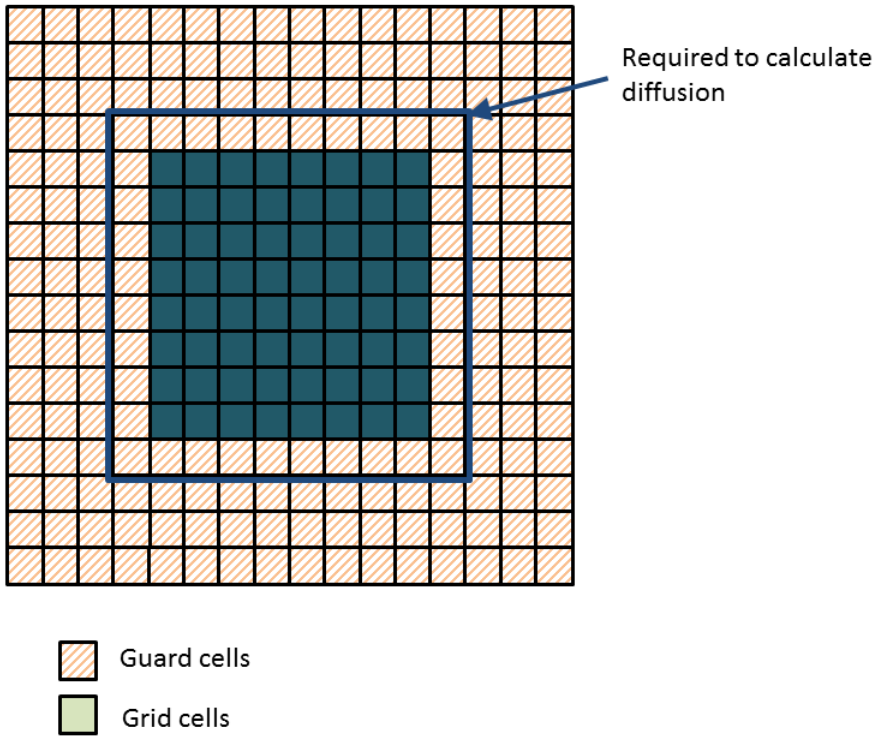

Figure 2.3: Guard cells in FLASH. At least one layer of guard cells must be up-to-date for a diffusion step.

the guard cells. This incorrect ordering caused a clearly visible grid effect in bubbles, as heat in the form of both thermal and turbulent energy was applied to all cells except guard cells, and so any cell bordering a guard cell will spuriously diffuse turbulent energy into the cooler guard cell — energy which is lost to the system when the guard cells are overwritten. This error is present in several publications that make use of this code (Scannapieco & Brüggen 2008; Scannapieco et al. 2009; Gray & Scannapieco 2011). The error was corrected by placing the turbulence subroutine *before* the heating and cooling subroutines. Our implementations of heating and cooling do not require updated information in guard cells, and so are not adversely affected by being placed after other subroutines, even if the guard cells are not updated to be consistent after those subroutines.

2.3.1.2 Guard cells & Diffusion: Domain of Physics Steps

The turbulence sub-grid model is implemented in two steps: the turbulent diffusion subroutine, and the turbulence source-terms subroutine. These track the production, diffusion and effects of turbulence generated by the Richtmyer-Meshkov (RM) and Rayleigh-Taylor (RT) instabilities. This model describes turbulence with two parameters defined across the domain: the turbulent length scale (L), and the turbulent kinetic energy (K).

However, in the code received by the author, the turbulent diffusion subroutine did not loop over the correct subset of cells. The corners of the non-guard-cell cells are given by (LowX, LowY, LowZ) and (HighX, HighY, HighZ). The turbulent diffusion step looped from (LowX+1, LowY+1, LowZ+1) to (HighX+1, HighY+1, HighZ+1), neglecting three entire faces of grid cells per block. This subroutine was corrected to loop from (LowX-1, LowY-1, LowZ-1) to (HighX+1, HighY+1, HighZ+1). A one-cell thick layer of guard cells is also updated in this step, as the pressure in guard cells is needed to calculate the RT and RM turbulent source terms.

The turbulent viscosity $\mu_t = C_\mu L\sqrt{2K}$ was also not updated before the turbulent diffusion step, even though L and K are altered by the heating, cooling, and

hydrodynamics routines, and so these quantities can be unsynchronized. This error was fixed by altering the subroutine *Turbulence_update* so that it updates μ_t in addition to its normal function.

2.3.1.3 Guard cells & Diffusion: Direction-dependent error

The turbulent diffusion was previously performed in a directionally split solver that could cause direction-dependent error. The turbulent diffusion equation for a quantity A is

$$\frac{DA}{Dt} = \nabla \cdot \left(\frac{\mu_t}{N_A} \nabla \cdot A \right), \tag{2.4}$$

where N_A is an order 1 constant that depends on the particular quantity A. This equation was discretised in the steps:

$$\begin{aligned}
A_{i,j,k} &\mapsto A_{i,j,k} + \Delta t \left(\frac{A_{i+1,j,k} - A_{i,j,k}}{\Delta x} \frac{\mu_{i+1,j,k} + \mu_{i,j,k}}{2} - \frac{A_{i,j,k} - A_{i-1,j,k}}{\Delta x} \frac{\mu_{i,j,k} + \mu_{i-1,j,k}}{2} \right), \\
A_{i,j,k} &\mapsto A_{i,j,k} + \Delta t \left(\frac{A_{i,j+1,k} - A_{i,j,k}}{\Delta y} \frac{\mu_{i,j+1,k} + \mu_{i,j,k}}{2} - \frac{A_{i,j,k} - A_{i,j-1,k}}{\Delta y} \frac{\mu_{i,j,k} + \mu_{i,j-1,k}}{2} \right), \\
A_{i,j,k} &\mapsto A_{i,j,k} + \Delta t \left(\frac{A_{i,j,k+1} - A_{i,j,k}}{\Delta z} \frac{\mu_{i,j,k+1} + \mu_{i,j,k}}{2} - \frac{A_{i,j,k} - A_{i,j,k-1}}{\Delta z} \frac{\mu_{i,j,k} + \mu_{i,j,k-1}}{2} \right).
\end{aligned} \tag{2.5}$$

To prevent this error, we altered the routine to calculate fluxes in all directions simultaneously. This modification makes it necessary to reduce the turbulent time-step. When diffusion in all directions is performed simultaneously, this is discretised as

$$\begin{aligned}
\frac{\Delta A}{\Delta t} = & \frac{A_{i+1,j,k} - A_{i,j,k}}{\Delta x} \frac{\mu_{i+1,j,k} + \mu_{i,j,k}}{2} - \frac{A_{i,j,k} - A_{i-1,j,k}}{\Delta x} \frac{\mu_{i,j,k} + \mu_{i-1,j,k}}{2} \\
& + \frac{A_{i,j+1,k} - A_{i,j,k}}{\Delta y} \frac{\mu_{i,j+1,k} + \mu_{i,j,k}}{2} - \frac{A_{i,j,k} - A_{i,j-1,k}}{\Delta y} \frac{\mu_{i,j,k} + \mu_{i,j-1,k}}{2}. \\
& + \frac{A_{i,j,k+1} - A_{i,j,k}}{\Delta z} \frac{\mu_{i,j,k+1} + \mu_{i,j,k}}{2} - \frac{A_{i,j,k} - A_{i,j,k-1}}{\Delta z} \frac{\mu_{i,j,k} + \mu_{i,j,k-1}}{2}
\end{aligned} \tag{2.6}$$

This discretisation can cause 0 to change sign if $|\Delta A| > |A|$, and so a simple criterion for a minimum time-step is that it will always prevent this. Even in the case of velocity (where negative values are permitted), a numerical instability can build when velocities can flip signs within a single time-step, although in practice we only apply this to scalars.

The maximum value of ΔA for each cell is found when $A_{i\pm1,j\pm1,k\pm1} = 0$ and $A_{i,j,k} \neq 0$ (or vice versa). Assuming μ is constant, and $\Delta x \sim \Delta y \sim \Delta z$ this gives

$$\frac{\Delta A}{\Delta t} = -6\frac{\mu A}{\Delta x^2} \tag{2.7}$$

which for the criterion of $A = |\Delta A|$ gives a minimum time-step of

$$\Delta t = \frac{1}{6}\frac{\Delta x^2}{\mu}. \tag{2.8}$$

This is the minimum required time-step to prevent negative values. While this time-step is three times smaller than the minimum time-step for an approach that sweeps through each directions in turn, the simultaneous approach does not have any direction dependent error. In practice, this prefactor of 1/6 is slightly too large to prevent numerical instabilities (an "oscillating checkerboard" effect), and after some tests we found a value of 1/20 maintained stability.

2.3.1.4 Temperature calculation

We also fixed an error that produced negative temperatures in situations with large K_{turb}/e_i. In the equation of state subroutine, temperature was calculated from the thermal component of the internal energy by

$$T = \frac{(\gamma - 1)(e_i - K_{\mathrm{turb}})}{k_B}, \tag{2.9}$$

where k_B is the Boltzmann constant, γ is the adiabatic index, and μ is the molecular mass of the gas. This formulation can cause major errors in temperature if K_{turb} is not updated consistently with e_i, as this is true in the hydrodynamic step. FLASH

can automatically advect any new grid variable specified in a module's *Config* file. Hence the advection of $K_{\rm turb}$ was performed correctly, and consistently with the internal energy e_i. However, the pdV work term is neglected for $K_{\rm turb}$, and so in expanding regions e_i will decrease by a greater factor than $K_{\rm turb}$. This omission can cause particularly large errors because the sound speed for the Courant condition is calculated from the total internal energy, and so it is possible when $f_{\rm turb} = K_{\rm turb}/e_i$ is large (i.e. close to 1) for a cell to lose more thermal energy than it contains, producing negative temperatures. To remedy this, we instead calculate the temperature from the turbulent energy fraction $f_{\rm turb} = K_{\rm turb}/e_i$, which was also advected in FLASH. Specifically, the temperature is calculated by applying the following equation,

$$T = \frac{(\gamma - 1)(f_{\rm turb} e_i)}{k_B}, \tag{2.10}$$

To maintain accuracy (i.e. prevent $f_{\rm turb} > 1$), we also advected the variable $f_{\rm thermal} = (1 - K_{\rm turb})/e_i$, and used the normalization feature in FLASH to force $f_{\rm turb} + f_{\rm thermal} = 1$. The normalization feature applies the steps

$$\begin{aligned} f_{\rm norm} &\mapsto f_{\rm turb} + f_{\rm thermal} \\ f_{\rm turb} &\mapsto f_{\rm turb}/f_{\rm norm} \\ f_{\rm thermal} &\mapsto f_{\rm thermal}/f_{\rm norm} \end{aligned} \tag{2.11}$$

every time-step. This procedure completely prevents negative temperatures.

2.3.1.5 Bubble positions

The feedback routine produces bubbles with random radial and azimuthal coordinates r and ϕ. To produce these coordinates, two pseudo-random numbers ξ_1, ξ_2 are generated from an even distribution between 0 and 1. The required radial coordinate r is selected from a $\rho^{3/2}$ weighted distribution. For an exponential disc with scale-length h, this can be produced by iteratively solving the equation $r = \log((1 + r)/(1-\xi_2))$ – i.e. simply setting $r_0 = \log((1)/(1-\xi_2))$ and $r_{i+1} = \log((1+r_i)/(1-\xi_2))$,

and then finding a sufficiently high i such that the sequence has converged (we use r_{13}). However, parentheses were missing in the code so that while the first three iterations were correct, the final ten iterations were incorrectly written as $r_{i+1} = \log(1 + r_i/(1 - \xi_2))$, i.e. neglecting a pair of parentheses. This process did not result in the desired distribution for r, and was corrected.

Chapter 3

Effective Viscosity due to Cloud Collisions in Galaxies

3.1 Introduction

Arguably,[1] the most successful model for the formation of disc galaxies is the ΛCDM model, in which galaxies are formed from the dissipational collapse of baryonic gas within a dark matter halo (White & Rees 1978; Blumenthal et al. 1984; Davis et al. 1985; White & Frenk 1991; Kauffmann et al. 1993; Cole et al. 1994; Baugh 2006; Benson 2010). While the physical viscosity of the baryonic gas is not anticipated to have a strong influence on gas evolution except in magnetized or hot environments such as a galaxy cluster (e.g Sijacki & Springel 2006), effective kinematic viscosities could in principle impact disc evolution. One-dimensional simulations by Lin & Pringle (1987) with a viscous time-scale close to the star-formation time-scale showed that viscous evolution with infall can reproduce the ubiquitous exponential density profile from a range of initial conditions. In our work the viscosity was assumed to be caused by large-scale turbulent motions dissipating kinetic energy and transporting angular momentum.

Feedback from supernovae can be a source of viscosity by feeding this turbulence (Vollmer & Beckert 2003). Additionally, the self-gravity of the gaseous disc can provide an effective viscosity (Vollmer & Beckert 2002). This viscosity can take the form of large-scale instabilities (Gammie 2001; Rafikov 2009), or of interactions between giant molecular clouds (Vollmer & Beckert 2002). These cloud interactions potentially generate viscosity through two different mechanisms. Firstly, gravitational

[1] This chapter is adapted from Williamson & Thacker (2012), but includes additional results from simulations with feedback that were not included in the published paper

scattering can increase the velocity dispersion of the cloud population, converting orbital energy into large-scale turbulence (Gammie et al. 1991; Fukunaga & Tosa 1989; Agertz et al. 2009). Secondly, during inelastic collisions between clouds, shocks convert orbital energy into turbulence and heat within the colliding clouds (e.g. Gittins et al. 2003; Kitsionas & Whitworth 2007; Anathpindika 2009). Radiative processes contribute to the dissipation of kinetic energy during these collisions, and are also important for dissipating turbulent energy that has cascaded into thermal energy. These processes are significant even in the absence of star-formation: the observations compiled by Dib et al. (2006) show that the velocity dispersion of HI gas does not strongly depend on the star-formation rate below a certain threshold, and the AMR simulations of Agertz et al. (2009) suggest that a 'baseline' turbulence is caused by interactions between clouds, and that this is only supplemented by supernova feedback at high star-formation rates.

It has been argued (Vollmer & Beckert 2002; Bell 2002, hereafter B02) that cloud-collisions are not an efficient source of viscosity. In particular, in B02 the time-scales for viscosity due to cloud collisions are estimated to be on the order of $t_\nu \sim 1000$ Gyr in most local spiral galaxies, although the time-scales might be considerably lower in earlier gas-rich galaxies or in galaxies where the velocity distribution of GMCs has been stirred up by some mechanism (such as galaxy interaction e.g. Hernquist & Mihos 1995). Vollmer & Beckert (2002) argue that because molecular clouds evaporate at an age of $\sim 10^7$ yr, and this is less than the time between collisions ($\sim 10^8$ yr), cloud collisions are very rare. However, cloud formation times, assuming that collapse and formation of H_2 are the dominant factors in forming a cloud, appear to be equally short (Glover & Mac Low 2007). The combination of these effects leads to a scenario in which the number density of clouds is roughly constant, although the short lifetime may affect the velocity dispersions of molecular clouds as they have less time to build up a large deviation from circular velocity through scattering events with other clouds. In this steady state, the effective collision time-scale should remain similar.

It has also been argued that physical collisions between clouds have a smaller effect than gravitational scattering (Jog & Ostriker 1988), particularly if magnetic fields are taken into account, cloud interaction cross-sections may be underestimated (Ozernoy et al. 1998). On the other hand, Das & Jog (1996) modelled a system of cloud particles, finding that cloud collisions rather than local gravitational interactions (scattering events) dominate the mass distribution and velocity dispersion of molecular clouds, suggesting that cloud collisions may indeed be important. However, as far as we are aware, the effective viscosity of direct cloud-cloud collisions has not yet been examined in global three dimensional numerical hydrodynamic models.

Many simulations of cloud formation and the associated disc dynamics have been performed in two dimensions and/or on a small scale using shearing-box studies (e.g. Kim & Ostriker 2007). However, as mentioned above, increased computing power and the availability of locally adaptive algorithms have recently enabled galaxy-scale simulations with sufficiently high resolution to resolve cloud-formation in discs. Numerical experiments have been performed using both AMR (Tasker & Tan 2009; Tasker 2011; Agertz et al. 2009) and SPH (Robertson & Kravtsov 2008) with resolutions as fine as 6 pc. The non-trivial cooling processes and chemistry make these simulations a significant technical challenge. Agertz et al. (2009) and Tasker & Tan (2009) ran suites of high resolution AMR simulations of Milky-Way and M33-like disc galaxies, and reported on the properties of the clouds generated by their models, including cloud-cloud velocity dispersion. However, neither study has provided an estimate of the viscous time-scale due to cloud-cloud collisions. Furthermore, the discs of Tasker & Tan (2009) are more uniform than the Milky Way, with a density distribution chosen to give a constant value of the Toomre Q parameter (Toomre 1964), and a static dark matter and stellar component, which may inhibit some of the instabilities important to cloud formation. In this thesis we revisit the calculations of B02 with full three dimensional SPH models.

Note that the analysis of processes related to clouds in hydrodynamic simulations is not entirely trivial since there is no universally agreed upon cloud finding

process. However, the use of a particle method enables the Friends-of-Friends (Davis et al. 1985) group finding methodology and we adapt that to our simulations. Hence given our cloud population our primary goal is to see whether the analytical calculations are supported, and if not what the implications are. It is important to note that the results of such simulations could highlight non-physical evolution in numerical schemes with artificial viscosities, of which SPH is a notable example (Valdarnini 2011). We also investigate the issue of numerical artefacts in our calculated results. Numerical artefacts are a key issue since structure formed within simulations starting from smooth initial conditions is inevitably the result of amplification of noise in the initial conditions.

While a full calculation in the cosmological context (e.g. Katz 1992; Thacker & Couchman 2001; Governato et al. 2007; Brook et al. 2008; Scannapieco et al. 2009; Stinson et al. 2010) is beyond the scope of this work, primarily due to resolution limitations, we instead consider two classes of isolated models. We examine an equilibrium system with similar parameters to the Milky Way consisting of a gas disc, a stellar disc and bulge, and a dark matter halo. Here the gas disc is stabilized by the other components which dominate the system's mass. We also consider the dissipational collapse problem that has been used extensively elsewhere (e.g. Gott & Thuan 1976; Carlberg 1984; Katz & Gunn 1991; Brook et al. 2004; Kaufmann et al. 2006). In contrast with the Milky Way model, this collapse produces a very unstable disc, and so we investigate both high-stability gas-poor systems and low-stability gas-rich systems. These models include hydrodynamics, gravitational interactions, cooling with a dynamic temperature floor, and in some cases feedback and star formation. The development of a fully self-consistent feedback algorithm with molecular cloud formation, so for most of our models we remove the numerous unknowns associated with star-formation and feedback (as discussed in numerous places e.g. Thacker & Couchman 2000; Ceverino & Klypin 2009; Christensen et al. 2010) we hope to to isolate the impact of cloud-cloud interactions and place lower bounds on the viscous time-scale.

For comparison we also perform simulations that include convential feedback and star formation, noting that this process is not entirely self-consistent.

3.2 Simulation

3.2.1 Simulation Code

These simulations were performed with HYDRA (Thacker & Couchman 2006), which we described in chapter 2, including the modifications made by the author. Here we describe the star formation and feedback algorithms (section 3.2.2) which we made use of, as well as our initial conditions for both of our scenarios (section 3.2.3).

3.2.2 Star formation and feedback

Feedback is the input of energy into the ISM, usually from stars and AGNs (for a general review see Baugh 2006). Outflows and radiation from these objects can inject mass, metals, heat, and momentum into the ISM. We do not consider AGN feedback in this work, as the Milky Way is not considered to have an AGN (although it is possible that the Milky Way harboured some AGN-type activity in the past (Guo & Mathews 2012)). However, stellar feedback has an important effect on gas in any galaxy.

Stellar feedback models typically assume that the dominant feedback mechanism is supernovae (Katz 1992, for example). Most of the supernovae in the galaxy are produced by bright young stars (Katz 1992), within ~ 8 Myr of their formation. Hence supernova feedback is often assumed to be simultaneous with star formation, or the properties that are resolved are considered "averaged". The star formation rate in a particle or cell is then taken as $\dot{M}_* = M_g/t_{sf}$, where $\dot{M}_*$ is the rate of change of the stellar mass, M_g is the gas mass, the star formation time-scale $t_{sf} = M_g/\dot{M}_* \propto t_{ff}$, and the free-fall time-scale t_{ff} is proportional to $\rho^{-1/2}$, specifically

$$t_{ff} = \frac{1}{4}\sqrt{\frac{3\pi}{2G\rho}}. \tag{3.1}$$

This results in a star formation rate that is proportional to $\rho^{3/2}$, which under the assumption that $\rho \propto \Sigma$ agrees with the well-known Keniccutt Schmidt law (Kennicutt 1998), $\Sigma_{sf} \propto \Sigma_{gas}^{\alpha}$, where Σ_{sf} is the star formation rate per unit area, Σ_{gas} is the gas surface density, and $\alpha \sim 1.5$ (Kennicutt 1997).

In our implementation (as in Thacker & Couchman 2000), this feedback is input by increasing the internal energy of the neighbour particles. To avoid the well-known problem of short cooling times causing all the inputted energy to be lost before the feedback region can have any dynamic impact on its surroundings, we turn off cooling for a fixed period of time for particles that have received feedback energy (as justified in Mori et al. 1997). Other approaches to mitigate this problem can involve inputting some fraction of the feedback energy directly into the velocity of the neighbouring particles, or, as in Chapter. 4, into sub-grid turbulent kinetic energy. We analyse two simulations with feedback, and vary this cooling shut-off period between them, setting it to 0.5 Myr in one and 1 Myr in the other. This parameter effectively sets the strength of the feedback, with a longer shut-off period producing stronger feedback.

This approach is best suited for lower resolution and becomes a progressively less accurate approximation as spatial and temporal resolutions increase. If the time-step is much shorter than 8 Myr, then forcing simultaneity between star formation and supernova feedback is not an accurate approximation, as gas can dynamically evolve within this time. Furthermore, observations have given evidence that small molecular clouds are disrupted before a supernova event (Murray 2011), suggesting that stellar winds and radiative pressure on dust can have a significant effect.

The discretisation required for particle and grid simulations produces further complications. Stars are typically modelled by particles even if gas is modelled by a grid, as an Eulerian approach is the most computationally straightforward method for simulating a collisionless system. However, if every cell or particle undergoing star formation produced a star particle of mass $\Delta_t M_g / t_{sf}$ at every time-step, the number of particles will increase far too rapidly for computation within a reasonable

time. Instead, many models maintain a star-formation count for gas cells or particles, which produces a star particle once it reaches a certain threshold. This threshold may be stochastic (e.g. Stinson et al. 2006), or may be set to some constant value (e.g. Thacker & Couchman 2001). While this method reduces the computational load, it also forces the gas and stars to be dynamically coupled until the particle is produced, which has a distinct impact on dynamical evolution as early creation of stars will spread mass out over a larger volume.

Overcoming these problems involves developing a more detailed feedback model, and such investigations are in progress (e.g. Hopkins et al. 2012b). The key factor is that sites of star formation (i.e. GMCs) are resolved and hence directly modelled. The details of these advanced models and their effects on cloud formation and interaction are sufficiently complex that they are beyond the scope of our work. Instead, we do not use a feedback algorithm for most of our models, and investigate the effect of the classical approach implemented by Thacker & Couchman (2000, 2001). The feedback simulations used in this thesis were run by James Wurster, and analysed by the author.

3.2.3 Inital Conditions

3.2.3.1 Milky Way Model

We produce our Milky Way model using the GALACTICS package (Kuijken & Dubinski 1995; Widrow & Dubinski 2005; Widrow et al. 2008) with the parameters in Table 2 of Widrow et al. (2008). Through an iterative process, this package produces an equilibrium system consisting of an exponential stellar disc, a stellar bulge and a dark matter halo. The stellar disc is exponential radially, follows sech^2 vertically, and has a radial dispersion profile of

$$\sigma_R^2(R) = \sigma_{R_0}^2 \exp(-R/R_\sigma), \tag{3.2}$$

Name	a_h (kpc)	r_h (kpc)	δr_h (kpc)	γ	σ_h (km s^{-1})	M_{halo}
Collapse haloes	25.75	300	50	1.0	351	1.1×10^{12}
MW haloes	13.6	275	25	0.81	330	7.3×10^{11}

Table 3.1: Halo parameters. As in Eq. 3.3, a_h is the halo scale parameter, r_h is the truncation radius, δr_h is the scale length for this truncation, γ is the cuspiness parameter, and σ_h is a velocity parameter that sets the halo mass, M_{halo}.

where R is the radial coordinate, σ_R is the radial velocity disperion, σ_{R_0} is the radial velocity dispersion at $R = R_0 = 0$, and R_σ is the scale length for radial velocity dispersion. We set $R_\sigma = R_d$, the scale length of the disc, for simplicity. We generate the gas disc by copying the disc star particle positions and flipping the coordinates across the $x = y$ plane to prevent particles having coincident positions. Bulge particles are not copied. The masses of the gas and star particles are scaled to give the appropriate mass ratio. The gas disc is given a dispersionless velocity profile output by GALACTICS and is initially isothermal at 10^4K. The disc scale length is 2.81 kpc, truncated at 30 kpc by the complementary error-function with a scale-length of 0.1 kpc. The scale height is initially 0.36 kpc, and the total disc mass is $5.2 \times 10^{10} M_\odot$. The halo density profile is

$$\rho = \frac{2^{2-\gamma}\sigma_h^2}{4\pi a_h^2} \frac{1}{(r/a_h)^\gamma (1 + r/a_h)^{3-\gamma}} \frac{1}{2} \mathrm{erfc}\left(\frac{r - r_h}{\sqrt{2}\delta r_h}\right), \tag{3.3}$$

where a_h is the halo scale parameter, r_h is the cutoff radius, δr_h is the scale length for the truncation, γ is the 'cuspiness' parameter (equal to unity for an NFW profile (Navarro et al. 1996)), and σ_h is a velocity parameter that sets the mass of the halo.

Halo parameters are given in Table 3.1. In addition to having an active dynamic n-body halo we also ran a test with a static analytic halo potential, to explore if the discretization of the halo has any effect on cloud formation.

The bulge density profile, $\rho_b(r)$ is

$$\rho_b(r) = \rho_{b0} \left(\frac{r}{R_e}\right)^{-p} \mathrm{e}^{-b(r/R_e)^{1/n}}, \tag{3.4}$$

where $p = 1 - 0.6097/n + 0.05/n^2$ gives a Sérsic profile with n the Sérsic index. R_e is the radial scale parameter, and ρ_{b0} is a parameter defined by velocity parameter $\sigma_b \equiv \{4\pi n b^{n(p-2)}\Gamma[n(2-p)]R_e^2\rho_{b0}\}^{1/2}$, where $\Gamma(x) = \int_0^\infty e^{-t}t^{x-1}dt$ is the standard extension of the factorial function to all real numbers. We set the parameters in this equation to $n = 1.32$, $\sigma_b = 272$ km s^{-1}, and $R_e = 0.64$ kpc, again following the Milky Way model of Widrow et al. (2008).

Name	l_{soft} (pc)	T_{foor} (K)	n_*	$n_{\rm g}$	$n_{\rm DM}$	$m_{\rm g}/m_*$	$t_{\rm end}$ (Gyr)	$h_{\rm disc}$ (kpc)	α, β	t_* (Myr)
LowSoftMW	60	300	5×10^5	4×10^5	5×10^5	0.1	1.116	0.36	1, 2	N/A
MedSoftMW	100	300	5×10^5	4×10^5	5×10^5	0.1	1.146	0.36	1, 2	N/A
HighSoftMW	500	300	5×10^5	4×10^5	5×10^5	0.1	1.542	0.36	1, 2	N/A
LowResMW	60	300	1×10^5	8×10^4	1×10^5	0.1	1.959	0.36	1, 2	N/A
LowFloorMW	60	10	5×10^5	4×10^5	5×10^5	0.1	1.004	0.36	1, 2	N/A
LowViscMW	60	300	5×10^5	4×10^5	5×10^5	0.1	1.002	0.36	0.5, 1	N/A
MedGasMW	60	300	5×10^5	4×10^5	5×10^5	0.2	0.485	0.36	1, 2	N/A
HighGasMW	60	300	5×10^5	4×10^5	5×10^5	0.5	0.434	0.36	1, 2	N/A
FlatMW	60	300	5×10^5	4×10^5	5×10^5	0.1	0.790	0.036	1, 2	N/A
HighResFlatMW	45	300	1.25×10^6	1×10^6	1.25×10^6	0.1	0.318	0.036	1, 2	N/A
WeakFeedMW	60	300	5×10^5	4×10^5	5×10^5	0.1	0.954	0.36	1, 2	0.5
StrongFeedMW	60	300	5×10^5	4×10^5	5×10^5	0.1	1.137	0.36	1, 2	1.0

Table 3.2: Summary of Milky Way runs. l_{soft} is the minimum softening length, T_{floor} is the temperature floor, n_*, $n_{\rm g}$, and $n_{\rm DM}$ are the numbers of star, gas and dark matter particles, $m_{\rm g}/m_*$ is the gas/star mass ratio for the disc, t_{end} is the total simulation time, $h_{\rm disc}$ is the scale height of the disc, α and β are the artificial viscosity parameters, and t_* is the cooling shut-off time.

We have named our fiducial run LowSoftMW. To test the effects of changing the resolution, softening length, temperature floor, gas mass fraction, and artificial viscosity we investigate a total of ten different runs, summarized in Table 3.2. Both MidSoftMW and HighSoftMW have higher gravitational softening lengths, while MedGasMW and HighGasMW have higher gas mass fractions, LowFloorMW has a lower temperature floor, LowViscMW has lower artificial viscosity parameters (α, β), and LowResMW has a lower resolution.

In addition, as a convergence check, we ran a higher resolution simulation (HighResFlatMW) with a total of 3.5×10^6 particles and a softening length of 45 pc, although we do not consider this our fiducial run as the simulation was too slow to evolve to 1 Gyr within a reasonable wall-clock time. We found when running a simulation of this high resolution with identical initial conditions to LowSoftMW that the disc was initially dominated by a strong ring-shaped shock propagating outwards. This shock is caused by a combination of the rapid vertical collapse of the disc as radiative cooling is turned on, and the rotation curve not being quite precise enough because GALACTICS is intended for collisionless mechanics and does not take into account gravitational softening or the pressure gradient of the gaseous disc. At the lower resolutions this shock is poorly captured, and the disc quickly returns to equilibrium, so this is only a problem at our highest resolution.

To prevent the shock becoming a problem it is necessary to start the simulation from an initially flattened state akin to the later evolution of the cooled disks. We therefore flattened the gas disc to a similar scale height as the cooled disks, which is a factor of 10 smaller. Circular velocities ($v_{\rm circ}$) were then set up using radial accelerations ($a_{\rm rad}$) generated from a single iteration of the HYDRA code, and explicitly setting $a_{\rm rad} = v_{\rm circ}^2/R$ for each gas particle, where R is the radial coordinate of the particle. We also performed a simulation (FlatMW) with these initial conditions but at our fiducial (moderate) resolution, for a fair comparison of the effects of resolution.

3.2.3.2 Monolithic Collapse Model

This model consists of a spherically symmetric distribution of gas within an equilibrium NFW dark matter halo. We generate the halo using GALACTICS according to the parameters in Table 3.1, giving a halo with $M = 1.1 \times 10^{12} M_{\odot}$.

For the gas we use the 'high-entropy' (high-S) profile of Kaufmann et al. (2009), which was produced from equation 1 of Kazantzidis et al. (2004),

$$\rho(r) = \frac{\rho_{\rm s}}{(r/r_{\rm s})^{\gamma}[1 + (r/r_{\rm s})^{\alpha}]^{(\beta-\gamma)/\alpha}} \ , \tag{3.5}$$

setting $c = 1$, $\alpha = 1$, $\beta = 3$, and $\gamma = 0$. Kaufmann et al noted that a gas density profile that is shallower than the NFW profile (as expected in models with pre-heating feedback e.g. Mo & Mao 2002) produces an angular momentum distribution in the final object that better fits observations. In this model, the gas collapses into clumps which combine to form an unstable disc.

As in Kaufmann et al. (2007), the initial temperature profile is calculated to provide hydrostatic equilibrium according to

$$T(r) = \frac{\mu}{k_B} \frac{1}{\rho_{\rm G}(r)} \int_r^{\infty} \rho_{\rm G}(r) \frac{G M_{\rm tot}(r)}{r^2} {\rm d}r, \tag{3.6}$$

where μ is the mean molecular weight of the gas (taken as its primordial value, $\mu \approx 0.59 m_H$), k_B is the Boltzmann constant, $\rho_{\rm G}$ is the initial gas density, and $M_{\rm tot}(r)$ is the total mass (gas and dark matter) within a sphere of radius r. We give the gas a flat velocity profile. The positions of the gas particles in our initial conditions are simply the generated positions of the dark matter particles flipped as in section 3.2.3.1.

To set up a rotating halo, GALACTICS swaps a fraction of the dark matter particles' velocities over the radial axis to increase the number of particles rotating in the same direction. We assume the gas and the dark matter have the same specific rotational momentum, i.e.

$$\frac{|L_G|}{M_G} = \frac{|L_{\rm DM}|}{M_{\rm DM}}, \tag{3.7}$$

Name	l_{soft} (pc)	T_{foor} (K)	$n_{\rm g}$	$n_{\rm DM}$	$m_{\rm g}/m_{\rm DM}$	$t_{end}(Gyr)$
HighSoftC	514	3×10^4	5×10^5	1×10^5	0.148	4.5
MidSoftC	200	3×10^4	5×10^5	1×10^5	0.148	3.9
LowSoftC	60	3×10^4	5×10^5	1×10^5	0.148	3.3
LowSoftFloorC	60	300	5×10^5	1×10^5	0.148	3.7
LowResC	60	300	1×10^5	1×10^5	0.148	4.6
LowMassC	512	3×10^4	5×10^5	1×10^5	0.030	7.8

Table 3.3: Summary of collapse runs. l_{soft} is the minimum softening length, T_{floor} is the temperature floor, $n_{\rm g}$ and $n_{\rm DM}$ are the numbers of gas and dark matter particles, $m_g/m_{\rm DM}$ is the gas/dark matter mass ratio, and t_{end} is the total simulation time.

so that the spin parameter (Binney & Tremaine 2008) of the gas is equal to the spin parameter of the halo,

$$\lambda_G = \frac{|L_G|}{M_G} \frac{\sqrt{|E_{\rm DM}|}}{GM_{\rm DM}^{3/2}} = \frac{|L_{\rm DM}|}{M_{\rm DM}} \frac{\sqrt{|E_{\rm DM}|}}{GM_{\rm DM}^{3/2}} = \lambda_{\rm DM}. \tag{3.8}$$

We used a spin parameter of $\lambda_G = 0.038$, close to the median value observed in simulations (Bullock et al. 2001; Barnes & Efstathiou 1987). After each gas/DM halo is produced, it is evolved for 0.5 Gyr with cooling switched off to ensure the initial conditions are stable. Our first model (HighSoftC) was run with the softening equal to Kaufmann et al. (2009)'s and the temperature floor equal to Kaufmann et al. (2009)'s cooling floor. We also investigated models with lower softening lengths and temperature floors to see if smaller clouds were resolved. A low resolution run was performed as a convergence check, and finally we performed a model with a low gas fraction to see the effect of increasing the disc's stability. These models are summarized in Table 3.3.

3.3 Analysis Code

3.3.1 Cloud tracking and identification

We measured the effects of cloud collisions in our models with a post-processing code. The basic principle of the algorithm is to examine every interaction between

clouds to determine the amount of kinetic energy lost through interactions, and hence determine viscous time-scales for the simulation.

Clouds are first identified with a friends-of-friends algorithm (Davis et al. 1985). In this algorithm, a particle that is within a certain distance of another particle – the linking length – is considered linked. This linking is transitive (hence "friends of friends"). That is, if particle A is linked to particle B, and particle B is linked to particle C, then particle A is also linked to particle C. This approach builds up groups of linked particles, where each group is separated from all other groups by gaps of at least the linking length in size. We make use of the University of Washington code FOF (U. Washington 2012) implementation.

In simulations with constant or near-constant particle mass, the linking length approximately corresponds to a density threshold. It can be used to select clumps of cool, dense, molecular gas. We considered any linked group of 30 or more particles to be a "cloud". However, we found in practice that the unmodified friends-of-friends algorithm was not sufficiently robust, as the distance to outer sections of clouds would often slip just above or below the linking length, which would be identified as the cloud splitting into two clouds and then recombining. This problem is exactly analogous to the "string of pearls" issue noted in collisionless simulations (Elahi 2009). Furthermore, it was difficult to avoid selecting the thin filaments produced by galactic shear or cloud collisions.

To resolve this, we modified the algorithm to only consider particles above an explicit density threshold, $\rho = 7\ M_\odot\ \mathrm{pc}^{-3}$, corresponding to the denser parts of a molecular cloud, and set the linking length to 50 pc. This linking represents a lower density that is geometry and resolution dependent. For a close-packed three-dimensional arrangement such as face-centred-cubic, this corresponds to a density of $\rho = 0.06 - 0.7 M_\odot\ \mathrm{pc}^{-3}$, depending on resolution. For other arrangements (e.g. a thin string of particles) this effective threshold density from the linking length can be lower, but may also strongly depend on the smoothing length. The explicit high density cutoff ensured that only dense molecular gas was considered (excluding thin

filaments), while the high linking length makes the algorithm more stable. This algorithm is applied to each simulation dump, and a list of clouds and their particles is produced.

To follow the evolution of an individual cloud, clouds must be tracked between dumps. Tracking clouds is comparatively easy in an SPH code, as we can identify clouds and their interactions by following the individual particles between dumps, which are dumped every 20 time-steps. If the cloud A at time t_i contains at least half of the particles contained by cloud B at the time of the following dump t_{i+1}, then A is a parent of B. If B contains at least half of the particles contained by cloud A, then B is a child of A. If B has several parents, then a merger has occurred. If A has several children, then a separation has occurred. If A is the only parent of B, and B is the only child of A, then B is identified as the *same cloud* as A. The factor of one-half gives the largest possible lee-way in redistributing particles between clouds, while still forcing clouds to be uniquely identified. This approach is illustrated in Fig. 3.1.

This categorization also allows for multiple parents to join in a merger and it is also possible for a parent to split into into multiple children. During simulations we observed that mergers can be complex with clouds merging and separating several times before settling into a single cloud, or in some cases while no longer interacting — that is, our interaction detecting algorithm is too sensitive. However, this does not produce a large error in the viscous time-scale, because the sum of energy lost over all of these detected interactions should be equal to the actual energy lost in a full merger, which also means our statistics are perhaps better thought of as recording 'interaction' rates (including 'self-interaction') rather than cloud collision rates.

3.3.1.1 Energy analysis

From the cloud energy budget we can obtain an estimate for the total time-scale for dissipation of kinetic energy from cloud-cloud interactions. We define this by analogy with the star-formation time-scale, which is typically defined as $t_{SFR} =$

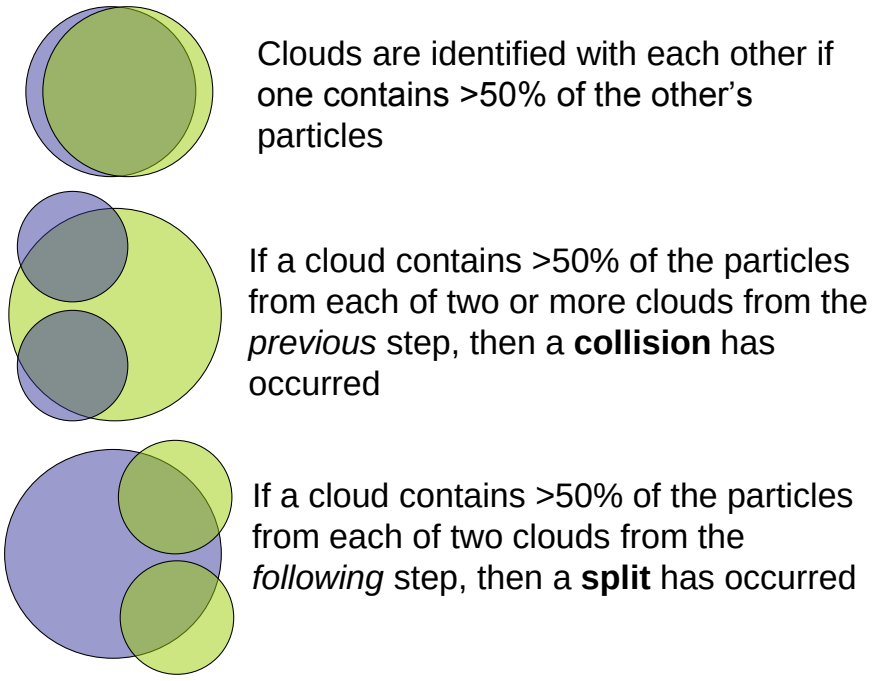

Figure 3.1: Our approach for determining if clouds have merged or split. Blue clouds are clouds from the previous simulation dumps, green clouds are clouds from the current dump.

$\Sigma_{gas}/(d\Sigma_*/dt)$, where Σ_{gas} is the surface density of gas, and $d\Sigma_*/dt = -\Sigma_{gas}$ is the rate at which this is converted into a stellar surface density. Hence we define the viscous time-scale due to cloud-cloud collisions to be the dissipative time-scale,

$$t_{\nu_{\rm col}} = \frac{K}{-{\rm d}K_C/{\rm d}t}, \tag{3.9}$$

where K is the total orbital kinetic energy of the gas, and $-{\rm d}K_C/{\rm d}t$ is the rate at which this kinetic energy is dissipated due to collisions. This dissipation rate can be written as

$$\frac{-{\rm d}K_C}{{\rm d}t} = C\Delta K_{\rm col}, \tag{3.10}$$

where C is the interaction rate (determined by counting the number of interactions that occur within a time period) and $\Delta K_{\rm col}$ is the energy lost per interaction. In practice, we average over $n_{\rm col}$ interactions so that

$$t_{\nu_{\rm col}} = \frac{\Delta t}{n_{\rm col}} \frac{\sum_{i=1}^{n_{\rm col}} K(t_i)}{\sum_{i=1}^{n_{\rm col}} \Delta K_i}. \tag{3.11}$$

where Δt is the time period that the $n_{\rm col}$ interactions occurred over (and hence $C = \frac{n_{\rm col}}{\Delta t}$), ΔK_i is the kinetic energy lost in a particular interaction i and $K(t_i)$ is the total kinetic energy in gas at the time of that interaction.

It is important that we connect this method of measuring the dissipative time-scale in our models with definitions used elsewhere. It is commonly argued (e.g. B02) that the form of the viscous time-scale is

$$t_\nu \approx \frac{R^2}{\nu}, \tag{3.12}$$

where R is the radial coordinate and ν the (effective) viscosity.

To see how this form arises in our measurements, consider the following argument: If we neglect radial velocity, then the kinetic energy per unit volume of a component of fluid in a rotating disc is $k = \rho(R\Omega)^2/2$, where Ω is the angular velocity at this radius. We can convert the rate of viscous dissipation for a generic fluid (Φ, the energy lost per unit volume per unit time) from Mihalas & Weibel Mihalas (1984) into cylindrical coordinates and again assume angular velocity dominates, simplifying it to:

$$\Phi = \rho\nu(R\Omega')^2, \tag{3.13}$$

where the prime indicates a radial derivative. We can substitute these values into our definition for $t_{\nu_{\rm col}}$ because $\Phi = -{\rm d}k_C/{\rm d}t$, so

$$t_{\nu_{\rm col}} = \frac{\rho(R\Omega)^2/2}{\rho\nu(R\Omega')^2} = \frac{\Omega^2}{2\nu(\Omega')^2}. \tag{3.14}$$

If we then take a power law for rotation $\Omega \propto R^{-\alpha}$ then

$$t_{\nu_{\rm col}} = \frac{1}{2\alpha^2}\frac{R^2}{\nu}, \tag{3.15}$$

which agrees with R^2/ν within a factor of $1/2\alpha^2$. For a flat rotation curve, $\alpha = 1$ and this factor is merely 1/2 — hence the dissipative time-scale is of the order of the traditional viscous time-scale. Note, Lin & Pringle (1987) give a different prefactor — $(2-\alpha)/(\alpha)$. However, these values all agree within an order of magnitude, provided α is not extremely large or small. Although our viscous time-scales are calculated over the whole disc to ensure sufficient numbers of interactions are measured, and the analytical R^2/ν is a local value at a specific radius, we should not expect this to have an effect beyond an order of magnitude, assuming analytical viscous time-scales have been calculated at a representative radius.

3.4 Results

3.4.1 Milky Way Model

3.4.1.1 General Evolution

The evolution of all models excluding HighSoftMW are similar[1]. In these models the initial state of the gaseous disc is close to a hydrodynamic equilibrium. However, the gas rapidly cools and becomes unstable, collapsing vertically (except in FlatMW and HighResFlatMW, which are produced from already-collapsed initial conditions), and forming spiral instabilities which fragment into large number of small ($m \sim 10^6$–$10^7 M_\odot$, $R \sim 100$ pc) clouds.

After this epoch of rapid cloud formation, the clouds merge and continue to accrete material. The number of clouds drops, as illustrated in Fig. 3.2, while the total mass within clouds continues to increase until both reach a less dramatic stage from around 0.8–1.0 Gyr, where the number of clouds decays only gradually as the mass within clouds gradually increases. A face-on view of the evolution of LowSoftMW is shown in Fig. 3.3, and a snapshot of HighResFlatMW is shown in Fig. 3.4. In HighSoftMW cloud collapse was quenched by the high softening length, and instead the disc was dominated by large scale instabilities (Fig. 3.5). The higher gas mass

[1] Animations for some models presented here are available at http://ap.smu.ca/~thacker/williams/cloudcols.html

in HighGasMW and MedGasMW reduced the hydrodynamic time-step and so these simulations could only be run for ~ 0.45 Gyr, while the increased computational load of the high resolution run HighResFlatMW also made a full simulation of 1.0 Gyr unfeasible, and so this simulation was evolved for ~ 0.3 Gyr.

The gas disc separates into two phases: diffuse gas which retains a moderate temperature ($\sim 10^3$ to $\sim 10^4$ K) though shock heating and a low cooling time, and dense gas whose temperature is tightly controlled by the Robertson-Kravstov dynamic temperature floor. It should be noted that while most of our models lack direct stellar feedback, the dynamic floor can heat the dense gas to temperatures as high as 3×10^4 K. This temperature is equivalent to a sound speed of ~ 26 km s^{-1}, which is on the order of the velocity dispersion generated by various feedback mechanisms (Thacker & Couchman 2000; Governato et al. 2007; Ostriker & Shetty 2011). Hence while (as we observe) implementing feedback changes our results, the difference is not large. This conclusion is further supported by the findings of Shetty & Ostriker (2008), who found that the properties of large clouds are not strongly sensitive to feedback.

Tests were also performed with a higher cooling floor of 3×10^4 K, and no clouds were formed. These tests demonstrate that a static cooling floor is a poor approximation to feedback as it inputs energy into any cool region of gas regardless of density, impeding any collapse that would have actually formed stars, in contrast with a dynamic temperature floor which inputs energy only into dense star-forming gas.

3.4.1.2 Cloud formation & numerical issues

We now draw attention to the differences between the simulations illustrated in Fig. 3.2. While LowResMW produces clouds at the same time as LowSoftMW (top left), it produces fewer of them as the mass spectrum is truncated. Similarly, FlatMW produces clouds at the same time as HighResFlatMW, but in smaller numbers (bottom right). Hence there is a trend of producing more clouds with increasing resolution. The total mass in clouds does not strongly vary between these two resolutions

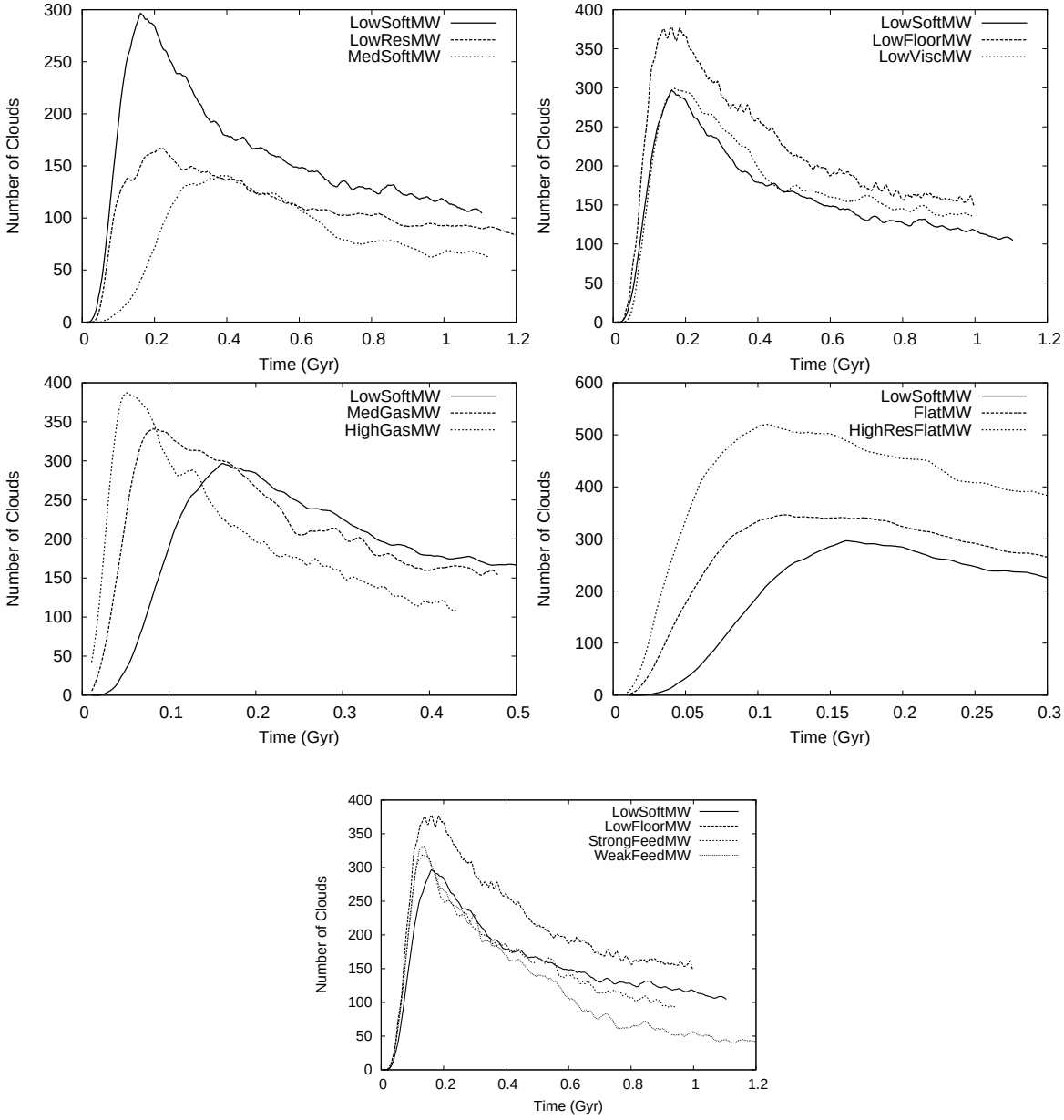

Figure 3.2: Number of clouds in Milky Way models. To smooth the data, each plotted point is an average of the 29 data points centred on it. The number peaks when many clouds are rapidly formed as the gas temperature drops below the Toomre instability threshold. It drops as these clouds merge.

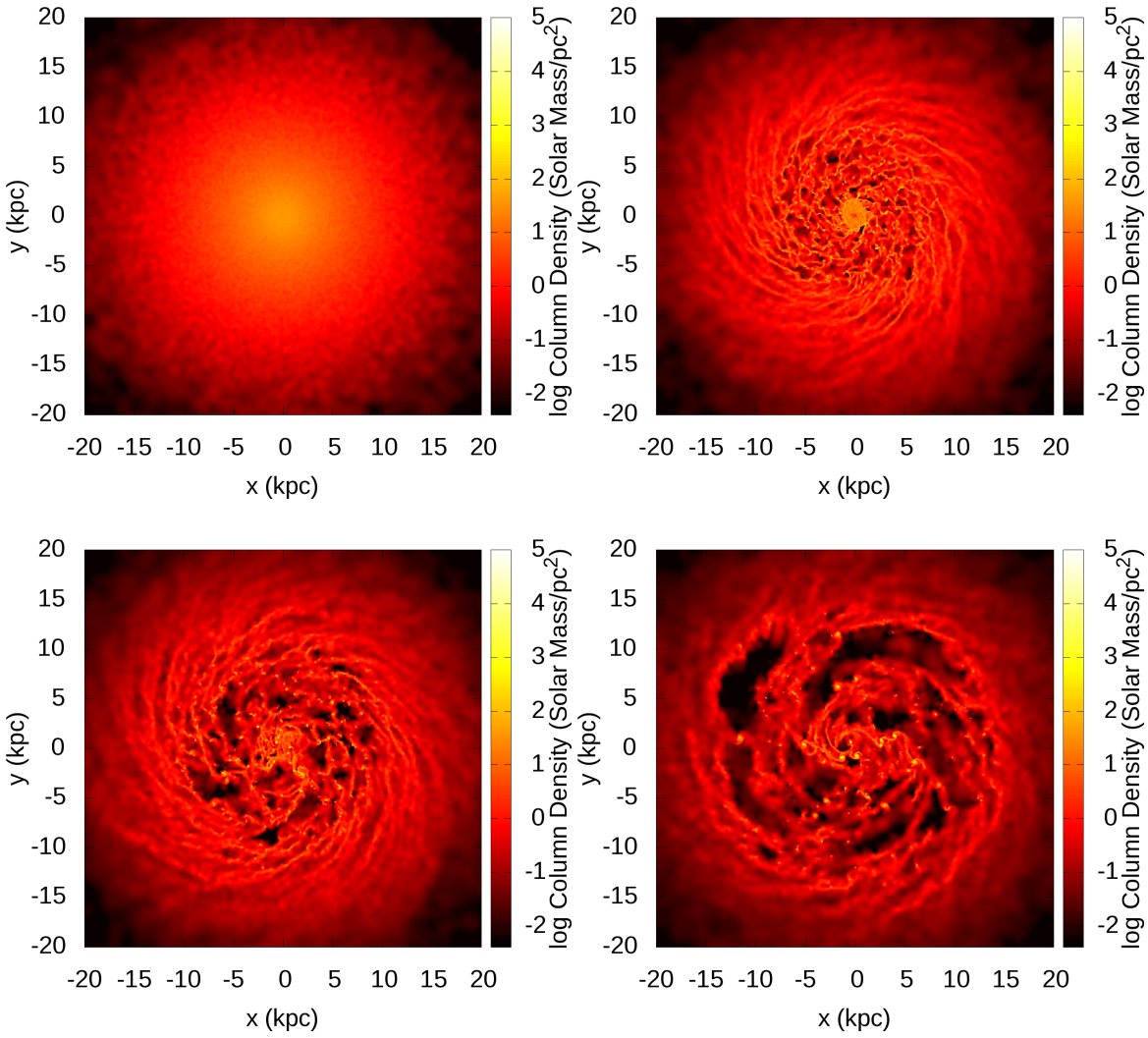

Figure 3.3: Evolution of LowSoftMW. A featureless disc (top-left) rapidly collapses into a larger number of clouds (top-right) after around 200 Myr of evolution. These clouds interact with each other and accrete material from 400 Myr (bottom-left) until the simulation ends after 1.1 Gyr (bottom-right).

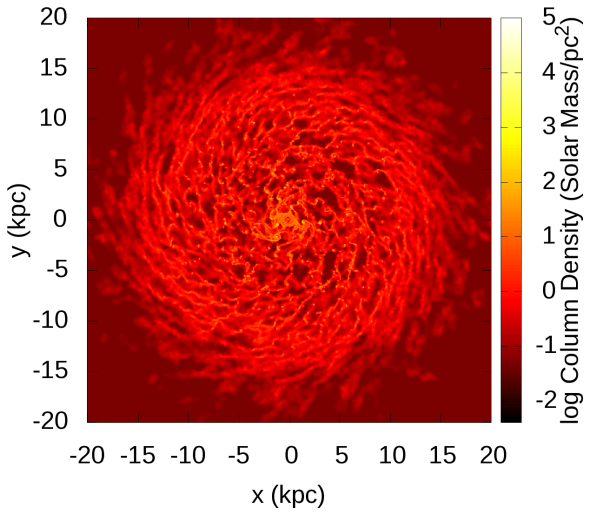

Figure 3.4: HighResFlatMW after 300 Myr of evolution.

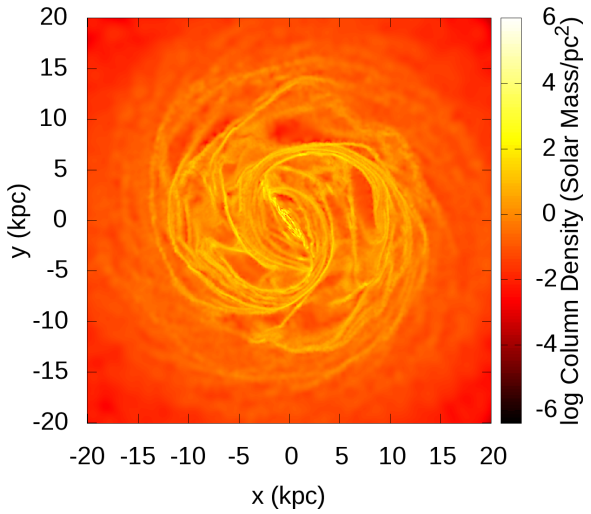

Figure 3.5: HighSoftMW after ~ 1.5 Gyr of evolution. Because of the large softening length, the disc does not undergo local fragmentation into clouds, and is instead dominated by bar and spiral instabilities.

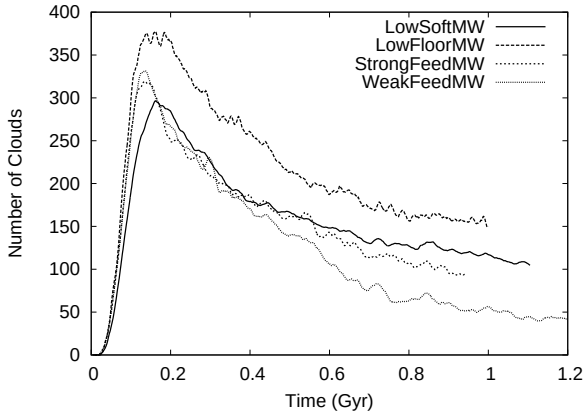

Figure 3.6: Resolution dependence of the total mass fraction of clouds.

(Fig. 3.6) — this demonstrates that any difference in viscous time-scale between these resolutions are due to the specific mass spectrum of the clouds, and not to the total mass of clouds. Overall, the flat initial conditions of FlatMW and HighResFlatMW produced clouds earlier and in greater numbers than in LowSoftMW. LowViscMW appears identical to LowSoftMW, suggesting that numerical artefacts due to artificial viscosity are not a significant effect (top right). LowFloorMW produced more clouds than LowSoftMW as the lower cooling floor allows the disc to become more unstable to cloud formation from Toomre instabilities. We also found that clouds formed earlier and were more numerous with increasing gas fraction, as demonstrated by HighGasMW and MedGasMW (bottom left).

We found that replacing the halo with a static potential did not have a significant effect — the mass spectra and number of clouds formed over 430 Myr of evolution were almost identical (Fig. 3.7). This agreement demonstrates that the large mass of the dark matter particles compared to gas particles did not significantly affect cloud formation by heating the disc or by single dark matter particles seeding over-densities. In both implementations, the halo's main role is to set the rotation curve for the gas and stars — it does not have a significant effect on the details of cloud formation beyond this.

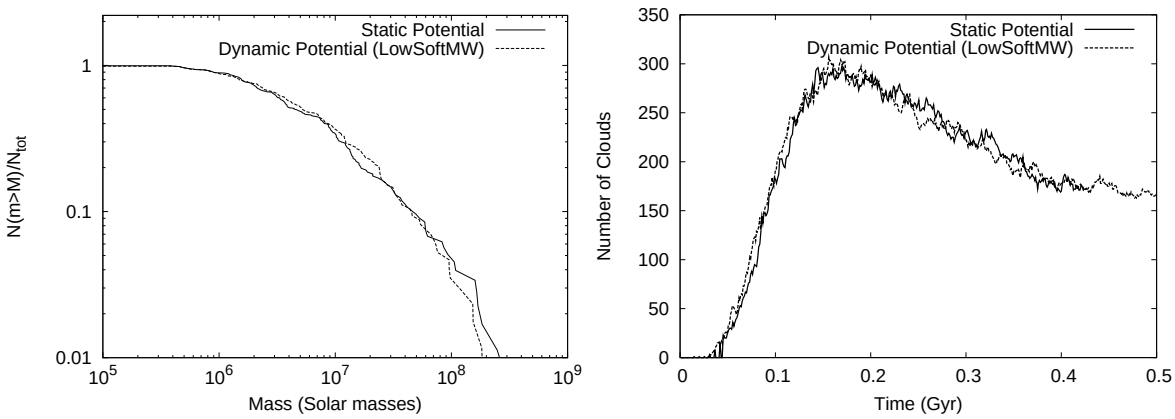

Figure 3.7: Mass spectra at 430 Myr (left) and cloud counts (right) for the fiducial model (LowSoftMW) and a test run with a static analytic potential.

As expected, the gravitational softening parameter has a significant effect on cloud formation. With a softening of 60 pc (LowSoftMW), a maximum of $\sim$ 300 clouds were formed at a time of 0.02 Gyr, while with a softening of 200 pc (MidSoftMW), half as many were formed ($\sim$ 150), and the peak number was achieved later (0.04 Gyr). It should be noted though, that both models have a similar fraction of mass in clouds ($\sim$ 80%). Increasing the softening yet further to 500 pc (HighSoftMW), leads to almost no clouds forming other than a few clouds in the centre of the galaxy after about a Gyr of evolution (not shown in Fig. 3.2). These results match what would be expected on theoretical grounds. Increasing the softening length delays cloud formation and produces fewer, more massive clouds, unless the softening length is increased above a certain threshold, beyond which cloud formation is prevented. The lack of cloud formation could potentially be a source of error in cosmological simulations, where a low resolution (i.e. large softening length) is necessary due to the immense size of the simulated domain. At low resolutions, smooth cloudless discs are formed, but as computational power increases and the softening length decreases below the thresholds for cloud formation, galaxies will become unstable to the formation of a small number of large clouds, who will have a larger impact on the dynamics of the galaxy than is realistic. Hence, this cloud formation must be suppressed by

setting a minimum softening length or by heating the discs, or cloud formation must be properly modelled by sufficient resolution, or this error must be accounted for in later analysis.

It seems most likely that this threshold softening length is related to the wavelength of the unstable mode that causes cloud formation. We can calculate this using the two-fluid (gas/star) Q_{gs} stability parameter from Jog & Solomon (1984), Rafikov (2001), and Li et al. (2005). The individual Q parameters for stars and gas are defined as

$$Q_s = \frac{\kappa\sigma_s}{\pi G\Sigma_s}, \quad Q_{\rm g} = \frac{\kappa c_{\rm g}}{\pi G\Sigma_{\rm g}}, \tag{3.16}$$

where Σ_s and $\Sigma_{\rm g}$ are the stellar and gas surface densities, σ_s the stellar radial velocity dispersion, $c_{\rm g}$ the gas sound speed, and κ the epicyclic parameter. Note that Q_s differs from Toomre (1964)'s definition of Q for a collisionless system by a factor of $3.36/\pi$. If we define

$$q = 2\pi\sigma_s/(\kappa\lambda_i), f = c_{\rm g}/\sigma_s, \tag{3.17}$$

where λ_i is the wavelength of a particular mode of instability, and treat the stars as a fluid with sound speed equal to σ_s as in Rafikov (2001) (who follows Jog & Solomon 1984), we can define a combined Q_{gs} by

$$\frac{1}{Q_{gs}} = \frac{2}{Q_s}\frac{q}{1+q^2} + \frac{2}{Q_{\rm g}}\frac{fq}{1+q^2f^2}, \tag{3.18}$$

with a stability condition of $Q_{gs} < 1$.

We calculate Q_{gs} by using azimuthal means of Ω, Σ, κ, $c_{\rm g}$ and σ_s, and setting λ_i to λ_{min}, the wavelength that minimizes Q_{gs}. It is worth cautioning that these parameters are derived from linear perturbation theory and may not adequately describe the system once clouds have formed. Nevertheless, λ_{min} does not rapidly vary (Fig. 3.8). λ_{min} is fairly small (< 1 kpc) from $t = 1$ Myr to $t = 200$ Myr for LowSoftC until a radius of 10 kpc at which point it triples in size. This jump is due to the small

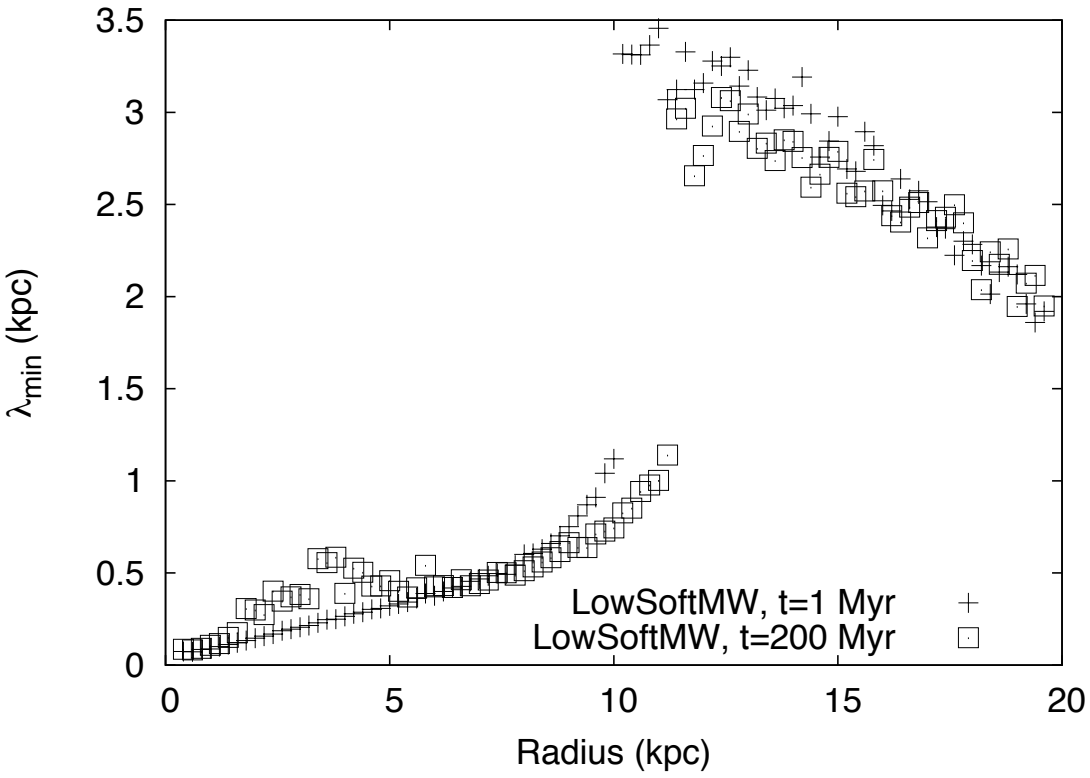

Figure 3.8: Wavelength $\lambda_{\min}$ of the most unstable mode for LowSoftMW at 1 and 200 Myr

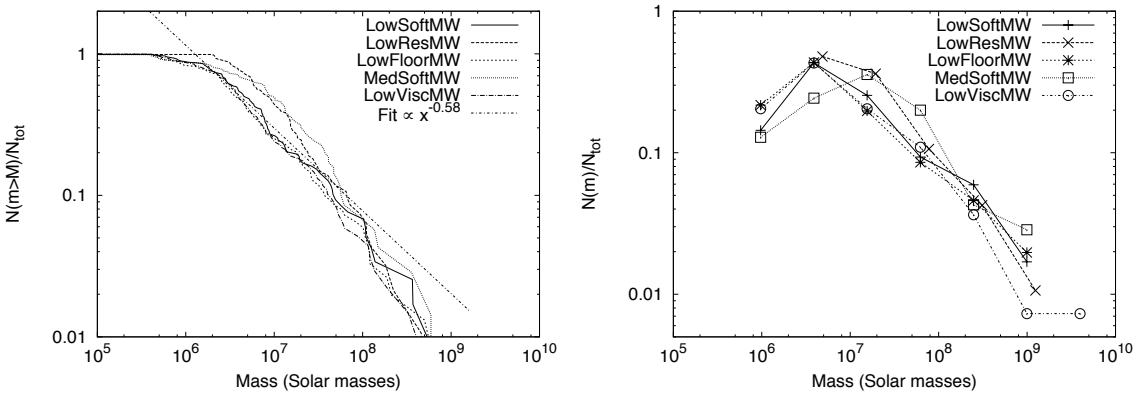

Figure 3.9: Mass spectra for clouds in Milky Way runs at 1 Gyr. Left: Cumulative mass spectra (for comparison with Agertz et al. 2009). Right: Differential mass spectra (for comparison with Tasker & Tan (2009)). The bins in the differential mass plot have a width of $\log(4) \approx 0.6$ dex.

wavelength gas instabilities starting to dominate over the large wavelength stellar instabilities. A comparison with the face-on density plots (e.g. Fig. 3.3) shows that clouds predominately form within 10 kpc of the galaxy's centre. In this region λ_{min} is of the order of 100s of pc. The 'threshold' resolution for cloud formation (assuming 4 to 5 softening lengths are required) in our models lies somewhere between 200 pc and 500 pc, and is consistent with this range. This quantifies an often quoted caveat for galaxy models — if the gravitational softening length is larger than the wavelength of the most unstable modes, then fragmentation is artificially frustrated.

The size of the unstable perturbations can be used to crudely estimate the masses of clouds. Assuming that the disc fragments into clumps of mass $\sim \pi\Sigma\lambda_{min}^2$, then for the LowSoftMW simulation (for example) the typical cloud masses should be the order of several $10^6 M_\odot$, which is admittedly significantly larger than average molecular cloud masses and actually much closer to giant molecular cloud complex masses. Nonetheless, this value is broadly consistent with our spectrum of cloud masses (e.g. Fig. 3.9). However, we caution against over interpretation as the mass spectrum convolves together an initial spectrum and its subsequent evolution. If this

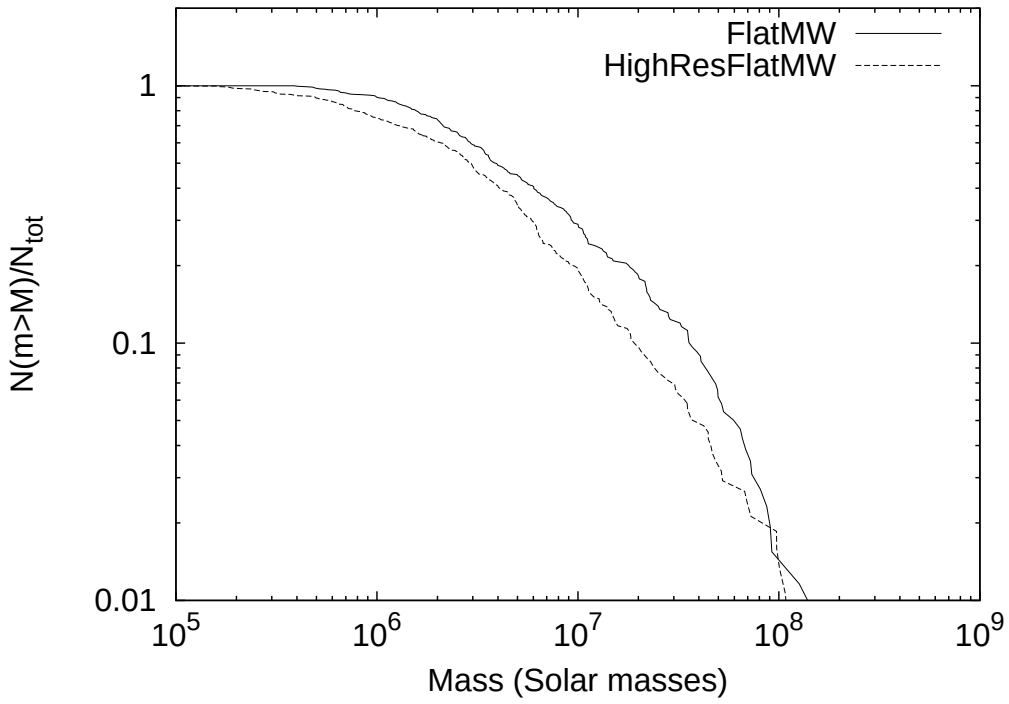

Figure 3.10: Cumulative cloud mass spectra from flat initial conditions, including our highest resolution model.

simple approach to calculating initial cloud masses were accurate we would not expect a higher resolution model to produce smaller clouds from this mode of instability, although non-azimuthally symmetric modes which may produce smaller scale instabilities have been excluded from this analysis. Smaller clouds could also be produced in a higher resolution Milky Way model by changing the initial conditions, or if these giant clouds undergo further fragmentation.

3.4.1.3 Cloud Mass Functions

The mass functions of our clouds (Fig. 3.9) differ from those of Tasker & Tan (2009) and Agertz et al. (2009) in that our clouds are more massive. However, neither

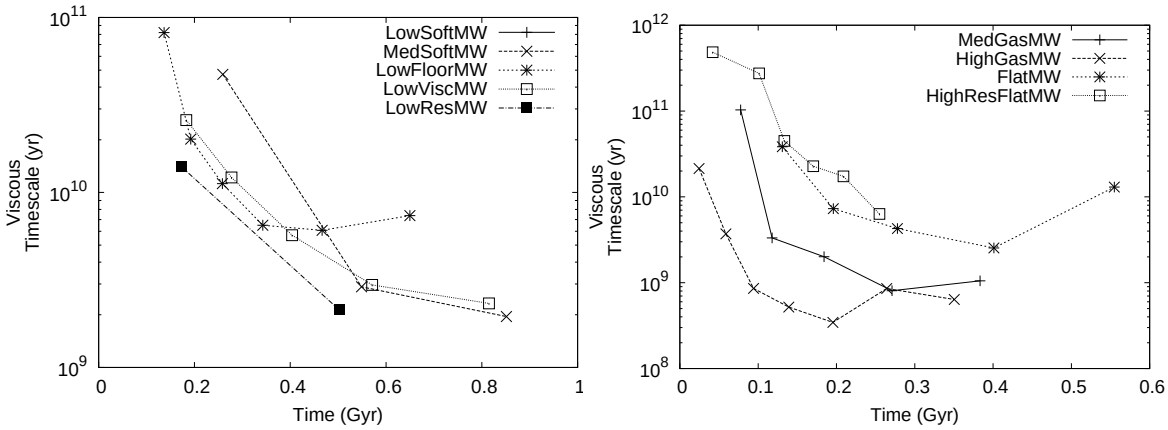

Figure 3.11: Viscous time-scales for disc models that ran for > 800 Myr (left) and ≤ 800 Myr (right). At early times, some models give negative time-scales, but as these values are large, they are not as dynamically important and are not plotted.

of these studies has equivalent physics. Tasker & Tan (2009) differ in that they do not include a dynamic stellar disc while Agertz et al. (2009) include feedback. Resolution could potentially also be an issue: although our mass function does not greatly vary between our low and moderate resolution models in our fiducial simulations, our high resolution flat model produced lower mass clouds than the moderate resolution flat model (Fig. 3.10).

The high-mass region of our cumulative mass spectrum plot follows a power law (i.e. $N(m) \propto m^{\alpha}$ or $N(m > M) \propto M^{\alpha+1}$). A least-squares fitting gives $\alpha \sim -1.5$. This value is slightly shallower than the ~ -1.8 in the simulations of Das & Jog (1996), and Dobbs & Bonnell (2008) but close to the values of -1.5 to -1.6 from observations (Sanders et al. 1985; Solomon et al. 1987; Solomon & Rivolo 1989; Williams & McKee 1997; Roman-Duval et al. 2010), and from the simulated mass spectra at around $10^6 M_{\odot}$ at 300 Myr in Tasker & Tan (2009) and at 1 Gyr in Agertz et al. (2009).

3.4.1.4 Viscous time-scales

The viscous time-scale is calculated using the method described in section 3.3.1.1 and is plotted in Fig. 3.11. Each point is calculated from 600 collisions.

Name	Interactions	Viscous time-scale (Gyr)	Simulation time (Gyr)
HighSoftC	104	2.0	4.5
MidSoftC	211	1.8	3.9
LowSoftC	566	0.8	3.5
LowSoftFloorC	3672	5.8	3.7
LowResC	397	2.1	4.6
LowMassC	0	-	7.8
HighSoftMW	39	-	1.5
MedSoftMW	1911	4.0	1.1
LowSoftMW (Full)	3942	4.5	1.1
(First 300 Myr)	1766	22.4	0.3
LowFloorMW	4514	8.8	1.0
LowResMW	1576	2.5	2.0
LowViscMW	3639	4.0	1.0
MedGasMW	3765	3.6	0.5
HighGasMW	4448	0.6	0.4
FlatMW (Full)	4124	5.7	0.8
(First 300 Myr)	2237	11.3	0.3
HighResFlatMW	4445	16.0	0.3
WeakFeedMW	7806	17.7	1.37
StrongFeedMW	7159	20.5	1.0

Table 3.4: Mean viscous time-scales and simulation lengths for all runs for the time from the first to the last recorded interaction. These time-scales are the mean time-scales during the time period from the first to the last recorded interaction. Time-scales are not given for LowMassC and HighSoftMW. There were no interactions in LowMassC, as it did not form clouds. Interactions were detected in HighSoftMW, but only in clumps within the central bar, which do not contribute to disc viscosity. The viscous time-scale for the first 300 Myr of LowSoftMW and FlatMW are also given for more direct comparison with HighResFlatMW.

There is a general trend toward shorter time-scales as the simulation evolves, and the final time-scales are generally below 10 Gyr, with many approaching 1 Gyr. This decreasing trend coincides with the trend of the number of clouds lowering and the mass of individual clouds increasing. The time-scales are less than a Hubble Time, and so should have some effect on the evolution of a galaxy, contrary to the predictions of B02.

The mean viscous time-scales from all interactions over each entire simulation for both the Milky Way and collapse models are tabulated in Table 3.4. Despite the

variation of parameters, many of the time-scales are within a narrow range, from 3–5 Gyr. Modifying the artificial viscosity (LowViscMW) did not appear to significantly change the viscous time-scale. The softening length in HighSoftMW (600 pc) was large enough to completely quench cloud formation, except for a few clumps that formed within the central bar instability. We do not include a viscous time-scale here as the mechanisms for formation and interaction are different to those of molecular clouds in nearly circular orbits. Feedback processes from star formation and AGN would also be more important here than in the other models. However, lowering the softening length from 100 pc to 60 pc (MedSoftMW to LowSoftMW), while increasing the number of clouds produced, did not significantly alter the viscous time-scale.

HighGasMW has a significantly shorter viscous time-scale at 0.6 Gyr, and indeed there appears to be a trend of decreasing viscous time-scale with increasing gas fraction. The effect is clearer if we compare the models over the same time period. The viscous time-scale over the first 430 Myr is 7.1 Gyr for LowSoftMW, 1.5 Gyr for MedGasMW, and 0.6 Gyr for HighGasMW. Increasing the gas fraction increases the mass of the cloud population (Fig. 3.12), which increases the frequency and dissipative efficiency of collisions.

HighResFlatMW is our highest resolution simulation, but has different initial conditions to LowSoftMW due to the more stringent stability requirements at high resolution (detailed in section 3.2.3.1). The flat discs of FlatMW and HighResFlatMW caused cloud formation to occur earlier than in LowSoftMW. A resolution dependence is also evident: The 2.5× increase in mass resolution from FlatMW to HighResFlatMW caused a 1.4× increase in the viscous time-scale, and the 5× increase in mass resolution from LowResMW to LowSoftMW caused a 1.8× increase in the viscous time-scale.

The inclusion of feedback in WeakFeedMW and StrongFeedMW also significantly increases the viscous time-scale — by a factor of $\sim 4-5$ from LowSoftMW, even though all three simulations produced similar numbers of clouds at similar times (Fig. 3.2). The weaker effective viscosity is likely because the clouds in the runs

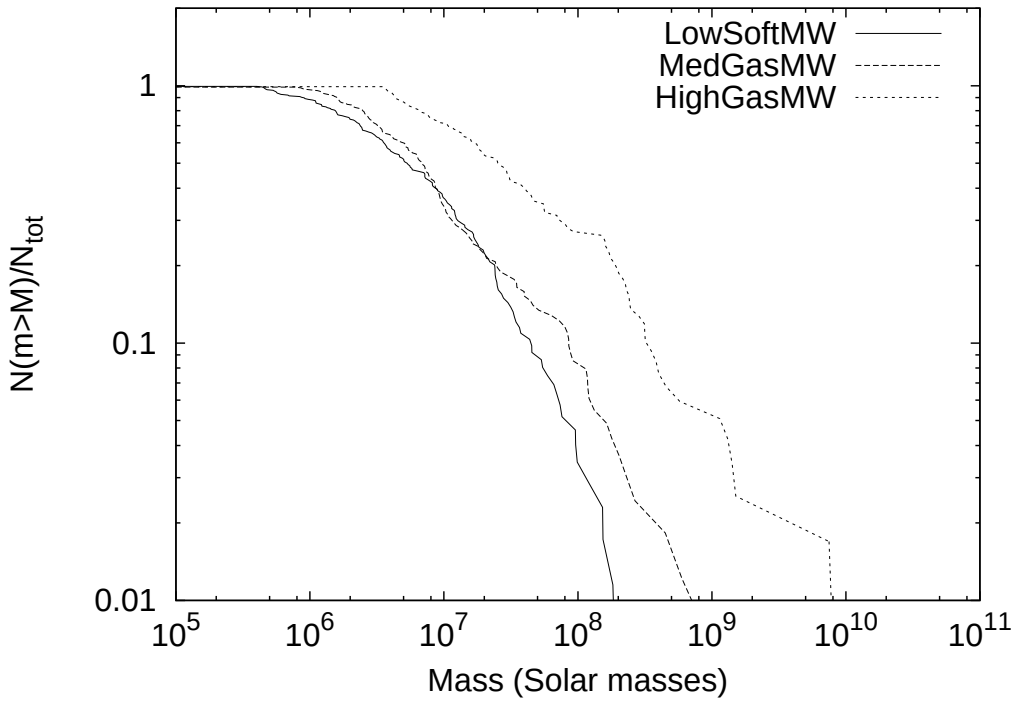

Figure 3.12: Cumulative cloud mass spectra across runs with varying gas fraction.

with feedback were considerably less massive than in the runs that included feedback (Fig. 3.13). As might be expected, the strong feedback model produced smaller clouds than the weak feedback model.

3.4.2 Monolithic Collapse Model

In all models the gas collapse proceeds as soon as cooling is turned on, thus breaking the hydrostatic equilibrium. The hot core caused by the implied preheating of the High-S profile (section 3.2.3.2) slowed the collapse sufficiently for the infalling gas to fragment into clouds at a large radius, although these clouds are too diffuse to be found by the cloud identification algorithm. As the simulation progresses, these

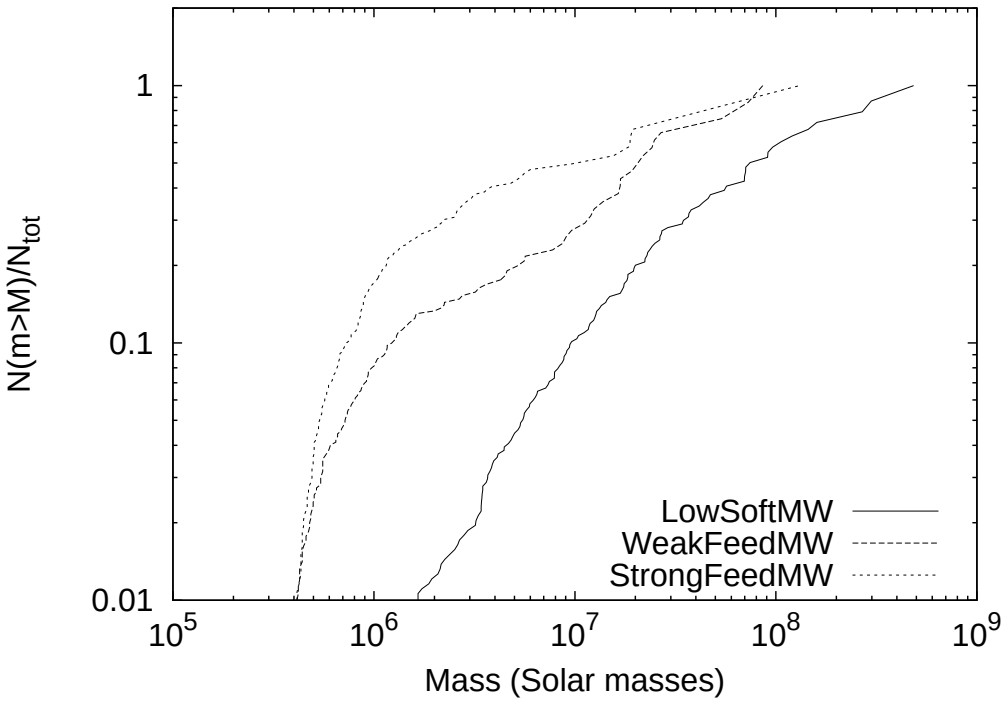

Figure 3.13: Cumulative cloud mass spectra including runs with feedback.

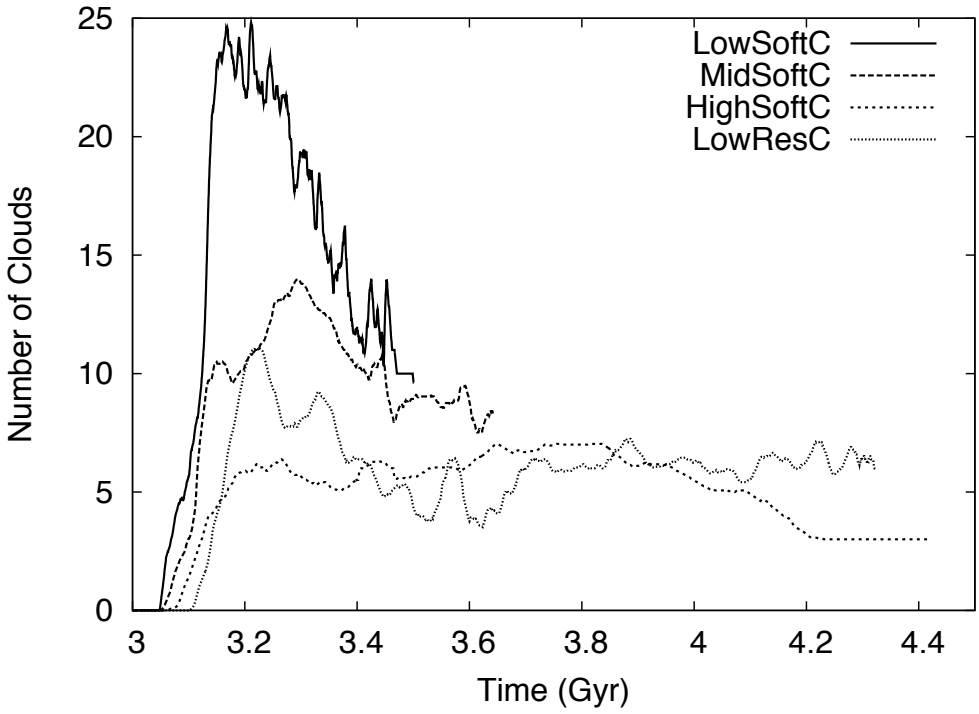

Figure 3.14: Number of clouds in collapse models (excepting LowSoftFloorC). To smooth the data, each plotted point is an average of the 29 data points centred on it. Being very unstable, these systems formed a few large clumps rather than many small clumps.

clouds start to merge (from $t \sim 3$ Gyr in all runs except for LowMassC), and reach the effective threshold density of our cloud-finder. The number of clouds quickly reaches a maximum (see Fig. 3.14). These clouds combine to form a disc. The number and size of clouds these discs fragment into varies greatly between our models.

In HighSoftC, MidSoftC, LowSoftC and LowResC, the disc is extremely unstable, collapsing into ~ 7 massive (several times $10^9 M_\odot$ in mass) clumps (Fig. 3.15). These are not small-scale GMC-style clumps as found in the Milky Way simulations, and perhaps this level of collapse is more analogous to the gas-rich clump-cluster galaxies found at high redshift (e.g. Elmegreen & Elmegreen 2005). In the simulations

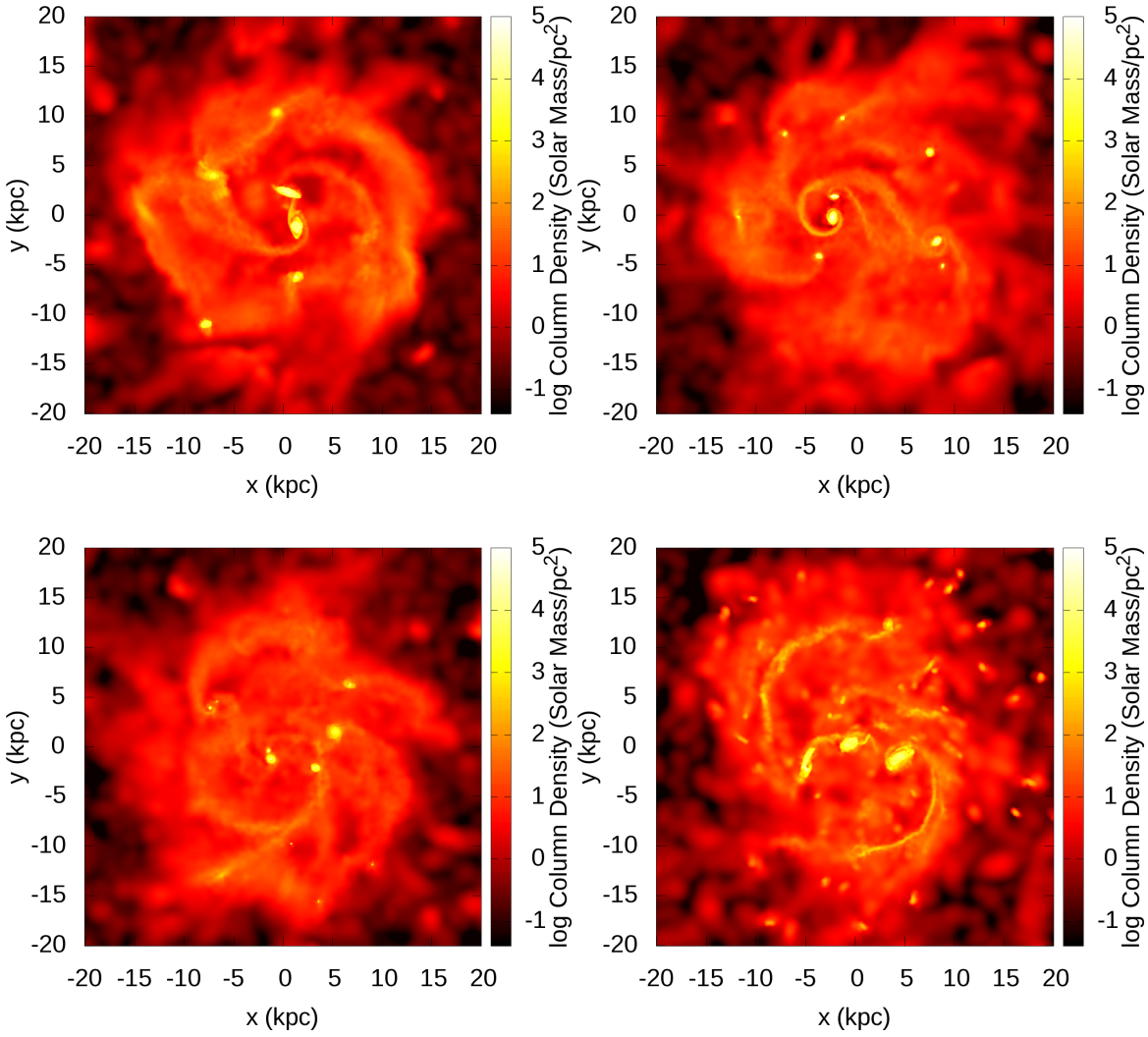

Figure 3.15: Impact of varying the softening length and resolution in collapse runs at t=3.5 Gyr. Top left is HighSoftC (514 pc, 3×10^4 K), top right is MidSoftC (200 pc, 3×10^4 K), bottom left is LowSoftC (60 pc, 3×10^4 K) and bottom right is LowResC (60 pc, 300 K). Although HighSoftC, MidSoftC and LowSoftC produce different numbers of clouds initially (more clouds for a shorter softening length), after $\sim$ 500 Myr of collisions all three models have $\sim$ 7 large clumps. Despite the low temperature floor, the limited resolution of LowResC produces an unstable disc, instead of a swarm of dense clumps as in LowSoftFloorC.

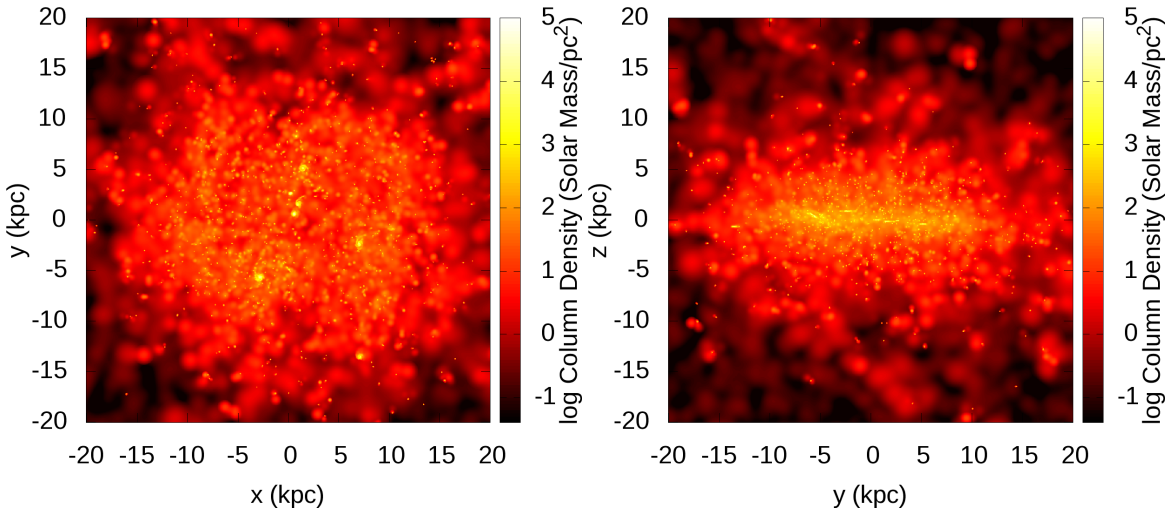

Figure 3.16: Face-on and side-on density plots of LowSoftFloorC at t=3.7 Gyr. The swarm of clumps has a half-mass height of 7.8 kpc. The disc is very chaotic: at 10 kpc, the azimuthally averaged tangential velocities and velocity dispersions are 180 km s^{-1} and 105 km s^{-1}.

of Bournaud et al. (2007) and Dekel et al. (2009), the large clumps in clump-cluster galaxies coalesce into a central bulge, forming a more stable disc. These simulations differ to ours particularly in that they include star-formation and feedback. With infalling material, Dekel et al. (2009) finds the clumpy phase can last for several Gyr.

The heavy clustering in our discs in this section dictated that they could only be evolved for < 1 Gyr after formation (which takes ~ 3 Gyr) due to problems with the SPH solver. The high densities cause a large increase in the number of particles with smoothing lengths at the minimum allowed which contributes to an $\mathcal{O}(n^2)$ slowdown.

The simulations of Kaufmann et al. (2009), while including star-formation (but not explicit feedback), also produce a disc with large-scale gravitational instabilites. Both our and Kaufmann's collapse models have a temperature floor of 3×10^4 K, as a very crude form of feedback, except in the case of LowSoftFloorC. Including star-formation and more self-consistent feedback method could produce a stable disc (Stinson et al. 2006; Christensen et al. 2010), but in this work we only include star-formation and explicit feedback in some of our Milky Way runs.

In LowSoftFloorC, the low temperature floor allows the halo clouds to condense into dense ($n \sim 10^4 - 10^5 \mathrm{cm}^{-3}$) clumps (Fig. 3.16). Their low cross-section means that their coalescence has properties of a collisionless collapse. So in addition to an unstable disc, there exists a swarm of clumps with a half-mass height of 7.8 kpc. Their ellipsoidal distribution and high densities are reminiscent of globular clusters, but the inclusion of feedback would definitely increase the cloud cross-sections and produce a more dissipated and flattened disc.

LowMassC is the only run that produces a disc that does not collapse into large clumps (Fig. 3.17), although it took considerably longer to form (~ 4.5 Gyr) and the disc is still dominated by spiral instabilities. Discs are unstable to bar formation when the disc mass fraction is greater than the spin parameter ($m_d > \lambda_{\mathrm{G}}$) (Efstathiou et al. 1982; Foyle et al. 2008), so a lower mass disc is more stable. If the bar is too strong, it may fragment into large clumps. This instability may well drive the infalling clouds into a few large clumps in the higher mass models.

As seen in Table 3.4, the viscous time-scales for the collapse runs trend toward lower values than the Milky Way simulations — around $1-2$ Gyr. Though the number of interactions is not as large as in the Milky Way models, they occur over a short period (e.g. all 566 interactions in LowSoftC are within ~ 500 Myr). The number of clouds is small, so each cloud undergoes many collisions, producing a short viscous time-scale.

3.4.3 Comparison with Analytical Model

B02 argued that while cloud collisions are not uncommon (occurring $\gtrsim 1$ time per orbit), the low efficiency of cloud collisions produces a long viscous time-scale. This efficiency is measured with a parameter η, equal to the fraction of a cloud's energy that is lost in a collision (not entirely dissimilar from a coefficient of restitution). When two clouds merge completely, the fraction of kinetic energy lost is well approximated by $\eta = (v_{\mathrm{rel}}/v_{\mathrm{rot}})^2$, where v_{rel} is the relative velocity of the clouds, and v_{rot} is their rotational velocity which is roughly constant for a galaxy.

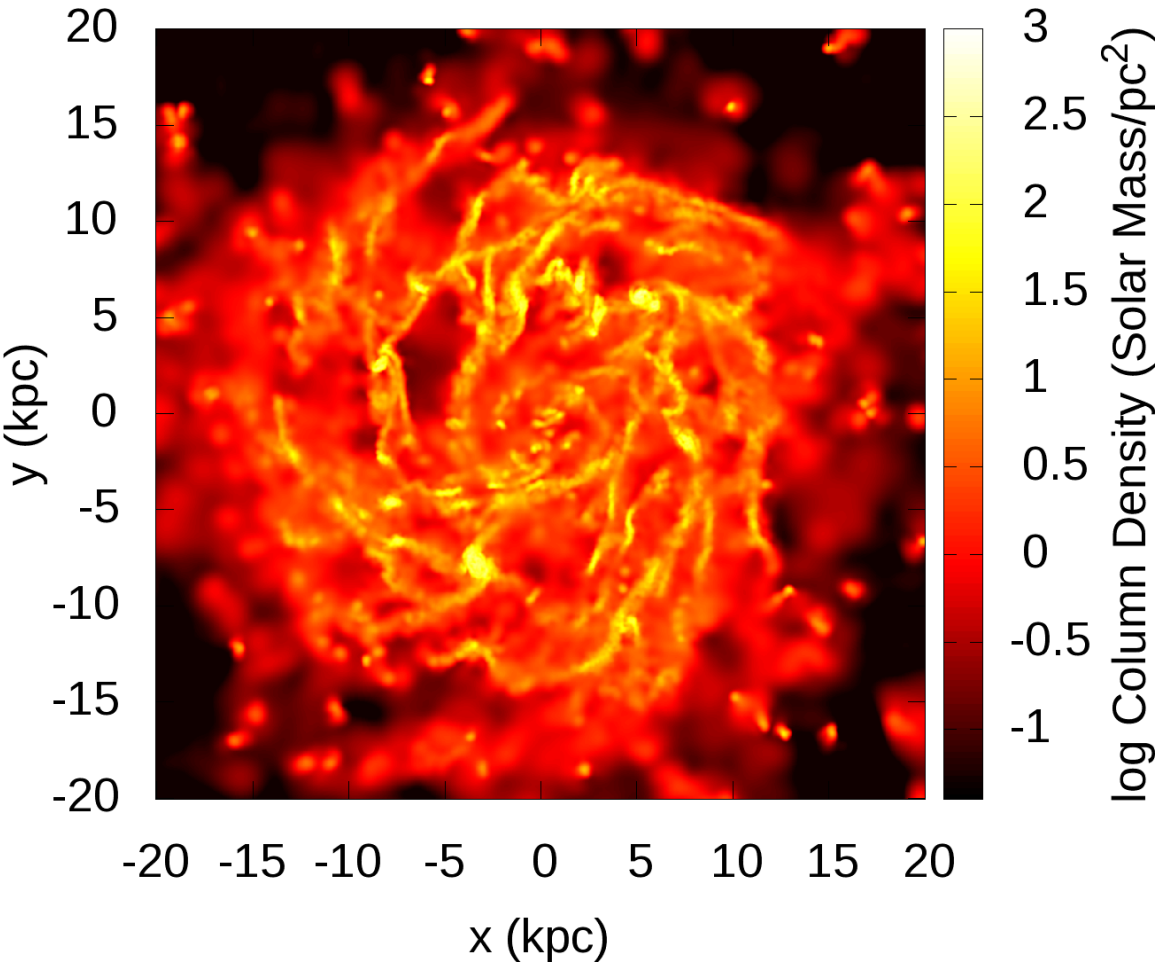

Figure 3.17: LowMassC at $t = 6.0$ Gyr. The disc undergoes spiral instabilities but does not fragment into clumps as the other collapse models do.

This relationship is consistent with our numerical results. The analytical model of B02, finds that $\eta \lesssim 10^{-2}$ for a Milky-Way-like model, concluding that cloud-cloud collisions are not an efficient sink of energy, with $t_\nu \sim$ 1000–2000 Gyr.

The complex interactions that occur between clouds in our simulation mean that it is not straightforward to determine values for η. Several of our merger and separation events can take place within what is really a single extended interaction, which lowers the average time between interactions significantly. Indeed, we find the interaction rates are on the order of one separation or merger event per cloud every $50 - 60$ Myr for LowSoftMW, MedSoftMW, LowFloorMW, LowViscMW, HighSoftC and LowMassC. The greatest interaction time-scale was in LowSoftFloorC (335 Myr), and the smallest was in LowSoftC (14 Myr).

It is difficult to track the number of interactions over a full merger process, as additional clouds often interact with the merging clouds. We carefully examined a span of time around each of a sample of 10 recorded interactions in LowSoftMW on an iteration-by-iteration basis to determine the number of recorded interactions per 'real' interaction. These interactions were selected so that they were evenly distributed across the simulation ($\sim$ 2 every 5000 iterations). We initially examined a period of $\pm$800 iterations around the interaction, and if no 'real' interaction was observed during this time, this was extended to $\pm$2000 iterations. Several different behaviours were observed:

- In two cases, no real interactions were observed; outer parts of a cloud were attaching and detaching to the main cloud, and dissolving and condensing across the cloud density threshold, causing a number of recorded interactions which did not correspond to any clear long-term merger, scattering or separation event.

- Three events were 'messy' interactions with 6, 7 and 16 recorded interactions per real event; the event consisting of 16 recorded split and merge events was a scattering event where the clouds passing by each other several times before separating for a final time.

- Four more events were more 'tidy' interactions, with 1, 2, 3, and 4 interactions per real event.

- The last event was a series of mergers in rapid succession — 3 recorded mergers, all of which were genuine mergers between distinct clouds.

Overall, there was a mean of 4.9 recorded interactions per examined period, with a standard deviation of 4.3. A total of 11 'real' interactions were observed, giving 4.5 recorded interactions per real interaction. Multiplying our interaction time-scale by 4.5 gives us one event per $\sim$ 250 Myr for the LowSoftMW-like models. This is approximately once per orbit at a solar radius. The analytic estimate in B02 of the cloud-cloud collision rate is $\sim$ 100 Myr, which is of similar order.

We can estimate an η for the interactions in our models by

$$\eta = -(\Delta K + \Delta\phi)/(K_c), \tag{3.19}$$

where ΔK and $\Delta\phi$ are the change in kinetic and potential energy of a cloud, and K_c is the total kinetic energy of both clouds before collision. η can be negative, as energy is converted from internal motions into orbital kinetic energy during separations. The clouds all have similar velocity because of the flat rotation curve, so the total energy lost is primarily dependent on η and the cloud masses. We find for most interactions $|\eta|$ is on the order of ~ 0.002 (Fig. 3.18). If we separate our η values into two sets, η_- for $\eta < 0$ and η_+ for $\eta > 0$, we find that the median value of $|\eta_-|$ is greater than the median value of $|\eta_+|$, even though the viscous time-scale is positive. This unintuitive result still produces a positive viscous time-scale because although η, the *relative* energy change is larger for interactions which increase orbital energy ($\eta_- < 0$) than those which decrease orbital energy ($\eta_+ > 0$), the *absolute* change in energy is larger for interactions which decrease orbital energy than *increase* it — i.e. interactions which decrease orbital kinetic energy tend to occur between clouds with greater mass than interactions with increase orbital kinetic energy. Although it is not apparent on these plots, there are several collisions for which η is very large, with $\eta > 0.1$. These

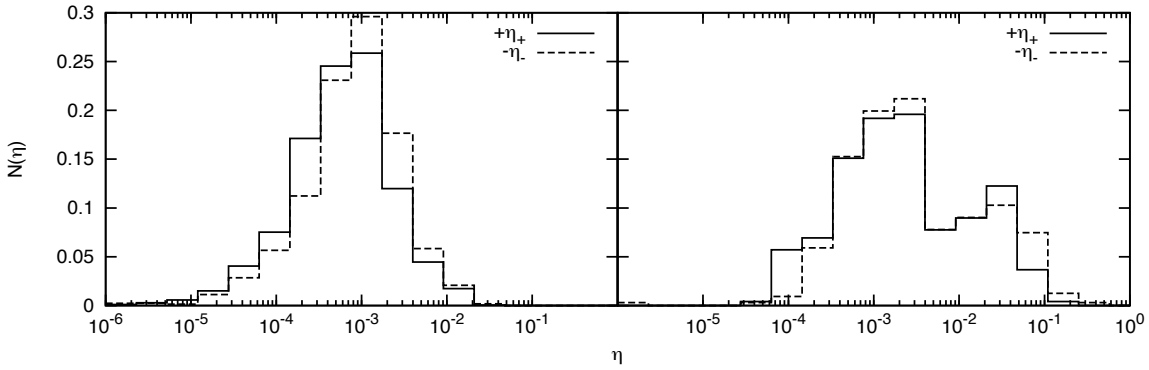

Figure 3.18: Distributions of the fraction of energy lost in a collision η, in bins of 0.35 dex. Left: LowSoftMW, Right: LowSoftC. For each simulation, the distribution of all $\eta_- < 0$ and $\eta_+ > 0$ are plotted separately. In both cases, the median value of $|\eta_-|$ is greater than the median value of $|\eta_+|$, even though both models show a positive viscous time-scale.

interactions occurred within the 1 kpc of galaxy centre, and only after $\sim$ 400 Myr. These are clouds that have been strongly scattered by interactions and fallen down the potential well, colliding with speeds of > 100 km s^{-1}.

Our interactions are no more efficient at removing energy than in B02, and are no more common, yet the B02 model predicts $t_\nu \sim$ 1000–2000 Gyr, while our simulations have $t_\nu < 10$ Gyr. Our simulated discs are more energetic than standard Milky Way models: the velocity dispersion in LowSoftMW is ~ 20 km s^{-1} at 7.5 kpc, more than triple the standard Milky Way value used in B02 (6 km s^{-1}). However, this is not the cause of the large difference between the model of B02 and our own. Here we derive our own model for η, and contrast this with the model in B02 to find the source of this disparity.

We can split the velocity components of $v_{\rm rel}$ into tangential and radial components to give

$$\eta \sim \frac{v_{\rm rel}^2}{v_{\rm rot}^2} = \frac{R^2(\dot{\phi}_1 - \dot{\phi}_2)^2 + (\dot{R}_1 - \dot{R}_2)^2}{v_{\rm rot}^2}. \tag{3.20}$$

If we make the epicyclic approximation (Binney & Tremaine 2008), that the deviation from a circular orbit is small compared to the radius of the orbit ($R = R_{\rm g} + x$,

where $R_{\rm g}$ is the 'guiding centre' of the orbit, and $x \ll R$ is the radial excursion), then $\dot{R} = \dot{x} = X\kappa\cos(\kappa t + \alpha)$, (where X is the maximum radial excursion of a cloud, κ the epicyclic frequency, and α is a phase parameter) and $\dot{\phi} = R_{\rm g} v_{\rm rot}/R^2$ from conservation of momentum in a flat rotation curve. Hence $R^2(\dot{\phi}_1 - \dot{\phi}_2)^2 = (v_{\rm rot}^2/R^2)(R_{\rm g,1} - R_{\rm g,2})^2$ — the tangential component of the difference in velocity depends only on the radial distance between the clouds' guiding radii.

The radial component is more difficult to calculate, as it depends on the phase of the interaction. We can estimate the maximum η by assuming the clouds are perfectly out of phase, that is,

$$\begin{aligned}(\dot{R}_1 - \dot{R}_2)^2 \sim (X_1\kappa_1 + X_2\kappa_2)^2 &\sim 2v_{\rm rot}^2\left(\frac{X_1}{R_{\rm g,1}} + \frac{X_2}{R_{\rm g,2}}\right)^2 \\ &\sim \frac{2v_{\rm rot}^2}{R^2}(X_1 + X_2), \end{aligned} \tag{3.21}$$

as $R \sim R_{\rm g}$. For clouds to collide precisely out of phase, they must have the same guiding radius, and so $R_{\rm g,1} - R_{\rm g,2} = 0$. Hence, if $X_1 \sim X_2 \sim X$, then $\eta_{\rm max,r} = 8X^2/R^2$. If the clouds are at their maximum deviation when they collide, then their radial velocities are zero, but their relative ϕ velocities are maximized, that is, $\dot{\phi}_1 - \dot{\phi}_2 = 2X$, and so $\eta_{\rm max,\phi} = 4X^2/R^2$. These coefficients give the maximum η, but we should nevertheless expect $\eta \sim X^2/R^2$, i.e. η depends on the radial excursion of clouds.

This can also be expressed in terms of a velocity dispersion. We can calculate the velocity dispersion by

$$v_s^2 = \langle(\boldsymbol{v} - \overline{\boldsymbol{v}})^2\rangle = \langle\dot{x}^2\rangle + \langle R^2(\dot{\phi} - \Omega_g)^2\rangle \tag{3.22}$$

Assuming a flat rotation curve and that X and κ are more or less constant within the region of interest, the radial component is $\dot{x} = X\kappa\cos(\kappa t + \alpha)$, hence

$$\langle\dot{x}^2\rangle = (1/2)X^2\kappa^2 = X^2 v_{\rm rot}^2/R^2, \tag{3.23}$$

and the tangential component is $R(\dot{\phi} - \Omega_g) = -2X\Omega_g \sin(\kappa t + \alpha)$, hence

$$\langle R^2(\dot{\phi} - \Omega_g)^2 \rangle = 2X^2\Omega_g = 2X^2 v_{\rm rot}^2/R^2. \tag{3.24}$$

This gives

$$v_s^2 = 3v_{\rm rot}^2(X^2/R^2), \tag{3.25}$$

and so

$$\eta \sim \frac{v_s^2}{v_{\rm rot}^2}. \tag{3.26}$$

From these expressions for η we can determine the dissipative time-scale from $t_\nu = t_c/\eta$.

We next summarize the model of B02. In the limit of rapid collisions, the kinematic viscosity due to cloud-cloud collisions can be modelled as a Reynolds stress and expressed as $\nu \sim \lambda_d v_s$ (Faber 1995), where v_s is the velocity dispersion, and λ_d is the mean free path. The mean free path is $\lambda_d = v_s t_c$, where t_c is the typical time between collisions. Similarly to our result, B02 states $\eta \sim \Delta R^2/R^2$, where ΔR is the radial distance between collisions. For the case of very rapid collisions, $\Delta R \sim \lambda_d$, so $\eta \sim \lambda_d^2/R^2$. This equation gives a viscous time-scale that should be equal to the dissipative time-scale,

$$t_\nu \sim \frac{R^2}{\nu} \sim \frac{R^2}{\lambda_d v_s} \sim t_c \frac{R^2}{\lambda_d^2} \sim \frac{t_c}{\eta}. \tag{3.27}$$

Hence if we follow the description given in B02, the results should be equivalent to ours. Continuing to follow B02, we can set $t_c = M_{\rm cloud} h/(\Sigma_{\rm g} v_s \pi r_{\rm cloud}^2)$, so

$$t_\nu = \frac{R^2}{v_s \lambda_d} \sim \frac{R^2}{v_s} \frac{\pi r_{\rm cloud}^2 \Sigma_{\rm g}}{M_{\rm cloud} h}. \tag{3.28}$$

We can evaluate this using the Milky Way parameters of B02, that $r = 7.5$ kpc, $v_{\rm rot} = 220$ km s^{-1}, $v_s = 6$ km s^{-1}, $\Sigma_{\rm g} = 50 M_\odot$ pc^{-2}, $M_{\rm cloud} = 10^5 M_\odot$, $h = 100$

pc, and $r_{\rm cloud} = 10$ pc to result in $t_\nu = 14$ Gyr. However, B02 states $t_\nu \sim 2000$ Gyr, which disagrees by a factor of $1/\eta$. It appears that B02 includes an additional factor of $\eta \sim 0.008$ in the denominator — i.e. $t_{\nu,Bell} \sim R^2/(\eta\nu)$. This η is not necessary, as it is already included in the radial excursion or velocity dispersion, and as is clear from equation 3.27, the expression $t_\nu \sim R^2/\nu\eta$ is not equivalent to the dissipative time-scale.

In B02's rare collision case, $\nu \sim v_s \Delta R(t_\kappa/t_c)$, where $t_\kappa = 2\pi/\kappa$ is the epicyclic time-scale. For a flat rotation curve $\kappa = \sqrt{2}\Omega \sim v_0/R$. The excursion ΔR is on the order of the radial excursion of the epicyclic motion of the clouds. B02 state $\Delta R \sim v_s/\kappa \sim v_s R/v_{\rm rot}$, which is consistent with our result in equation 3.25. Putting this together gives

$$t_\nu \sim \frac{t_c/(2\pi)v_{\rm rot}^2}{v_s^2}, \tag{3.29}$$

i.e. $\eta \sim 2\pi v_s^2/(v_{\rm rot}^2) \sim 0.023$. B02 uses a low surface brightness galaxy in this case, with $\Sigma_{\rm g} = 10 M_\odot$ pc^{-2} and $v_{\rm rot} = 100$ km s^{-1}, which results in $t_\nu \sim 23$ Gyr. Again, the value in B02 is much larger, $t_\nu \sim 1000$ Gyr, which again is higher than our calculated value by a factor of approximately $1/\eta$.

These models are intended to apply in the limits of very frequent or very infrequent collisions where $t_c\Omega \ll 1$ or $t_c\Omega \gg 1$. In our simulations, we found that clouds collide about once per orbit, i.e. $\Omega t_c \sim 1$. However, we can contrast these results with those of Goldreich & Tremaine (1978), who solve the Boltzmann equation for a system of inelastically colliding particles in a disc, and find for arbitrary Ωt_c that the viscosity is of order

$$\nu \sim v_s \lambda_d \frac{1}{1 + (\Omega t_c)^2}, \tag{3.30}$$

after we make the substitution that $\lambda_d \sim v_s t_c$. For $\Omega t_c = 1$, $\nu = 1/2(\lambda_d v_s)$. The frequent collision case of B02, $\nu \sim v_s \lambda_d$, is accurate to this within an order of magnitude if we exclude the erroneous factor of $1/\eta$.

Substituting our typical cloud and disc parameters at 7.5 kpc ($h \sim 25$ pc, $\Sigma_{\rm g} \sim 100 M_\odot/{\rm pc}^{-2}$, $v_s \sim 20$ km s^{-1}, $r_{\rm cloud} \sim 35$ pc, and $M_{\rm cloud} \sim 10^7 M_\odot$) for LowSoftMW at $t = 1$ Gyr into this model gives a viscous time-scale of 1.1 Gyr. This value somewhat underestimates our numerical results for the Milky Way models in Table 3.4, for most of which $t_\nu \geq 4.0$ Gyr. The unstable disc of LowSoftC, forming from a collapse without stars, has very different properties at $R = 7.5$ kpc, with $h \sim 250$ pc, $\Sigma_{\rm g} \sim 5000 M_\odot/{\rm pc}^{-2}$, $v_s \sim 100$ km s^{-1}, $r_{\rm cloud} \sim 100$ pc, and $M_{\rm cloud} \sim 10^9 M_\odot$. These properties produce $t_\nu = 0.35$ Gyr, which agrees with our simulation result (0.8 Gyr) within a factor of ~ 2. The analytical expression for t_ν was evaluated from order-of-magnitude arguments and assumptions that may not be entirely valid in our simulations — particularly in models with very few clouds, such as LowSoftC. Numerical factors also vary our simulation results by a factor of ~ 4. Given these issues, it is not surprising that the agreement is not exact.

Interestingly, despite the different disc properties, LowSoftC and LowSoftMW have similar viscous time-scales in both our numerical simulations and in this analysis. This agreement is to be expected from equation 3.28. We should expect the typical cloud mass to increase with the gas density and typical cloud radius, and so $M_{\rm cloud}/(\pi r_{\rm cloud}^2 \Sigma_{\rm g})$ should vary only weakly. Hence the viscous time-scale will primarily depend primarily on h and v_s. This degree of parameter-independence suggests that time-scales will not vary greatly for models beyond those simulated here — perhaps even of higher resolution. To quantify this, we note that there appears to be a correlation between the maximum number of clouds formed ($N_{\rm cloud,max}$) and the viscous time-scale (Fig. 3.19). Performing a fit to a power-law $t_\nu \propto (N_{\rm cloud,max})^m$, we find a power index of $m = 0.39 \pm 0.19$. This fit predicts a viscous time-scale of $t_\nu \sim 23$ Gyr for $N_{\rm cloud,max} = 10^4$, and $t_\nu \sim 60$ Gyr for $N_{\rm cloud,max} = 10^5$, although we caution that this is a purely empirical fitting and is not likely to be very accurate.

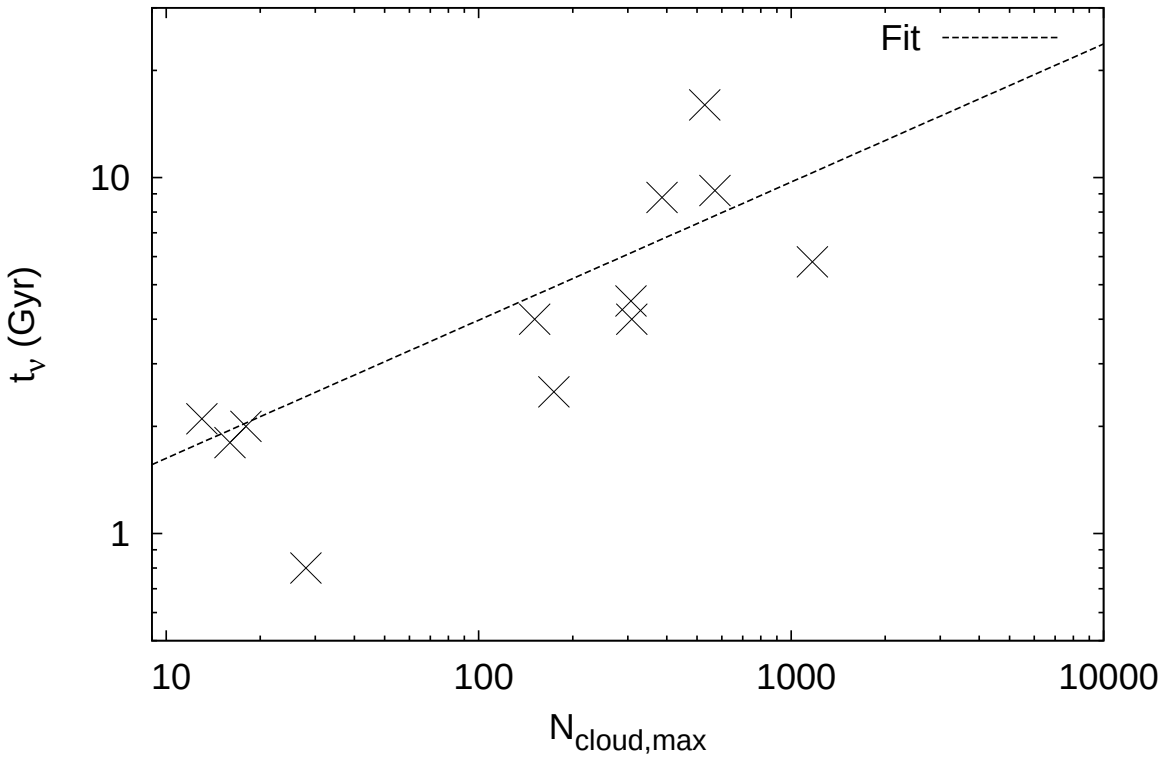

Figure 3.19: Correlation between peak number of clouds ($N_{\rm cloud,max}$) and viscous time-scales (t_ν) for all models whose time-scale is given in Table 3.4. The plotted fit is $t_\nu = (0.67\ {\rm Gyr})(N_{\rm cloud,max})^{0.39}$.

3.5 Conclusions

Previous estimates of the viscous time-scale suggest that the viscous time-scale for cloud-cloud collisions in a Milky-Way-like galaxy is large, with $t_\nu > 1000$ Gyr. To test the hypothesis that the viscous time-scale is long, we performed simulations using the AP^{3}M-SPH code HYDRA with cooling down to 10 K and a dynamic temperature floor. The simulations fell into two sets of models: initially stable gaseous discs within dark-matter halos and stellar discs, and a gaseous spheres collapsing inside dark-matter halos. These two sets of models were chosen to bracket a wide range of stability. The viscous time-scale was measured by tracking clouds with a friends-of-friends algorithm, and determining the energy loss when clouds collided.

Although our cloud masses are larger than those found in other simulations, potentially due to insufficient resolution, a simple analysis suggests that we are resolving the wavelength of the most unstable mode. However, further instabilities (in particular, non-axisymmetric turbulent instabilities that we have not accounted for in our linear stability analysis) may appear at higher resolutions, and while the inclusion of energy input from stellar feedback may not greatly alter the properties of clouds, it may contribute to cloud evaporation and affect their collisional behaviour by increasing their cross-section through heating.

Identifying clouds and interactions between clouds is still a difficult task, as clouds have complex structures and dynamics. The friends-of-friends algorithm often identifies clouds as merging and separating several times over a period that upon visual inspection appears to be a single interaction. Through a detailed examination of 10 interaction events, we determined that each 'real' interaction corresponds to ~ 4.5 interactions found by our algorithms. The complex nature of these interactions also complicated our estimates for $\eta = \Delta K_{\rm cloud}/K_{\rm cloud}$, the efficiency of energy loss per cloud interaction. We found that despite our low viscous time-scales, η was not large, with $\eta \sim 0.002$ per recorded interaction.

Most models from both sets of initial conditions collapsed into discs dominated by clumps of gas. The Milky Way models produced a more stable disc with a large

number of small clouds, while the collapse models produced a highly unstable disc consisting of a small number of massive clumps. Despite this large disparity, the viscous time-scales were similar, with $t_\nu = 4.5$ Gyr for LowSoftMW, and $t_\nu = 0.8$ Gyr for LowSoftC. These values are much smaller than estimates using the formulation of B02, which overestimate the viscous time-scale by appearing to erroneously include inefficiency of cloud collisions twice. Removing this factor gives analytic estimates of $t_\nu = 1.1$ Gyr for LowSoftMW and $t_\nu = 17$ Gyr for LowSoftC. These values do not exactly coincide with our measured values as they are based on simple arguments that are particularly inaccurate for LowSoftC. However, they all agree with the general statement that viscosity due to cloud-cloud collisions is not negligible.

The scatter of t_ν across our models was moderate (0.6–16.0 Gyr), despite the range of cloud properties. Hence our viscous time-scales are applicable for a wider range of galaxies than those modelled here, although viscous time-scales will likely increase somewhat as resolution improves. For a simulation capable of resolving 10^5 clouds, we predict a viscous time-scale of around 60 Gyr, admittedly making the effect comparatively weak within a Hubble time, but nonetheless over an order of magnitude faster than previous estimates.

These results suggest that viscosity due to cloud-cloud collisions, while not dominant, does not have a completely negligible effect on the evolution of a galaxy. Although our models may underestimate the viscous time-scales due to resolution effects, it still appears that cloud-cloud viscosity is more significant than previously estimated. While numerical models of galaxies may be able to model this directly (as we do in this work), it may be necessary to include a cloud-cloud viscous term in analytical and semi-analytical models of disc evolution.

Chapter 4

The Formation of Cold Clouds in Outflows

4.1 Introduction

Increasing computational power combined with a greater understanding of the turbulent nature of the interstellar medium has stimulated a surge of interest in simulations of turbulence in a galactic context. These simulations generally fall into two categories: simulations which lack a sub-grid turbulence model (including Direct Numerical Simulations (DNS), which resolve all of the key scales), and Large-Eddy Simulations (LES) (Smagorinsky 1963; Lesieur et al. 2005; Garnier et al. 2009), which include a sub-grid turbulence model. Direct simulations of turbulence are particularly useful for performing tests which help to determine the characteristics of turbulence in the ISM regime — this information can be used to further develop sub-grid models for larger scale simulations. These simulations are often performed in a periodic box, where the effects of varying parameters such as the strength and nature (e.g. compressive or solenoidal) of turbulent forcing, magnetic field strength, and self-gravity, can be more easily disentangled. Examples of this approach include Mac Low et al. (1998); Stone et al. (1998); Mac Low (1999); Porter et al. (1999); Klessen (2000); Klessen et al. (2000); Klessen (2001); Boldyrev et al. (2002); Li et al. (2003); Padoan et al. (2004); Jappsen et al. (2005); Ballesteros-Paredes et al. (2006); Pavlovski et al. (2006); Dib et al. (2008); Federrath et al. (2008); Offner et al. (2008); Federrath et al. (2009); Schmidt et al. (2009); Federrath et al. (2010); Konstandin et al. (2012), and they have been useful in constraining velocity power spectra and probability density functions. These simulations are usually applied to star formation in molecular clouds, and have been used to clarify the relationship between turbulence and the initial mass function of stars. Simulations without a sub-grid model are also

often performed on more realistic initial and boundary conditions, as well as more self-consistent physics. This approach is applied to simulations of molecular clouds (e.g. Price & Bate 2008; Tilley & Pudritz 2007; Vázquez-Semadeni et al. 2005; Li et al. 2004; Li & Nakamura 2006), or the intracluster-medium (e.g. Vazza et al. 2012, 2009; Maier et al. 2009; Iapichino & Niemeyer 2008; Dolag et al. 2005), for example.

However, the scale-independent nature of turbulence implies that unresolved scales will be important in many of these circumstances, and sub-grid-scale turbulence models can be essential, if numerical models are to be considered realistic. Direct simulations can have a strong resolution dependence if the dissipation scale is not resolved, with turbulent energy levels increasing with resolution (Stone et al. 1998), as the turbulent cascade is shut off at increasingly small length scales. Sub-grid turbulence models have been well-used in various other fields, particularly under the formalism of Large Eddy Simulations (LES) (Smagorinsky 1963; Lesieur et al. 2005; Garnier et al. 2009), with the eddy viscosity first being introduced in a meteorological context (Smagorinsky 1963), and with a great deal of practical application in engineering fields such as aerospace (Piomelli 1999). However, the large range of critical lengths, temperatures, velocities (i.e. Mach numbers), and densities (i.e. the strong compressibility) in galactic simulations has reduced the utility of direct application of these methods. Recently however, sub-grid turbulence models for the ISM and IGM have received increasing attention (e.g. Schmidt et al. 2006; Scannapieco & Brüggen 2008; Joung et al. 2009; Maier et al. 2009; Oppenheimer & Davé 2009; Scannapieco & Brüggen 2010; Schmidt & Federrath 2011). In this chapter, we apply the sub-grid turbulence model of Scannapieco & Brüggen (2010) to the problem of cold high velocity-dispersion gas in ULIRG outflows, in addition to performing simulations without sub-grid turbulence.

As noted in section 1.4, observations of absorption in ULIRG outflows have detected broad NaI lines, which reveal the presence of large column-densities of cold gas. This gas is too cold to provide sufficient thermal broadening to generate these

lines, and so non-thermal broadening must be present — i.e. the gas is likely *turbulent* with a large velocity-dispersion. One explanation for the origin of this gas has been investigated by the simulations of Fujita et al. (2009), where the cold gas is produced by Rayleigh-Taylor (RT) fragmentation of the radiatively-cooled shockfront of a super-bubble that has been inflated by an intense starburst. This situation is difficult to analyze numerically, because the cooling rate can vary rapidly with temperature (and hence with time) and a very short time-step is required to capture this correctly. Also, the RT instability can be strong at a wide range of wavelengths, and so this instability will not converge without very high resolution. Furthermore, the RT instability can produce turbulent gas, which cascades to smaller scales and requires very high resolution or a sub-grid turbulence model. To better resolve the scales relevant to turbulent formation and destruction of clouds, the simulations of Fujita et al. (2009) are performed in two dimensions with cylindrical symmetry. While this allows a resolution of as fine as 0.1 pc in a 100 pc by 200 pc box, it suppresses modes of instability and gas flow that may be present in three dimensions. Furthermore, even at this high resolution, Fujita et al. (2009) note a significant resolution dependence in the scale of these clouds, which suggests that the turbulence is still not fully resolved.

There is thus motivation to reexamine this scenario with a fully three dimensional hydrodynamic model, and to test the effects of sub-grid turbulence to counteract the resolution dependence. However, we are not able to attain an equivalent resolution in 3D models on our available equipment within a reasonable wall-clock time, even with adaptive mesh approaches. Instead we develop models with two scales of size — one with the same scale as Fujita et al. (2009) but lower resolution, and a full-scale galaxy model to examine large-scale effects. We perform simulations with and without sub-grid turbulence. As suggested by the strong resolution dependence of cloud formation found in Fujita et al. (2009), clouds are formed at the limit of the model's resolution, and hence any sub-grid model should have a significant effect here: the expectation is that the models with sub-grid turbulence should show a weaker

resolution dependence, and hence allow us to make more robust conclusions from our simulations. We also vary the initial conditions, mass loading rates, and components of the sub-grid turbulence model, and thus produce a suite of models to investigate numerical effects. To facilitate a more direct comparison with observations, we have also produced a raytracing code for calculating mock NaI absorption spectra of our models.

Following this introduction, this chapter is divided into six sections. In section 4.2 we give the initial conditions of our models, in addition to outlining our models of other physical processes such as feedback and cooling. In section 4.3 we motivate our sub-grid turbulence model. In section 4.4 we detail our algorithms for raytracing and producing spectra, and detecting clumps. In section 4.5 we give our techniques for analyzing spectra and predicting clump trajectories. In section 4.6 we present our results, and in section 4.7 we gives our conclusions.

4.2 Simulation model

4.2.1 Initial Conditions

The initial conditions were generated using the galactic disc generator of Scannapieco & Brüggen (2010) with some modifications. In this model, only the gaseous component is explicitly evolved, while the dark matter component is represented by a gravitational potential, and the stellar component is modelled by both a gravitational potential and a feedback algorithm. The gaseous disc is initially axisymmetric, following a sech profile in both the radial and vertical directions:

$$\rho(r,z) = \frac{M_{gas}}{4C\pi^2 h_r^2 h_z}\mathrm{sech}(r/h_r)\,\mathrm{sech}(z/h_z) + \rho_{amb}, \tag{4.1}$$

where M_{gas} is the total gass mass, h_r and h_z are the radial and vertical scale heights, ρ_{amb} is the ambient IGM density, and C is Catalan's constant, defined by

$$2C = \int_0^\infty x\,\mathrm{sech}(x)\mathrm{d}x. \tag{4.2}$$

Pressure is set to provide vertical hydrostatic equilibrium by

$$P(r,z) = P_{amb} - \int_{z_{max}}^{z} \rho(r,z) g(r,z) \mathrm{d}z, \tag{4.3}$$

where P_{amb} is the ambient pressure of the IGM, z_{max} is the height of the computed volume, and $g(r,z)$ is the acceleration due to gravity. This gravity is given by a combination of a halo and a thick-disc potential. We use the halo potential already implemented in FLASH by Scannapieco & Brüggen (2010), which was defined in Burkert (1995) and given explicitly in Mori & Burkert (2000). The halo potential is an phenomenological model based on observations of dwarf galaxies, where the dark matter density profile can be more directly probed. This potential is designed to resemble an isothermal profile at low radii, preventing the problem of "cuspiness", while agreeing with the commonly used Navarro-Frenk-White profile at large radii (Navarro et al. 1996). Our halo potential is given by

$$\begin{aligned} \phi_{\mathrm{halo}} = -\pi G \rho_{d0} r_{d0}^2 \Big\{ & -2\left(1+\frac{r_{d0}}{R}\right) \mathrm{atan}\left(\frac{r_{d0}}{R}\right) \\ & + 2\left(1+\frac{r_{d0}}{R}\right) \ln\left(1+\frac{R}{r_{d0}}\right) \\ & - \left(1-\frac{r_{d0}}{R}\right) \ln\left[1+\left(\frac{R}{r_{d0}}\right)\right] \Big\}, \end{aligned} \tag{4.4}$$

where r_{d0}, and ρ_{d0} are the parameters that define the spatial and mass scale of the halo, and R is the radius in spherical coordinates.

The disc potential is a Plummer-Kuzmin disc (Binney & Tremaine 2008), which is given by

$$\phi_{\mathrm{disc}} = \frac{-GM_{\mathrm{disc}}}{\sqrt{r^2 + [h_r + (z^2 + h_z^2)^{1/2}]^2}}, \tag{4.5}$$

where M_{disc} is the mass of the disc, h_r and h_z are the radial and vertical scale heights, and r and z are position in cylindrical coordinates. We do not include a bulge potential — given that our initial conditions do not accurately account for the complex irregular structure of a ULIRG, including a bulge potential is an unnecessary detail that should not significantly improve our model.

To break the symmetry of the small-scale disc model, we have also produced models that included asymmetric density perturbations. Using the cartesian coordinate system (x, y, z) where $(x, y, z) = (0, 0, 0)$ is the centre of the feedback region and $(x, y, 0)$ defines the plane of the ULIRG disc, the perturbation is applied by defining a factors ξ and f by

$$\begin{aligned}\xi =&[1 + A\cos(\pi(x+\delta)/\lambda)\cos(\pi(y+\delta)/\lambda)]^2 \\ &\times[1 - A\cos(\pi(x+\delta)/\lambda)\cos(\pi(y+\delta)/\lambda)]^2\end{aligned} \tag{4.6}$$

$$\text{and} f = [1 - (1-\xi)\text{erfc}(-y/10h_z)/2] \tag{4.7}$$

and defining the perturbed density $\rho'(x, y, z)$ by

$$\rho'(x, y, z) = \rho(x, y, z) f^{\cos[\pi(z+\delta)/\lambda]}. \tag{4.8}$$

This provides an approximately sinusoidal perturbation that is dampened as the z direction increases, which prevents extreme temperature variations in the sparse higher-altitude gas. Here λ is the wavelength of the perturbation, δ is the offset to break symmetry, the complementary error function term (erfc) smoothly reduces the amplitude of the perturbation towards zero over several scale heights, A is the amplitude of the perturbation, and the term that is sinusoidal in the z-direction is placed in the exponential in order for the perturbation to be significant when compared to the rapid exponential rate of change of density in the vertical direction. To further reduce symmetry, we apply this to the density twice, using $\lambda = 37.3$ pc and $\delta = 0$ pc in the first instance, and $\lambda = 97.2$ pc and $\delta = 22.7$ pc in the second, with $A = 0.5$ in both cases. These values are not intended to closely match the details of the density field in the central region of a real ULIRG, but are chosen such that the wavelength of the perturbation is large enough to be well-resolved, but still small enough that at least one wavelength can fit within the simulated domain. The

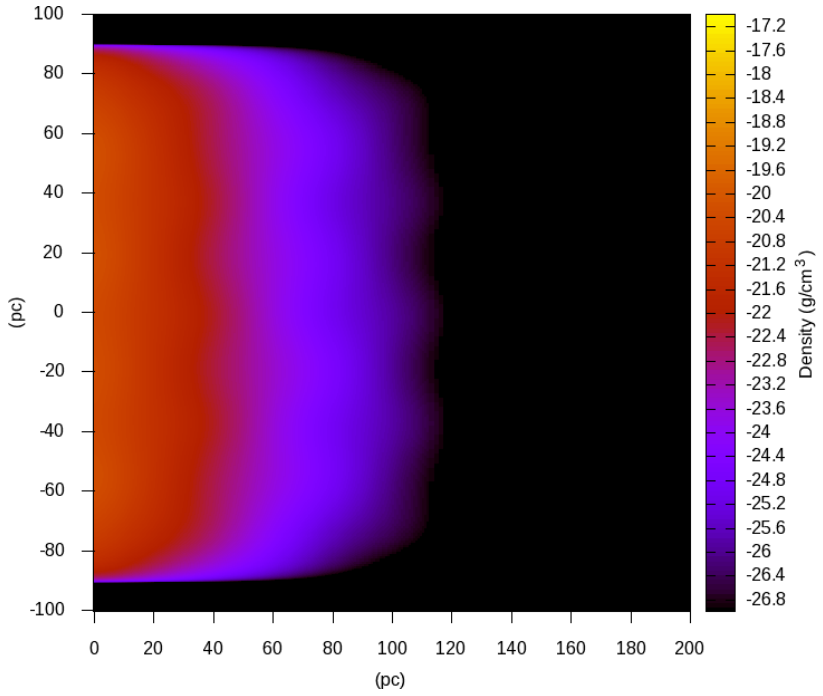

Figure 4.1: Side-on density slice of initial conditions for SHighResNoTurbLumpy.

intention here is only to test the reaction of our model to asymmetric perturbations. These "lumpy" initial conditions are plotted in Fig. 4.1.

4.2.2 Feedback from Star Formation

We use the feedback model implemented by Scannapieco & Brüggen (2010), with some modifications. In this model, the number of supernovae is tallied over iterations. Informed by the cosmic SN rate (Dahlen et al. 2004; Giavalisco et al. 2004; Scannapieco & Bildsten 2005) and by initial mass functions (Scannapieco et al. 2002), it is assumed that $150M_{\odot}$ of star formation is required to produce a single supernova. When the cumulative count of supernovae exceeds a certain parameter, a bubble of hot gas is produced in the disc, and these supernovae are decremented from the total supernova count. The number of supernovae required to produce a bubble is determined by generating a random variable $\zeta \in [0, 1]$ by

$$N_{\rm SN} = \frac{N_{\rm SN,min}}{1-\zeta}, \tag{4.9}$$

where $N_{\rm SN,min}$ is a model parameter. If $N_{\rm SN} > N_{\rm SN,max}$, where $N_{\rm SN,max}$ is another model parameter, then ζ is recalculated. $N_{\rm SN,min}$ and $N_{\rm SN,max}$ determine whether feedback consists of a small number of large bubbles, or a large number of small bubbles. The radius of the bubble is set such that it is at least the size of the region containing twice the mass in gas of the mass converted into stars, as well as being greater than some resolution-dependent minimum size that ensures that the bubble covers at least one cell.

In the large-scale disc models, each bubble is placed randomly, with positions weighted according to $\rho(r,z)^{3/2}$, where $\rho(r,z)$ is the initial analytic distribution of density. This procedure is based on the assumption that the star formation rate is proportional to ρt_{ff}, where the free-fall time t_{ff} is proportional to $\rho^{1/2}$. Three random numbers $\xi_1, \xi_2, \xi_3 \in [0,1]$ determine the position of the bubble. Defining a cartesian coordinate system $\vec{r} = (x,y,z)$ where the disc lies in the (x,y) plane, the position is given by

$$x = r\cos(2\pi\xi_1) \tag{4.10}$$

$$y = r\sin(2\pi\xi_1) \tag{4.11}$$

$$z = h_z \ln(\xi_3), \tag{4.12}$$

where r is determined by iteratively solving the equation

$$r = \log((1+r)/(1-\xi_2)), \tag{4.13}$$

as mentioned in section 2.3.1.5.

In the small-scale central-disc models, we model the outflow as a central starburst. While $N_{\rm SN}$ is calculated as above, the bubbles are always placed in the centre

of the disc at $z = 0$pc, and have a constant radius of $R_{\rm bub} = 10$pc. This approach is similar to that of the Fujita et al. (2009), and allows a more direct comparison of the important differences in the models: that we are performing our simulation in three dimensions instead of two (at the cost of lower resolution), and that some of our models include sub-grid turbulence.

The bubble is implemented by first calculating the mass density $\rho_{\rm SN}$ and energy density $e_{\rm SN}$ added to the feedback region,

$$\rho_{\rm SN} = M_{\rm SN} \frac{N_{\rm SN}}{4\pi R_{\rm bub}^3} \tag{4.14}$$

$$e_{\rm SN} = \frac{N_{\rm SN}}{4\pi R_{\rm bub}^3} f_{\rm SN} 10^{51} {\rm erg}, \tag{4.15}$$

where $f_{\rm SN}$, the fraction of the supernovas' energy transferred to the bubble, and $M_{\rm SN}$, the amount of mass ejected into the bubble, are adjustable parameters. Next we apply the transforms

$$\rho_{\rm new} \mapsto \rho_{\rm old} + \rho_{\rm SN} {\rm erfc}\left(\frac{\vec{r}_{\rm cell} - \vec{r}_{\rm bub}}{0.05 R_{\rm bub}}\right) \tag{4.16}$$

$$e_{i,{\rm new}} \mapsto \left[e_{i,{\rm old}}\rho_{\rm old} + e_{\rm SN} {\rm erfc}\left(\frac{\vec{r}_{\rm cell} - \vec{r}_{\rm bub}}{0.05 R_{\rm bub}}\right)\right] / \rho_{\rm new} \tag{4.17}$$

to all gas cells with centres ($\vec{r}_{\rm cell}$) within $2R_{\rm bub}$ of the centre of the bubble ($\vec{r}_{\rm bub}$). The complementary error function erfc is used to smooth the edges of the bubble. This function ensures that the only sharp discontinuities in density and temperature are those caused by the evolution and interaction of bubbles, and not those directly imposed by the feedback algorithm. In simulations including sub-grid turbulence, we also apply

$$K_{\rm new} \mapsto (K_{\rm old}\rho_{\rm old} + f_{\rm turb} e_{\rm SN} {\rm erfc}\left(\frac{\vec{r}_{\rm cell} - \vec{r}_{\rm bub}}{0.05 R_{\rm bub}}\right))/\rho_{\rm new} \tag{4.18}$$

$$L \mapsto R_{\rm bub} \tag{4.19}$$

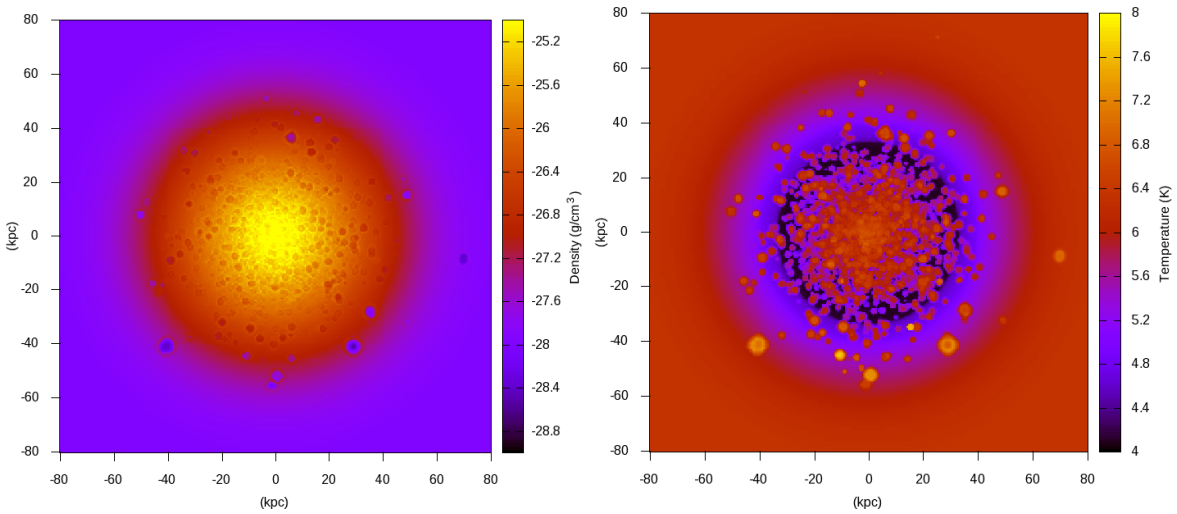

Figure 4.2: Density (left) and temperature (right) slices at $z = 0$ pc of BHighResNoTurb at $t = 5$ Myr

to the same region, where $f_{\rm turb}$, the fraction of feedback that is inputted as turbulent energy, is a model parameter. The significance of K and L, the turbulent kinetic energy and length scale, are given in section 4.3.

In our fiducial models we set $f_{\rm SN}$ to $f_{\rm SN} = 0.6$, and $M_{\rm SN} = 6{\rm M}_\odot$, which allows us to parameterize the feedback's luminosity, $L_{\rm FB}$, in addition to the mass loading rate, $\dot{M}$, in terms of the star formation rate $\dot{M}_*$, through the following equations:

$$L_{\rm FB} \approx \quad 1.3 \times 10^{43} {\rm ergs}^{-1} \left(\frac{\dot{M}_*}{100 {\rm M}_\odot/{\rm yr}} \right) \tag{4.20}$$

$$\dot{M} \approx \qquad\qquad \left(\frac{\dot{M}_*}{18.75} \right). \tag{4.21}$$

Face-on $z = 0$ pc slices through BHighResNoTurb at $t = 5$ Myr are plotted in Fig. 4.2 to demonstrate the properties of the generated population bubbles once the star formation rate has inflated several bubbles, but before differential rotation, buoyancy and turbulence have had sufficient time to cause significant perturbations. With a star formation rate of 200 $M_\odot$/yr, this corresponds to $10^9 M_\odot$ of star formation.

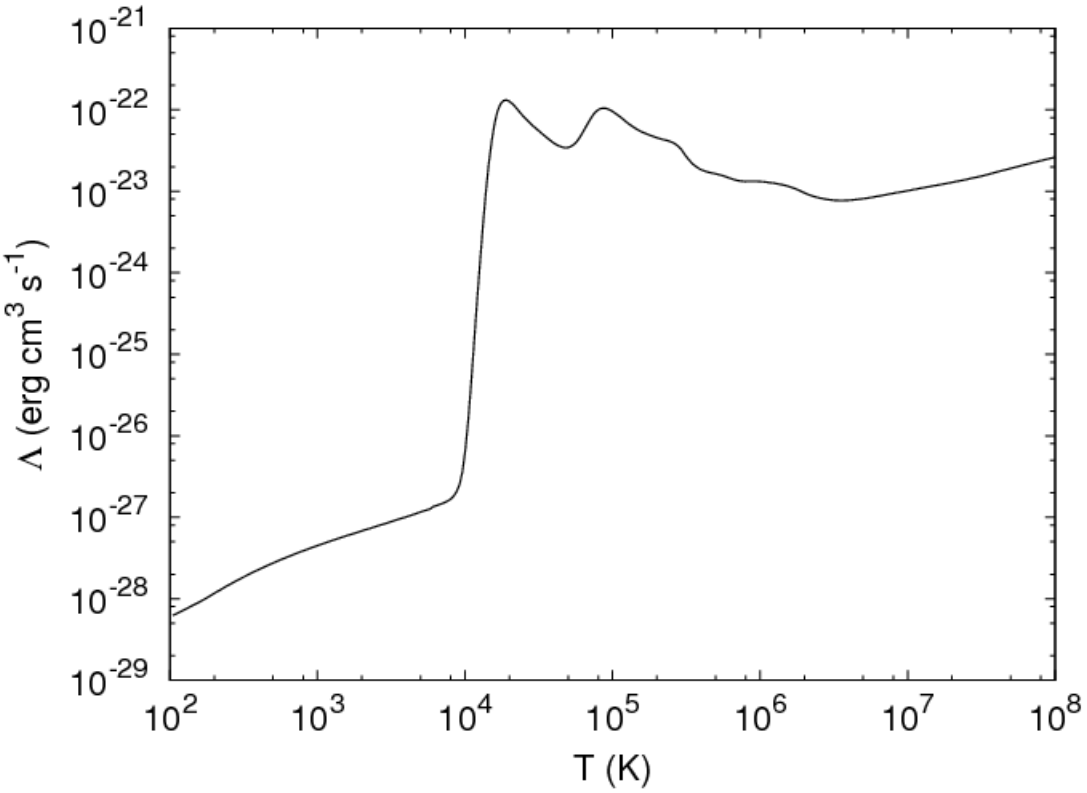

Figure 4.3: Cooling curve used in our FLASH simulations

In some models we also investigated the effect of different mass loading rates by altering $M_{\rm SN}$. We include some unrealistically large values to investigate the effects of very large mass-loading rates.

4.2.3 Cooling Function

For this code, we make use of the cooling curves ($\Lambda(T)$) of Raymond et al. (1976) and Sarazin (1986), plotted in Fig. 4.3. The cooling algorithm simply applies the discretised form of equation 1.13) to the internal energy e_i of each cell several times, each with a shorter time-step than the true time-step. That is, $\Delta e_i = \Lambda n^2 \Delta t_j$, with cooling time-step Δt_j set such that $|\Delta e_i| < |e_i|/10$ in each step, and that $\sum \Delta t_j$ is equal to the true time-step.

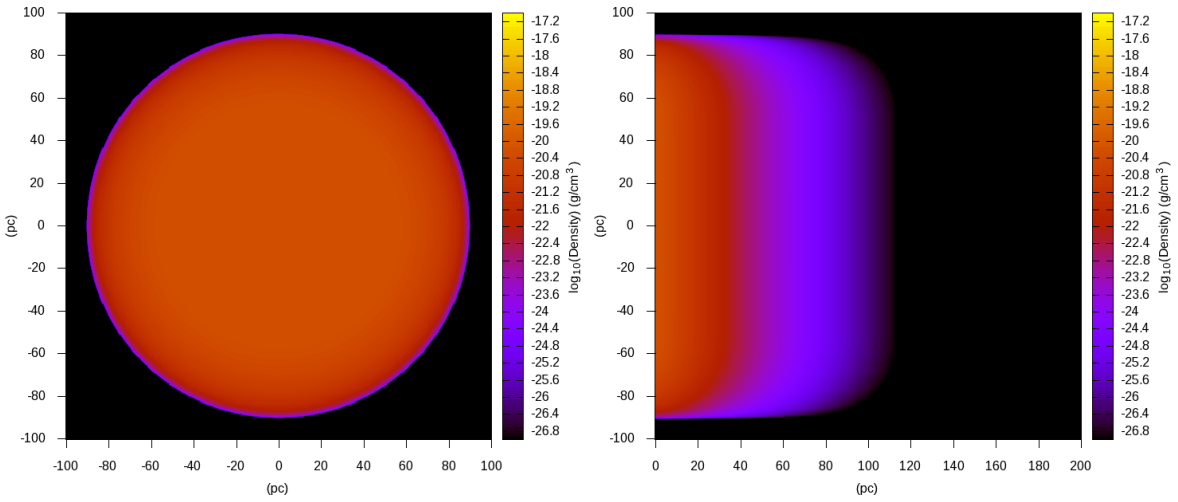

Figure 4.4: Face-on ($z = 0$ pc) and edge-on ($x = 0$ pc) slices of SHighResNoTurb at $t = 0$ yr.

4.2.4 Galaxy-centre model

The simulated domain of central-disc model is a cartesian grid of size 200^3 pc^3. We reduce the computational load by using reflective boundary conditions across the $z = 0$ plane – which is justified due to the symmetry of the flow in this situation. Following Fujita et al. (2009), the disc has a vertical scale-height of 7 pc, a radial scale-length of 700 pc, and a mass of $10^{10} M_{\odot}$. As the scale-length is much larger than the box size, this produces a disc that has almost no radial density variation within the box. We truncate this disc using the complementary error function

$$\mathrm{erfc}(r) = \frac{2}{\sqrt{\pi}} \int_r^{\infty} e^{-t^2} dt \tag{4.22}$$

This ensures the density at the edge of the box is small, and large amounts of gas do not rotate out of the box. As this truncation is much shorter than the radial scale-length, this truncation does not accurately represent the density profile, and we stop the simulation when the inflated bubble reaches the truncated region. Density plots of these initial conditions for SHighResNoTurb are given in Fig. 4.4. The parameters for all of our galaxy-centre models are summarized in the top section of Table. 4.1.

Name	$M_{\rm SN}$	$l_{\rm ref}$	Turb	$f_{\rm lumpy}$
SVLowResNoTurb	6	1	No	0.
SLowResNoTurb	6	2	No	0.
SMedResNoTurb	6	3	No	0.
SHighResNoTurb	6	4	No	0.
SVLowResTurb	6	1	Yes	0.
SLowResTurb	6	2	Yes	0.
SMedResTurb	6	3	Yes	0.
SHighResTurb	6	4	Yes	0.
SLowResNoTurbLumpy	6	2	No	0.5
SMedResNoTurbLumpy	6	3	No	0.5
SHighResNoTurbLumpy	6	4	No	0.5
SMedResTurbLumpy	6	3	Yes	0.5
SMedResNoTurbHeavy	16	2	No	0.
SMedResNoTurbLight	4	3	No	0.
SMedResNoTurbMassless	0	3	No	0.
BMedResNoTurb	6	2	No	0.
BHighResNoTurb	6	3	No	0.
BMedResTurb	6	2	Yes	0.
BHighResTurb	6	3	Yes	0.

Table 4.1: Parameters in disc outflow models. The prefix "S" refers to the "small" central-disc models, while the prefix "B" refers to the "big" full-scale galaxy models. $M_{\rm SN}$ is the mass ejected in each supernova (i.e. the mass-loading), $l_{\rm ref}$ is the number of refinement levels (including the top level), "Turb" indicates whether sub-grid turbulence is active in the simulation, and $f_{\rm lumpy}$ gives the amplitude of perturbations to the initial conditions.

Fujita et al. (2009) used a range of luminosities from 10^{41}–10^{43} erg/s for the feedback region. In this model we set $\dot{M}_* = 50 {\rm M}_\odot/{\rm yr}$, which is equivalent to a luminosity of 6.3×10^{42} erg/s, on the upper edge of their energy range. These parameters result in a mass-loading rate of 2 $\rm M_\odot$/yr.

4.2.5 Full galaxy model

The full galaxy model is simulated within a cartesian grid of size $240^3 {\rm kpc}^3$. The asymmetry of the feedback does not permit reflective boundary conditions for this model.

This disc is intended to be a simple ULIRG prototype, without a companion galaxy. As ULIRG discs are obscured by dust and are locally rare, their characteristics are poorly constrained by observations. However, we should still choose parameters that are at least consistent with observations. Farrah et al. (2008) performed a mid-infrared survey of 32 ULIRGs at $z \sim 1.5 - 2$, estimating star formation rates of $1000 - 2000 M_{\odot}$/yr. Aravena et al. (2011) estimate the total mass of the elliptical host galaxy for one ULIRG/QSO transition object to be $2.1 \times 10^{12} M_{\odot}$, with the dynamical mass of the CO source being $\sim 80\%$ of this. They estimate the molecular gas mass to be $8 \times 10^{9} M_{\odot}$. The semi-analytical models of Swinbank et al. (2008) return dynamical masses of around $2 - 5 \times 10^{11}$ within $4 - 8$ kpc from CO line-widths, and gas masses of $\sim 3 \times 10^{10} M_{\odot}$ within 2 kpc. Sub-millimetre Galaxies (SMGs) are thought to be the high-redshift analogues for ULIRGs (Narayanan et al. 2009), and Baugh et al. (2005) gives masses of $10^{10} h^{-1} M_{\odot}$ and $10^{12} h^{-1} M_{\odot}$ for the stellar and dark matter components of $z \sim 2$ SMGs, where $h = H/(100$ km/s/Mpc) and H is the Hubble constant. Davé et al. (2010) select likely SMGs from cosmological simulations at $z \sim 2$, and report stellar masses of $\sim 10^{11 - 11.7} M_{\odot}$, and star formation rates of $180 - 500 M_{\odot}$/yr. Dust-obscured Galaxies (DOGs) may also be high-redshift optically-faint ULIRGs, and Narayanan et al. (2010) show that luminous DOGs are gas-rich mergers in extremely massive ($5 \times 10^{12-13}$ $M_{\odot}$) haloes with high star formation rates ($500 - 1000 M_{\odot}$/yr) and/or very strong AGNs.

We can also use the precedent of previous models to inform our choices of parameters. Matsui et al. (2012) modelled merging galaxies (i.e. ULIRG progenitors) each with dark matter haloes of mass $1.1 \times 10^{11} M_{\odot}$, stellar discs of mass $5.1 \times 10^{9} M_{\odot}$ and radial scale-length 4 kpc, and gaseous discs of mass $1.2 \times 10^{9} M_{\odot}$ and radial scale-length 8 kpc. Saitoh et al. (2009) also performed galaxy interaction simulations, with dark-matter halo masses of $1.05 \times 10^{11} M_{\odot}$, stellar discs of mass $6.3 \times 10^{9} M_{\odot}$ with scale-length 4 kpc, a gaseous halo component with 1% of the dark-matter halo mass, and a gaseous disc with 20% of the stellar disc-mass – these were produced with the GalactICs package we use in chapter. 3. The merger simulations of Bekki et al. (2006)

included a disc of mass $6 \times 10^{10} M_{\odot}$ and scale-length 17.5 kpc, but are not performed in a full 3D hydrodynamical code and do not need to model all the components of a ULIRG. The parameters from all of these previous studies are summarized in Table. 4.2.

SFR $M_\odot(yr)^{-1}$	M_*	$M_{\rm DM}$ or $M_{\rm dynamic}$	M_g	h_z (kpc)	h_r (kpc)	Reference
1000–2000	-	-	-	-	-	Farrah et al. (2008)
180–500	-	$\sim 10^{11-11.7}$	-	-	-	Davé et al. (2010)
500–1000	$5 \times 10^{12-13}$	-	-	-	-	Narayanan et al. (2010)
-	$10^{10}h^{-1}$	$10^{12}h^{-1}$	-	-	-	Baugh et al. (2005)
-	1.05×10^{11}	6.3×10^9	-	1.05×10^9 (halo) 1.3×10^9 (disc)	4	Saitoh et al. (2009)
-	1.1×10^{11}	5.1×10^9	1.2×10^9	-	4 (gas) 8 (star)	Matsui et al. (2012)
-	-	2.1×10^{12}	$\sim 1.7 \times 10^{12}$	-	-	Aravena et al. (2011)
-	-	2-5$\times 10^{11}$	$\sim 3 \times 10^{10}$	-	-	Swinbank et al. (2008)
-	-	6×10^{10}	-	-	17.5	Bekki et al. (2006)

Table 4.2: Parameters from previous studies used to inform our initial conditions. The SFR is the star formation rate, M_* is the stellar mass, $M_{\rm DM}$ is the mass of the dark matter halo, $M_{\rm dynamic}$ is the total dynamic mass of the system (which may be mostly dark matter by mass), M_g is the mass of the gaseous component (or sometimes *a* gaseous component) and h_z and h_r are the vertical and radial scale heights of the stellar disc.

Informed by these results and preceding simulations, we employ a gaseous disc with mass of $1.0 \times 10^{10} M_{\odot}$, scale-length 8 kpc, and scale-height 2 kpc, and a background potential equivalent to a stellar disc of mass $4.0 \times 10^{10} M_{\odot}$ with a scale-length of 16 kpc and a scale-height of 4 kpc, superimposed on a dark-matter halo of mass $3.0 \times 10^{12} M_{\odot}$ and scale-radius 100 kpc. We set our star formation rate to $200 M_{\odot}$/yr, which is at the lower end of ULIRG SFRs.

The parameters for our galaxy-scale models are summarized in the bottom section of Table. 4.1.

4.3 Sub-grid Turbulence Model

Before specifically discussing our chosen turbulence model, we develop the theory behind sub-grid approaches in more detail.

4.3.1 Decomposition of equations

Sub-grid turbulence in astrophysics can follow the methodology of Large Eddy Simulations by separating a problem into a large scale and a small scale component. The Navier-Stokes equations for momentum conservation are

$$\rho \left(\frac{\partial \boldsymbol{v}}{\partial t} + \boldsymbol{v} \cdot \nabla \boldsymbol{v} \right) = \rho \boldsymbol{g} - \nabla P + \nabla \cdot \boldsymbol{\tau}, \tag{4.23}$$

where $\boldsymbol{g}$ is the sum of all body forces (in particular, gravitational acceleration), P is the thermal pressure, and the deviatoric stress tensor $\boldsymbol{\tau}$ is defined by

$$\boldsymbol{\tau}_{ij} = \nu \rho \left(\frac{\partial v_i}{\partial x_j} + \frac{\partial v_j}{\partial x_i} \right) + \delta_{ij} \lambda \frac{\partial v_k}{\partial x_k}, \tag{4.24}$$

where δ_{ij} is the Kronecker delta, ν is the kinematic viscosity, and λ is the coefficient of dilatational viscosity, which assuming the Stokes hypothesis (Mihalas & Weibel Mihalas 1984) is set to $\lambda = -(2/3)\rho\nu$. The Stokes hypothesis ensures that $\boldsymbol{\tau}$ is traceless, and hence that the mechanical pressure on a fluid is equal to the thermodynamic

pressure (Gad-el Hak 1995). When decomposing into large-scale and small-scale components, it is more convenient to express equation 4.23 as

$$\frac{\partial}{\partial t}(\rho \boldsymbol{v}) + \nabla \cdot (\rho \boldsymbol{v} \otimes \boldsymbol{v}) = \rho \boldsymbol{g} - \nabla P + \nabla \cdot \boldsymbol{\tau}, \tag{4.25}$$

which is equivalent under the condition of mass conservation. Here $\boldsymbol{x} \otimes \boldsymbol{y}$ represents the outer product of $\boldsymbol{x}$ and $\boldsymbol{y}$ — i.e. a tensor defined by $[\boldsymbol{x} \otimes \boldsymbol{y}]_{ij} = (x_i)(y_j)$.

To separate out an average large scale component, we convolve equation 4.25 with a filter function, G. A filter function smooths out small-scale variations below some length-scale Δ, which in numerical simulations is generally the cell size. A simple example of a filter is the Box Filter, defined by

$$G(\boldsymbol{x} - \boldsymbol{r}) = \begin{cases} 1/\Delta, & \text{for } |\boldsymbol{x} - \boldsymbol{r}| \leq \Delta/2, \\ 0, & \text{otherwise} \end{cases}, \tag{4.26}$$

and this is applied to a field variable $\phi(\boldsymbol{x})$ through a convolution,

$$\overline{\phi}(\boldsymbol{x}) = \int \phi(\boldsymbol{r}) G(\boldsymbol{x} - \boldsymbol{r}) \mathrm{d}\boldsymbol{r}. \tag{4.27}$$

Defining the smoothed large-scale variables in this way by e.g. $\overline{\rho} = G * \rho$ (where $*$ represents a convolution) results in a set of equations in terms of these large-scale variables that is similar in form to the Navier Stokes equations. A filter function must commute with differentiation and with constants, but not necessarily with scalars or vectors that vary across the field. For an incompressible fluid (where $\rho = \overline{\rho}$ is a constant), the filtered momentum conservation equations are

$$\rho \frac{\partial}{\partial t}(\overline{\boldsymbol{v}}) + \rho \nabla \cdot \overline{\boldsymbol{v} \otimes \boldsymbol{v}} = \rho \overline{\boldsymbol{g}} - \nabla \overline{P} + \nabla \cdot \overline{\boldsymbol{\tau}}. \tag{4.28}$$

Even for an incompressible fluid the non-linearity of the $\nabla \cdot \boldsymbol{v} \otimes \boldsymbol{v}$ term is a source of difficulty, as $\nabla \cdot \overline{\boldsymbol{v} \otimes \boldsymbol{v}}$ can not be determined without detailed knowledge of the small scale velocity field, which for numerical simulations requires a sub-grid model. This

equation can conveniently be rearranged into the familiar momentum conservation equation (in terms of $\rho\overline{\boldsymbol{v}}$) with an additional term due to sub-grid scale (SGS) effects:

$$\rho\frac{\partial}{\partial t}\left(\overline{\boldsymbol{v}}\right)+\rho\nabla\cdot\left(\overline{\boldsymbol{v}}\otimes\overline{\boldsymbol{v}}\right)=\rho\overline{\boldsymbol{g}}-\nabla\overline{P}+\nabla\cdot\overline{\boldsymbol{\tau}}+\rho\nabla\cdot\left(\overline{\boldsymbol{v}}\otimes\overline{\boldsymbol{v}}-\overline{\boldsymbol{v}\otimes\boldsymbol{v}}\right), \tag{4.29}$$

where $\rho(\overline{\boldsymbol{v}}\cdot\nabla\overline{\boldsymbol{v}}-\overline{\boldsymbol{v}\cdot\nabla\boldsymbol{v}})$ is the SGS term. To close the equations, some prescription must be given for this term. In models where small scale velocity perturbations are considered unimportant it may be acceptable to completely neglect this term, otherwise it must be approximated by a sub-grid turbulence model.

The situation is slightly more complicated for a compressible fluid, as ρ no longer commutes with the filter function convolution. Hence we use a mass-weighted average (Favre 1983) for the velocity field. The Favre-average of a quantity ϕ is depicted here by $\tilde{\phi}$, and is defined by

$$\overline{\rho}\tilde{\phi}=\overline{\rho\phi}. \tag{4.30}$$

This can be applied to any expression, hence

$$\widetilde{\boldsymbol{v}\otimes\boldsymbol{v}}=\frac{\overline{\rho\boldsymbol{v}\otimes\boldsymbol{v}}}{\overline{\rho}}. \tag{4.31}$$

The compressible filtered momentum conservation equations including sub-grid effects are then given by

$$\frac{\partial}{\partial t}\left(\overline{\rho}\tilde{\boldsymbol{v}}\right)+\nabla\cdot\overline{\rho}\left(\tilde{\boldsymbol{v}}\otimes\tilde{\boldsymbol{v}}\right)=\overline{\rho}\tilde{\boldsymbol{g}}-\nabla\tilde{P}+\nabla\cdot\tilde{\boldsymbol{\tau}}+\nabla\cdot\left(\overline{\rho}\tilde{\boldsymbol{v}}\otimes\tilde{\boldsymbol{v}}-\widetilde{\boldsymbol{v}\otimes\boldsymbol{v}}\right), \tag{4.32}$$

and so the SGS effects are given by the $\nabla\cdot\left(\overline{\rho}\tilde{\boldsymbol{v}}\otimes\tilde{\boldsymbol{v}}-\widetilde{\boldsymbol{v}\otimes\boldsymbol{v}}\right)$ term. We can represent this term with the divergence of a tensor, which we call the sub-grid scale stress tensor, $\boldsymbol{\sigma}_{\mathrm{SGS}}$. This tensor represents the effects of all unresolved motions in the fluid, and some expression for it must be assumed in order to close the momentum equation. We can interpret this tensor by comparison with the fluid's intrinsic stress tensor, $\boldsymbol{\sigma}$.

This stress tensor is typically separated into a traceless component – the deviatoric stress tensor, $\boldsymbol{\tau}$, – and a pressure component, which is equal to one third of the trace of the stress tensor, i.e. $(1/3)\sum_i \boldsymbol{\tau}_{ii} = P$. The deviatoric stress tensor gives the effect of shear, usually through viscosity. For a Newtonian fluid, this is

$$\tau_{ij} = \mu \left(\frac{\partial v_i}{\partial x_j} + \frac{\partial v_j}{\partial x_i} \right). \tag{4.33}$$

Similarly, we can produce an *effective* pressure term from $\sigma_{\rm SGS}$, where $P_{\rm SGS} = (1/3){\rm Tr}(\tau)$. The kinetic energy density of the sub-grid scale is

$$K_{\rm SGS} = \frac{1}{2}\overline{\rho}\tilde{\boldsymbol{v}} \cdot \tilde{\boldsymbol{v}} - \frac{1}{2}\overline{\rho}\widetilde{\boldsymbol{v} \cdot \boldsymbol{v}} = \frac{1}{2}{\rm tr}(\sigma_{\rm SGS}), \tag{4.34}$$

and so

$$P_{\rm SGS} = \frac{3}{2}K_{\rm SGS}. \tag{4.35}$$

Furthermore, it makes sense to model the remaining sub-grid-scale deviatoric stress tensor as an effective viscosity. This viscosity can simply be the eddy viscosity (i.e. a Reynold's stress), that is, $\mu \propto LV$, where L is the length-scale and $V = \sqrt{2K_{\rm SGS}}$ is the velocity-scale of the turbulent eddies. Calculating viscosity as the product of a length-scale and a velocity-scale is the same process we used in analytically estimating the effective viscosity due to cloud-cloud collisions in section 3.4.3. L and V can be estimated from coarse-grid properties, or evolved with a parallel set of equations.

These two terms (effective pressure and eddy viscosity) represent the simplest sub-grid turbulence models, but more complex models have been developed. For example, the model of Schmidt & Federrath (2011) includes additional terms to account for highly compressible astrophysical turbulence, and includes turbulent source terms from the turbulent cascade.

4.3.2 Dimonte-Tipton Sub-grid Turbulence Model

This sub-grid turbulence model was developed by Dimonte & Tipton (2006) to model turbulence from the self-similar growth of the Rayleigh-Taylor (RT) and Richtmyer-Meshkov (RM) instabilities. In this method, turbulence is modelled by two field variables, the turbulent eddy size L, and the turbulent kinetic energy per unit mass, K. These affect the evolution of the system through the addition of a turbulent viscosity, turbulent pressure, and an explicit energy source term.

The RT instability occurs when a denser fluid is located "above" a lower density fluid in a gravitational field, or equivalently, if a denser fluid is accelerated by a lower density fluid, as happens when hot supernova gas propels a cold dense front of swept-up gas, or when a molecular cloud is impacted by a shock. Even though these systems may be in pressure equilibrium, they are not stable, and the less dense fluid will penetrate the denser fluid with bubbles of increasing amplitude, producing a mixing region whose size grows as

$$h_b = \alpha_b A_0 g t^2, \tag{4.36}$$

where h_b is the amplitude of the bubbles, g is the acceleration or external gravitational field, t is time, and A_0 is the Atwood number. A_0 is defined by $A_0 = (\rho_2 - \rho_1)/(\rho_2 + \rho_1)$, where ρ_1 the the density of the lighter fluid, and ρ_2 is the density of the denser fluid. $\alpha_b \sim 0.03 - 0.07$ is a parameter determined by experiments and numerical simulations.

The RM instability can be thought of as the instantaneous limit of the RT instability. In this case, the interface between fluids is accelerated by a sudden impulse such as a passing shock, instead of a continuous acceleration such as that caused by a gravitational field. This impulse imparts a speed v to the interface, and amplifies any interfacial perturbations. On moderate time-scales, this produces a mixing region which grows as

$$h_b \propto (vt)^{\theta_b} \tag{4.37}$$

with $\theta_b \sim 0.025 \pm 0.05$ for 3D perturbations.

Equations 4.36 and 4.37 can be combined into a more generic differential equation for bubble growth for $V_b = dh_b/dt$,

$$\frac{dV_b}{dt} = C_B A_0 g - C_D \frac{\rho_2}{\rho_2 + \rho_1} \frac{V_b^2}{h_b}, \tag{4.38}$$

provided the coefficients C_B and C_D are chosen to correctly fit α_b and θ_b. This formulation demonstrates that both of these instabilities can be modelled by a single equation, known as the buoyancy-drag model. However, it is more useful and convenient in a numerical model to track physical quantities such as the scale-length and kinetic energy of turbulent instabilities, instead of directly tracking bubble amplitudes. Tracking these physical parameters is the principle behind the approach used by Dimonte & Tipton (2006).

The energy equation in this model is

$$\frac{\partial \overline{\rho} E}{\partial t} + \frac{\overline{\rho} E \tilde{v_j}}{\partial x_j} = \frac{\partial}{\partial x_j} \left(\frac{\mu_t}{N_e} \frac{\partial E}{\partial x_j} \right) - \frac{\partial P \tilde{v_j}}{\partial x_j} - S_K, \tag{4.39}$$

where μ_t is the turbulent viscosity, the Prandtl number $N_e \sim 1$ is a model parameter, and S_K is the turbulent source term. This source term includes the growth of instabilities from Rayleigh-Taylor and Richtmyer-Meshkov instabilities which act as a sink of (thermal) internal energy and a source of turbulent kinetic energy, and a decay rate that is assumed to be proportional to $\overline{\rho} V^2/L^2$, where $V = \sqrt{2K}$ is the turbulent velocity scale. The source from RT and RM instabilities is based on the buoyancy-drag model (Equation. 4.38), and gives the combined form:

$$S_K = \overline{\rho} V \left[C_B A_i g_i - C_D \frac{V^2}{L} \right], \tag{4.40}$$

where C_B and C_D are model parameters, g_i is the acceleration in the i direction, A_i is the Atwood number in the i direction, and $g_i A_i$ is a sum over i. $C_B = 0.84$ and $C_D = 1.25$ are determined from experiment (Scannapieco & Brüggen 2008), while A_i is given by

$$A_i = \frac{\overline{\rho}_+ - \overline{\rho}_-}{\overline{\rho}_+ + \overline{\rho}_-} + C_A \frac{L}{\overline{\rho} + L|\partial\overline{\rho}/\partial x_i|} \frac{\partial \overline{\rho}}{\partial x_i}, \tag{4.41}$$

where $C_A = 2.0$ is another model parameter (Scannapieco & Brüggen 2008), and $\overline{\rho}_+$ and $\overline{\rho}_-$ are the densities on the front and back cell boundaries in the i direction. The definitions of $\overline{\rho}_+$ and $\overline{\rho}_-$ form an important approximation in the model, as the Atwood number is intended to describe the density contrast across a discontinuity, while density is typically assumed to vary smoothly across a cell. It is also worth noting that this is a resolution dependent term. For a constant density slope in the i direction $\partial\overline{\rho}/\partial x_i$ across a cell of size $2h$, the density at the front of the cell with central density $\overline{\rho}_c$ is $\overline{\rho}_+ = \overline{\rho}_C + h\partial\overline{\rho}/\partial x_i$ while the density at the back of the cell would be $\overline{\rho}_- = \overline{\rho}_C - h\partial\overline{\rho}/\partial x_i$. For an initially non-turbulent system ($L = 0$), this gives an Atwood number of

$$A_i = \frac{h\partial\overline{\rho}/\partial x_i}{\overline{\rho}_c}. \tag{4.42}$$

That is, the source term is smaller at higher resolutions. This result also holds to first order for any smooth $\overline{\rho}$, which is a reassuring feature of the model, as it indicates that as resolution increases, the production of sub-grid turbulence should approach zero — i.e. the model approaches the limit of direct simulation of turbulence.

The turbulent viscosity is given by

$$\mu_t = C_\mu \overline{\rho} L V, \tag{4.43}$$

where $C_\mu = 1.0$ is a model parameter (Scannapieco & Brüggen 2008). Note that this is equivalent to a Reynolds stress with a characteristic length of L and a characteristic velocity of V.

By energy conservation, both the source term and the turbulent viscosity terms must also be included in the turbulent kinetic energy equation, which is

$$\frac{\partial \overline{\rho} K}{\partial t} + \frac{\partial \overline{\rho} K \tilde{v}_j}{\partial x_j} = \frac{\partial}{\partial x_j}\left(\frac{\mu_t}{N_K}\frac{\partial K}{\partial x_j}\right) - \tau_{\mathrm{SGS},ij}\frac{\partial \tilde{v}_i}{\partial x_j} + S_K, \tag{4.44}$$

where the terms on the right hand side represent turbulent diffusion, turbulent stress, and the source and decay of turbulence, and $N_K = 1$ is a model parameter. Only the pressure component of the turbulent stress $\tau_{\rm SGS}$ is considered (i.e. it is assumed to be isotropic and a diagonal tensor), as shear-driven turbulence has not yet been implemented, hence

$$\tau_{{\rm SGS},ij} = C_P \delta_{ij} \overline{\rho} K, \tag{4.45}$$

where C_P is a model parameter. Off-diagonal terms are not included as they can cause a pathological overamplification of preexisting turbulence by a shock (Sinha et al. 2003; Dimonte & Tipton 2006). Off-diagonal terms would however be necessary to describe the Kelvin-Helmholtz instability.

The evolution of the eddy length scale must also be considered in this approach, as it sets the decay rate of K, as well as the turbulent viscosity μ_t. The evolution of L is given by

$$\frac{\partial \overline{\rho} L}{\partial t} + \frac{\partial \overline{\rho} L \tilde{v}_j}{\partial x_j} = \frac{\partial}{\partial x_j}\left(\frac{\mu_t}{N_L}\frac{\partial L}{\partial x_j}\right) + \overline{\rho} V + C_C \overline{\rho} L \frac{\partial \tilde{v}_i}{\partial x_i}, \tag{4.46}$$

where N_L and C_C are model parameters. The terms on the right-hand-side correspond to turbulent diffusion, the growth of eddies due to turbulent velocity, and the change in eddy scale to the compression and expansion of the fluid.

Finally, the momentum equation (neglecting off-diagonal terms in the SGS tensor) is simply

$$\frac{\partial \overline{\rho} \tilde{v}_i}{\partial t} + \frac{\partial \overline{\rho} \tilde{v}_i \tilde{u}_j}{\partial x_j} = -\frac{\partial P}{\partial x_i} - C_P \frac{\partial \overline{\rho} K}{\partial x_i}, \tag{4.47}$$

where the isotropic $C_P \overline{\rho} K$ term acts as an effective pressure.

In summary, momentum and energy are evolved through equations 4.47 and 4.39, which are the basic equations for conservation of momentum and energy, modified to include the effects of sub-grid turbulence. The energy equation includes a diffusion term from turbulent viscosity and a source term, while the momentum equation includes an additional effective pressure term. The source term (equation 4.40), the turbulent viscosity (equation 4.43), and the effective pressure all depend on the

turbulent kinetic energy (evolved by equation 4.44) and the turbulent length scale (evolved by equation 4.46), which are additional fluid variables for this model. The turbulent source term also depends on a modified Atwood number (equation 4.41), which in turn depends on the turbulent length-scale.

There are a large number of input parameters in this model. While many of these parameters (N_K, N_F, N_ϵ, C_C) can be set by physical assumptions such as self similarity and mass conservation, others (C_D and C_B in particular) must be tweaked to fit observations from experiments and direct numerical simulations. These fits are performed under the assumption of moderate Mach number ($\mathcal{M} \sim 1$) and incompressibility, and are likely not be entirely applicable across our entire simulation — in regions of high Mach number, $C_P \sim 0.4$ may be more appropriate, a difference of a factor of two. Nevertheless, we retain the values of Dimonte & Tipton (2006) for simplicity.

4.3.3 Implementing Sub-grid Turbulence in FLASH

The Dimonte-Tipton model has been implemented in FLASH by Scannapieco & Brüggen (2008, 2010). The grid variables for turbulent kinetic energy, eddy length scale, and turbulent viscosity are automatically advected by FLASH, and diffused with an additional subroutine. FLASH's internal energy array is implicitly redefined to be the sum of the sub-grid turbulent kinetic energy and the thermal internal energy, from which FLASH will naturally produce a pressure that includes contributions from both thermal energy and sub-grid turbulence. Temperature is derived by $T = A(\gamma - 1)(e_i - k_{turb})/R$, where the adiabatic index $\gamma = 5/3$, the atomic mass is $A = 16/27$ g/mol, and R is the gas constant.

Several issues in the implementation had to be fixed. These are discussed in detail in Chapter 2. In brief, the sub-grid turbulence equations were applied in an incorrect order (causing grid properties to become unsynchronized, and a directionally dependent error), an incomplete subset of cells was updated by some subroutines, the

equation of state was not numerically stable, and lastly there was a pair of small typographical errors.

4.4 Raytracing and Simulated Spectra

To compare our results with observations, we developed a code to perform ray-tracing on FLASH data dumps, and hence obtaining a synthetic spectrum from the output. This spectrum covers the NaI line, as this is a useful tracer of cold gas. In particular, Martin (2005) produced spectra for a sample of $z \sim 1$ ULIRGs, and we use these as a basis for our comparison. This comparison can be used to attempt to answer the three questions posed in Fujita et al. (2009),

1. Why do the absorption line widths tend to greatly exceed the thermal velocity dispersion of warm neutral gas?

2. Why do the terminal velocities of the cold gas approach the escape velocities from the starburst galaxies (Martin 2005)

3. What do the maximum and mean velocities measured in the line profiles really represent physically?

4.4.1 Raytracing Algorithm

Our raytracing algorithm tracks a ray or a grid of rays with arbitrary angles through data from a FLASH simulation data dump. As the raytracing is performed on a single dump, the gas can not evolve as the rays pass through it. Using a single static dump is a reasonable approximation if the light travel time is shorter than the evolutionary time-scales of the simulation. For our small-scale 200 pc models, the light travel time is $\sim$ 650 yr, much shorter than our evolutionary time-scales

(for a 1000 km/s outflow velocity, this gives an error of $\sim$ 0.7 pc). For our large-scale 200 kpc models, the light travel time is $\sim$ 650 kyr, which is still not large - given our typical outflow velocites of $\sim$ 300 km/s, this gives an error of $\sim$ 200 pc, which is often close to our resolution limit. We also assume that the rays follow a straight path through the simulated region — we are not performing a fully calculation including scattering processes, but are only integrating the optical depth along a line of sight. Most radiative processes — including scattering — are either outside the narrow range of wavelengths we simulate observations of, or if part of the continuum, are implicitly normalised out. This is acceptable because — given our low optical depths — scattering will not greatly alter the intensity of the ray, and because we are comparing with observations which have also performed this normalisation.

Various quantities can be integrated along a ray. Performing this integration a large number of times can produce a column density or optical depth plot from arbitrary angles. The integrators are separate C++ objects that are passed into and called by the raytracing class, and this modular design leaves the code easily open to expansion to new quantities to integrate or trace along a ray.

This algorithm is optimized towards the FLASH data structure. FLASH stores cell data in regular rectangular blocks. This approach is convenient in an MPI AMR code, as hydrodynamics, gravity and source-terms can be calculated on a block-by-block basis, without requiring explicit information on the refinement level or global position. In our simulation, we use blocks of 8x8x8 cells, with a 4-cell width of guard cells on each face. These blocks are organized into an oct-tree structure, where each node on the tree represents a block, and each node can have eight smaller "child" nodes. The eight child blocks are half the size of their parent blocks, and fit as a 2x2x2 grid within their parent. A block that contains child blocks has been "refined", and its children are "at a higher level of refinement". Nodes that do not have child nodes are called "leaf nodes", and represent the blocks where the highest resolution physics is performed. Nodes with children are "branch nodes", and exist primarily to track the connections between blocks of different refinement levels. FLASH tracks the

geometry of blocks using the grid geometry array (named *gid* in FLASH), which gives the coordinates for the neighbouring, parent, and child blocks of every block.

The first step in the algorithm is generating a grid of rays. The direction of the rays $\boldsymbol{v}$ is set by the user. To set up the grid, the positions of the FLASH cells are rotated from a set of points $\boldsymbol{r}$ into a coordinate system $\boldsymbol{r'}$ defined so that $\boldsymbol{v}$ is rotated into $\boldsymbol{v'} = (1, 0, 0)$. This is done by by transforming the coordinates of every corner (x, y, z) of every FLASH block by the appropriate rotation matrices.

This approach is used to calculate the grid of starting points for the rays, which is a rectangular grid in y' and z' coordinates, parallel to the $x' = 0$ plane. The x' coordinate of the grid is the lowest x' over all corners of blocks in the FLASH data. The maximum and minimum y' and z' coordinates of the grid are the maximum and minimum y' and z' coordinates over all corners of blocks in the FLASH data (see Figure 4.5). The initial positions of rays are evenly spaced in the y' and z' directions. This process produces a grid of rays that encompasses the entire data set even if some rays may miss the data set entirely. Typically we generate grids of 128x128 to 512x512 rays.

This grid is then transformed back into (x, y, z) coordinates by inverting the earlier rotation. Next, the first cell that each ray intersects must be calculated. This first step is done by simply looping across every cell. To detect the intersection between the face of a cell and a ray, the intersection between the ray and the plane defined by the cell is determined. This process is trivial in a rectangular cartesian grid as each face can be used to define a plane of constant x, y, or z. We only perform this calculation across the three closest faces of all cells, e.g. for a ray with direction $(x, y, z) = (1, -1, -2)$, only the faces on the negative x side, positive y side, and positive z side of each cell are considered (See Figure 4.5). Next, if the either of the other two coordinates of the intersection point is outside the boundaries of the cell, then the intersection is discarded. Finally, the distance between the ray's initial coordinate and each intersection point is calculated, and intersection point at

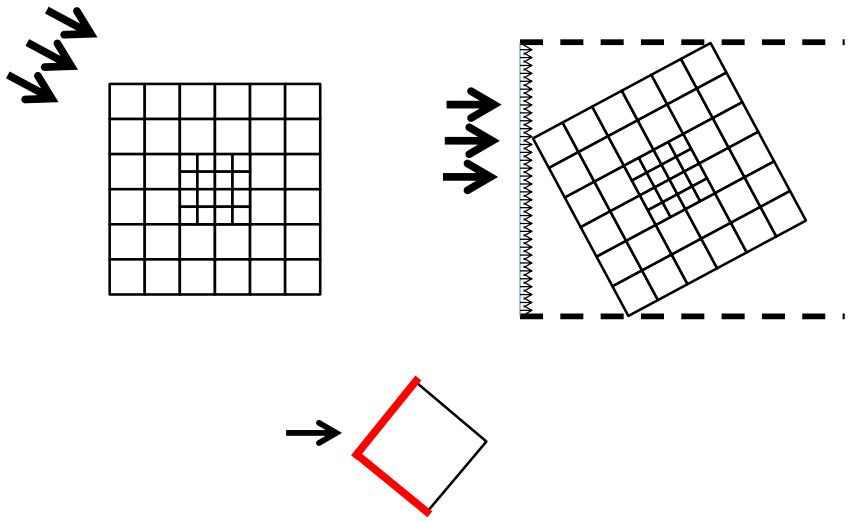

Figure 4.5: Top: Our system is rotated such that rays are moving in the x direction. This geometry allows us to easily find the projected size of the simulated grid, and hence generate a grid of rays to cover this entire domain. Bottom: When calculating the intersection of a ray with a cell, only the "near" edges are considered.

the smallest distance will give the cell that the ray first intersects. Only leaf-node cells are considered in this step.

For the subsequent evolution of the ray, the intersection points of adjacent cells are calculated similarly, but only the three faces of the cell containing the ray are considered. This calculation gives coordinates for the entry and exit of the ray from the cell, from which a distance can be calculated, and this is passed along with the cell's data and the ray's direction into the integration routine.

When the ray reaches the face of a block, the grid geometry array is consulted to determine what block the ray will pass into. Each block can have 8 child blocks, 1 parent block, and 6 neighbouring blocks. These neighbouring blocks connect to the faces of the block. If the appropriate neighbouring block is at the same refinement level, then ray is passed into the new block. If this block is not a leaf node, the ray is passed into the appropriate child until it is in a leaf node. If the neighbouring block is at a higher refinement, then the ray passes to its "parent" block, until the neighbouring block matches its refinement level, and a sole correct neighbouring block can be found. In the rare event that a ray hits the face of the block at an edge or corner (within numerical accuracy), it is stepped through blocks that share a face with its current block, until it reaches the appropriate block. This approach is illustrated in Fig. 4.6 and Fig. 4.7.

This approach naturally and efficiently follows a ray through a complex structure of refinements without the extra memory or drop in resolution necessary to convert FLASH AMR data to a uniform grid. Furthermore, as the evolution and output of each ray is independent of all other rays, this is a good example of an "embarrassingly parallel" problem, and parallelizing this code with OpenMP produces nearly linear speed-up with processor number in the range available to us (up to 32 processors) — e.g. for building a line profile from an array of 512×512 rays through a low resolution test grid, the program completed in 24.7s when using 16 cores, and 12.5s when using 32 cores.

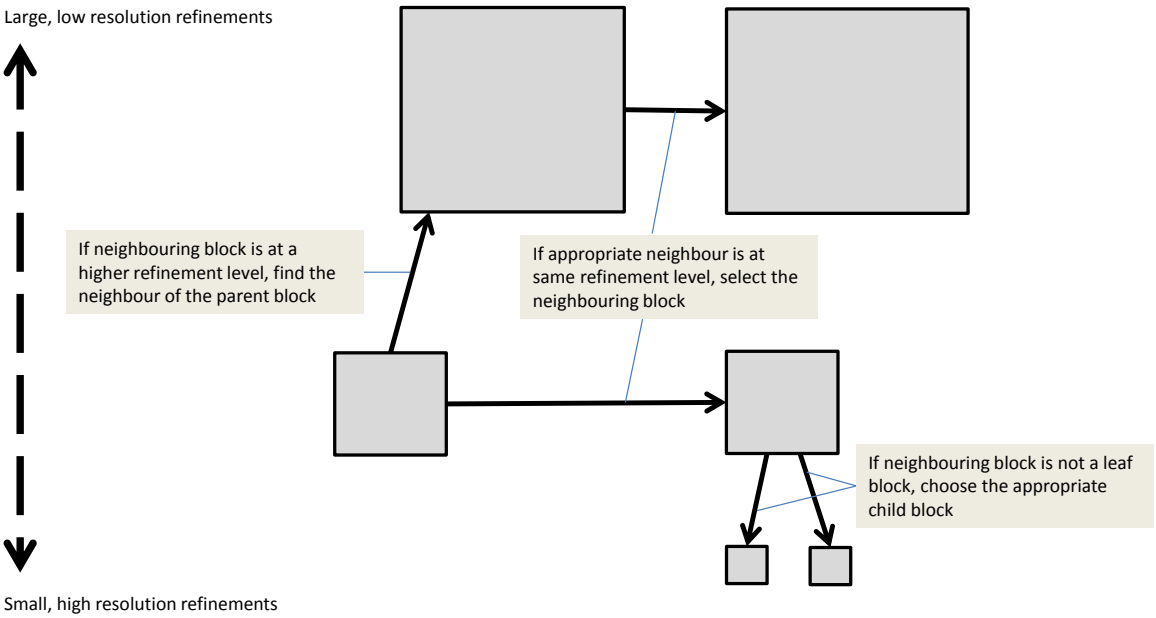

Figure 4.6: The procedure for propagating a ray across FLASH's mesh of blocks. Arrow indicate a transition of the ray from one block to another.

4.4.2 NaI Line spectrum

4.4.2.1 General process

To model the NaI line, we assume a constant HI/NaI ratio, taken from Martin (2005). Following Fujita et al. (2009), we assume that any cell with a temperature below 5×10^4 K will contain some cold NaI absorbing gas. As justified below, we also make a density cut at $10^{-21}\mathrm{g/cm}^3$, with the assumption that any gas above this density will contain some regions that have cooled sufficiently to absorb the NaI doublet. We assume that any gas which fulfils either of these criteria will contain NaI absorbing gas. The line is calculated by integrating the optical depth through a ray across a range of wavelengths. The optical depth is summed for each cell the ray passes through, emissivity is ignored, and the continuum intensity is normalized to 1, so the final intensity of each frequency is given by

$$I(\nu) = \exp(-\tau_\nu) = \exp\left(-\sum \tau_{\nu,i}\right), \tag{4.48}$$

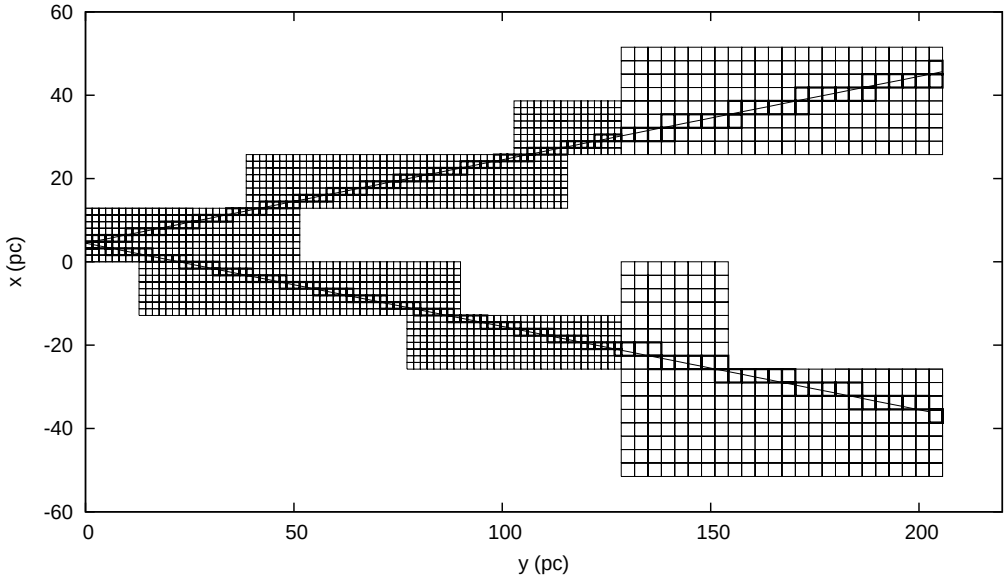

Figure 4.7: 2D projection of a ray tracing through a low-resolution AMR grid. Intersected cells have thicker borders.

where $\tau_{\nu,i}$ is the optical depth at frequency ν through cell i. The optical depth is calculated according to Spitzer (1978)

$$\tau_{\nu,i} = N_i \alpha \lambda \Phi(\nu), \tag{4.49}$$

where the frequency-integrated cross-section for the interaction (α) is given by $\alpha = 0.015924$ cm^2 s, N_i is the NaI column density, and the doppler profile $\Phi(\nu)$ is given by

$$\Phi(\nu) = \frac{1}{\sqrt{\pi} b} \exp(-v^2/b^2). \tag{4.50}$$

The optical depth is binned in 1000 bins, representing line of sight velocities of -500 through 500 km/s. Each optical depth bin is summed through a ray's path, and converted to intensity in the final step.

4.4.2.2 Sub-grid turbulence

In the simulations with sub-grid turbulence, the density and temperature recorded on the grid represent average values, and hot turbulent cells can still contain a component of cold gas. Isothermal compressible turbulence gives a lognormal density probability density function (PDF) (Vazquez-Semadeni 1994),

$$dP(s)/ds = \frac{1}{\sqrt{2\pi}\sigma_s} \exp\left[\frac{-(s-s_0)^2}{2\sigma_s^2}\right], \tag{4.51}$$

where $s = \ln(\rho)$, $s_0 = \ln(\rho_0)$ for a cell of average density ρ_0, and σ_s is the standard deviation of the distribution. It is not accurate to assume that gas in our models is isothermal at a sub-grid level due to the strong density dependence of the cooling rate, but it has been reported (Mac Low et al. 2005; Pavlovski et al. 2006) that the PDF remains close to lognormal even in a system with explicit heating and cooling, although there may be a power-law tail at low densities (which is not critical to this work, as we are primarily concerned with the densest structures).

Federrath et al. (2008) suggest that σ_s can be paramerised in terms of the Mach number $\mathcal{M}$ of the flow, and another factor b,

$$\sigma_s = \sqrt{\ln(1 + b^2\mathcal{M}^2)}. \tag{4.52}$$

This b depends on the nature of the turbulence. It has been found that $b \sim 1/3$ with purely solenoidal turbulence in both grid (Kritsuk et al. 2007; Beetz et al. 2008) and particle (Li et al. 2008) simulations. Federrath et al. (2008) find $b \sim 1$ for purely compressive turbulence, while confirming $b \sim 1/3$ for purely solenoidal turbulence — i.e. compressive turbulence produces a broader density PDF. Turbulence caused by the R-T instability should be primarily solenoidal with a compressive component largely resulting from further evolution, so we set $b = 1/3$. We also examine $b = 1$ to test the effects of a broader PDF, noting that the turbulence from supernovae should be primarily compressive, and that this is a better fit for turbulence directly induced by feedback.

The Mach number, $\mathcal{M}$, is defined as the ratio of the turbulent velocity to the sound speed, i.e. $\mathcal{M} = v_{\rm turb}/c_s$. The sound speed can be calculated from the pressure and density,

$$c_s = \sqrt{\gamma\frac{p}{\rho}}, \tag{4.53}$$

where for an ideal monoatomic gas the adiabatic constant is $\gamma = 5/3$, and $p = (\gamma - 1)\rho e_{\rm thermal}$, and so $c_s = \sqrt{(10/9)e_{\rm thermal}}$. The turbulent velocity $v_{\rm turb}$ can be represented by $v_{\rm turb} = \sqrt{2K_{\rm turb}}$, and so the Mach number can be written as

$$\mathcal{M}^2 = \frac{9}{5}\frac{K_{\rm turb}}{e_{\rm thermal}}, \tag{4.54}$$

or, because $K_{\rm turb} = f_{\rm turb}e_i$ and $e_{\rm thermal} = (1 - f_{\rm turb})e_i$,

$$\mathcal{M}^2 = \frac{9}{5}\frac{f_{\rm turb}}{1 - f_{\rm turb}}. \tag{4.55}$$

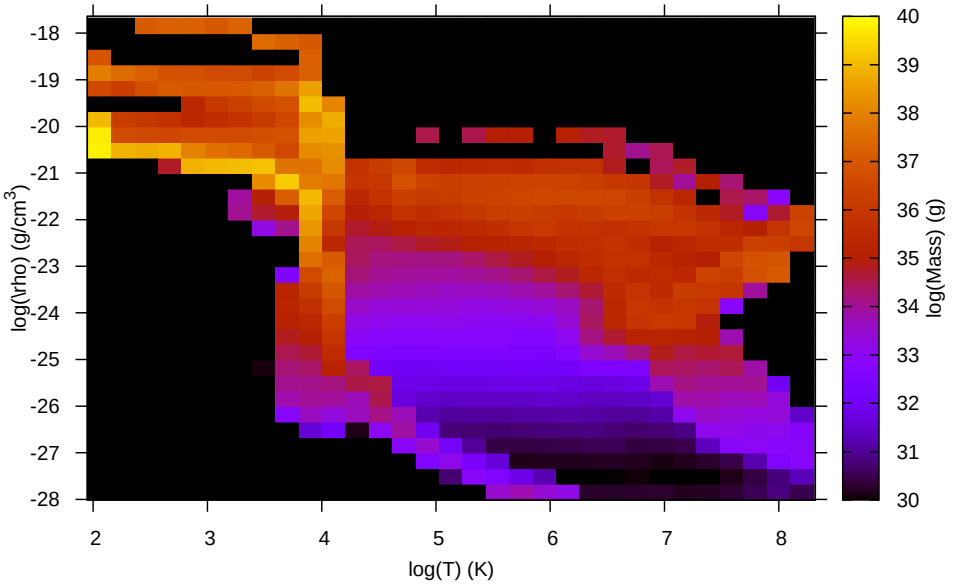

Figure 4.8: Temperature/density phase plot for SHighResNoTurb

This is convenient as the Mach number is now parametrised by a single variable $f_{\rm turb}$, which is directly calculated in our FLASH subroutines.

Although this PDF is for an isothermal distribution, we can assume that gas above a certain threshold density will rapidly cool to NaI absorbing temperatures. Fig.4.8 shows that much of the gas denser than 10^{-21}g/cm^3 has cooled dramatically. We therefore make the simple assumption that any gas above 10^{-21}g/cm^3 is cool enough to absorb the NaI doublet. Thus the fraction of absorbing gas in a cell with sub-grid turbulence is

$$f_{\rm NaI} = \int_{10^{-21}{\rm g/cm^3}}^{\infty} \frac{1}{\sqrt{2\pi}\sigma_s} \exp\left[\frac{-(s-s_0)^2}{2\sigma_s^2}\right] \quad (4.56)$$

$$= \frac{1}{2}{\rm erfc}\left[\log\left(\frac{10^{21}{\rm g/cm^3}}{\sqrt{2}\sigma_s}\right)\right], \quad (4.57)$$

where

$$\sigma_s = \sqrt{\ln\left(1+\frac{9}{5}b^2\frac{f_{\rm turb}}{1-f_{\rm turb}}\right)}. \quad (4.58)$$

4.4.2.3 Spatial and Spectral Resolution

The above procedure produces a line profile for an infinitely narrow beam passing through the system. This geometry represents the limit where an instrument can spatially resolve scales considerably smaller than the typical scale-lengths of any structures in the observed object.

As noted in Martin (2005), individual clouds are not spatially or spectrally resolved when using the Echelle Spectrograph and Imager on Keck II. To represent this finite spatial resolution, we create a grid of rays intersecting the grid at different points. We evaluate a single spectrum by averaging the spectral lines over all rays produced by this grid. Hence the final spectrum is not the spectrum of an infinitesimal beam, but is taken from a sample that covers a finite region of the galaxy, which better represents the finite spatial resolution of a real instrument. Specifically, the total spatial size of this grid is the effective spatial resolution. We found the qualities of the spectrum can vary strongly on this spatial resolution. Because the filling factor of dense clouds is small, at very high spatial resolution the grid of rays will generally either all pass through a cloud, or all entirely miss all clouds. This dramatic dichotomy will produce either a narrow saturated absorption line, or the complete absence of any absorption lines. At lower spatial resolutions the line strengths can be weak, because most of the rays will miss the cloud region entirely. However, at low resolution a large number of clouds are included within the simulated aperture, causing non-thermal

broadening in the sodium-line, as observed by Martin (2005). Martin's observations were Keck absorption-line studies, with the ULIRG galactic discs as the background light-source for the absorption.

The resolution in Martin (2005) is given as $\sim 1''$, which corresponds to a spatial resolution of ~ 2 kpc at a distance of $z \sim 0.1$. For our galaxy-centre models, this is larger than our entire simulated domain, and so the best approximation is to reduce our spatial resolution to be equal to the size of the entire simulated domain, i.e. 200 pc. In the full galaxy models, our smallest cells are 250 pc in size, and a ~ 2 kpc spatial resolution is equal to only ~ 8 cell-widths. While ~ 8 cells may be sufficiently large to resolve the entirety of a small clump, it is not sufficient to resolve a large number of clumps and produce the observed non-thermal broadening. However, if we assume that the filling factor and velocity dispersion of dense NaI-absorbing clouds do not depend strongly on scale, then we should expect the absorption spectrum of a real galaxy to not strongly depend on spatial resolution, and we can justifiably reduce the spatial resolution in our simulated spectra from ~ 2 kpc to a much larger value, and hence observe a significant number of clumps in our spectra. The assumption of scale-independence is not unreasonable, as these clouds are produced by turbulent motions, and the statistics of turbulence do not depend strongly on scale.

We have plotted the effects of varying the spatial resolution on the line profile of BHighResNoTurb in Fig. 4.9 for a ray of altitude 45° and azimuth 45°. For the range $80 - 120$ kpc, all of the NaI absorbing gas is within the beam. At these low spatial resolutions, changing the resolution does not change the line profile shape, but only changes the strength of the line, as more rays "miss" the NaI absorbing regions entirely. The line-depth here is proportional to $1/l^2$ where l is the spatial resolution. As l drops further (e.g. 40 kpc and below), the line not only strengthens, but noticeably changes its shape. However, this is strongly dependent on the ray's path — as noted above, for narrow beams the ray generally either hits one clump, or misses every clump. This sensitivity is not the case for broader spatial resolutions, and so we choose 100 kpc as our spatial resolution. The strength of the line is still strongly

resolution dependent in this regime, and so we should not consider the line-strength to be comparable to observations. However, the velocity-width and velocity at line centre should not be affected by these issues (given the assumption of only weak scale-dependence), and these are the properties that we emphasize for comparison with observation.

We also removed the circular component of velocity before calculating the line profiles, as at low spatial resolution this can be a source of velocity dispersion. At later times, much of the rotation is no longer coherent (e.g. Fig. 4.10), but some residual rotational velocity remains. We bin the mass and horizontal angular momentum of each cell into annuli 2 kpc thick and 2 kpc tall to produce a set of rotation curves (an averaged rotation curve is shown in Fig. 4.11). The rotational velocity of each cell is then calculated with a simple 2-parameter linear interpolation from this table and subtracted from the cell.

We also found the shape of the spectrum depended weakly on the number of rays produced by the grid. For a small number of rays (e.g. 32×32), the produced spectrum was jagged and did not show the smooth shape produced when a larger number of rays (e.g. 512×512) were used (Fig. 4.12, left). We found that the line was fairly well converged for an $L \times L$ grid for $L > 64$ (Fig. 4.12, right). We hence used a 128×128 grid of rays as it was slightly more accurate and still computationally efficient.

Our method for incorporating finite spatial resolution incorporates a number of assumptions, which we list here. Given the low resolution of our simulations, we do not believe it is necessary to model these effects in detail. Firstly, we have assumed uniform background illumination by weighting our grid of rays evenly when performing an average. It would be more accurate to give greater weight to rays that originate in more luminous regions. A more detailed weighting would put more weight in the bright central regions, which could have an effect on the output spectra if the absorbing clouds have a radial dependence.

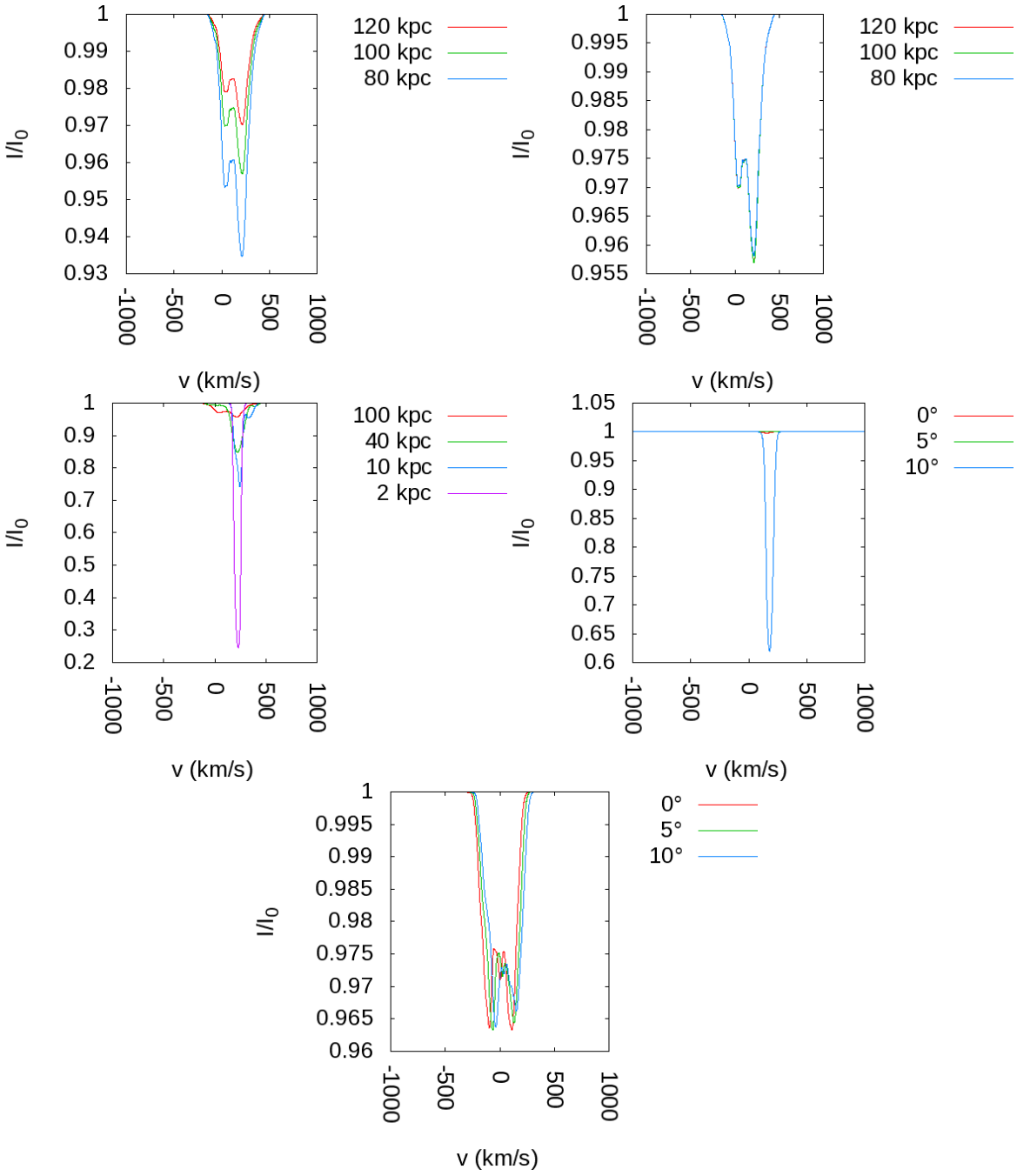

Figure 4.9: Examining the effect of spatial resolution on line profiles. Top left: Lines with spatial resolutions of $80 - 120$ kpc. Top right: Lines with spatial resolutions of $80 - 120$ kpc, normalized according to $1/l^2$, where l is the spatial resolution. This plot demonstrates there is no significant deviation between the line shapes. Centre left: Lines with spatial resolutions of $2 - 100$ kpc. Centre right: 2 kpc spatial resolution line at three different altitudes. Bottom: 100 kpc spatial resolution line at three different altitudes.

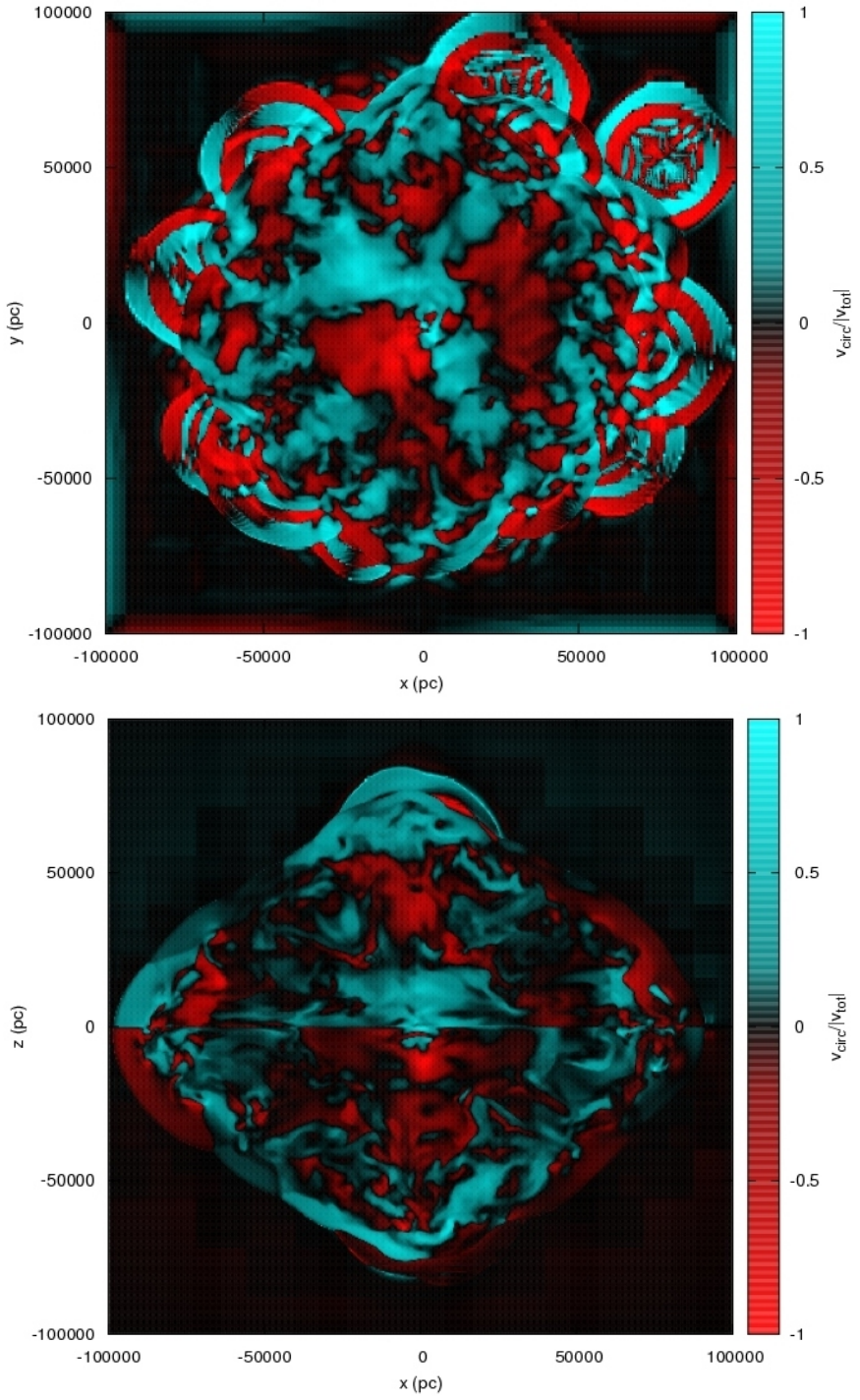

Figure 4.10: Slices of circular velocity divided by total velocity for each cell. Top: Slice through plane of disc ($y = 0$). Bottom: Horizontal slice ($z = 0$). While "positive" rotation is slightly more prominent, the overall structure is turbulent. Erroneous values at the edge of the domain are caused by rounding errors where velocities are small (i.e. a small circular velocity is divided by a small total velocity).

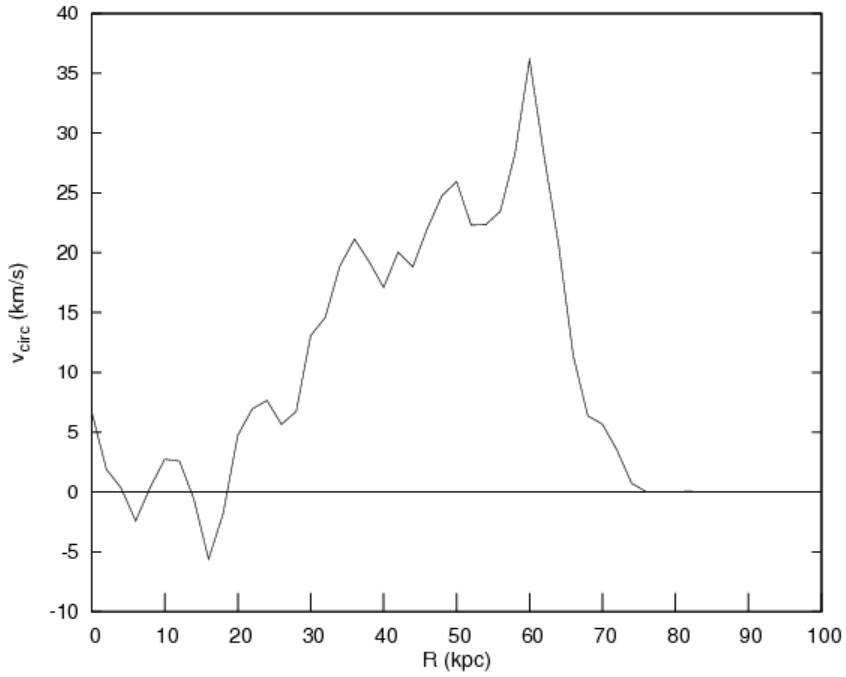

Figure 4.11: Rotation curve for run BHighResNoTurb at $t = 100$ Myr.

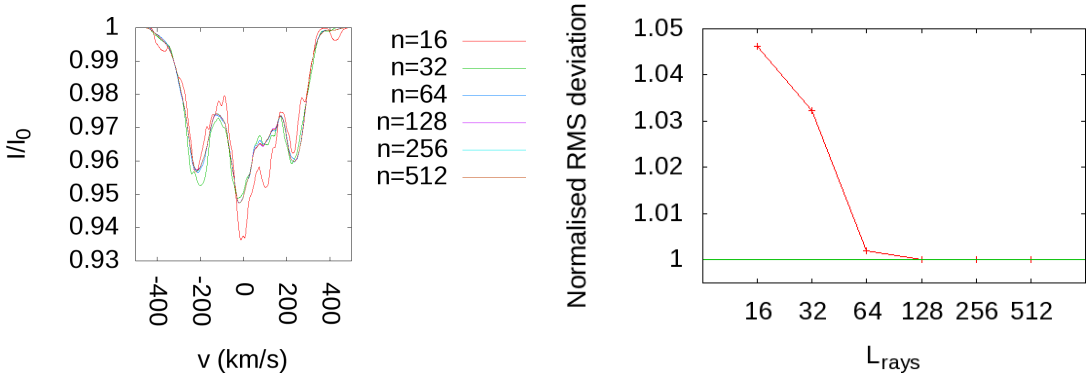

Figure 4.12: Varying the number of rays fired through the grid, from 16×16 to 512×512. Left: line shape. Right: Root-mean-squared deviation from $I = 1$ across each line, normalised so that this is equal to 1 for a 512×512 grid.

Secondly, we have not accounted for dust, which has a significant effect in ULIRGs. Dust attenuates radiation, often in a spatially complex manner. This may also affect the observed spectra, but it is difficult to predict what these effects would be.

Finally, we have ignored any spatial broadening from the Earth's atmosphere or from the instrument. Here, the smearing w ould also be radially dependent. These effects are too fine to be incorporated into our relatively simple model, but should be considered in more detail as resolution and physical complexity increases.

To represent finite *spectral* resolution, we can convolve the output line profile with a Gaussian curve. However, this is computationally expensive, as the convolution

$$I_{\text{smooth}}(v) = \int_{v_{\min}}^{v_{\max}} I(v') \frac{1}{\sigma\sqrt{\pi}} \exp\left(\frac{(v-v')^2}{\sigma^2}\right) dv', \tag{4.59}$$

(where the standard deviation σ is a instrument-dependent parameter that represents the size of the broadening) is discretised as

$$\forall i \in [0, N) : I(v_i) = \sum_{j}^{N} I(v_j) \frac{1}{\sigma\sqrt{\pi}} \exp\left(\frac{(v_i - v_j)^2}{\sigma^2}\right) \tag{4.60}$$

which is an $O(N^2)$ operation. With 128×128 rays and $N = 1000$ intensity bins, this requires 1.6×10^{10} calculations. To reduce this computational load, we make use of the convolution theorem. If we represent the Gaussian curve with $G(v)$, then the smoothed line profile is $I(v) * G(v)$, where $*$ represents a convolution. If we let $\mathcal{F}$ represent the Fourier transform (and $\mathcal{F}^{-1}$ its inverse), then the convolution theorem states that

$$I(v) * G(v) = \mathcal{F}^{-1}\{\mathcal{F}\{I(v)\} \cdot \mathcal{F}\{G(v)\}\}. \tag{4.61}$$

This is less computationally expensive, as we can use a "fast-Fourier transform" (FFT) (Cooley & Tukey 1965; Brigham 1988). We make use of the *Fastest Fourier Transform in the West* (FFTW) library(Frigo & Johnson 2012). FFTW adapts its algorithm according to the size, dimensionality, and field (whether complex or strictly

real) of the Fourier transform, and so performs very well across many applications. Making use of this algorithm allows us to perform this convolution without excessive computational load.

4.4.3 Clump finding and tracking

To determine the properties of the cold clumps of NaI-absorbing gas produced in these simulations, we developed an algorithm to identify, track, and plot them. The basic assumption of this algorithm is that all cells of sufficiently low temperature or high density are "clumpy" cells, and that any cell that is orthogonally adjacent to another cell (i.e. a cell that share face with another cell) is labelled as part of the same clump — i.e. any contiguous region of Na-absorbing gas is considered a single clump, regardless of the shape or density profile of the region, even if it contains many over-dense "cores". This assumption is equivalent to a "flood fill" algorithm, and is less complex than the Friends of Friends algorithm used in Chapter 3, as is it straightforward to find which cells neighbour a region, and it is not necessary to calculate the distances between a large number of particles. The clump finding algorithm performs the following steps:

1. All cells that were above our density threshold or below our temperature threshold for Na absorption (10^{-21}g/cm^3 and 5×10^4 K respectively) are identified. A list of these "cold" cells is recorded for each $8 \times 8 \times 8$ block of cells. (As mentioned above, FLASH divides the system into blocks of $8 \times 8 \times 8$ cells, and lists "links" to neighbouring blocks for filling the boundary conditions on each block).

2. The algorithm sweeps through each block in this list of cold cells. Each cell has from three to six orthogonal neighbours within the block, depending on whether the cell is in the centre of the block or on a face, edge, or corner of the block. These orthogonal neighbours are queried, to determine if any are "cold" blocks, and whether they already belong to a clump. We refer to the cell

whose neighbours we are finding as "current" cell. If the current cell and the neighbouring cell are both "cold" blocks, then the following logic is followed to determine how to join these blocks into a single clump

- If both the current cell and the other cell do not already belong to a clump, then create a new clump containing these two cells. A linked list is created, where the current cell points to the other cell, and the "head" and the "tail" of this linked list are recorded — in this case, the "head" is the current cell, and the "tail" is the other cell. The clump number for each of the two cells is also recorded in an array, so that it is straightforward for neighbouring cells to determine what clump each cell belongs to.
- If exactly one of the two cells belongs to the clump, then the other cell joins that clump. The clump array entry for the other cell is updated to the correct clump number. The linked list is updated — the previous "tail" cell is modified to point to the new cell, and the "tail" of the linked list is now the new cell.
- If both cells belong to a clump, then these clumps must be merged. This process is efficient due to the linked list structure — by propagating through the linked list, we can find all cells throughout the domain that belong to a clump, and update them to the new clump. The tail of one linked list is updated to point towards the head of the other linked list. This is a fast and memory-efficient method for combining clumps. One of the clumps must also be deleted. All clumps have sequential identification numbers, and to avoid any "holes" in this array, the identification number for the last clump in this array is swapped with the clump that must be deleted (propagating through the linked list to update all cells), and the number of clumps is decremented by one.

Once all cells within each block are properly linked into clumps, comparisons of cells between blocks are performed to link clumps that touch across a block face.

This linking the procedure outlined above for cell, although only the cells on the face of each block are considered, and because blocks can have different refinement levels, adjacent cells can differ in size by a factor of two, and so the larger cell will have four neighbours per face.

To track clumps between data dumps, we are not able to reuse the method detailed in Chapter. 3, as this is an Eulerian calculation, and unlike a Lagrangian particle code, we can not easily track the history of a parcel of mass. Instead we use a method similar to that used by Tasker & Tan (2009). For each clump, the centre-of-mass position and velocity were calculated. These values were used to predict the position of the clump in the following dump, i.e. if the positions and velocities in successive files $\boldsymbol{v}_i, \boldsymbol{r}_i$ and $\boldsymbol{v}_{i+1}, \boldsymbol{r}_{i+1}$ are separated by a time Δt, the estimated position is

$$\boldsymbol{r}_{\rm est} = \boldsymbol{r}_i + \boldsymbol{v}_i \Delta t. \tag{4.62}$$

The clump closest to this position (i.e. the clump which corresponds to the minimum of $||\boldsymbol{r}_i - \boldsymbol{r}_{i+1}||$) is identified as the "same clump". In our full galaxy simulations, dumps are performed every 5 Myr, while in our central scale simulations, dumps are performed every 10 kyr, and these values are used for our time-step here. These values were selected so that 10–20 dumps were produced for each simulation.

By repeating this cloud identification procedure over several dumps we can track the history of each clump, determining whether it is being significantly slowed by drag and ram pressure, and whether it is losing mass due to the impact of hot winds, or gaining mass as fluid cools and accretes. To test this process, we produced animations tracking a sample of clouds, and did not observe any unexpected discontinuities.

4.5 Analysis

4.5.1 Line fitting

Having produced line profiles over a large range of angles for a series of parameters, we can fit a Gaussian to the result and estimate the line-width for comparison

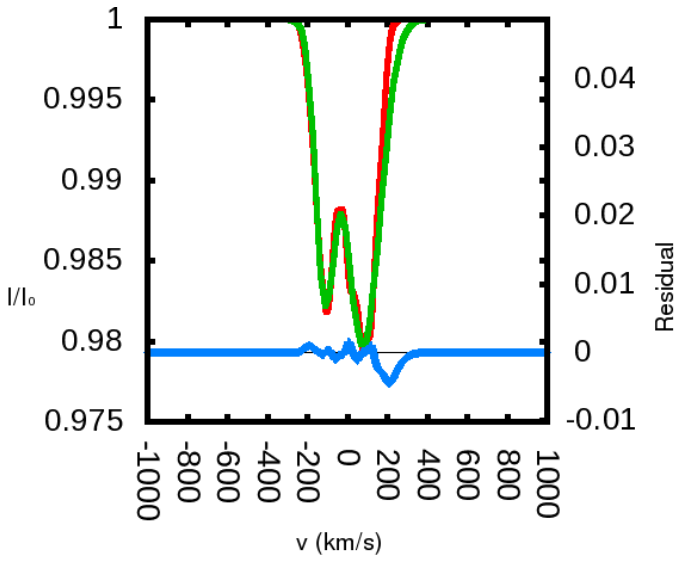

Figure 4.13: Edge-on line profile for the simulation BHighResNoTurb, demonstrating a double-peak. The red line is the line profile, while the green line is a Gaussian fit, both described the y-axis labels on the left of the plot. The blue line is the residual, described by the y-axis labels on the right of the plot. The x-axis is velocity in km/s.

with Martin (2005). This was performed with a standard χ^2 fit. To ensure the line-centres were well-fit, we reduced the weight of wavelengths with zero NaI opacity (i.e. $I = 1$), by weighting each point in the line according to $W = (1.0001 - I)^2$, where the value of 1.0001 is used instead of 1.0 prevent divide-by-zero errors. This weighting improved our algorithm's ability to correctly fit the width and strength of each line.

In edge-on orientations, a strong double-peak is visible (Fig. 4.13). These two peaks have a similar velocity relative to the rest frame of the galaxy (i.e. the peaks at are $\pm v_0$ for some v_0) and are clearly distinct in the line profile. However, the clumpy nature of the outflow can produce several peaks in the line that do not correspond to distinct outflow components — they are merely part of the velocity dispersion *within* the outflow, and should be modelled by a single broad Gaussian. To automatically capture both cases, we perform two fits on each line — one with a single Gaussian curve, and one with two Gaussian curves, both of whose parameters are allowed to vary freely. To determine which fit is most appropriate, we examine

the fit parameters. If the two Gaussians have a similar velocity at line centre — where "similar" is defined by $||v_1| - |v_2||/(|v_1| + |v_2|) < 0.5$ — then the double-peak fit is used. Otherwise, the single-line fit is used. In the double-peak case, the parameters of each peak (FWHM, line-centre velocity, line-strength) are averaged to produce one set of parameters for each spectrum.

4.5.2 Predicting cloud trajectories

In some cases we predict the trajectory of clouds using the ballistic approximation. The gravity field is produced from the subroutine used by FLASH to produce its table of gravitational accelerations during a simulation's initialization. The initial position and velocity of each cloud is calculated from the FLASH output by the algorithm detailed above. The cloud's position and velocity are integrated using a form of the leapfrog algorithm:

$$x_{i+1} = x_i + v_i \Delta t + \frac{1}{2} a_i \Delta t^2 \tag{4.63}$$

$$v_{i+1} = v_i + \frac{1}{2}(a_i + a_{i+1}) \Delta t. \tag{4.64}$$

with a fixed time-step. It is also possible to produce an analytic expression for the speed of the clump over time as in Fujita et al. (2009), by relating the potential at the end of the simulation ϕ_i, the potential at some more distant equipotential surface ϕ_f, and the speed of the clump at these points (v_i and v_f) through

$$v_f = \sqrt{v_i^2 + 2(\phi_i + \phi_f)}, \tag{4.65}$$

but we perform the numerical integration in order to also calculate the vector components of the velocity.

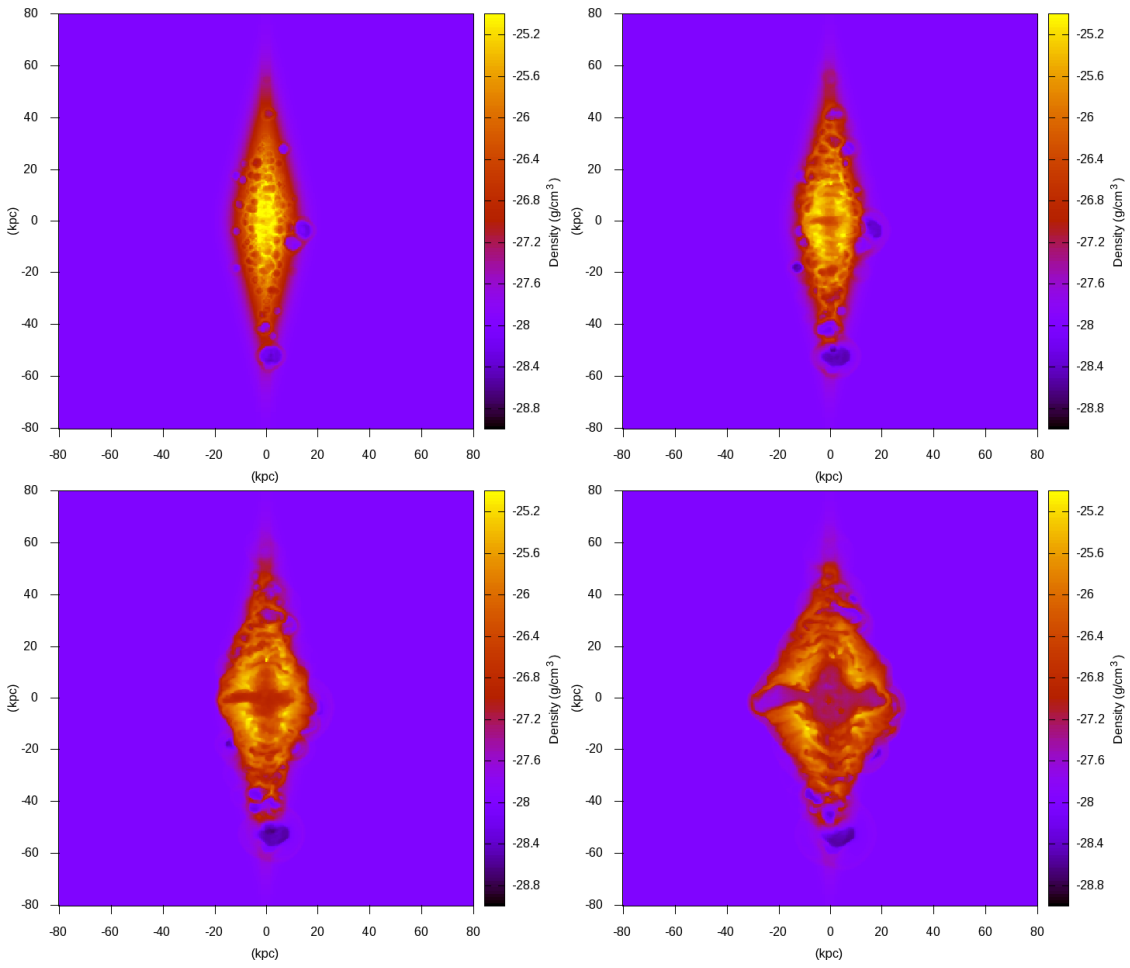

Figure 4.14: Edge-on slices of BHighResNoTurb at $t = 10, 20, 30, 40$ Myr.

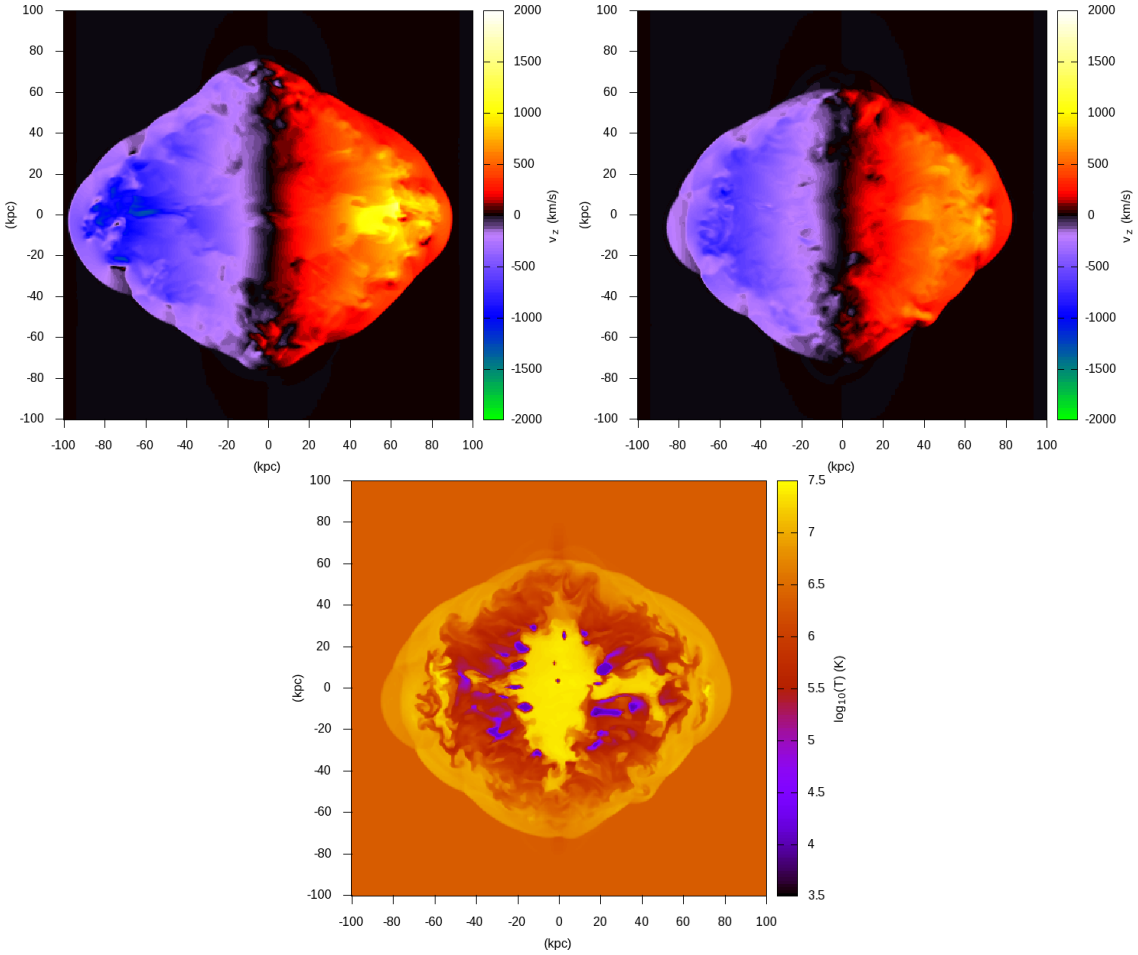

Figure 4.15: Vertical velocity slices of BHighResNoTurb at $t = 100$ Myr at $x = 0$ kpc (above, left), and $x = 20$ kpc (above, right). A temperature slice at $x = 20$ kpc is also given (bottom) to show the positions of clumps.

4.6 Results

4.6.1 Full Galaxy Models

4.6.1.1 General Evolution

In all model, the bubbles very quickly combine to form a single coherent outflow (See Fig. 4.14 for example). Although feedback is spread throughout the disc, and all of the disc gas has a large vertical velocity, the flow is strongest near the centre (Fig. 4.15). As almost all of the disc gas is incorporated into the outflow, the outflow front is very dense. This cool, dense front is followed by a hot low-density medium which has been directly heated by feedback. In some of the simulations, cool clumps are carried with the wind, while in others the interior of the wind remains hot. Column density plots of BHighResNoTurb in Fig. 4.16 illustrate these clumps. The origin of these clumps does not appear to be the Rayleigh-Taylor instability acting on the cold front of the super-bubble, as we detail in the following subsection.

4.6.1.2 Formation and evolution of clumps

The evolution of the number of clumps in these models is plotted in Fig. 4.17. Both models with sub-grid turbulence and BMedResNoTurb show an initial peak in clump formation, which is extinguished within 40 Myr. BMedResNoTurb then forms additional clumps at 60 Myr, and while BHighResNoTurb also shows an initial peak, it manages to maintain a large number of clumps through the simulation. The reason for this is apparent if we track the positions of this cold gas, as shown in Fig. 4.18. The disc initially cools, producing a large quantity of Na-absorbing gas. Feedback bubbles divide this gas into discrete regions, causing a large number of separate clumps of cool gas to be detected. In all models except BHighResNoTurb, the feedback fills the entire disc with hot gas, destroying all of the cold gas regions. However, in BHighResNoTurb, the cold clumps are not destroyed, and instead are pushed out of the disc by the hot winds, forming the cold high-velocity-dispersion component of the wind while continuing to accrete cooling gas from the surrounding hot wind. These

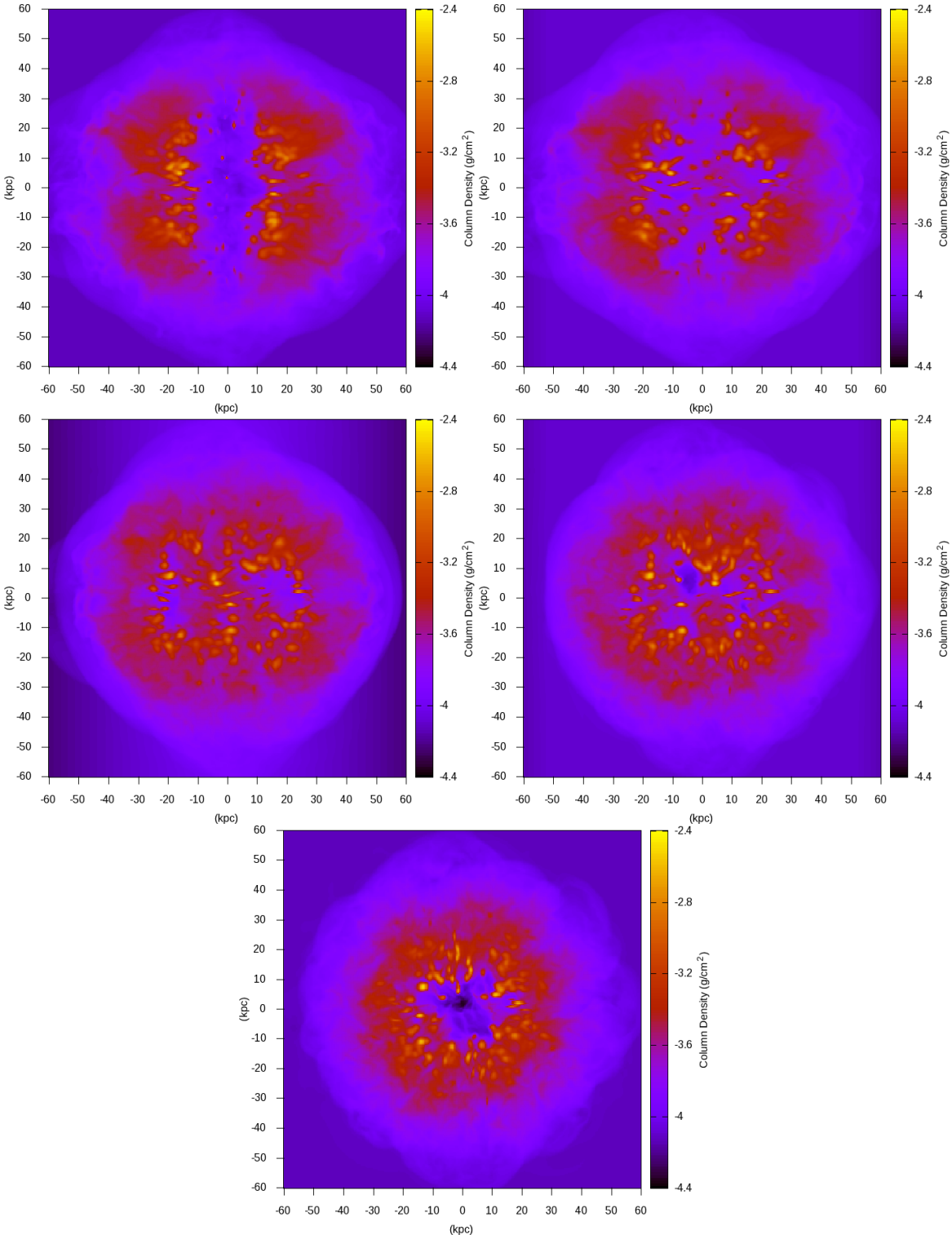

Figure 4.16: Density ray-trace plots of BHighResNoTurb at $t = 100$ Myr with altitudes in 22.5° intervals. Top left: $\phi = 0°$, i.e. an edge-on view. Top right: $\phi = 22.5°$. Centre left: $\phi = 45°$. Centre right: $\phi = 67.5°$. Bottom: $\phi = 90°$, i.e. a face-on view.

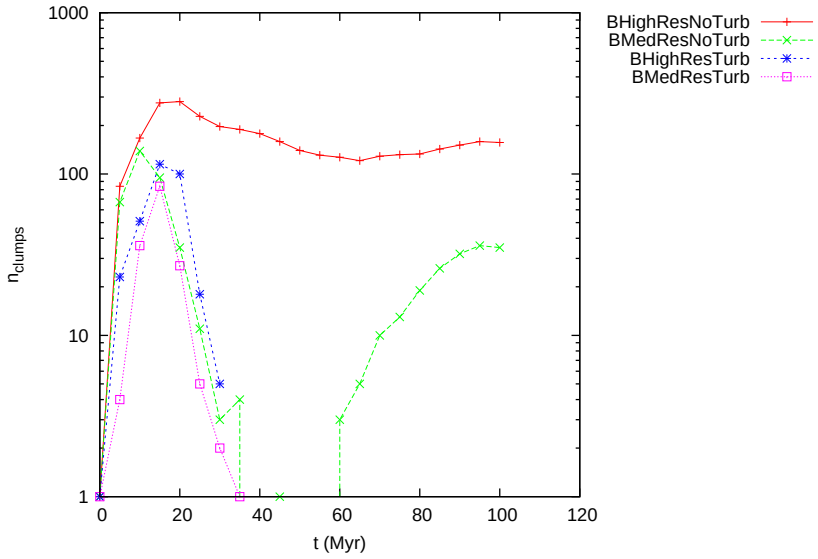

Figure 4.17: Number of clumps in full galaxy models.

cool regions can only form above and below the plane of the disc, as the feedback is too intense in the plane to allow any cold gas to exist. In BMedResNoTurb there is also a cold high-velocity dispersion component in the wind, but this is caused solely by gas cooling within the wind. This cooling is allowed because the starburst has completed, and because the hot gas is now free to adiabatically expand into the regions above the disc.

Hence, contrary to the findings of Fujita et al. (2009) where cold gas is produced in Rayleigh-Taylor induced break-up of a cold bubble wall, the cold gas in BHighResNoTurb is produced by the cool regions between hot bubbles being pushed out of the disc by the pressure of the hot outflow beneath them, while the cold gas in both BMedResNoTurb and further cold gas in BHighResNoTurb is produced by cooling in the outflow itself.

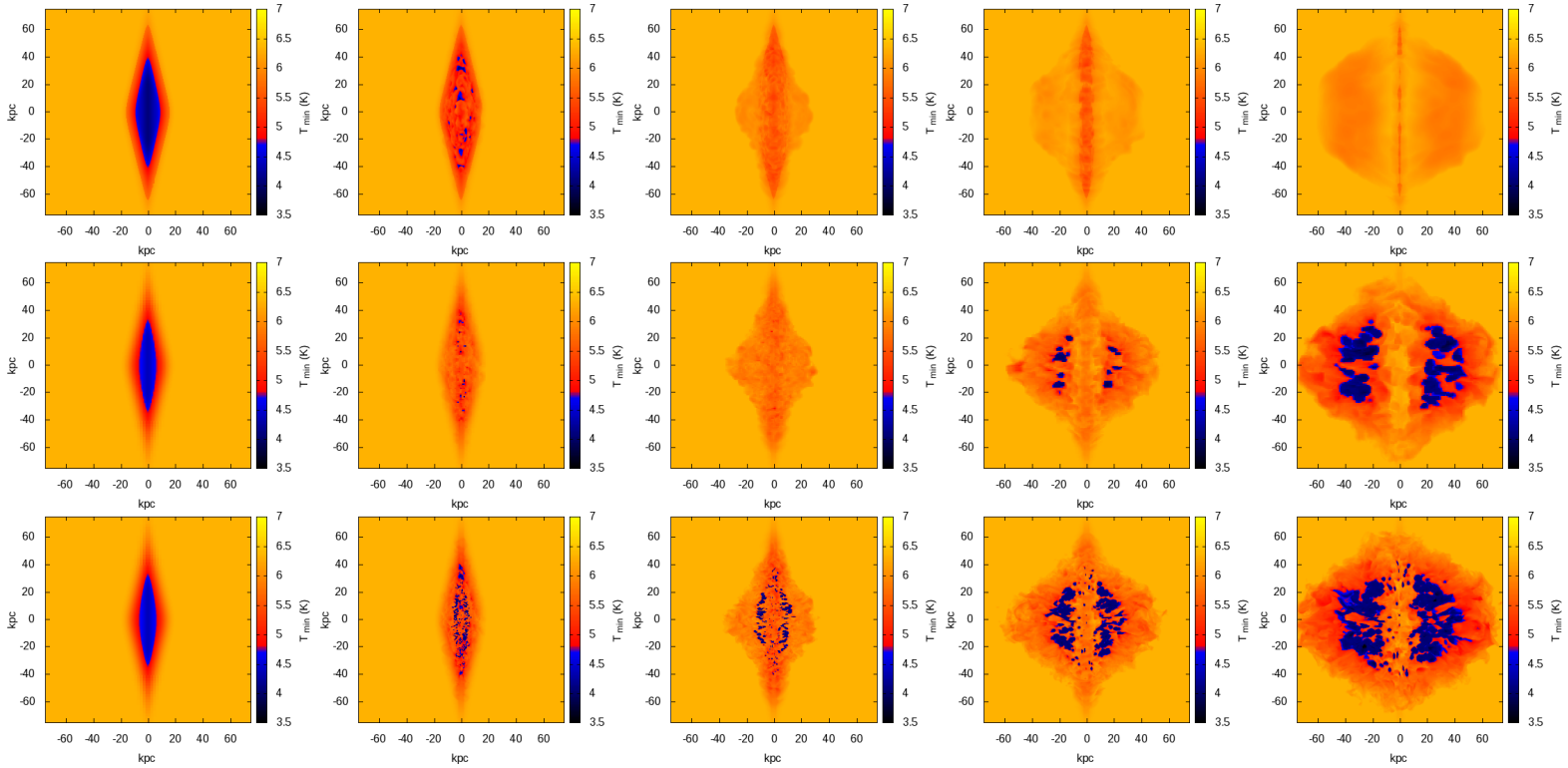

Figure 4.18: Evolution of cold gas in BHighResTurb (top), BMedResNoTurb (centre), and BHighResNoTurb (bottom), in snapshots at $t = 0, 25, 50, 75, 100$ Myr (left to right). These plots show the temperature of the coldest gas of all cells along the line of sight (the z direction), and hence the proximity of clouds is exaggerated. The colour scheme has also been chosen to distinguish the $T < 5 \times 10^4$ K gas which will produce NaI absorption.

The inclusion of sub-grid turbulence suppresses the formation and survival of clumps. Similarly to the models without sub-grid turbulence, the early peak in clump number is due to the cooling disc being fragmented by hot bubbles, until these hot bubbles fill the entire disc. The turbulent kinetic energy is a reservoir of non-thermal energy that is not subject to radiative cooling, and this turbulent energy continues to cascade into thermal energy as the outflow continues, supporting a high temperature in the outflow. As a result, there are no cells that explicitly contain cold gas by the end of the simulations.

The formation of cold clumps of gas in these simulations is resolution dependent, and so even in our highest resolution model without subgrid turbulence (BHighResNoTurb) only a small number (~ 150) of these clumps form by the end of our simulation time, as visible in a ray-traced column-density plot (Fig. 4.16). A 2D slice through the disc of this model (Fig. 4.19, top left) does not show this structure — only one clump is visible near the centre. This lack of clumps suggests that the additional avenues for gas flow permitted in 3D simulations inhibit the formation of these clumps. The number and mass of these clumps depends on resolution, with fewer clumps forming at lower resolution. As the mass spectrum plots in Fig. 4.20 demonstrate, the clumps at higher resolution are also more massive, possibly because we can resolve higher densities, and hence cooling instabilities are more dramatic, but also because these clumps have formed at an earlier time from a denser medium (i.e. the disc rather than the outflow).

We can calculate the escape velocities of these clouds using $v_{\rm escape} = \sqrt{2\phi}$, where ϕ is the gravitational potential given by Flash's subroutines — i.e. $d\boldsymbol{v}/dt = \nabla\phi$. Most of the clouds have exceeded the escape velocities at their positions (Fig. 4.21). Making use of the ballistic approximation detailed above, there is very little change in each cloud's velocity over a period of 100 Myr, as also shown in Fig. 4.21. Taking this at face value (i.e. ignoring hydrodynamics), this implies that most of the cold gas will not eventually rain back onto the disc as a "galactic fountain", but will instead continue outwards and enrich the intergalactic medium.

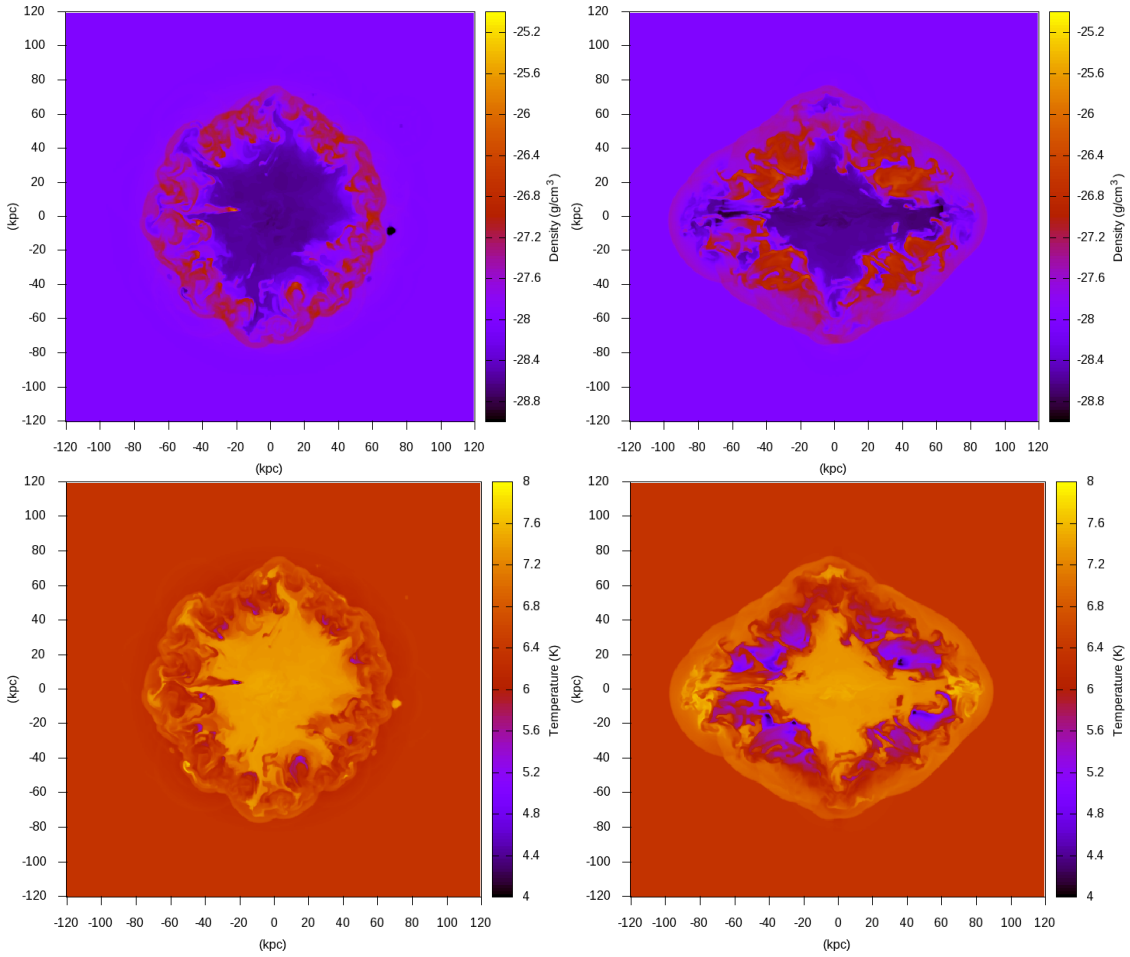

Figure 4.19: Face-on (left) and edge-on (right) slices of density (top) and temperature (bottom) for BHighResNoTurb at $t = 100$ Myr.

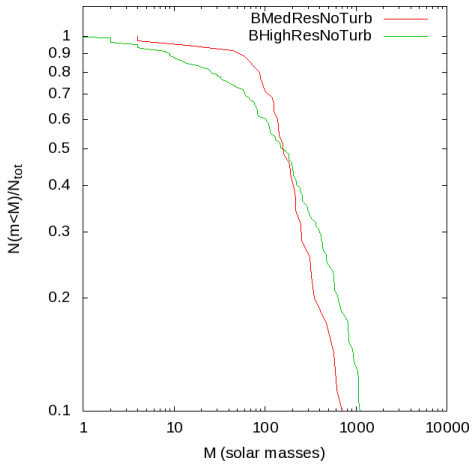

Figure 4.20: Cumulative mass spectra for BHighResNoTurb and BMedResNoTurb.

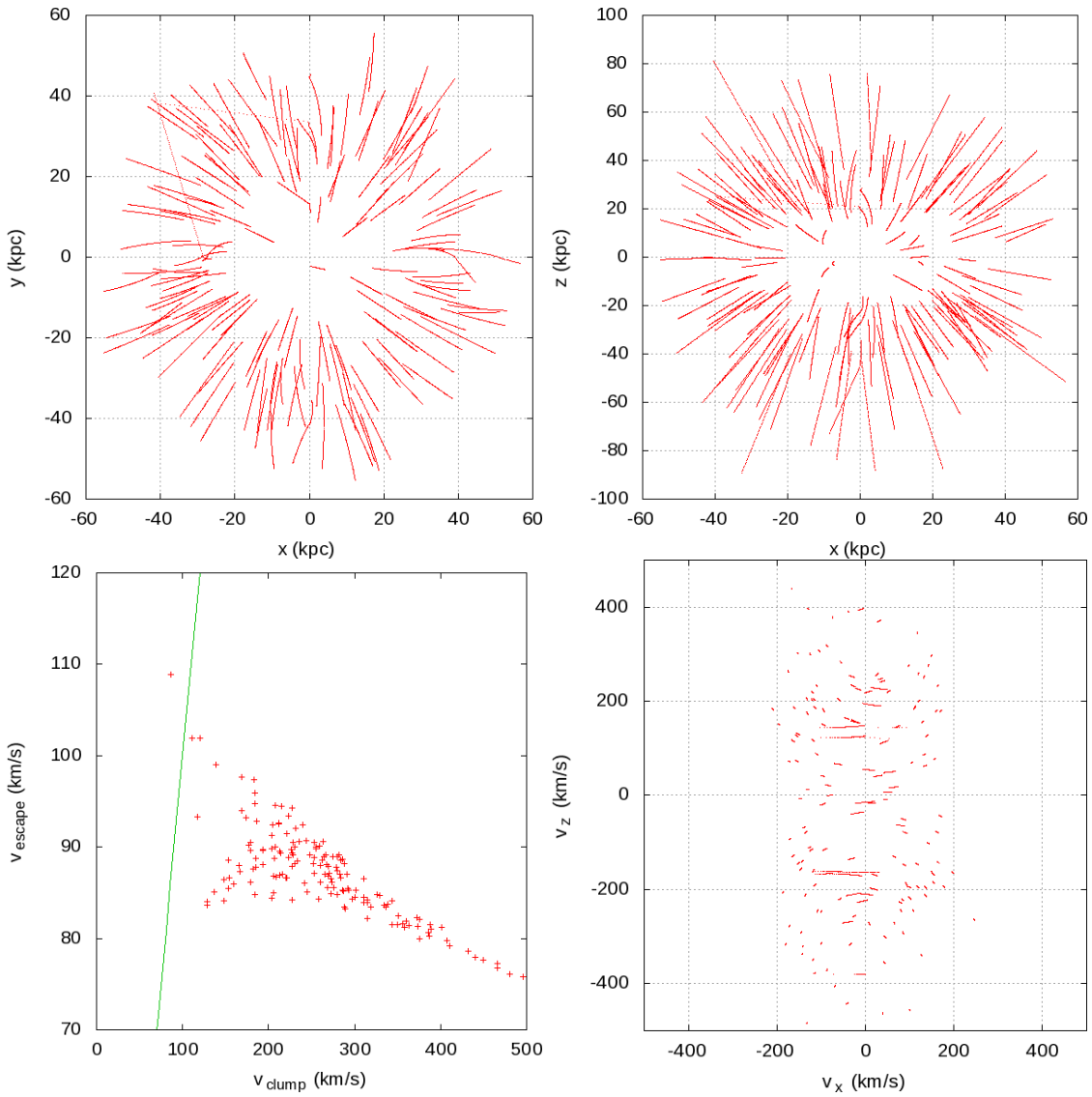

Figure 4.21: Top: Face-on (left) and edge-on (right) plots of the predicted trajectories for all clumps in BHighResNoTurb. Bottom-left: Escape velocities and net velocities for all clumps. The line indicates where $v_{\rm escape} = v_{clump}$. Bottom-right: Velocity space trajectories for all clumps. The clumps do not decelerate significantly over 100 Myr.

The next question is whether we might expect hydrodynamic effects to dissolve the clouds instead. We can estimate this effect by examining the history of the clumps, to see if they have begun to lose mass. The mass history of a sample of clumps is plotted in Fig. 4.22 (left panel), and it is clear that at the end of the simulation the clumps are still *gaining* mass, as additional gas is cooling and being accreted. The continual increase in clump mass fits the overall trend of cold gas plotted in Fig. 4.23 (where we have defined "cold" gas cells to be cells that would be considering Na-absorbing according to our treatment in section 4.4.2). The large density of gas ejected from the galaxy permits efficient cooling, catalysing clump-forming instabilities.

However, even though the clumps are gaining mass, they are still in the process of dissolving into the intergalactic medium. The top-left and top-right panels of Fig. 4.22 show that after $\sim$ 25 Myr, the clumps are gaining volume more rapidly than they are gaining mass — in fact, the mean density of each clump is dropping exponentially (as shown in the bottom panel of Fig. 4.22). If this continues, we would expect the clumps to reach the background density of $10^{-29}\mathrm{g/cm}^3$ in only $\sim$ 250 Myr, and will likely be disrupted by hot flows well before then. Hence we should not expect these clouds to remain coherent as they rise to large distances from the disc. Martin (2006) observed that NaI absorption extends out to distances of around 4–18 kpc. Although the hot outflows in BHighResNoTurb extend much further than this, out to almost 100 kpc, the cold clumps are closer to the disc, agreeing with this result.

However, x-ray emission maps from Chandra surveys (Ptak et al. 2003) only reveal hot gas at scales of $\sim$ 10 kpc, much closer to the disc — either the hot gas at large altitudes must be currently undetectable in x-ray wavelengths (perhaps it is not dense enough), or our outflows are too energetic. We propose two possible explanations for this discrepancy.

Firstly, our limited resolution does not permit us to model the detailed structure of the interaction between hot bubbles and cool gas in the disc, and hence instead of hot under-dense gas escaping through narrow avenues, almost the entire gaseous mass of the disc is propelled outwards, providing a large reservoir of momentum to

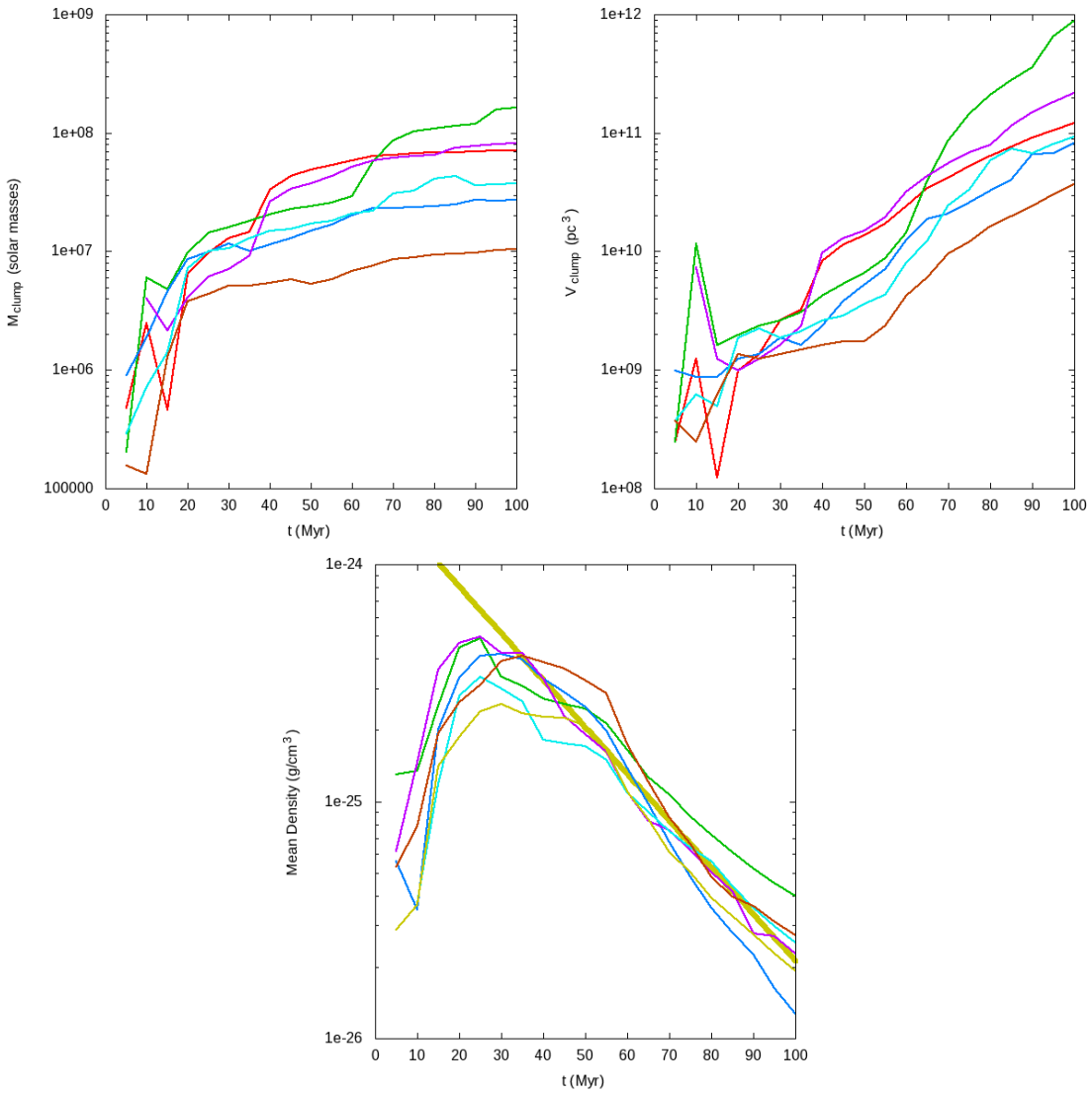

Figure 4.22: The histories of a sample of clumps in BHighResNoTurb. Top left: Mass history. Top right: Volume history. Bottom: Mean density (i.e. mass/volume) history. The thick line is $2 \times 10^{-24} \exp(-t/22\text{Myr})$ g/cm^3.

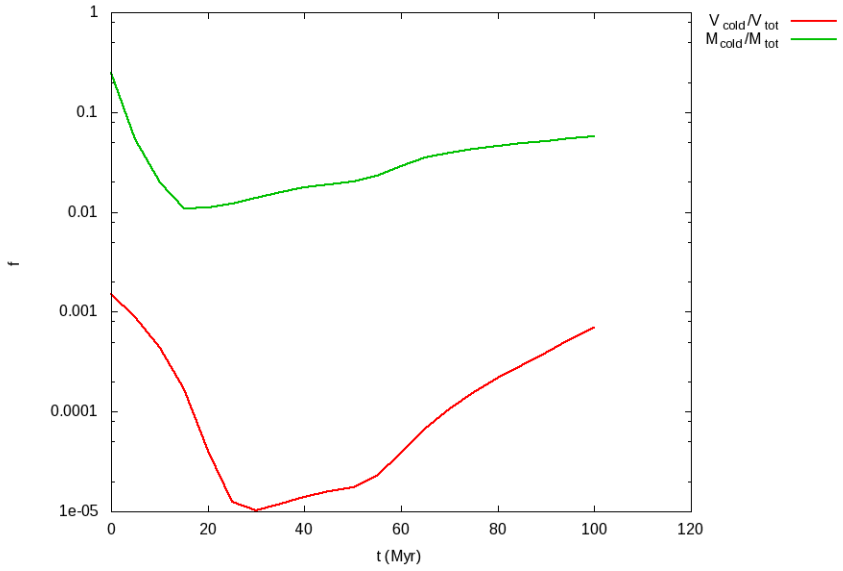

Figure 4.23: The evolution of the mass fraction and volume fraction of cold gas in BHighResNoTurb.

plough through the halo. This unrealistically powerful flow might be exacerbated by our stochastic feedback mechanism, which is not entirely consistent with realistic star formation, especially as resolution limits force a lower limit on the size of hot bubbles — e.g. a hot bubble is likely to be placed directly on top of an existing hot bubble, even though star formation is unlikely in such a hot low-density environment.

Our second explanation is that our halo model lacks density contrasts, and that a more detailed model of the gaseous halo will provide additional impediments to hot outflowing gas.

4.6.1.3 Simulated spectra: Models without sub-grid turbulence

Using our raytracing code, we have produced a suite of NaI lines at various viewing angles and with various parameters. In figures 4.24 and 4.25 we have plotted lines for BHighResNoTurb at viewing angles with altitude intervals of 10°. These plots are for a single NaI line, and do not include instrumental broadening. Absorption

lines from the disc are not visible as the disc does not retain any cold gas in this simulation.

It is clear from these plots that there is substantial broadening in the outflow. If we remove the thermal contribution to the broadening, replacing each Gaussian line profile with a top-hat function with width equal to our spectral resolution (our best approximation to the Dirac delta function), then this broadening is still present (Fig. 4.26), showing that this broadening is non-thermal. This plot in itself confirms that instabilites in outflows can produce cold gas with large non-thermal broadening.

Fig. 4.27 shows the line-centre outflow velocity as a function of viewing angle. The trend is closely modelled by an absolute sine function, which demonstrates that the outflow appears to be a single coherent flow. This is not surprising as our spatial resolution is essentially the entire disc, and so any small-scale deviations will be smoothed out. There is also no significant variation with azimuthal angle. This result is consistent with the line-widths below, and so we can conclude that on a broad scale, this model is azimuthally symmetric. Note that this does not necessarily justify the accuracy of two-dimensional simulations: on smaller scales (i.e. not summing over the entire galaxy), non-axisymmetric instabilities and flows are still dominant, as is clear in Fig. 4.10.

These outflow velocities are significantly smaller than the average observed by Martin (2005) of 330 ± 100 km/s. Our maximum (i.e. face-on) outflow velocity is 240 km/s, which (just barely) agrees with Martin's result, but at any other angle our outflow velocities are slower. The cause may be simply that our star formation rate is smaller than a typical ULIRG, or that we have neglected the significant energy impact from an AGN. However, there is also a significant scatter in the relationship between star formation rate and outflow velocity (Martin 2005), and indeed there are observed ULIRGs with star formation rates of ~ 300 $M_\odot$/yr with outflow velocities of ~ 100 km/s. Of course, it may also be the case that "real" cold outflows are formed by a completely different method, and that our model is not capturing the "true" effect at all, but the large scatter in the observational data does not allow us to draw

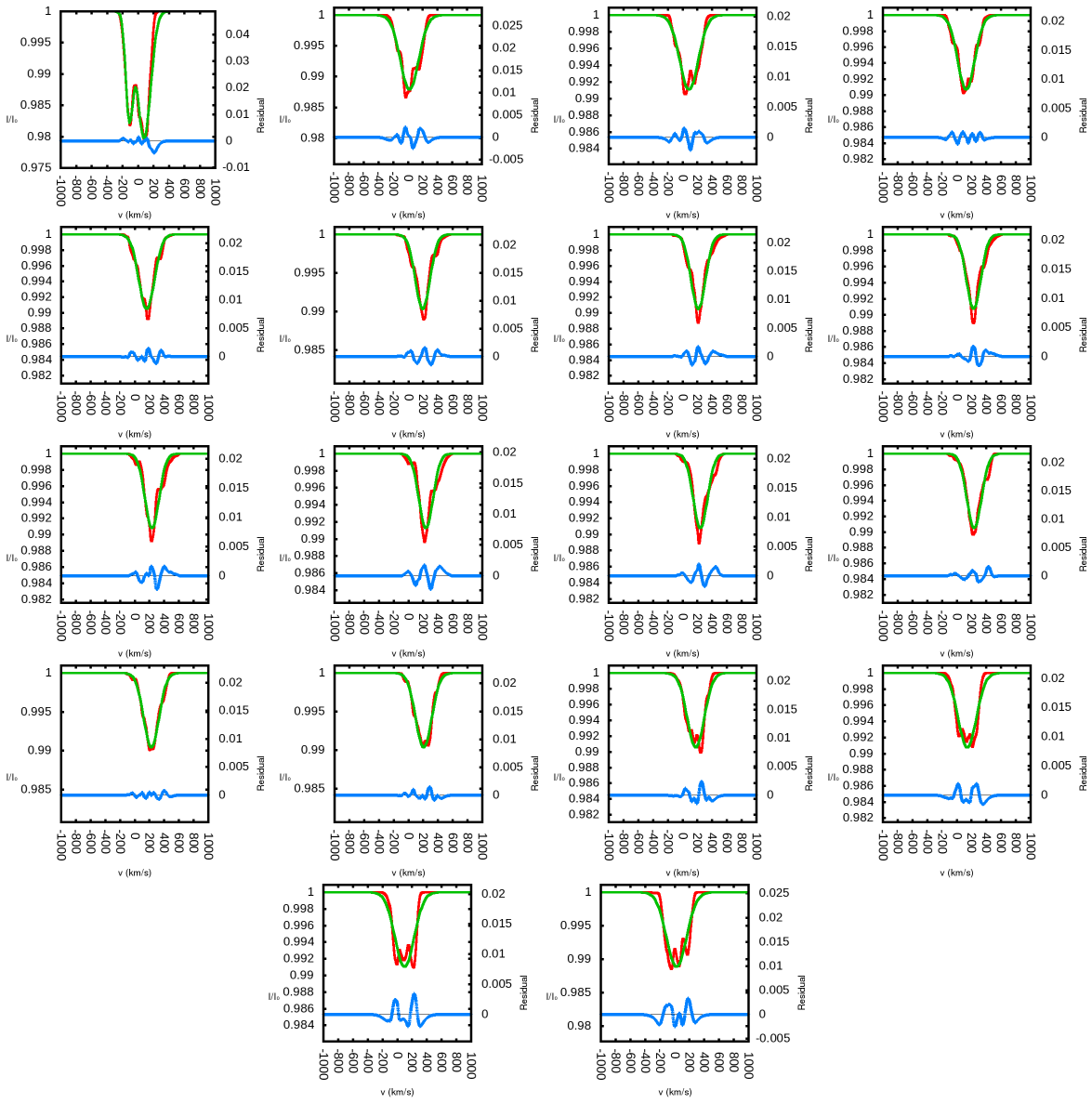

Figure 4.24: Line profiles for altitudinal angles of $0 - 170°$, and azimuthal angles of $45°$, for the simulation BHighResNoTurb. The altitudinal angle increases from left to right. The red line is the line profile, while the green line is a Gaussian fit, both described the y-axis labels on the left of each plot. The blue line is the residual, described by the y-axis labels on the right of each plot. The x-axis is velocity in km/s.

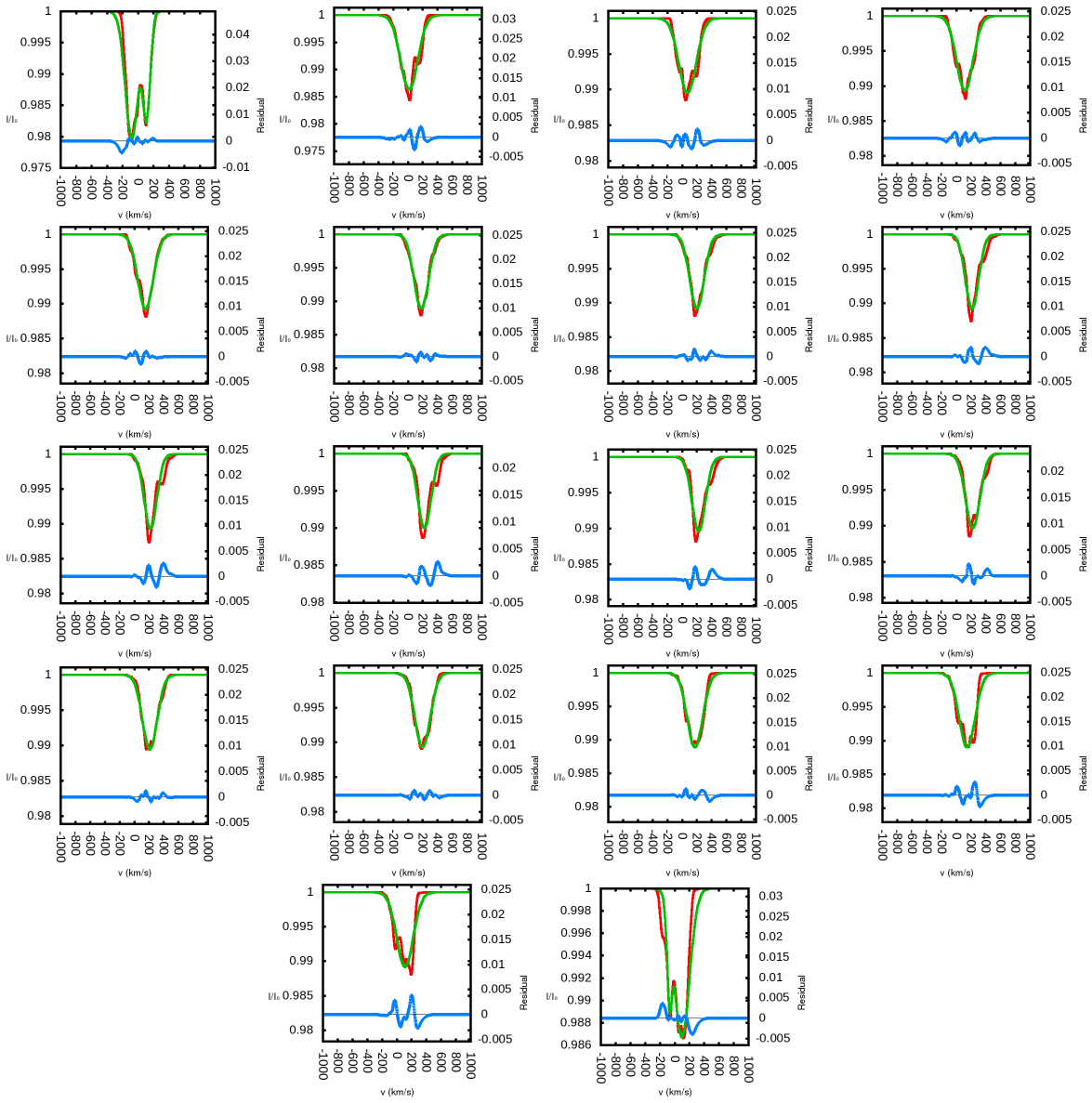

Figure 4.25: Line profiles for altitudinal angles of $180 - 350°$, and azimuthal angles of $45°$, for the simulation BHighResNoTurb. The altitudinal angle increases from left to right. The red line is the line profile, while the green line is a Gaussian fit, both described the y-axis labels on the left of each plot. The blue line is the residual, described by the y-axis labels on the right of each plot. The x-axis is velocity in km/s.

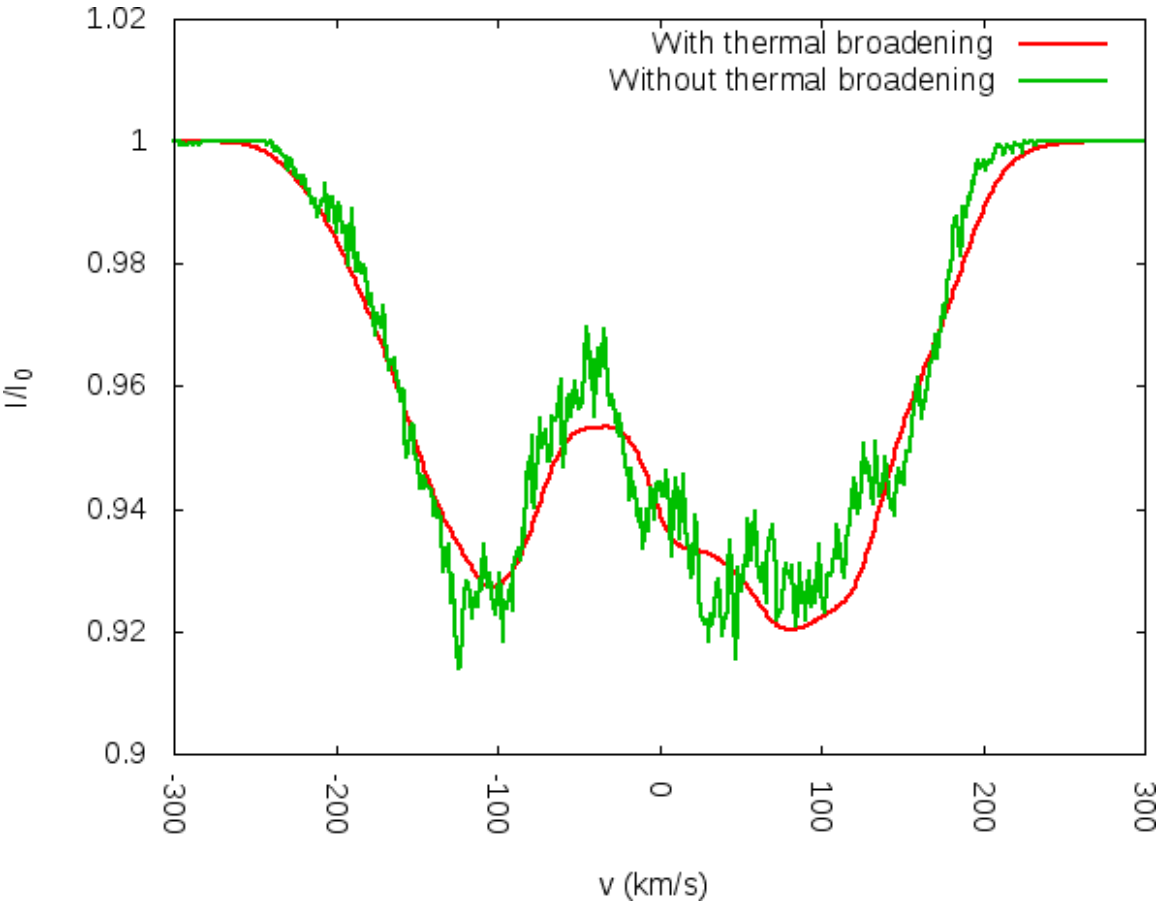

Figure 4.26: Line profiles with and without thermal (i.e. Doppler) broadening in a simulation without sub-grid turbulence. The strength of the un-broadened lines are dependent on the spectral resolution of the code, and so we arbitrarily rescale the intensity to allow a closer comparison with the thermal broadened lines. These lines are sight-lines through the BHighResToTurb model at an altitudinal angle of 0° and an azimuthal angle of 45°.

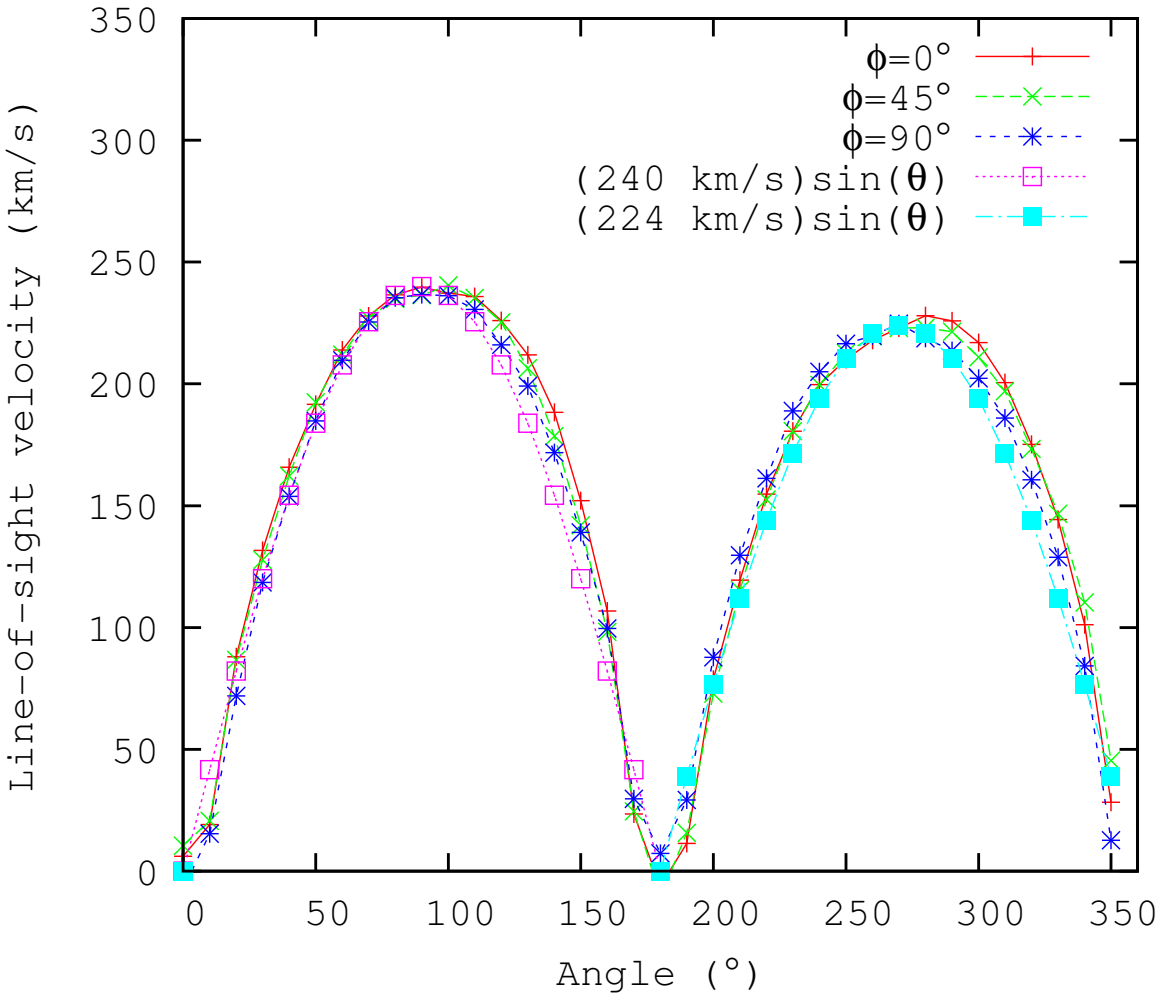

Figure 4.27: Fitted outflow velocities at line-centre as a function of angle for BHighResNoTurb.

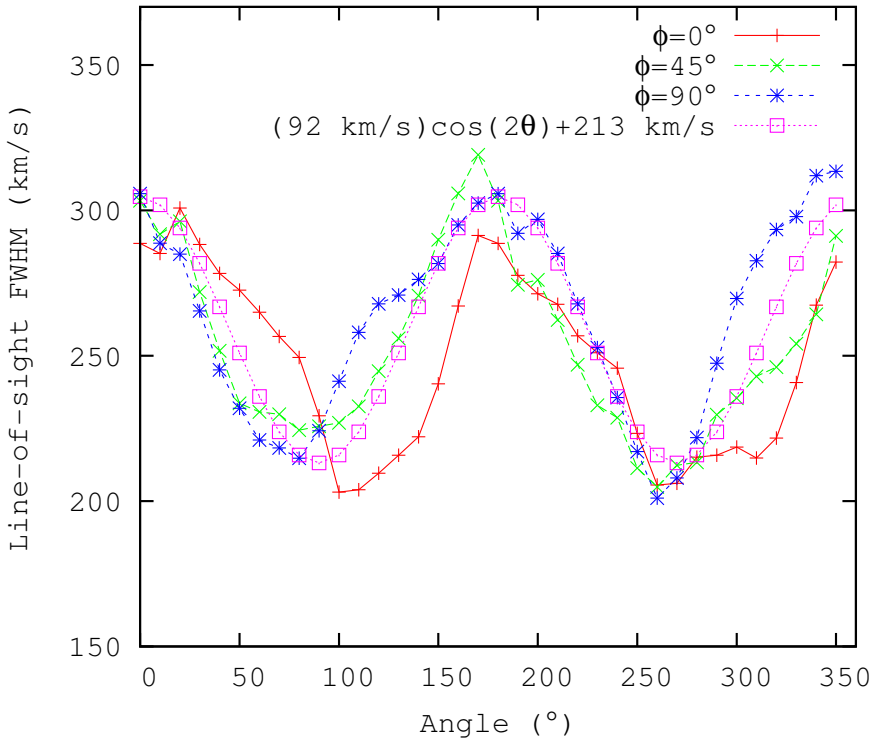

Figure 4.28: Line width vs altitude for three azimuthal angles

absolute conclusions at this point. By comparison, the hot gas in this simulation reaches extremely high velocities. As shown in the top left panel of Fig. 4.15, the hot gas can reach velocities as high as 2000 km/s, although most of the volume of gas still has velocities of less than 1000 km/s. The velocity of the hot gas greatly exceeds that of the cold clumps. However, the cold clumps do not have significantly slower velocities than the hot gas at their altitude (Fig. 4.15, centre and right panel). This agreement suggests that once cold clumps are formed, they are efficiently carried along with the hot wind.

Fig.4.28 shows the full-width at half-maximum (FWHM) of the NaI lines as a function of viewing angle. The line-width peaks at edge-on viewing angles, and is at a minimum for face-on viewing angles, approximately fitting a sine wave. This fit appears to show that most of the velocity dispersion is parallel to the plane of

the disc. This dispersion may be seeded by the rotation of the disc, although the outflowing gas is no longer coherently rotating (Fig. 4.10).

The FHWMs of these NaI lines range from 200 km/s to 300 km/s, which agrees with the lower range of Martin (2005)'s observations of 320 ± 120 km/s. This agreement shows that it is indeed possible for cold clumps formed by Rayleigh-Taylor instabilities in outflows to have sufficient velocity dispersion to explain the large line-widths of NaI gas observed in outflows.

4.6.1.4 Simulated spectra: Models with sub-grid turbulence

Introducing turbulence smooths out the cold structure in our models. This effect is quite dramatic, and as density slices and raytraced column density plots show (Figs. 4.29 and 4.30), no dense cold clumps are formed. Even incorporating a lognormal density distribution for the turbulentmedium (section 4.4.2), negligible gas is cold enough to absorb in the NaI line.

The possible causes are that either the sub-grid turbulence model is too strong — that it smooths and heats flows more dramatically than it should for its energy fraction — or that our assumption that the sub-grid density distribution is lognormal is not a suitable simplification (i.e. self-gravity and cooling are significant), or that both of these problems are serious contributions. This first option is the most likely, as the turbulence is almost universally subsonic (Fig. 4.31), and should not be able to maintain the broad density PDF required for NaI absorbing clouds to be present in cells — we require the densest cells to contain gas $\sim 10^5$ times denser than their mean density. Self-gravity can provide a high-density tail to the density PDF (Fig. 4.31), but we have already demonstrated that it is possible to create these dense clumps in the absence of self-gravity.

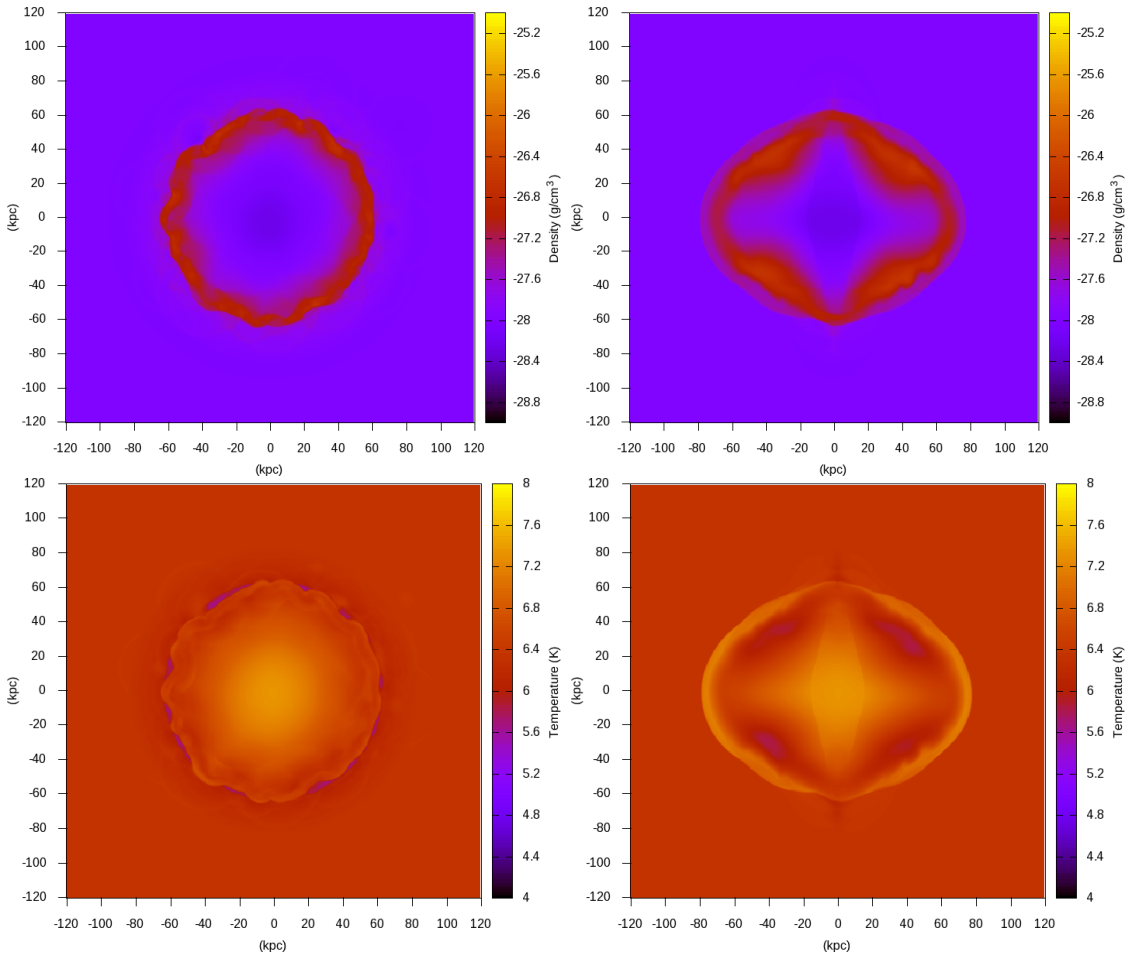

Figure 4.29: Face-on (left) and edge-on (right) slices of density (top) and temperature (bottom) for BHighResTurb.

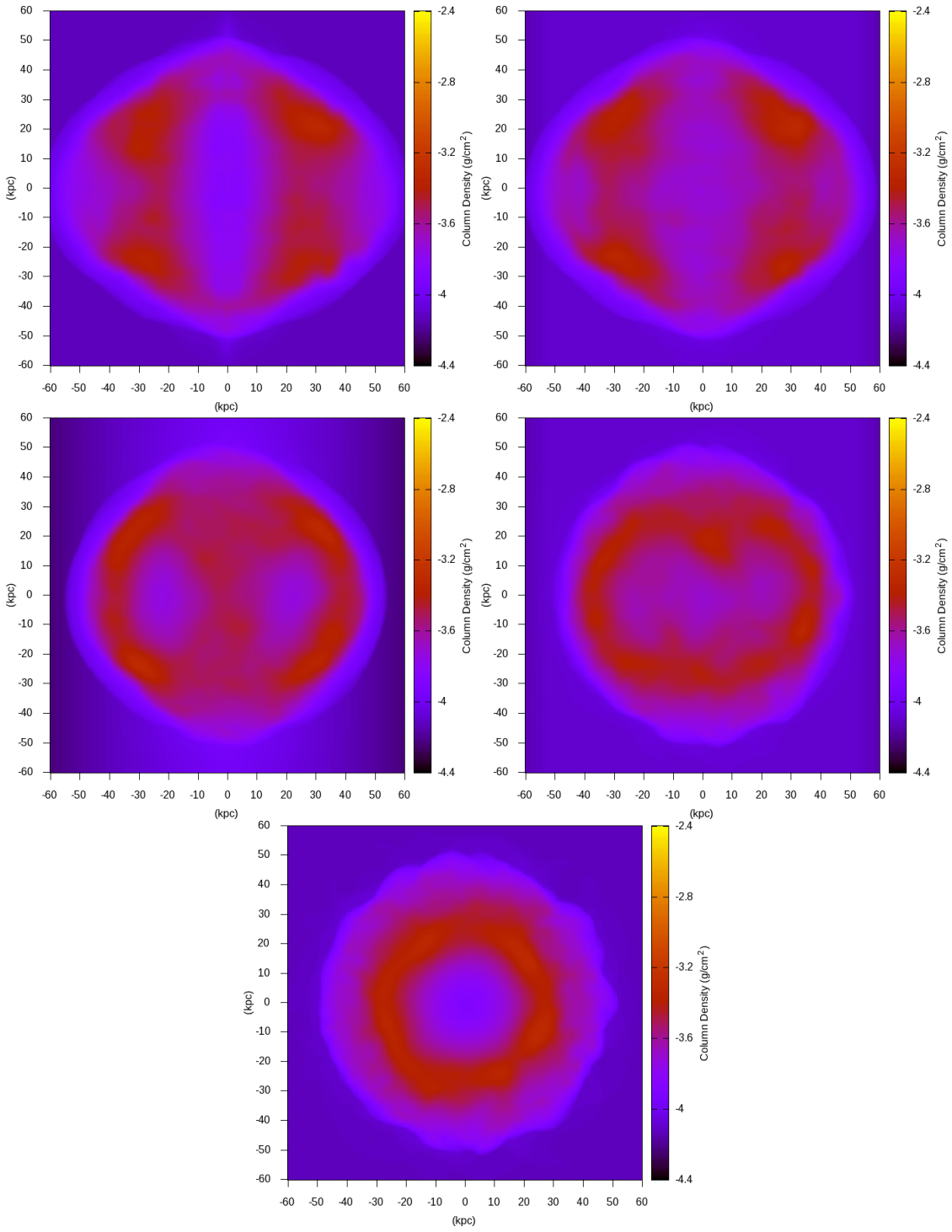

Figure 4.30: Density ray-trace plots of BHighResTurb with altitudes in 22.5° intervals. Top left: $\phi = 0°$, i.e. an edge-on view. Top right: $\phi = 22.5°$. Centre left: $\phi = 45°$. Centre right: $\phi = 67.5°$. Bottom: $\phi = 90°$, i.e. a face-on view.

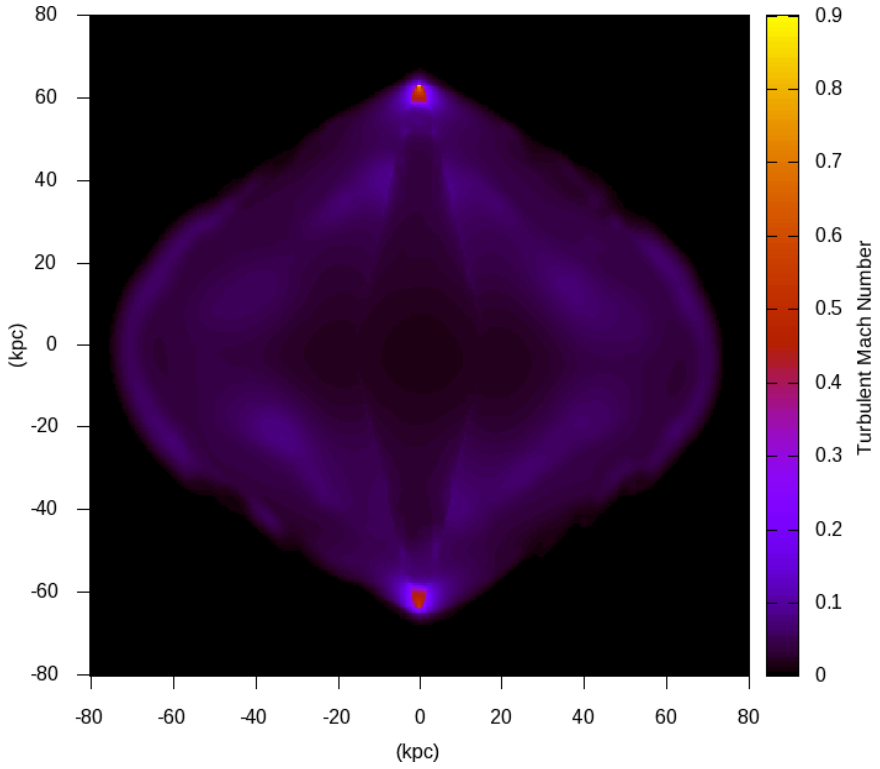

Figure 4.31: Edge-on $x = 0$ pc slice of Mach number for BHighResTurb

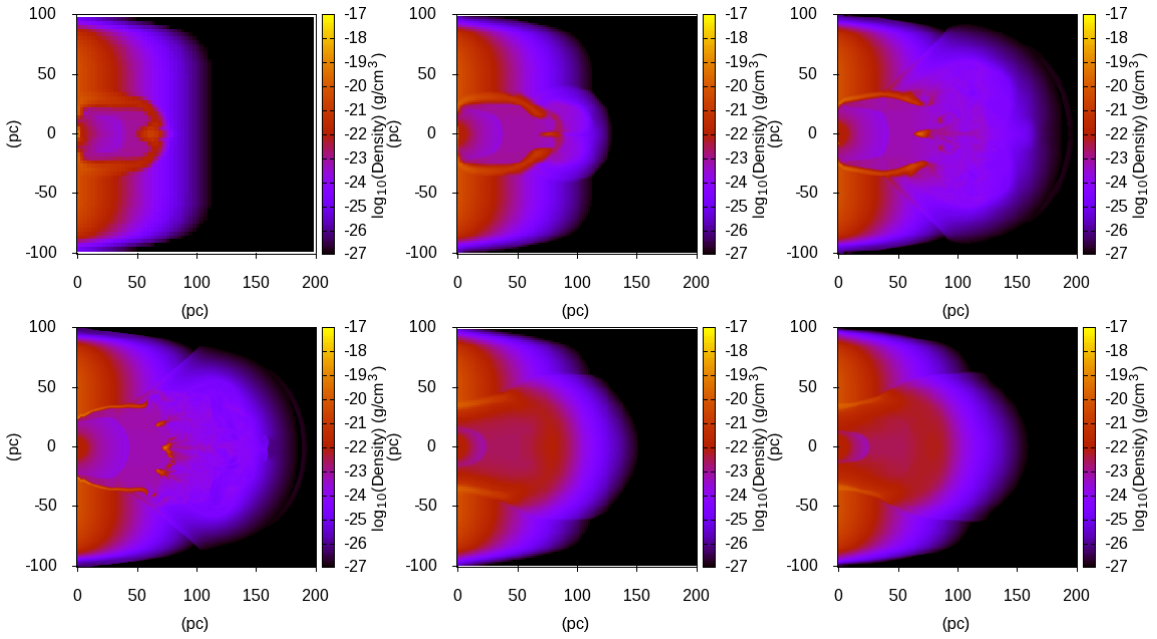

Figure 4.32: Density slices of galaxy-centre models at various resolutions. Slices of models without sub-grid turbulence ("NoTurb") are taken at 130 kyr, slices from models with sub-grid turbulence ("Turb") are taken at 110 kyr. Top left:SVLowResNoTurb, effective resolution 64^3. Top centre: SLowResNoTurb, 128^3. Top right: SMedResNoTurb, 256^3. Bottom left: SHighResNoTurb, 512^3. Bottom centre: SLowResTurb, 128^3. Bottom right: SMedResTurb, 256^3.

4.6.2 Galaxy-centre Models

4.6.2.1 General evolution with and without sub-grid turbulence

In these models, the centralized feedback inflated a bubble which rapidly rises through the disc, sweeping up dense matter until instabilities allow the hot gas to break through the bubble. At lower resolutions, the entire centre of the bubble "blows out", and no complex structure is formed. However, at higher resolutions the bubble wall fragments into a number of dense regions, around which the hot gas flows. These results are illustrated in Figure. 4.32. Here — as in Fujita et al. (2009) — the origin of fragmentation does indeed appear to be the RT and RM instabilities, but the nature of the fragmentation differs greatly in our models.

The evolution of the system is quite different with the inclusion of the sub-grid turbulence model (Fig. 4.33). Here, turbulence is produced by the density gradient

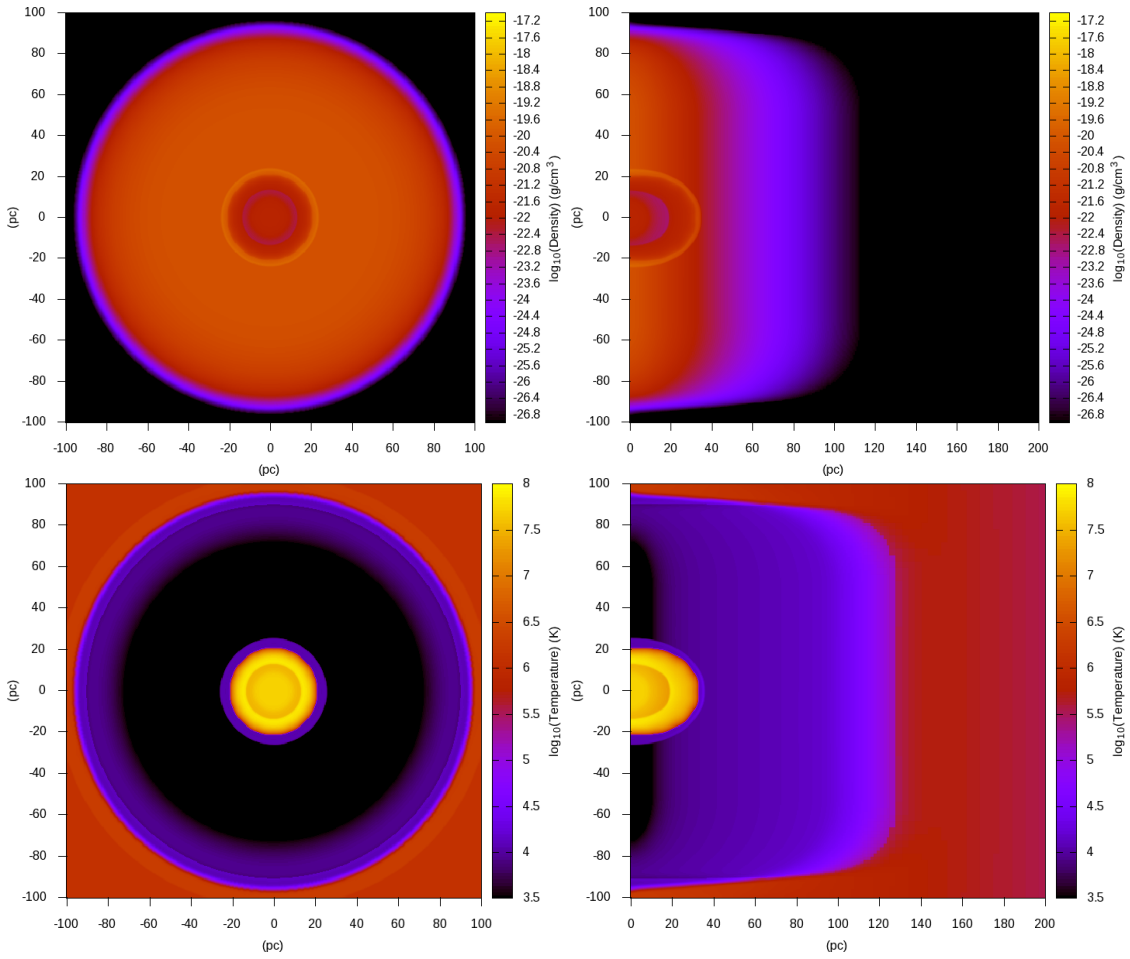

Figure 4.33: Face-on (left) and edge-on (right) slices of density (top) and temperature (bottom) for SHighResTurb.

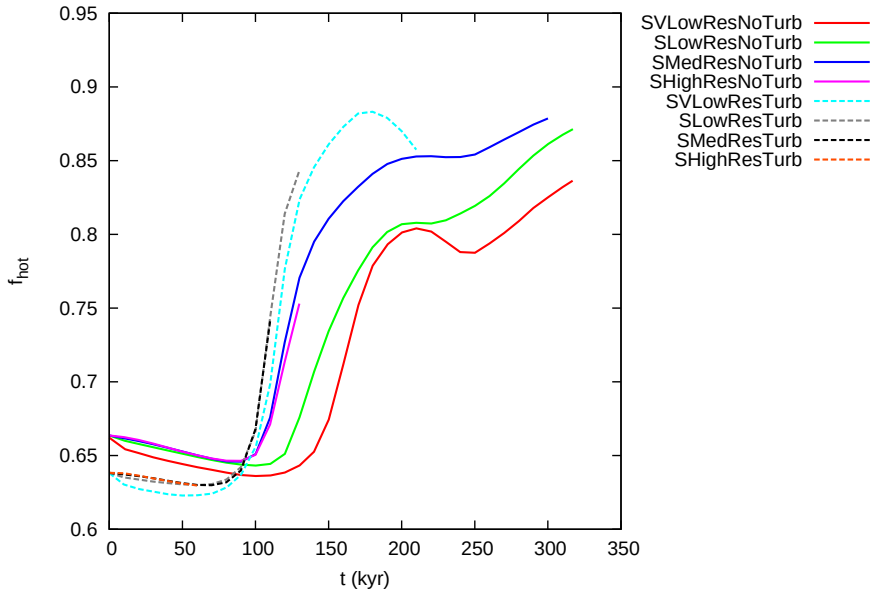

Figure 4.34: Evolution of hot gas volume fraction as resolution is varied, for models with sub-grid turbulence (dotted lines), and without (solid lines). The drop in hot gas fractions at the end of some simulations is due to hot gas escaping the simulated region.

of the bubble's wall. Further turbulent energy is diffused into the bubble wall from the disc and the bubble interior. The presense of turbulent energy in the bubble wall gives it a large effective pressure, causing it to spread out. As a result, after some time there is no longer a strong dense barrier that must be disturbed for gas to escape, and gas will freely flow out of the bubble. This free flow is of course intended to represent the effects of instabilities below the resolution of the grid — and indeed, the gross picture shows this to be the case: a bubble is inflated with a dense wall, which is disrupted, allowing hot gas to stream out of the region of energy input. The bubble wall does not visibly fragment into cold clumps, as this is assumed to take place beneath the grid resolution. More critically, the pseudo blow-out phase occurs at a similar time to the highest-resolution simulations without the sub-grid model (Fig. 4.34), even for the lowest resolution model with sub-grid turbulence.

The opening angle of the hot-gas after blow-out is also less constrained when the sub-grid turbulence model is included (e.g. Fig. 4.35). The sub-grid turbulence model destroys the bubble interface fairly uniformly, allowing gas to pass through

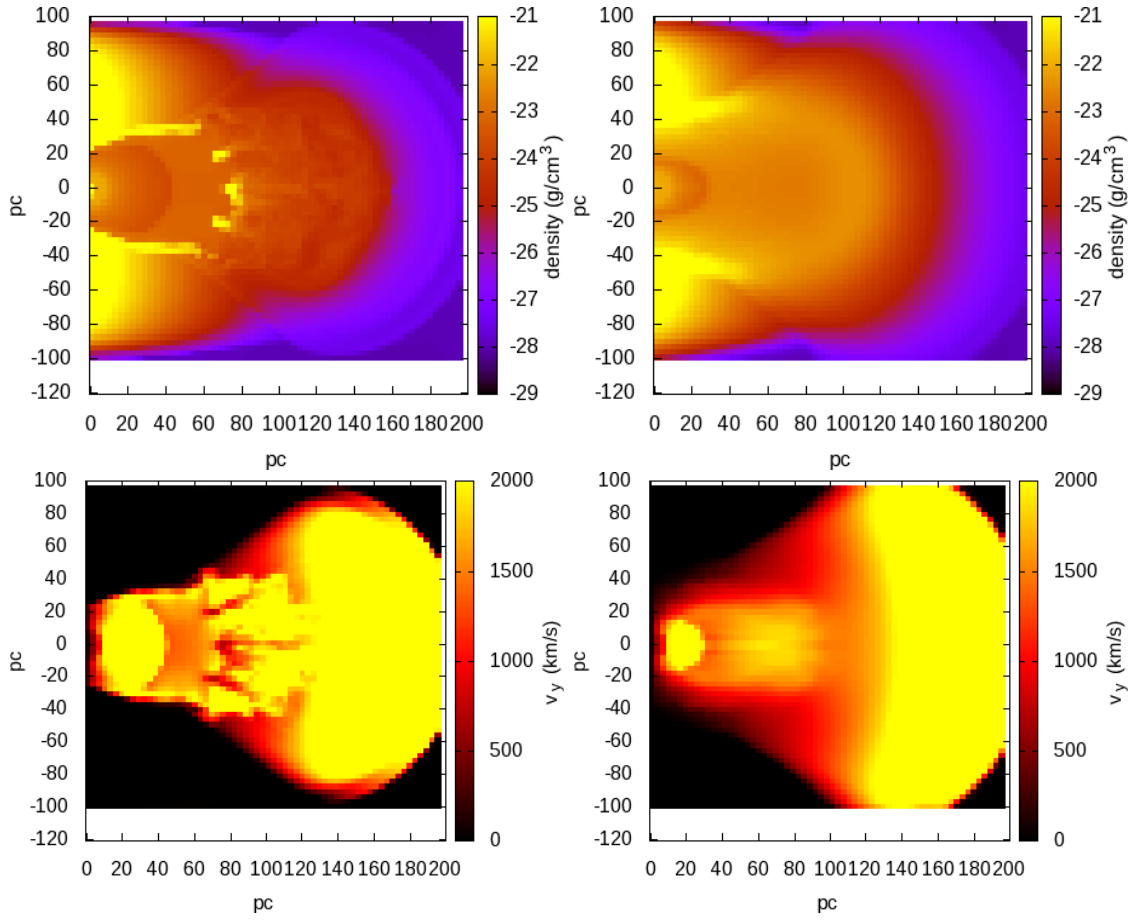

Figure 4.35: Density (top) and z-velocity (bottom) slices of smoothed SHighResNoTurb (left), and unsmoothed SVLowResTurb (right).

the entire region. Without this model, hot gas can only flow through the holes in the bubble interface that have been created by the Rayleigh-Taylor instability. These holes are initially near the centre of the bubble face, and so the outflowing gas has less spatial spread.

4.6.2.2 Fragmentation of the bubble wall

Although at $t = 130$ kyr, a 2D slice of SHighResNoTurb appears to show clumps forming from the bubble wall e.g. Fig. 4.36, it is clear from Fig. 4.37 that rather than a series of clumps, the cold gas is still in a single contiguous structure. It appears that the hot gas has punched holes in the cold shock front, but that

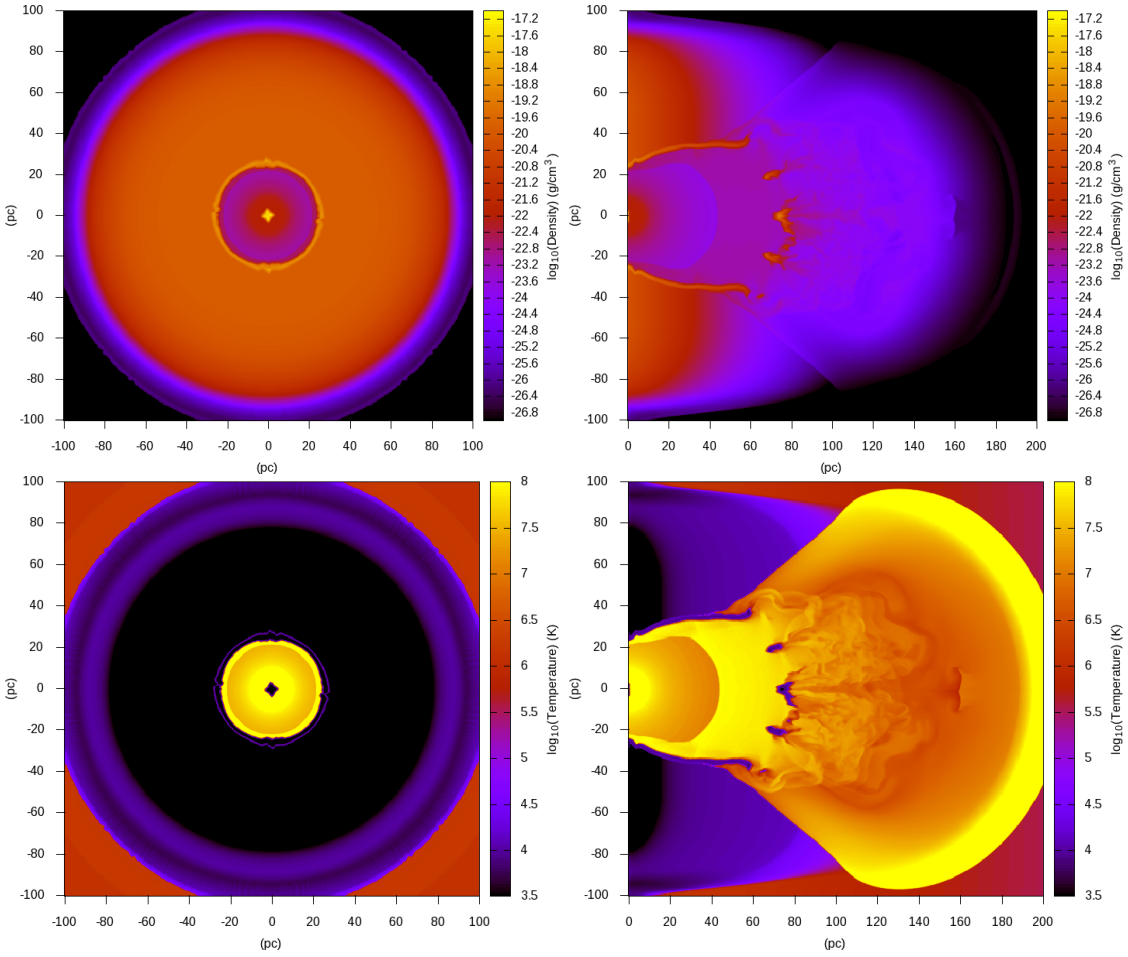

Figure 4.36: Face-on (left) and edge-on (right) slices of density (top) and temperature (bottom) for SHighResNoTurb.

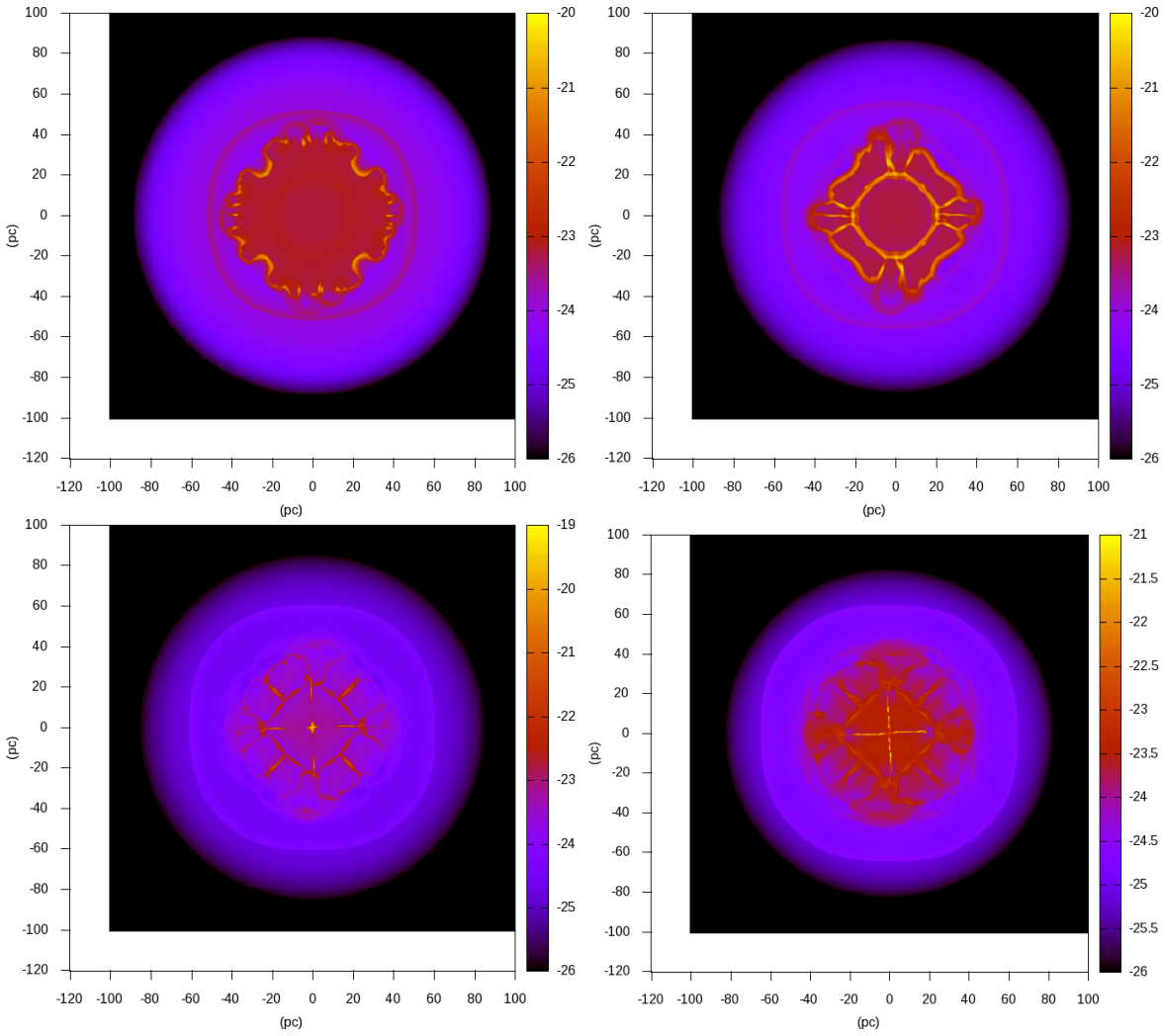

Figure 4.37: Face-on density slices of SHighResNoTurb through $z = 65, 70, 75$ and 80 pc (top left to bottom right) at $t = 130$ kyr.

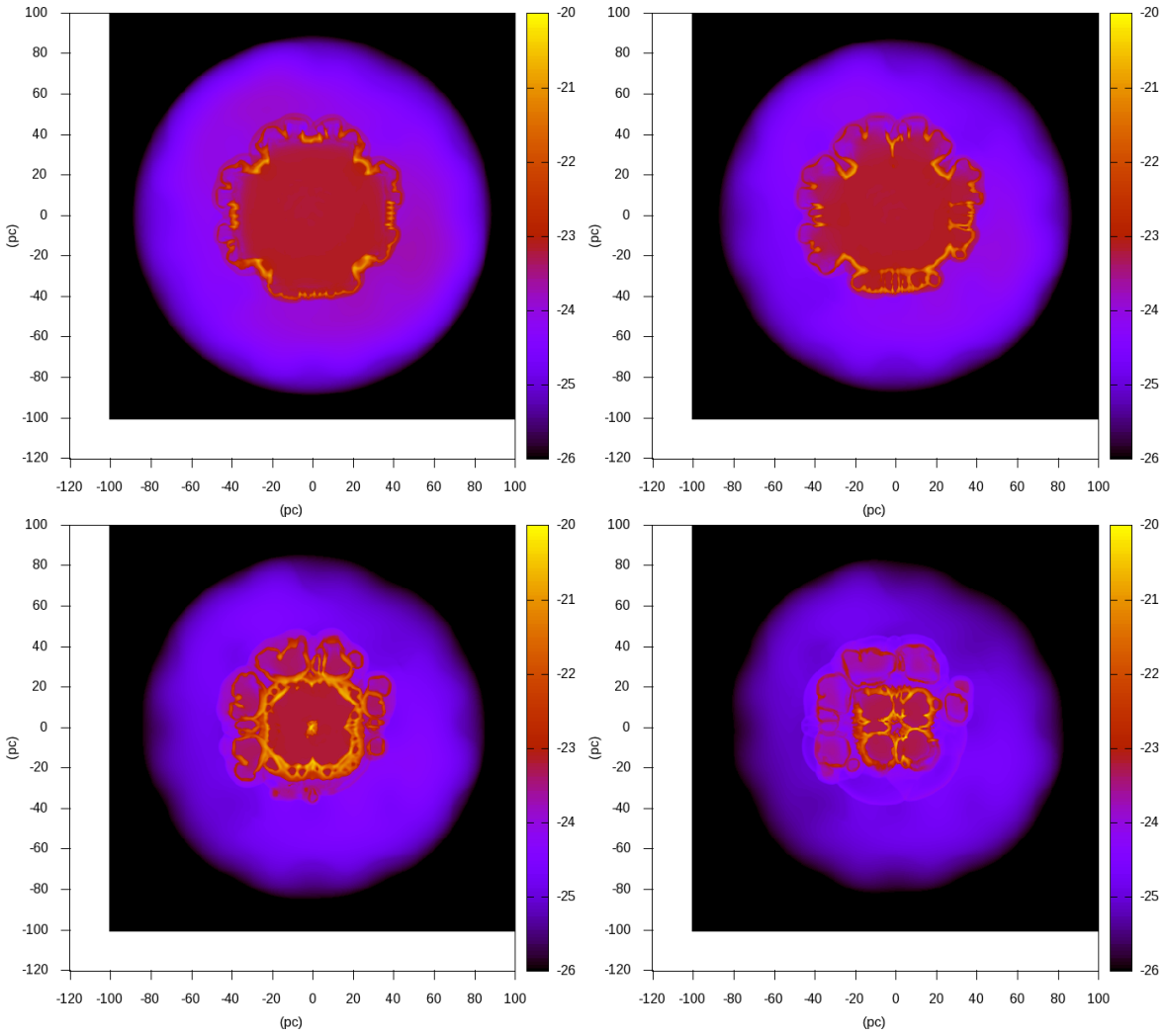

Figure 4.38: Face-on density slices of SHighResNoTurbLumpy through $z = 65, 70, 75$ and 80 pc (top left to bottom right) at $t = 130$ kyr.

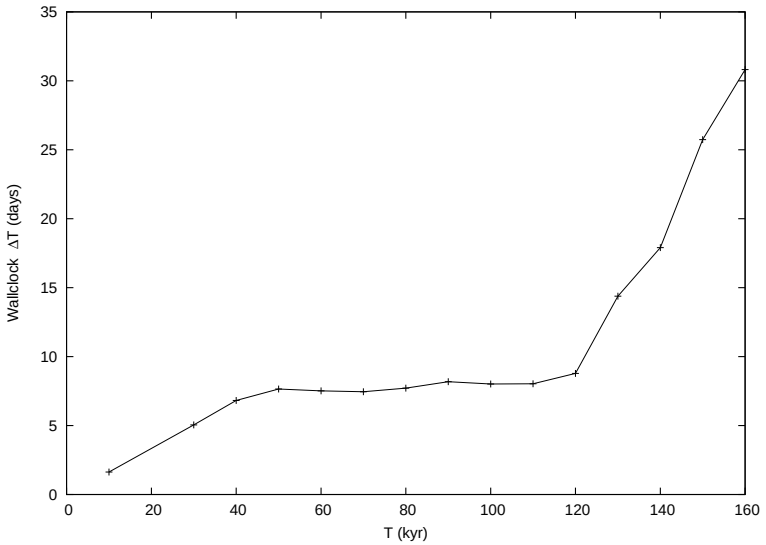

Figure 4.39: Wall-clock time per 10 kyr dump in SHighResNoTurbLumpy.

the walls surrounding these holes have remained largely intact. The structure of these walls is strongly symmetrical, due to the symmetry of the feedback and initial conditions. The inclusion of asymmetric density perturbations in the initial conditions of SHighResNoTurbLumpy breaks this pattern (Fig. 4.38,4.41).

At this point in the simulation, hot gas can flow through the fragmenting bubble wall, filling much of the simulated domain with hot high-speed gas. This high-speed gas drives down the time-step and forces refinements across a greater volume of the simulation, dramatically increasing the wall clock time per output (Fig. 4.39). As a result, we did not have sufficient wall-clock time to fully evolve every high resolution simulation. However, we have allowed one simulation – SHighResNoTurbLumpy – to be further evolved so that we can examine the evolution of the fragmenting bubble wall. Our fiducial line profiles are taken from SHighResNoTurbLumpy at $t = 160$ kyr. We compare this with the lower resolution simulations SMedResNoTurbLumpy and SMedResTurbLumpy.

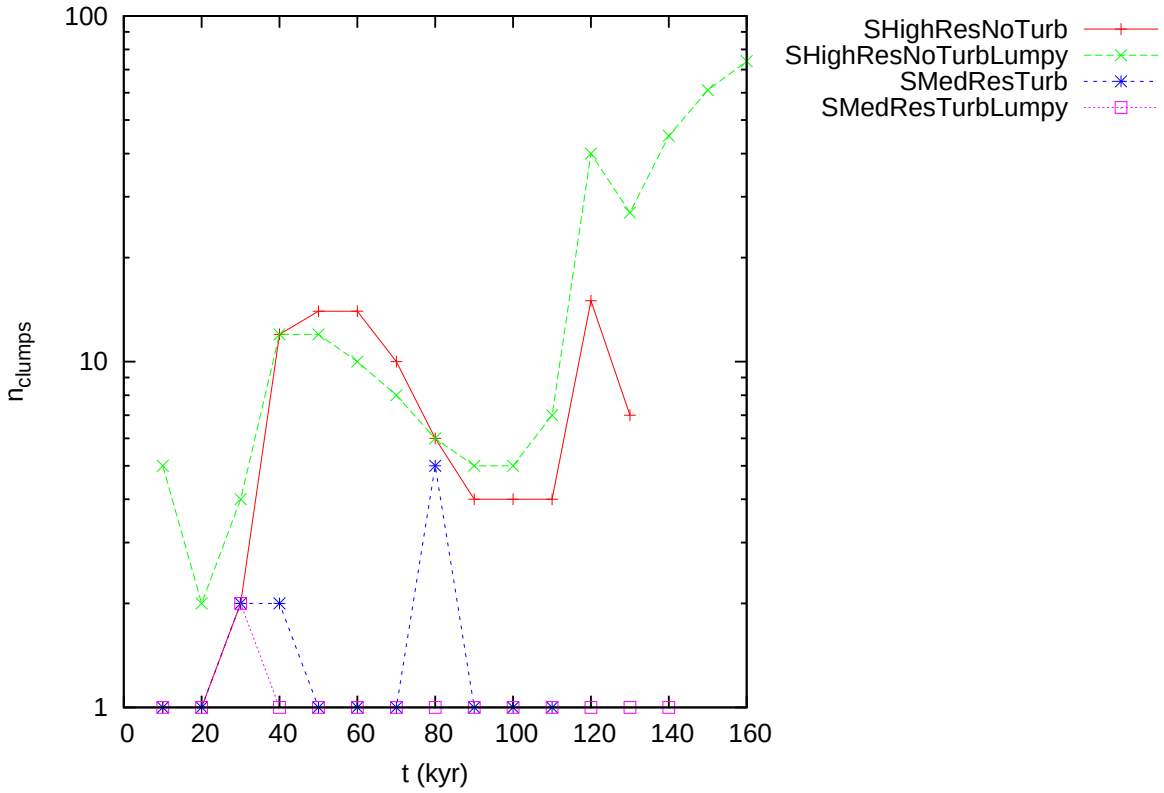

Figure 4.40: Number of clumps in galaxy-centre models. In these models, the portions of the disc not included in the outflow are cold and contiguous, and hence are counted as a single ever-present clump.

We applied our clump finding algorithm to these simulations (Fig. 4.40). Most of the models did not have sufficient time to fragment into a large number of small clumps, but SHighResNoTurbLumpy produced > 70 clumps by the end of the simulated time. These clumps are still being strongly accelerated by the hot gas by the end of the simulation, and so it is not at all appropriate to use the ballistic approximation here to predict their trajectories. However, these clumps will still contribute to the non-thermal broadening of the NaI line, which we analyze in the following section.

4.6.2.3 Simulated spectra

We applied our raytracing code to produce simulated spectra of the models SHighResNoTurbLumpy. In contrast to the full-galaxy run, in this model the initial

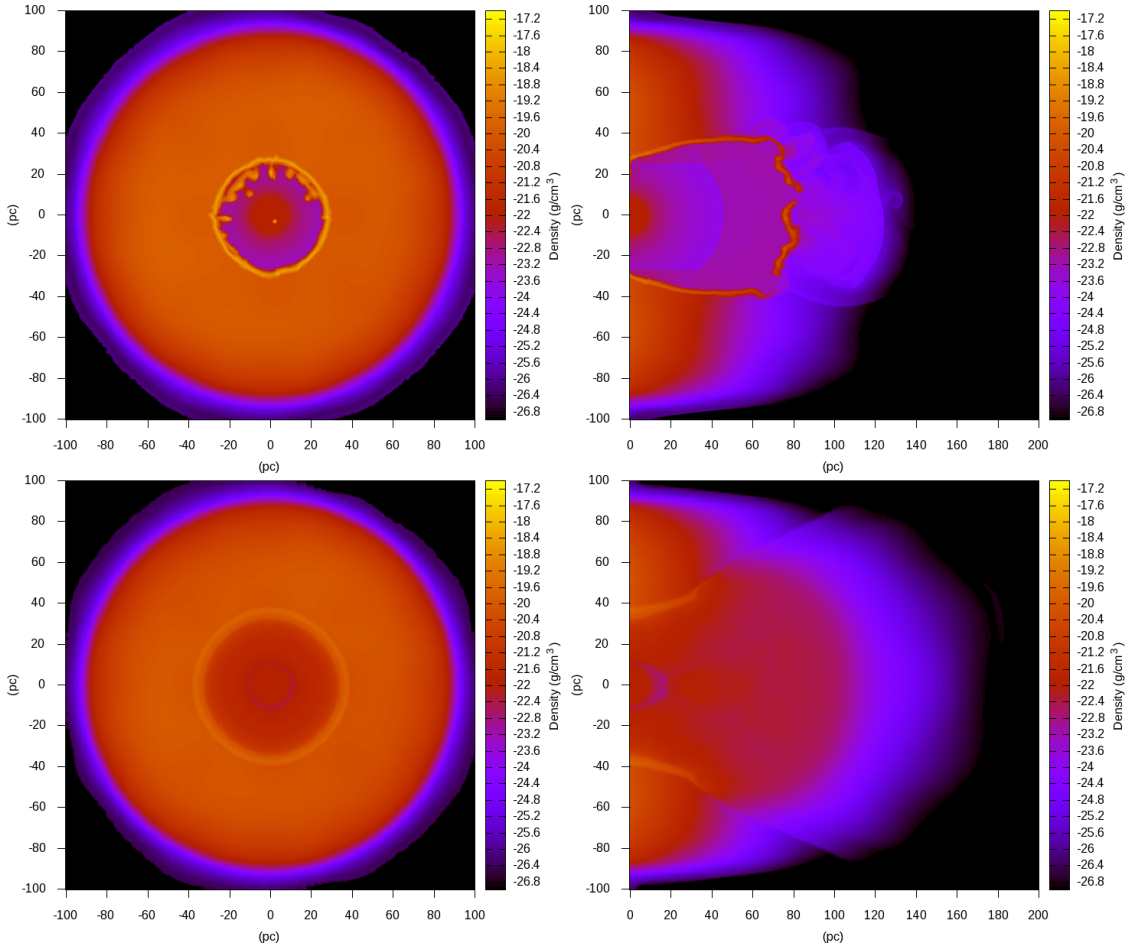

Figure 4.41: Face-on (left) and edge-on (right) slices of density for SHighResNoTurbLumpy (top) at $t = 130$ kyr and SMedResTurbLumpy (bottom) at $t = 110$ kyr.

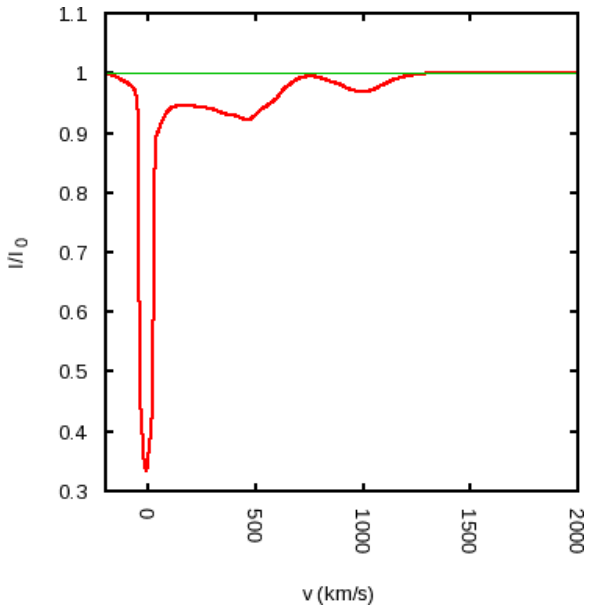

Figure 4.42: Face-on spectrum of SHighResNoTurbLumpy at $t = 160$ kyr, with an effective spatial resolution equal to the size of the simulation.

disc is largely intact outside of the central feedback region. Furthermore, even after blow-out, the lower portions of the bubble wall also remain intact. These regions are both dense and cold, and will absorb the NaI line. An unfiltered face-on spectrum of SHighResNoTurbLumpy at $t = 160$ kyr (with an effective spatial resolution broad enough to cover the entire simulated region) shows three components (Fig. 4.42) — a sharp line at $v \sim 0$ km/s, a broad line at $v \sim 500$ km/s and a weaker line at $v \sim 1000$ km/s. The bottom right panel of Fig. 4.43 shows the z-velocities of a slice through the simulation at $t = 160$ kyr, with a colour scheme chosen to emphasize these three broad regions of velocity. The $v \sim 0$ km/s line clearly corresponds to the intact disc, while the $v \sim 500$ km/s line corresponds largely to the outer portions of the burst-open bubble wall. Only the $v \sim 1000$ km/s line corresponds to fragmenting material within the outflow. As we are primarily interested in outflowing gas, we can neglect the disc component, and we do this by cutting out all gas below 70 pc from our raytracing algorithm. The lower components of the wall have significant velocities (~ 500 km/s), but this dense gas is not entrained within the hot flow, and

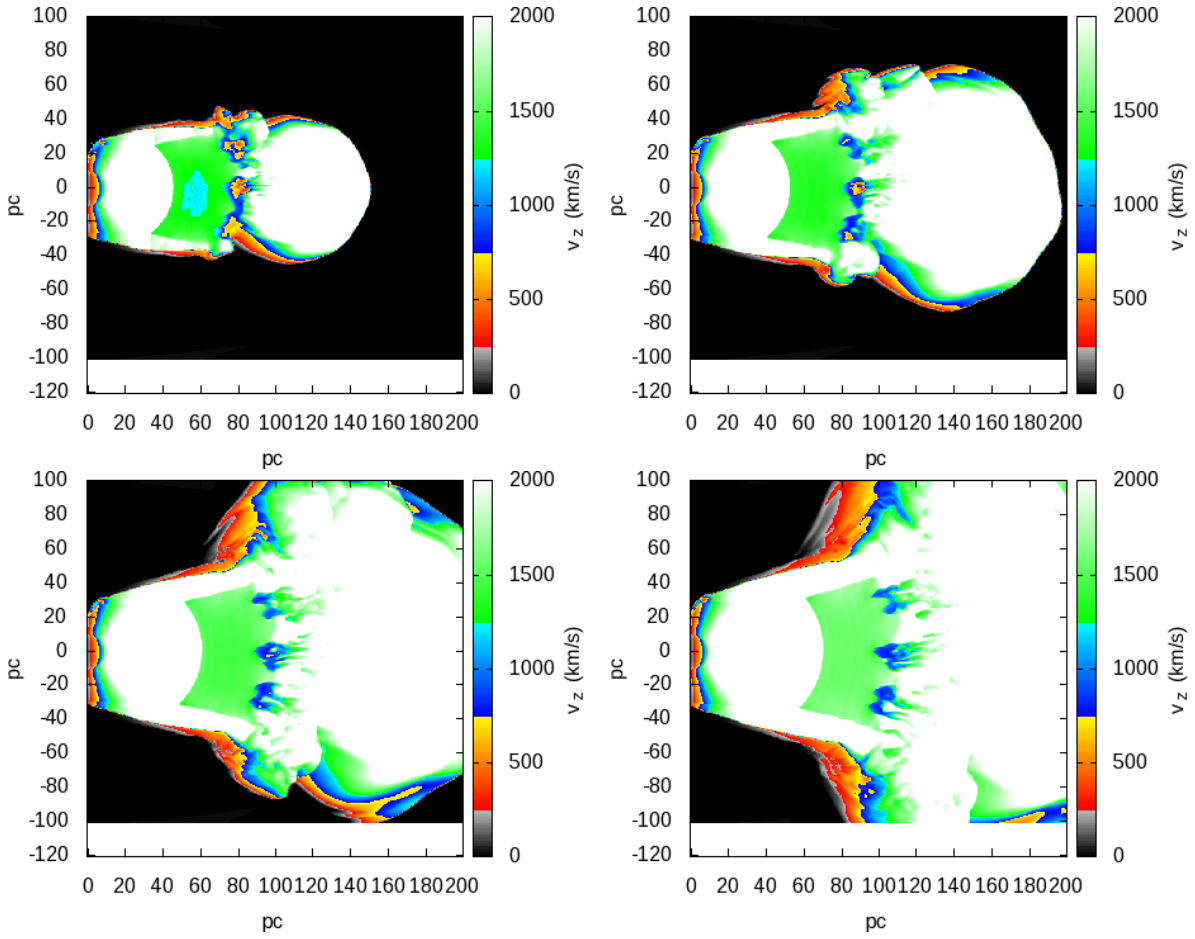

Figure 4.43: Vertical velocity (i.e. v_z) of SHighResNoTurbLumpy at $t = 130$ kyr (top left), $t = 140$ kyr (top right), $t = 150$ kyr (bottom left), $t = 160$ kyr (bottom right). The colour scheme is chosen to divide the gas into four categories: $v \sim 0$ km/s, $v \sim 500$ km/s, $v \sim 1000$ km/s, and $v \gg 1000$ km/s.

is not being accelerated by it. As shown in Fig. 4.43, the clumps are accelerated from ~ 500 km/s to ~ 1000 km/s from $t = 130$ kyr to $t = 160$ kyr, while the lower walls remain at a roughly constant speed. Hence the gas of interest only consists of the clumps near the centre of the outflow. To cut out this outer wall, we narrow the beam-width to 60 pc.

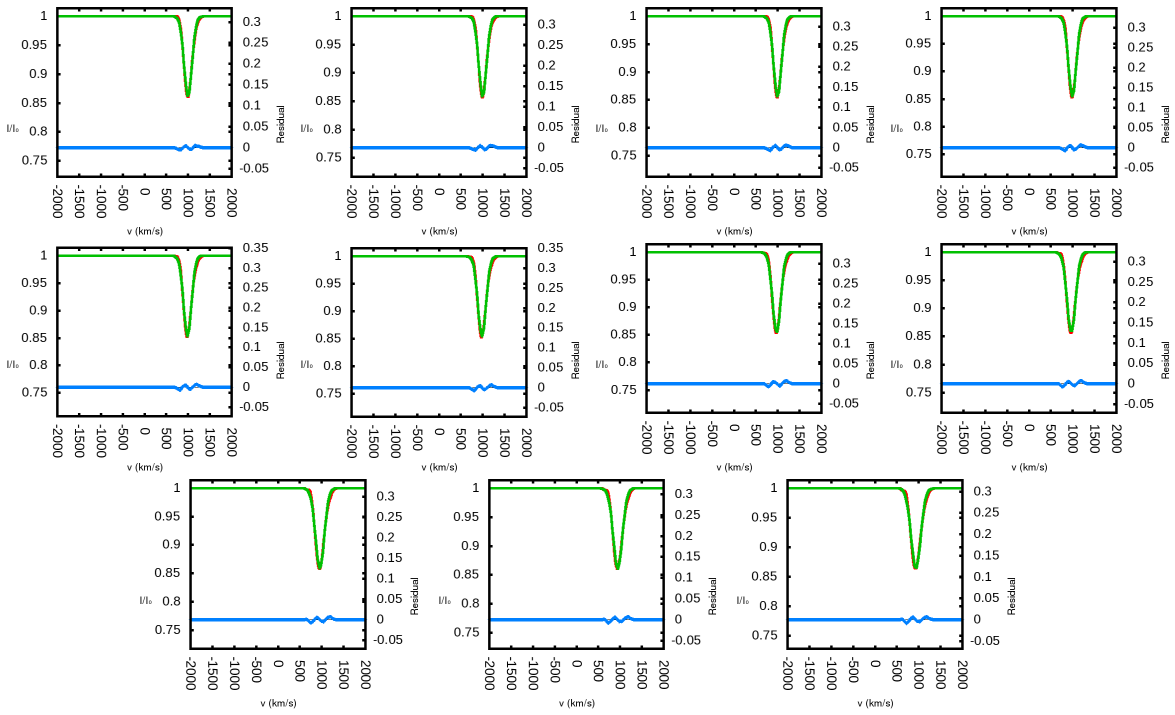

Figure 4.44: Line profiles for altitudinal angles of $0-20°$, for the simulation SHighResNoTurb. The red line is the line profile, while the green line is a Gaussian fit, both described the y-axis labels on the left of each plot. The blue line is the residual, described by the y-axis labels on the right of each plot. The x-axis is velocity in km/s.

We also attempted to produce spectra of SMedResTurbLumpy, but no absorption lines were produced. The sub-grid turbulence suppresses the resolved Rayleigh-Taylor instabilities by diffusing turbulent energy through the bubble wall, which cascades into heat, preventing the bubble wall from cooling into a dense barrier. Instead, hot gas freely flows outwards. As in the full galaxy models, the assumption that turbulent gas follows a lognormal PDF is not sufficient to produce noticeable absorption.

Fig. 4.44 shows the line profiles from rays through SHighResNoTurbLumpy at angles of $0-20°$ from face-on. We are not able to produce meaningful spectra from rays at angles greater than this, as the still intact lower bubble wall blocks the view. The velocity dispersion of the clouds produces a curve that is well approximated by a Gaussian. There is no strong difference between the lines as we change the viewing angle by this small amount. However, as shown in Fig. 4.45, the velocity at line-centre

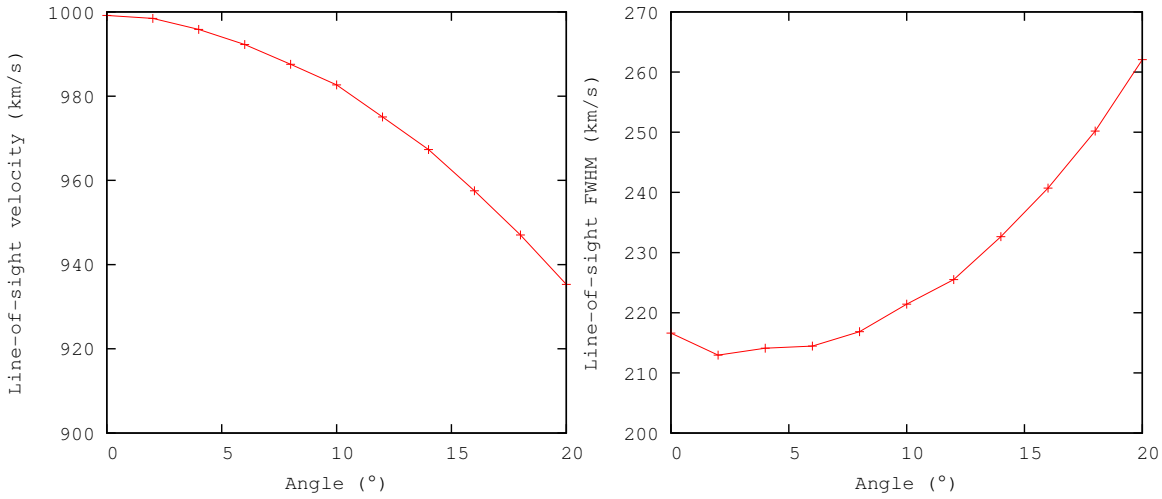

Figure 4.45: Line-of-sight velocity at line centre (left), and line-width (right) as a function of viewing angle for SHighResNoTurbLumpy, with the disc removed and a spatial resolution that resolves the outflow while missing the lower bubble wall.

decreases and the velocity dispersion increases as we move away from a direct face-on view. These trends are unsurprising, as the main component of the net velocity is in the vertical direction, while the main component of the velocity dispersion is in the horizontal direction.

Interestingly, despite the large difference in initial conditions and system evolution, the FWHM of the lines here are similar to the full galaxy case, both reaching a minimum of around 220 km/s for a face-on view. These agree with the lower limit of Martin (2005)'s value of 330 ± 100 km/s, and so we have confirmed that the break-up of the bubble wall does indeed produce sufficient velocity dispersion to explain the observed broadening. However, here the outflow velocity ($\sim$ 1000 km/s) greatly exceeds the observed velocities of 330 ± 100 km/s. This may simply be a product of our feedback conditions — we may have overestimated the energy input rate, or underestimated the size of the feedback region, producing unrealistically intense feedback.

4.6.2.4 Mass-loading

We also examined the effects of varying the mass-loading rate. As mentioned above, this is parameterised by $M_{\rm SN}$, the mass of gas ejected in each supernova. Modifying this value is roughly equivalent to a combination of varying the initial mass function of massive star formation, including a low mass-loading AGN, and/or varying the amount of gas that completely escapes a supernova. We have produced simulations with $M_{\rm SN} = 4{\rm M}_\odot$ and $M_{\rm SN} = 16{\rm M}_\odot$ in addition to the fiducial $M_{\rm SN} = 6{\rm M}_\odot$. These simulations are performed at a low resolution, and so we can not perform a detailed analysis of the variation in clump formation and properties with mass-loading. However, we can investigate the impact on bubble evolution and blow-out. The evolution of a hot bubble is a scenario that has been well-studied in the past (e.g. Mac Low et al. 1989; Norman & Ikeuchi 1989; Ferriere et al. 1991; Koo & McKee 1992; Stil et al. 2009; Zaninetti 2012).

The primary result is that bubble inflation and blow-out occurs much more rapidly and violently at smaller mass-loading rates. During blow-out, the volume of hot gas increases dramatically, and so we can plot the volume fraction of hot gas in our models over time to compare the times at which blow-out occurs. With "hot gas" defined as gas above 10^5 K, this is plotted in Fig. 4.46, and it is clear that blow-out is weakened and delayed with increasing mass-loading (the initial gentle downwards slope is caused by cooling). The addition of mass raises the density within the bubble, which decreases the cooling time, reducing the effectiveness of heating. A greater mass also requires more kinetic energy to reach a high velocity. The greater mass loading also reduces the density contrast across the bubble interface, weakening the Rayleigh-Taylor instability.

4.6.2.5 Resolution Dependence

We examined models with four different maximum levels of refinement, with effective resolutions ranging from 64^3 to 512^3. The effect on blow-out times is clear in the hot gas fraction plots, Fig. 4.34. As in section 4.6.2.4, the hot gas fraction initially

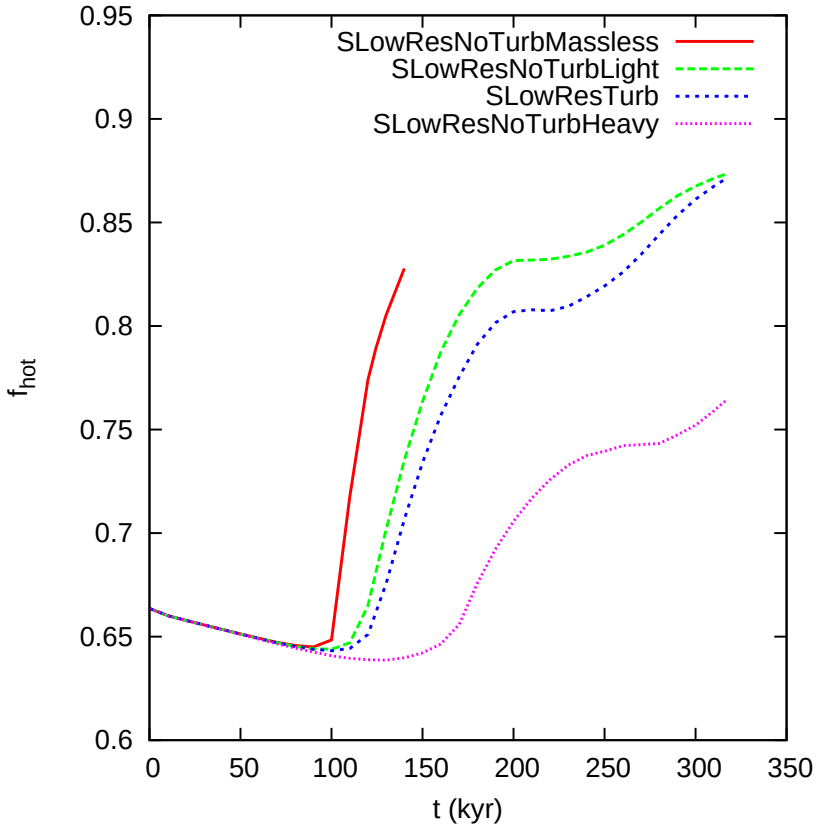

Figure 4.46: Evolution of hot gas volume fraction as mass-loading is varied.

decreases slowly as gas radiatively cools throughout the disc, until the hot fraction dramatically rises as "blow-out" occurs and hot gas streams out of the bubble. Without the sub-grid turbulence model, a resolution dependence is clear: blow-out occurs at earlier times as resolution is increased, although this may have reached convergence at the higher resolutions, as SMedResNoTurb and SHighResNoTurb appear to be consistent. This resolution dependence is likely because the growth-rate of the Rayleigh-Taylor instability increases with decreasing wavelength — for an inviscid medium, the growth rate of an instability with amplitude η in a gravitational field of acceleration g is given by

$$\frac{d\eta}{dt} = (Agk)^{1/2}\eta, \tag{4.66}$$

where A is the Atwood number, and $k = 2\pi\lambda$ is the wave-number of the instability (Chandrasekhar 1961). As resolution is increased, the stronger instabilities at shorter wave-lengths are no longer suppressed by the discretization of the grid, and the bubble-wall can fragment and allow blow-out earlier. Our medium and high resolution runs appear to follow the same locus, but this does not mean the simulation has converged — while blow-out occurs at a similar time, the level of fragmentation is clearly different (Fig. 4.32).

By contrast, and largely by design, the models including sub-grid turbulence do not show such a strong resolution dependence. The diffusion of energy stabilizes the system against small-scale instabilities, which in this case is sufficient to apparently stabilize the bubble wall against all wavelengths of instability, so that the bubble wall never fragments, regardless of resolution. The evolution of the hot gas volume fraction is identical at all but the lowest resolution (Fig. 4.34), although we were not able to follow the evolution of the highest resolution model up to the pseudo blow-out stage because the computational load for each time-step had become too arduous. Density slices are almost identical between SLowResTurb and SMedResTurb (Fig. 4.32), except that the bubble's lateral walls are a thinner and denser at the higher resolution.

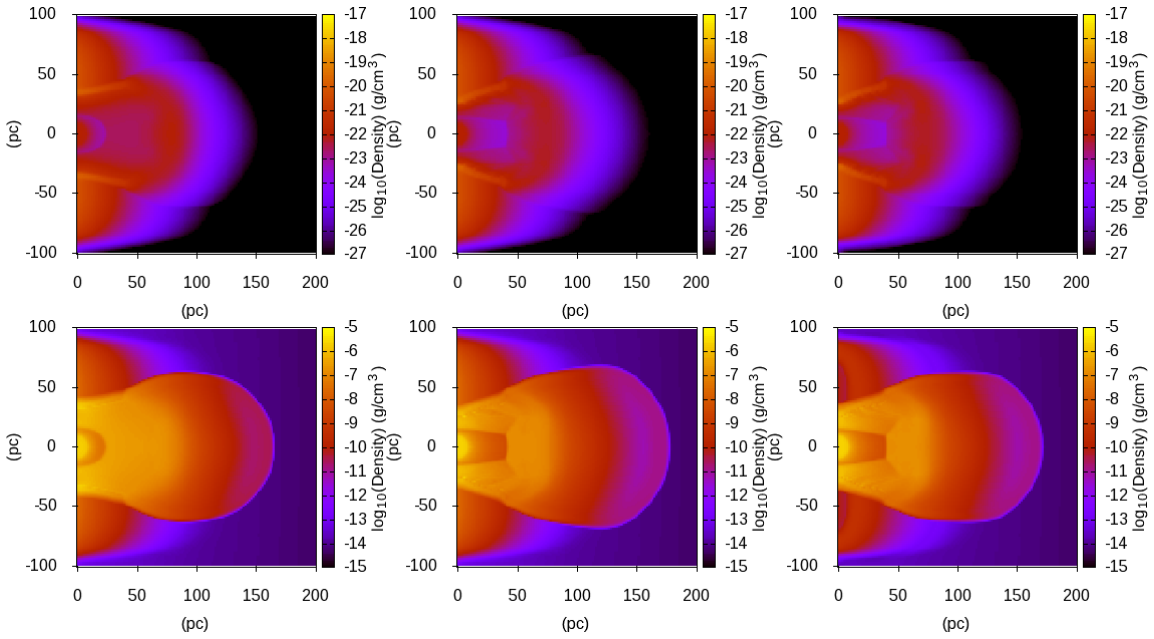

Figure 4.47: Density (above) and pressure (below) slices for SLowResTurb (left), SLowResTurbNoOutflow (middle), and SLowResTurbNoOutflowNoDisc(right).

4.6.3 Investigating the Sub-grid Turbulence Model

To further investigate the particular effects of the sub-grid turbulence model, we can vary the implementation of the sub-grid turbulence model to investigate the importance of different sources of turbulence. There are three sources of turbulence in our model. Firstly, the disc can contain some initial turbulence. Secondly, turbulence can be generated by the Rayleigh-Taylor and Richtmyer-Meshkov instabilities. Thirdly, turbulence can be injected into the feedback region. We ran tests switching these effects on and off in various permutations.

We found that the general evolution was qualitatively the same in all three cases (see Fig. 4.47) — the gas mixes well, and no cold dense structures are formed. However, the bubble itself has a different shape in the absence of turbulent injection from the feedback region. The inclusion of sub-grid turbulence narrowed the bubble's size at low z, as this region's high density allows it to cool efficiently, greatly reducing its pressure in the absence of sub-grid turbulence. Removing the turbulent support

from the disc's initial conditions allows radiative cooling to reduce the pressure in the lower portions of the disc, but this does not appear to have an effect on the bubble's shape.

We found in general that the simulations with the sub-grid turbulence model ran much slower than the simulations without it. The additional load from directly executing the subroutines for the sub-grid source terms and diffusion are not the main source of this. Instead, as the turbulent diffusion is efficient at spreading and maintaining large thermal and turbulent energies (and hence pressures and effective sound speeds), the time-step becomes short, and the mesh must be more heavily refined. The additional time-step criterion from turbulent diffusion further contributes to this.

A critical test of this sub-grid turbluence model model is whether a low resolution model with sub-grid turbulence is an accurate approximation to a high resolution model without sub-grid turbulence. We can compare SHighResNoTurb with SVLowResTurb by smoothing density and velocity slices of SHighResNoTurb by a factor of 2^3 so that the resulting plots have equivalent resolution. This smoothing is done by taking a simple arithmetic average. As shown in Fig. 4.35, the result is that the models do not agree even in the general size and shape of the blowout and outflow. However, as Fig. 4.32 shows, the models without turbulence are not yet converged in resolution, and it is still possible that sub-grid turbulence model accurately represents the behaviour of the system in the limit of high resolution, but only higher resolution tests can confirm this.

The sub-grid turbulence model, as implemented here, does not successfully model the production of cold clumps by the Rayleigh-Taylor instability, while adding to the computational load. Either sub-grid turbulence is not an adequate model for the large density and temperature range in this scenario, or our sub-grid turbulence model is not adequate. Indeed, it may be possible to improve this model by including the full turbulent cascade (Schmidt & Federrath 2011), and by including off-diagonal terms in the sub-grid tensor (Gray & Scannapieco 2011).

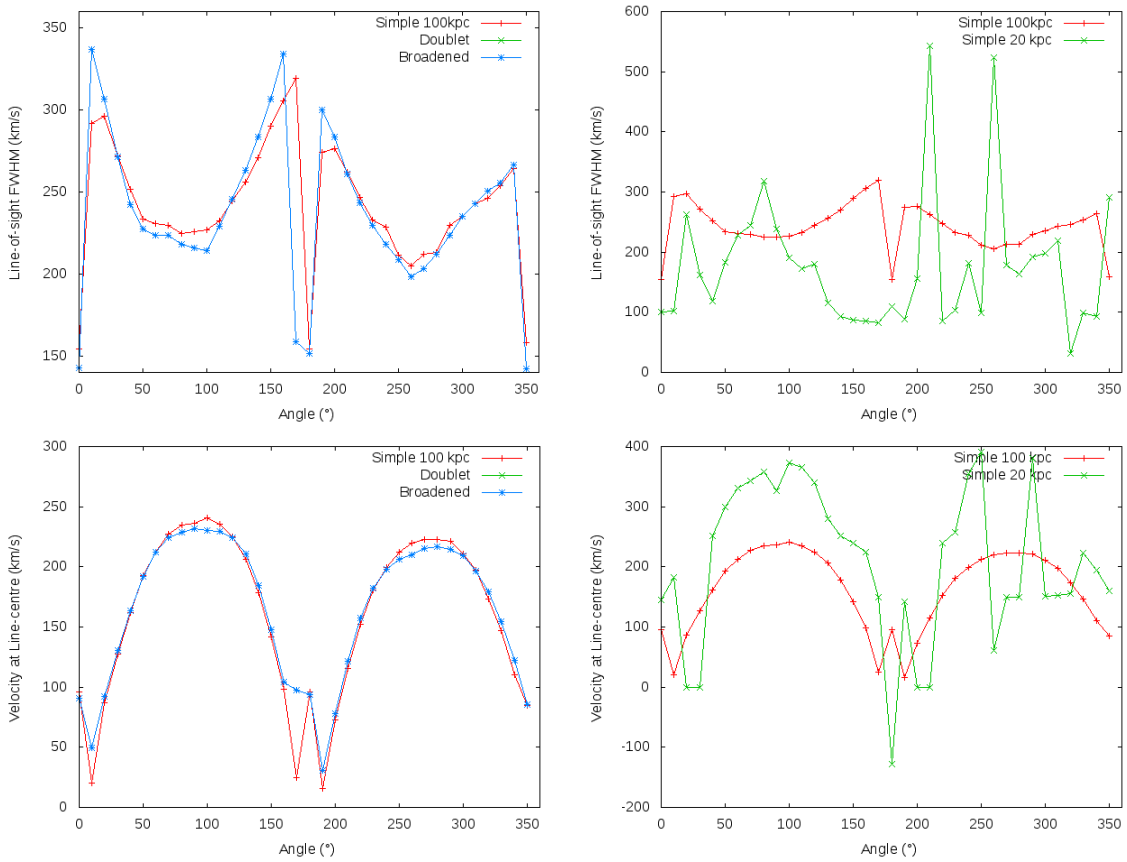

Figure 4.48: The effects of extensions to the line profile models (left), and the effects of narrowing the "beam-width" (right).

4.6.4 Line profiles: Extended models

We examined the effects of a more "realistic" line profile, including broadening from limited spectral resolution, and line confusion from inclusion of both lines in the Na D doublet. We also explored the results of using a raytracing model with a much tighter spatial resolution (i.e. beam width), using 10 kpc instead of our fiducial 100 kpc. The results of these examinations are plotted in Figure. 4.48.

The second line in the doublet is simply a copy of the first line, transposed by $\Delta\lambda = 5.97$ Å. The contribution of this to the optical depth profile is calculated for each cell the ray passes through. That is, if the contribution to the optical depth at

frequency ν by cell i for a single line is

$$\tau_{\nu,i} = N_i \alpha \lambda \Phi(\nu), \tag{4.67}$$

(where λ is the wavelength, N_i the number density, α the cross-section, and $\Phi(\nu)$ the doppler profile as in section 4.4.2), then for a doublet line (under the assumption that both components of the line have the same amplitude) this is replaced with

$$\tau_{\nu,i} = N_i \alpha \lambda (\Phi(\nu) + \Phi(\nu - \Delta\nu)), \tag{4.68}$$

where $\Delta\nu = \Delta\lambda c/(\lambda^2)$. Our fitting algorithm was modified to include the assumption that every Gaussian curve centred at λ had an identical partner at $\lambda - \Delta\lambda$, i.e. a "single" Gaussian fit is a fit to the function

$$I(\lambda) = 1 - \{A \exp[-(\lambda - b)/c^2] + A \exp[-(\lambda - b - \Delta\lambda)/c^2]\}, \tag{4.69}$$

where A, b, c are fitted parameters.

As mentioned in section 4.4.2, the effective broadening due to spectral resolution is produced by convolving the intensity with a Gaussian curve. We set the full-width at half-maximum (FWHM) of the Gaussian to 65 km/s as in Fujita et al. (2009), to match the observations of Martin (2005). Here, the fitting algorithm is not changed.

It is clear (left panels of Fig. 4.48) that these additions do not significantly alter the line profile properties. Even when there is confusion due to one line of the disc's doublet being superimposed on one line of the outflow's doublet, the fits correctly disentangle the lines. Furthermore, the intrinsic broadening (both thermal and non-thermal) is large enough that the additional 65 km/s does not significantly change the profile's properties.

However, tightening the effective spatial resolution of the simulated observer *does* significantly change the line properties (right panels of Fig. 4.48). Resolution

limits in our simulation place a lower limit on the length-scale of any structure. As a result, a tight beam will not capture the details of the structure of the outflow — the beam will likely intersect with only a few clouds, or none at all. Furthermore, a tight beam produces a smaller outflow FWHM, as non-thermal broadening is reduced, and also produces a strongly irregular variation with viewing angle, as clouds pass in and out of the raytraced region. There is a similar effect in the outflow velocities, with some angles even producing a *negative* outflow velocity, which is not at all indicative of the overall structure of the outflow. While the very broad effective spatial resolution used in our fiducial models effectively smooths large-scale structure into an average, a tight beam misses the structure entirely. We conclude that, given the resolution limits of our hydrodynamic simulation, the "broad beams" used in our fiducial raytracing calculations are the most appropriate choice.

4.7 Conclusions

In this chapter we performed three-dimensional numerical simulations to explain the source of cold high velocity-dispersion gas in ULIRG outflows (as observed by Martin 2005, in particular). Our initial conditions were set up to produce a scenario where clouds are produced by the Rayleigh-Taylor induced fragmentation of the wall of a galactic super-bubble (as in Fujita et al. 2009). This was done in two scenarios, one focusing on the central 200 pc of the galaxy, and another where the entire galaxy is included in the simulated domain. To account for a lack of convergence with respect to resolution, we also investigated a sub-grid turbulence model (implemented in FLASH by Scannapieco & Brüggen 2010). Finally, we produced spectra of our simulations with a raytracing algorithm to facilitate comparison with observation.

Our models were indeed successful at producing cold outflowing gas with similar velocity dispersions to the observations, at our higher resolutions when the sub-grid turbulence is switched off. Our two scales of simulation produce this cold outflowing gas through different means. In our highest resolution full galaxy models the cold disc gas is fragmented by the large number of hot bubbles produced in the disc. This

gas is then pushed into the outflow by the intense pressure of the feedback beneath it. In our central-scale models, the cold gas is produced by the Rayleigh-Taylor induced fragmentation of the bubble-wall produced by the feedback. Hence we have developed two distinct explanations for the origin of this cold gas. We can not choose which of these models most closely resembles observations without more thorough testing at higher resolutions, larger domain sizes, and longer simulation times.

However, the velocities of the cold gas do not completely agree with the observations, being somewhat lower than average in the full galaxy simulations (although not entirely inconsistent with soem observed ULIRGs), but much too large in the galaxy-centre simulations. Hence, we can not be completely confident that our models are an accurate representation of the mean behaviour that produce this cold high-velocity dispersion gas. Rectifying this disagreement may only require an adjustment of model parameters, which are based on observations that have large uncertainties because ULIRGs are dust-obscured and locally rare. However, because the results are not converged with resolution, higher resolution simulations should produce different results — perhaps even affecting these outflow velocities. Furthermore, improving the physical model to include self-gravity and a more self-consistent feedback algorithm may also improve the result.

The inclusion of the sub-grid turbulence model has a dramatic effect, smoothing away much of the substructure that forms in models that lack it. However, we did not find evidence of cold gas in these models — indeed the sub-grid turbulence model is effective at maintaining high pressures and temperatures across the domain. Assuming a lognormal PDF for the turbulent gas did not alleviate this problem. A more complex model for the temperature and density variations within a turbulent cell may perhaps solve this problem, but these variations must be very large indeed to reveal any cold gas in such hot cells. However, we note that the sub-grid turbulence model does indeed appear to be converged with respect to resolution, and hence the *gross* evolution of these models may perhaps represent the high resolution limit of the models without sub-grid turbulence. More research needs to be done to produce a

model that accurately evolves the mass fractions and velocity dispersions of sub-grid cold gas.

Chapter 5

Conclusions

While detailed conclusions are presented at the end of each chapter, I summarize here the key results that were outlined in this thesis. I also discuss outstanding questions, and make suggestions for future avenues of research.

5.1 Code Development

We improved HYDRA by extending its cooling curve down to 10 K to allow formation of molecular clouds, and (more critically) modified the parallelization algorithm. In the existing code, large refinements were distributed across the entire machine, while smaller refinements were assigned one processor at time. We extended this logic to the individual cells within a refinement, so that if a single cell contained more than a threshold number of particles, its particle-particle (gravity and SPH) calculation would also be distributed across the entire machine. This adjustment improved the performance of the code by a factor of ~ 7 in certain simulations of disc evolution.

This improvement allowed our simulations to be performed within a reasonable time frame. Our higher resolution HYDRA simulations took about a month to run — for example, LowSoftMW took 33 days to reach 1.1 Gyr. Without this modification to load-balancing, this simulation would have likely required at least half a year to complete. This significant reduction in computating time highlights the importance of good load-balancing in simulations, as here it is essentially the difference between our simulations being tractable or intractable. Additionally, applying the widely-used code GADGET-2 to our problem did not noticeably improve the performance. These issues demonstrate the problems in a "black-box" approach

to numerical simulations — neither of these well-established SPH codes produced the optimal load-balancing for our model in their "off-the-shelf" forms for our particular problem and computational architecture, with HYDRA only performing well after a significant modification was made. Hence we can emphasize how important it is to know the internal workings of simulation codes, so that the user can modify them to be more appropriate for their particular model.

Our modifications to FLASH were primarily fixing mistakes in the feedback subroutines implemented in Scannapieco & Brüggen (2010) and the sub-grid turbulence subroutines implemented in Scannapieco & Brüggen (2008). The mistake in the feedback subroutine (a single missing pair of parentheses) was not pathological — it altered the distribution of feedback bubbles to not correctly follow the Kennicutt-Schmidt law, but as both Scannapieco & Brüggen (2010) and this work concentrated on the properties of the outflow and not the disc, this would not have produced a large error. Furthermore, this algorithm has not been used outside of those two works (to the author's knowledge).

The errors in the sub-grid turbulence subroutine are more critical, with large numbers of cells being incorrectly updated, and the fraction of turbulent kinetic energy in a cell sometimes exceeding 100%, amongst other issues. This algorithm was first implemented in 2008, and has been used in a series of publications since then (Scannapieco & Brüggen 2008; Scannapieco et al. 2009; Gray & Scannapieco 2011). These publications may have failed to catch these mistakes, as they are most noticeable — and most likely to cause FLASH to exit with an error — when the turbulent kinetic energy fraction in a cell is large, and this regime was not explored in these publications[1]. Our models included particularly intense feedback, which triggered this condition, and brought the mistakes to our attention. Tracking the source of these errors proved difficult, and required learning all of the details of the implementation of the algorithm, switching on and off the various sub-grid subroutines to determine which are the sources of the errors, and then tracing through the offending

[1]To prevent these errors from surviving in the code-base, I contacted E. Scannapieco personally and let him know how to correct the subroutines

subroutines one line at a time to determine which lines are incorrect. These tests took several months, and was one of the most intensive parts of this component of this thesis. Again, this stresses that a code can not be used as a black-box — not only can a code be not entirely optimal for a given model (as above), but the code can simply be incorrect, even if it has been used in several refereed publications.

5.2 Effective viscosities due to cloud-cloud collisions in disc galaxies

We performed SPH simulations using HYDRA of Milky-Way-like galaxies to investigate the strength of the effective viscosity due to cloud-cloud collisions. Here we found that the viscous time-scale was on the order of ~ 10 Gyr — which, while long, is much shorter than previous analytic estimates of ~ 1000 Gyr. We also found that these analytic estimates contained an error that when corrected also produces a viscous time-scale of similar order.

However, the viscous time-scale from our simulations appears to be resolution dependent, increasing with improving resolution. This trend corresponds with an increase in the number of clouds produced in the models — a small number of large clouds has a larger effective viscosity than a large number of small clouds. This trend contributes to an interesting situation where very low-resolution simulations — i.e. simulations that do not have sufficient resolution to produce molecular clouds in a galactic disc — will not produce this effective viscosity, but moderate resolution simulations — simulations that resolve molecular cloud formation, but overestimate the mass and underestimate the number of clouds — will produce an effective viscosity that is stronger than it should be.

The first situation applies in particular to cosmological simulations, where the large size of the simulated domain does not usually allow each galaxy to be extremely well-resolved. Here, the problem of the absence of the effects of resolved clouds could be alleviated by the explicit inclusion of an additional viscosity term to account for the effective viscosity of cloud-cloud collisions — indeed, as one of the outcomes of

viscous evolution is to redistribute angular momentum out from the centre of a disc, this might help to overcome issues with overconcentration of angular momentum, at the cost of exacerbating the issues with overconcentration of mass. This effective viscosity should also be included in high-accuracy semi-analytic models (Baugh 2006).

The second situation is more relevant to simulations of individual galaxies, as the highest resolution simulations that are currently being performed are still just falling short of the resolutions required to resolve individual molecular clouds. Unfortunately, there is no "antiviscosity" term that can be applied to remedy this. Simulations must either have sufficient resolution that the difference between the cloud-cloud viscosity is accurate enough for the purposes of the model, or they must have feedback or a temperature floor tuned to prevent explicit cloud formation, instead treating star formation and cloud-cloud collisions with a sub-grid model.

5.3 Cold clouds in outflows

We performed simulations in FLASH of a ULIRG at both a 200 pc galaxy-centre scale and a full-galaxy scale to determine the source of cold high velocity-dispersion gas in hot ULIRG outflows, and wrote a raytracing code to produce artificial spectra for comparison with observations. While we found we could produce this cold high velocity-dispersion gas, this gas was produced by different processes in the different scales, and hence the true source of the gas remains ambiguous. Furthermore, these simulations are not well-converged with respect to resolution and in some cases have not had sufficient time to fully evolve, and so the details of these processes may change if resolution was increased and the simulation was allowed to continue. The heavy computational cost of improving resolution and running the simulation for a long time did not permit us to do this. This work reemphasizes the difficulty of modeling cooling and turbulence accurately in simulations.

The Dimonte-Tipton (DT) sub-grid turbulence model was used to attempt to remove this strong resolution dependence. While the simulations that included the sub-grid turbulence model did indeed show a much weaker resolution dependence, we

were not able to produce any cold gas in the outflow. This cold gas would have to be included in an additional sub-grid model. We have implemented a simple model for this by allowing giving each cell a lognormal PDF with a width based on its turbulent kinetic energy, and assuming that any gas above a certain density in this PDF is cold enough to absorb the NaI line, but this still does not produce any cold gas. While the DT sub-grid turbulence might be sufficiently accurate in describing the bulk motion of the gas, a more detailed model is required to follow the PDFs of gas produced by the RT and RM instabilities.

There are many opportunities to improve the DT model, such as the inclusion of turbulence produced by the Kelvin-Helmholtz instability as well as turbulent viscosity terms, and the production of turbulence from the cascade of larger scale kinetic energy. However, these improvements will still not solve the problem of determining the fraction of gas within a turbulent cell that is cool enough to absorb in the NaI line.

This problem has applications beyond absorption line studies, as identifying cool sub-resolution gas is critical to understanding the unresolved formation of molecular clouds and the stars within them. Here, turbulence is not uniform, isothermal, or incompressible, and so it is a difficult situation to analyze, and the problem currently remains open.

5.4 Future work

In the FLASH models of ULIRG outflows, there are two important avenues for improvement. One is that we can increase the resolution of the simulations without the sub-grid turbulence model. As these simulations are not yet converged, this is more critical than improving the physics of the simulations. However, performing these simulations at a higher resolution will require a great deal of computational resources — either occupying a large amount of time, or requiring access to a larger machine. The other avenue for development is improving the sub-grid turbulence model to better account for the PDFs of gas produced by the RT and RM instabilities.

The models with sub-grid turbulence are indeed better converged, and so improving the physics is the primary concern. However, producing a sub-grid model of this complexity is by no means a trivial task, and the approximations required for any sub-grid model may outweigh the advantages of this method over simply increasing the resolution of the models without sub-grid terms.

The issue of improving the resolution of our disc simulations is more interesting, as these simulations are reaching a stage where sub-grid models (i.e. feedback) have a similar length-scale to resolved physics (i.e. molecular cloud formation). Feedback and star formation have generally been implemented as an unresolved or spatially averaged phenomenon, but if molecular clouds are being resolved, this is no longer self-consistent. Here it is not necessarily helpful to improve resolution ad infinitum, as smaller scale physics requires different sub-grid models. For example, if the spatial resolution is large enough for individual molecular clouds to be resolved, and the time resolution is sufficient for individual supernovae to be resolved, then it is necessary to represent events and structures in an accurate way, perhaps including the effects of photoionization (i.e. HII regions) and other radiative transport effects, as well as the explicit disruption of the molecular cloud and the stars formed within it. If we improve the resolution of our simulations to resolve smaller and smaller scales, we will need to consider these issues.

A more pragmatic concern in improving the resolution of our simulations is the computational load. Here we may be reaching the limits of HYDRA's OpenMP implementation. OpenMP limits a program to shared memory machines, which generally provide fewer processors than distributed memory machines. While large shared-memory machines exist, distributed memory machines are more numerous and hence more accessible to numerical astrophysicists. While we could attempt to further improve the load-balancing of HYDRA, it may be that the best approach is to apply our load-balancing improvements from HYDRA in an MPI code such as GADGET, removing the effective "cap" on processor number. Indeed, the unreleased GADGET-3 already contains a number of load-balancing improvements. However, MPI is not the

best approach for our most accessible hardware. As the nodes in our SMU computing cluster contain a large number of processors (16–32), a pure MPI code will have to pass a large number of messages between any two nodes. A hybrid implementation combining MPI and OpenMP, would be the best approach for our architecture. The upcoming *Phantom* code (Lodato & Price 2010; Price & Federrath 2010) — a hybrid MPI/OpenMP SPH code to be released in 2013 — may perhaps be useful here.

5.5 Conclusion

Despite constantly improving computational power and decades of study in numerical algorithms, we are still far from being able to resolve the critical scales in many astrophysical systems. As such, for the foreseeable future we should expect to continue to rely on approximate models. Nevertheless, we can continue to progress by improving these approximate methods with observation, theory and numerical simulations. Furthermore, these approximate methods can still provide deep physical insight into the modelled phenomenon. Explicitly selecting and refining the physics of the system to build an approximate model helps to clarify the results of each component. Hence, despite the perhaps irresolvable problem of finite resolution, we can, with confidence, continue to establish meaningful conclusions about the universe.

Bibliography

Aarseth S. J., 1963, MNRAS, 126, 223

Agertz O., Kravtsov A. V., Leitner S. N., Gnedin N. Y., 2012, ArXiv e-prints

Agertz O., Lake G., Teyssier R., Moore B., Mayer L., Romeo A. B., 2009, MNRAS, 392, 294

Anathpindika S., 2009, A&A, 504, 437

Angulo R. E., Springel V., White S. D. M., Jenkins A., Baugh C. M., Frenk C. S., 2012, MNRAS, 426, 2046

Aravena M., Wagg J., Papadopoulos P. P., Feain I. J., 2011, ApJ, 737, 64

Armus L., Heckman T., Miley G., 1987, AJ, 94, 831

Ballesteros-Paredes J., Gazol A., Kim J., Klessen R. S., Jappsen A.-K., Tejero E., 2006, ApJ, 637, 384

Ballesteros-Paredes J., Hartmann L. W., Vázquez-Semadeni E., Heitsch F., Zamora-Avilés M. A., 2011, MNRAS, 411, 65

Balsara D. S., 1995, Journal of Computational Physics, 121, 357

Barger A. J., Cowie L. L., Sanders D. B., 1999, ApJ, 518, L5

Barnes J., Efstathiou G., 1987, ApJ, 319, 575

Barnes J. E., Hernquist L., 1992, ARA&A, 30, 705

Bate M. R., Burkert A., 1997, MNRAS, 288, 1060

Baugh C. M., 2006, Reports on Progress in Physics, 69, 3101

Baugh C. M., Lacey C. G., Frenk C. S., et al., 2005, MNRAS, 356, 1191

Beetz C., Schwarz C., Dreher J., Grauer R., 2008, Physics Letters A, 372, 3037

Bekki K., Shioya Y., Whiting M., 2006, MNRAS, 371, 805

Bell E. F., 2002, ApJ, 581, 1013

Benson A. J., 2010, Phys. Rep., 495, 33

Berger M. J., Colella P., 1989, Journal of Computational Physics, 82, 64

Berger M. J., Oliger J., 1984, Journal of Computational Physics, 53, 484

Bertoldi F., Carilli C. L., Menten K. M., et al., 2000, A&A, 360, 92

Bertschinger E., Meiksin A., 1986, ApJ, 306, L1

Binney J., Tremaine S., 2008, Galactic Dynamics: Second Edition, Princeton University Press

Blain A. W., Kneib J.-P., Ivison R. J., Smail I., 1999, ApJ, 512, L87

Blitz L., 1988, in Millimetre and Submillimetre Astronomy, edited by R. D. Wolstencroft, W. B. Burton, vol. 147 of Astrophysics and Space Science Library, 269–279

Blitz L., 1991, in NATO ASIC Proc. 342: The Physics of Star Formation and Early Stellar Evolution, edited by C. J. Lada, N. D. Kylafis, 3

Blitz L., Shu F. H., 1980, ApJ, 238, 148

Blumenthal G. R., Faber S. M., Primack J. R., Rees M. J., 1984, Nature, 311, 517

Boldyrev S., Nordlund Å., Padoan P., 2002, ApJ, 573, 678

Borys C., Smail I., Chapman S. C., Blain A. W., Alexander D. M., Ivison R. J., 2005, ApJ, 635, 853

Bournaud F., Elmegreen B. G., Elmegreen D. M., 2007, ApJ, 670, 237

Brigham E., 1988, The fast Fourier transform and its applications, Prentice-Hall signal processing series, Prentice Hall

Brook C. B., Governato F., Quinn T., et al., 2008, ApJ, 689, 678

Brook C. B., Kawata D., Gibson B. K., Flynn C., 2004, MNRAS, 349, 52

Bullock J. S., Dekel A., Kolatt T. S., et al., 2001, ApJ, 555, 240

Burkert A., 1995, ApJ, 447, L25

Carlberg R. G., 1984, ApJ, 286, 403

Carlson J., Jaffe A., Wiles A., Institute C. M., Society A. M., 2006, The Millennium Prize Problems, Amsns AMS non-series Title Series, American Mathematical Society

Ceverino D., Klypin A., 2009, ApJ, 695, 292

Chandrasekhar S., 1961, Hydrodynamic and hydromagnetic stability

Christensen C. R., Quinn T., Stinson G., Bellovary J., Wadsley J., 2010, ApJ, 717, 121

Clemens D. P., Sanders D. B., Scoville N. Z., Solomon P. M., 1997, VizieR Online Data Catalog, 7114, 0

Clements D. L., Sutherland W. J., McMahon R. G., Saunders W., 1996, MNRAS, 279, 477

Cole S., Aragon-Salamanca A., Frenk C. S., Navarro J. F., Zepf S. E., 1994, MNRAS, 271, 781

Colella P., Woodward P. R., 1984, Journal of Computational Physics, 54, 174

Colina L., Arribas S., Clements D., 2004, ApJ, 602, 181

Conselice C. J., Chapman S. C., Windhorst R. A., 2003, ApJ, 596, L5

Cooley J. W., Tukey J. J., 1965, Math. Comp., 19, 297

Dahlen T., Strolger L.-G., Riess A. G., et al., 2004, ApJ, 613, 189

Das M., Jog C. J., 1996, ApJ, 462, 309

Davé R., Finlator K., Oppenheimer B. D., et al., 2010, MNRAS, 404, 1355

Davis M., Efstathiou G., Frenk C. S., White S. D. M., 1985, ApJ, 292, 371

de Grijp M. H. K., Miley G. K., Lub J., de Jong T., 1985, Nature, 314, 240

Dekel A., Sari R., Ceverino D., 2009, ApJ, 703, 785

Dib S., Bell E., Burkert A., 2006, ApJ, 638, 797

Dib S., Brandenburg A., Kim J., Gopinathan M., André P., 2008, ApJ, 678, L105

Dimonte G., Tipton R., 2006, Physics of Fluids, 18, 8, 085101

Dobbs C. L., Bonnell I. A., 2008, MNRAS, 385, 1893

Dobbs C. L., Bonnell I. A., Pringle J. E., 2006, MNRAS, 371, 1663

Dolag K., Vazza F., Brunetti G., Tormen G., 2005, MNRAS, 364, 753

Durier F., Dalla Vecchia C., 2012, MNRAS, 419, 465

Efstathiou G., Jones B. J. T., 1979, MNRAS, 186, 133

Efstathiou G., Lake G., Negroponte J., 1982, MNRAS, 199, 1069

Elahi P. J., 2009, Simulations of scale-free cosmologies for the small-scale cold dark matter universe, Ph.D. thesis, Queen's University (Canada

Elmegreen B. G., Elmegreen D. M., 2005, ApJ, 627, 632

Elmegreen B. G., Scalo J., 2004, ARA&A, 42, 211

Everett J. E., Churchwell E., 2010, ApJ, 713, 592

Faber T. E., 1995, Fluid Dynamics for Physicists

Fall S. M., Efstathiou G., 1980, MNRAS, 193, 189

Farrah D., Lonsdale C. J., Weedman D. W., et al., 2008, ApJ, 677, 957

Farrah D., Surace J. A., Veilleux S., Sanders D. B., Vacca W. D., 2005, ApJ, 626, 70

Favre A., 1983, Physics of Fluids, 26, 2851

Federrath C., Klessen R. S., Schmidt W., 2008, ApJ, 688, L79

Federrath C., Klessen R. S., Schmidt W., 2009, ApJ, 692, 364

Federrath C., Roman-Duval J., Klessen R. S., Schmidt W., Mac Low M.-M., 2010, A&A, 512, A81

Ferriere K. M., Mac Low M.-M., Zweibel E. G., 1991, ApJ, 375, 239

Flagey N., Noriega-Crespo A., Boulanger F., et al., 2009, ApJ, 701, 1450

Fox M. J., Efstathiou A., Rowan-Robinson M., et al., 2002, MNRAS, 331, 839

Foyle K., Courteau S., Thacker R. J., 2008, MNRAS, 386, 1821

Frigo M., Johnson S. G., 2012, Astrophysics Source Code Library, 1015

Fryxell B., Olson K., Ricker P., et al., 2000, ApJS, 131, 273

Fujita A., Martin C. L., Mac Low M.-M., New K. C. B., Weaver R., 2009, ApJ, 698, 693

Fukunaga M., Tosa M., 1989, PASJ, 41, 241

Gad-el Hak M., 1995, Journal of Fluids Engineering, 117, 3

Gammie C. F., 2001, ApJ, 553, 174

Gammie C. F., Ostriker J. P., Jog C. J., 1991, ApJ, 378, 565

Garnier E., Adams N., Sagaut P., 2009, Large Eddy Simulation for Compressible Flows

Genzel R., Baker A. J., Tacconi L. J., et al., 2003, ApJ, 584, 633

Genzel R., Lutz D., Sturm E., et al., 1998, ApJ, 498, 579

Giavalisco M., Dickinson M., Ferguson H. C., et al., 2004, ApJ, 600, L103

Gingold R. A., Monaghan J. J., 1977, MNRAS, 181, 375

Gittins D. M., Clarke C. J., Bate M. R., 2003, MNRAS, 340, 841

Glover S. C. O., Mac Low M., 2007, ApJS, 169, 239

Goldreich P., Kwan J., 1974, ApJ, 189, 441

Goldreich P., Tremaine S. D., 1978, Icarus, 34, 227

Gott III J. R., Thuan T. X., 1976, ApJ, 204, 649

Governato F., Willman B., Mayer L., et al., 2007, MNRAS, 374, 1479

Gray W. J., Scannapieco E., 2011, ApJ, 733, 88

Greve T. R., Bertoldi F., Smail I., et al., 2005, MNRAS, 359, 1165

Guedes J., Callegari S., Madau P., Mayer L., 2011, ApJ, 742, 76

Guo F., Mathews W. G., 2012, ApJ, 756, 181

Heckman T. M., Dahlem M., Eales S. A., Fabbiano G., Weaver K., 1996, ApJ, 457, 616

Heckman T. M., Lehnert M. D., Strickland D. K., Armus L., 2000, ApJS, 129, 493

Hernquist L., Mihos J. C., 1995, ApJ, 448, 41

Hirt C. W., Amsden A. A., Cook J. L., 1974, Journal of Computational Physics, 14, 227

Hockney R. W., Eastwood J. W., 1988, Computer simulation using particles

Hockney R. W., Hohl F., 1969, AJ, 74, 1102

Hohl F., 1976, AJ, 81, 30

Hohl F., Hockney R. W., 1969, Journal of Computational Physics, 4, 306

Hopkins P. F., Hernquist L., Cox T. J., Di Matteo T., Robertson B., Springel V., 2006, ApJS, 163, 1

Hopkins P. F., Quataert E., Murray N., 2012a, MNRAS, 421, 3522

Hopkins P. F., Quataert E., Murray N., 2012b, MNRAS, 421, 3488

Houck J. R., Schneider D. P., Danielson G. E., et al., 1985, ApJ, 290, L5

Hutchings J. B., Neff S. G., 1991, AJ, 101, 2001

Iapichino L., Niemeyer J. C., 2008, MNRAS, 388, 1089

Jappsen A.-K., Klessen R. S., Larson R. B., Li Y., Mac Low M.-M., 2005, A&A, 435, 611

Jeans J. H., 1902, Royal Society of London Philosophical Transactions Series A, 199, 1

Jog C. J., Ostriker J. P., 1988, ApJ, 328, 404

Jog C. J., Solomon P. M., 1984, ApJ, 276, 114

Joung M. R., Mac Low M.-M., Bryan G. L., 2009, ApJ, 704, 137

Katz N., 1992, ApJ, 391, 502

Katz N., Gunn J. E., 1991, ApJ, 377, 365

Kauffmann G., White S. D. M., Guiderdoni B., 1993, MNRAS, 264, 201

Kaufmann T., Bullock J. S., Maller A. H., Fang T., Wadsley J., 2009, MNRAS, 396, 191

Kaufmann T., Mayer L., Wadsley J., Stadel J., Moore B., 2006, MNRAS, 370, 1612

Kaufmann T., Mayer L., Wadsley J., Stadel J., Moore B., 2007, MNRAS, 375, 53

Kazantzidis S., Magorrian J., Moore B., 2004, ApJ, 601, 37

Kennicutt R. C., 1997, in Astrophysics and Space Science Library, vol. 161 of Astrophysics and Space Science Library, 171–195

Kennicutt Jr. R. C., 1998, ApJ, 498, 541

Khokhlov A., 1998, Journal of Computational Physics, 143, 519

Kim J., Park C., Rossi G., Lee S. M., Gott III J. R., 2011, Journal of Korean Astronomical Society, 44, 217

Kim W., Ostriker E. C., 2007, ApJ, 660, 1232

Kitsionas S., Whitworth A. P., 2002, MNRAS, 330, 129

Kitsionas S., Whitworth A. P., 2007, MNRAS, 378, 507

Klessen R. S., 2000, ApJ, 535, 869

Klessen R. S., 2001, ApJ, 556, 837

Klessen R. S., Heitsch F., Mac Low M.-M., 2000, ApJ, 535, 887

Konstandin L., Federrath C., Klessen R. S., Schmidt W., 2012, Journal of Fluid Mechanics, 692, 183

Koo B.-C., McKee C. F., 1992, ApJ, 388, 103

Kritsuk A. G., Norman M. L., Padoan P., Wagner R., 2007, ApJ, 665, 416

Kuijken K., Dubinski J., 1995, MNRAS, 277, 1341

Larson R. B., 1981, MNRAS, 194, 809

Larson R. B., 1994, in The Structure and Content of Molecular Clouds, edited by T. L. Wilson, K. J. Johnston, vol. 439 of Lecture Notes in Physics, Berlin Springer Verlag, 13

Laurent O., Mirabel I. F., Charmandaris V., Le Floc'h E., Lutz D., Genzel R., 2000, in ISO Beyond the Peaks: The 2nd ISO Workshop on Analytical Spectroscopy, edited by A. Salama, M. F. Kessler, K. Leech, B. Schulz, vol. 456 of ESA Special Publication, 249

Lebofsky M. J., Rieke G. H., 1979, ApJ, 229, 111

Leonard A., 1974, Advances in Geophysics, 18, A237

Lesieur M., Métais O., Comte P., 2005, Large-Eddy Simulations of Turbulence

Li P. S., McKee C. F., Klein R. I., Fisher R. T., 2008, ApJ, 684, 380

Li P. S., Norman M. L., Mac Low M.-M., Heitsch F., 2004, ApJ, 605, 800

Li Y., Klessen R. S., Mac Low M.-M., 2003, ApJ, 592, 975

Li Y., Mac Low M., Klessen R. S., 2005, ApJ, 626, 823

Li Z.-Y., Nakamura F., 2006, ApJ, 640, L187

Lin D. N. C., Pringle J. E., 1987, ApJ, 320, L87

Lodato G., Price D. J., 2010, MNRAS, 405, 1212

Lohner R., 1987, Computer Methods in Applied Mechanics and Engineering, 61, 323

Lonsdale C. J., Farrah D., Smith H. E., 2006, Ultraluminous Infrared Galaxies, 285, Springer Verlag

Lucy L. B., 1977, AJ, 82, 1013

Mac Low M.-M., 1999, ApJ, 524, 169

Mac Low M.-M., Balsara D. S., Kim J., de Avillez M. A., 2005, ApJ, 626, 864

Mac Low M.-M., Klessen R. S., Burkert A., Smith M. D., 1998, Physical Review Letters, 80, 2754

Mac Low M.-M., McCray R., Norman M. L., 1989, ApJ, 337, 141

MacNeice P., Olson K. M., Mobarry C., de Fainchtein R., Packer C., 2000, Computer Physics Communications, 126, 330

Maier A., Iapichino L., Schmidt W., Niemeyer J. C., 2009, ApJ, 707, 40

Martin C. L., 2005, ApJ, 621, 227

Martin C. L., 2006, ApJ, 647, 222

Matsui H., Saitoh T. R., Makino J., et al., 2012, ApJ, 746, 26

McDowell J. C., Clements D. L., Lamb S. A., et al., 2003, ApJ, 591, 154

McKee C. F., Ostriker J. P., 1977, ApJ, 218, 148

Melnick J., Mirabel I. F., 1990, A&A, 231, L19

Meshkov E., 1969, Fluid Dynamics, 4, 101

Mihalas D., Weibel Mihalas B., 1984, Foundations of radiation hydrodynamics

Mo H. J., Mao S., 2002, MNRAS, 333, 768

Monaghan J. J., 1992, ARA&A, 30, 543

Monaghan J. J., 2005, Reports on Progress in Physics, 68, 1703

Monaghan J. J., Lattanzio J. C., 1985, A&A, 149, 135

Mori M., Burkert A., 2000, ApJ, 538, 559

Mori M., Yoshii Y., Tsujimoto T., Nomoto K., 1997, ApJ, 478, L21

Murante G., Monaco P., Giovalli M., Borgani S., Diaferio A., 2010, MNRAS, 405, 1491

Murray N., 2011, ApJ, 729, 133

Murray N., Quataert E., Thompson T. A., 2005, ApJ, 618, 569

Naab T., Johansson P. H., Ostriker J. P., Efstathiou G., 2007, ApJ, 658, 710

Narayan R., Medvedev M. V., 2001, ApJ, 562, L129

Narayanan D., Cox T. J., Hayward C. C., Younger J. D., Hernquist L., 2009, MNRAS, 400, 1919

Narayanan D., Dey A., Hayward C. C., et al., 2010, MNRAS, 407, 1701

Navarro J. F., Frenk C. S., White S. D. M., 1996, ApJ, 462, 563

Neri R., Genzel R., Ivison R. J., et al., 2003, ApJ, 597, L113

Norman C. A., Ikeuchi S., 1989, ApJ, 345, 372

Offner S. S. R., Klein R. I., McKee C. F., 2008, ApJ, 686, 1174

Oppenheimer B. D., Davé R., 2009, MNRAS, 395, 1875

O'Shea B. W., Bryan G., Bordner J., et al., 2004, ArXiv Astrophysics e-prints

Ostriker E. C., Shetty R., 2011, ApJ, 731, 41

Ozernoy L. M., Fridman A. M., Biermann P. L., 1998, A&A, 337, 105

Padoan P., Jimenez R., Nordlund Å., Boldyrev S., 2004, Physical Review Letters, 92, 19, 191102

Pavlovski G., Smith M. D., Mac Low M.-M., 2006, MNRAS, 368, 943

Peebles P. J. E., 1970, AJ, 75, 13

Peebles P. J. E., 1971, A&A, 11, 377

Pérez-Torres M. A., Alberdi A., Romero-Cañizales C., et al., 2008, in The role of VLBI in the Golden Age for Radio Astronomy

Phillips A. C., 1993, AJ, 105, 486

Piomelli U., 1999, Progress in Aerospace Sciences, 35, 335

Porter D., Pouquet A., Sytine I., Woodward P., 1999, Physica A Statistical Mechanics and its Applications, 263, 263

Price D. J., Bate M. R., 2008, MNRAS, 385, 1820

Price D. J., Federrath C., 2010, MNRAS, 406, 1659

Ptak A., Heckman T., Levenson N. A., Weaver K., Strickland D., 2003, ApJ, 592, 782

Rafikov R. R., 2001, MNRAS, 323, 445

Rafikov R. R., 2009, ApJ, 704, 281

Raymond J. C., Cox D. P., Smith B. W., 1976, ApJ, 204, 290

Richtmyer R. D., 1960, Communications on Pure and Applied Mathematics, 13, 2, 297

Rieke G. H., Low F. J., 1972, ApJ, 176, L95

Robertson B. E., Kravtsov A. V., 2008, ApJ, 680, 1083

Roman-Duval J., Jackson J. M., Heyer M., Rathborne J., Simon R., 2010, ApJ, 723, 492

Saitoh T. R., Daisaka H., Kokubo E., et al., 2009, PASJ, 61, 481

Sanders D. B., Scoville N. Z., Solomon P. M., 1985, ApJ, 289, 373

Sanders D. B., Soifer B. T., Elias J. H., et al., 1988, ApJ, 325, 74

Sanders R. H., 1977, ApJ, 217, 916

Sanders R. H., Huntley J. M., 1976, ApJ, 209, 53

Sarazin C. L., 1986, Reviews of Modern Physics, 58, 1

Scalo J., 1990, in Physical Processes in Fragmentation and Star Formation, edited by R. Capuzzo-Dolcetta, C. Chiosi, A. di Fazio, vol. 162 of Astrophysics and Space Science Library, 151–176

Scannapieco C., White S. D. M., Springel V., Tissera P. B., 2009, MNRAS, 396, 696

Scannapieco E., Bildsten L., 2005, ApJ, 629, L85

Scannapieco E., Brüggen M., 2008, ApJ, 686, 927

Scannapieco E., Brüggen M., 2010, MNRAS, 405, 1634

Scannapieco E., Ferrara A., Madau P., 2002, ApJ, 574, 590

Scannapieco E., Oh S. P., 2004, ApJ, 608, 62

Schmidt W., Federrath C., 2011, A&A, 528, A106

Schmidt W., Federrath C., Hupp M., Kern S., Niemeyer J. C., 2009, A&A, 494, 127

Schmidt W., Niemeyer J. C., Hillebrandt W., 2006, A&A, 450, 265

Schneider N., Bontemps S., Simon R., et al., 2011, A&A, 529, A1

Schuessler I., Schmitt D., 1981, A&A, 97, 373

Scoville N. Z., Yun M. S., Sanders D. B., Clemens D. P., Waller W. H., 1987, ApJS, 63, 821

Sharp D. H., 1984, Physica D Nonlinear Phenomena, 12, 3

Shetty R., Ostriker E. C., 2008, ApJ, 684, 978

Shu F. H., 1992, Physics of Astrophysics, Vol. II, University Science Books

Sijacki D., Springel V., 2006, MNRAS, 371, 1025

Sinha K., Mahesh K., Candler G. V., 2003, Physics of Fluids, 15, 2290

Smagorinsky J., 1963, Monthly Weather Review, 91, 99

Smail I., Ivison R. J., Blain A. W., Kneib J.-P., 1998, ApJ, 507, L21

Solomon P. M., Rivolo A. R., 1989, ApJ, 339, 919

Solomon P. M., Rivolo A. R., Barrett J., Yahil A., 1987, ApJ, 319, 730

Spitzer L., 1978, Physical processes in the interstellar medium

Springel V., 2005, MNRAS, 364, 1105

Springel V., 2010, MNRAS, 401, 791

Springel V., White S. D. M., Jenkins A., et al., 2005, Nature, 435, 629

Staniforth A., Côté J., 1991, Monthly Weather Review, 119, 2206

Stil J., Wityk N., Ouyed R., Taylor A. R., 2009, ApJ, 701, 330

Stinson G., Seth A., Katz N., Wadsley J., Governato F., Quinn T., 2006, MNRAS, 373, 1074

Stinson G. S., Bailin J., Couchman H., et al., 2010, MNRAS, 408, 812

Stone J. M., Ostriker E. C., Gammie C. F., 1998, ApJ, 508, L99

Surace J. A., Sanders D. B., Vacca W. D., Veilleux S., Mazzarella J. M., 1998, ApJ, 492, 116

Sutherland R. S., Dopita M. A., 1993, ApJS, 88, 253

Swinbank A. M., Lacey C. G., Smail I., et al., 2008, MNRAS, 391, 420

Tasker E. J., 2011, ApJ, 730, 11

Tasker E. J., Tan J. C., 2009, ApJ, 700, 358

Taylor G., 1950, Royal Society of London Proceedings Series A, 201, 192

Teng S. H., Veilleux S., Anabuki N., et al., 2009, ApJ, 691, 261

Teyssier R., 2002, A&A, 385, 337

Thacker R. J., Couchman H. M. P., 2000, ApJ, 545, 728

Thacker R. J., Couchman H. M. P., 2001, ApJ, 555, L17

Thacker R. J., Couchman H. M. P., 2006, Computer Physics Communications, 174, 540

Thomas P. A., Couchman H. M. P., 1992, MNRAS, 257, 11

Tilley D. A., Pudritz R. E., 2007, MNRAS, 382, 73

Tomisaka K., Ikeuchi S., 1986, PASJ, 38, 697

Toomre A., 1964, ApJ, 139, 1217

Truelove J. K., Klein R. I., McKee C. F., Holliman II J. H., Howell L. H., Greenough J. A., 1997, ApJ, 489, L179+

U. Washington, 2012, University of Washington N-Body Shop, fof code

Valdarnini R., 2011, A&A, 526, A158+

Vazquez-Semadeni E., 1994, ApJ, 423, 681

Vázquez-Semadeni E., Kim J., Ballesteros-Paredes J., 2005, ApJ, 630, L49

Vazza F., Brüggen M., Gheller C., Brunetti G., 2012, MNRAS, 421, 3375

Vazza F., Brunetti G., Kritsuk A., Wagner R., Gheller C., Norman M., 2009, A&A, 504, 33

Veilleux S., 2006, New A Rev., 50, 701

Voigt L. M., Fabian A. C., 2004, MNRAS, 347, 1130

Vollmer B., Beckert T., 2002, A&A, 382, 872

Vollmer B., Beckert T., 2003, A&A, 404, 21

Wada K., Norman C. A., 2001, ApJ, 547, 172

Wadsley J. W., Stadel J., Quinn T., 2004, New A, 9, 137

Webb T. M. A., Lilly S. J., Clements D. L., et al., 2003, ApJ, 597, 680

White S. D. M., Frenk C. S., 1991, ApJ, 379, 52

White S. D. M., Rees M. J., 1978, MNRAS, 183, 341

Widrow L. M., Dubinski J., 2005, ApJ, 631, 838

Widrow L. M., Pym B., Dubinski J., 2008, ApJ, 679, 1239

Williams J. P., McKee C. F., 1997, ApJ, 476, 166

Williamson D. J., Thacker R. J., 2012, MNRAS, 421, 2170

Woodward P., Colella P., 1984, Journal of Computational Physics, 54, 115

Wulf W. A., McKee S. A., 1995, SIGARCH Comput. Archit. News, 23, 1, 20

Zakamska N. L., Narayan R., 2003, ApJ, 582, 162

Zaninetti L., 2012, MNRAS, 425, 2343

Zuckerman B., Palmer P., 1974, ARA&A, 12, 279